

# Examination of Histotaphonomic and Histochemical Methods in Establishing the Early Postmortem Interval

by

Ashley Ciúine Smith

A thesis submitted in conformity with the requirements  
for the degree of Doctor of Philosophy

Department of Anthropology  
University of Toronto

© Copyright by Ashley C. Smith 2025

# Examination of Histotaphonomic and Histochemical Methods in Establishing the Early Postmortem Interval

Ashley C. Smith

Doctor of Philosophy

Department of Anthropology  
University of Toronto

2025

## Abstract

One of the more difficult tasks in the assessment of human remains is establishing the postmortem interval (PMI). Anthropologists and pathologists typically rely on various histochemical, soft tissue decomposition, or bone degradation methodologies in the assessment of PMI, however as time progresses postmortem, precision with these methodologies decreases. Difficulty arises after the current favoured histochemical methodologies (vitreous humor) becomes non-viable and soft tissue decomposition becomes the remaining avenue of assessment. This difficulty is increased when soft tissue degradation has progressed beyond usefulness yet before degradation of bone has taken place. This study (the culmination of Ch. 2.2, 2.3, 3.2, 4.2, and 5.1) used laser scanning confocal microscopy to examine potential avenues of fluorescent histotaphonomic and histochemical means to determine if such methods could be used in PMI estimation.

This cumulative study examined histotaphonomic changes, as well as the degradation of osteopontin, osteocalcin, and osteoclasts. It utilized animal remains, archaeological human remains, and cadaveric material from 18 individuals. The histotaphonomic study utilized basic

fuchsin and toluidine blue, as well as unstained bone, while the protein portions utilized cadaveric iliac samples labeled with osteopontin and osteocalcin primary antibodies with Alexa Fluor™(tm) 555, labeled independently. Ch. 4.2 used iliac samples labeled with MitoTracker™ Red FM Dye to label the osteoclasts. The samples of Ch. 3.2 and 4.2 were divided into 4 time-groups consisting of a biopsy sample that was fixed within 3 hours to represent the “perimortem,” period and 3 cadaveric groups including early-postmortem (defined as 48 hours or less), 7-day, and 14-day postmortem groups; noting the same individuals were used in both chapters.

Relying on a variety of analyses but primarily Kruskal-Wallis H-tests, Spearman Rho correlation analyses, and Freidman repeated measures tests, with outliers included and removed, the results of this study found that there is a significant degradation in both osteopontin fluorescence though with a weak to moderate correlation, while the osteocalcin fluorescence remained relatively stable. However, closer analyses within the protein studies found that no clear pattern could be discerned within either protein. This study also found a significant and strongly correlated decrease in osteoclasts over time, with a strong level of predictability using a Kernal Ridge Regression analysis, and there were significant differences using histotaphonomy as well, particularly in the fluorescence channels registered. The overall results of this study found that there is potential in using LSCM in examining histotaphonomy and histochemistry as a tool in calculating the PMI, but that the best avenues are limited to histotaphonomy and osteoclast degradation.

## Acknowledgments

To begin, I wish to acknowledge those individuals who has donated their earthly remains to science via the Willed Body Donation Program through the Division of Anatomy at the University of Toronto, as well as those who consented to donate tissue through the Centre Hospitalier de l' Université de Montréal. I would also like to thank Ian Bell with the Division of Anatomy, University of Toronto, and Natalie Dion of the Department of Pathology, Laboratory of Bone Histomorphometry, Centre Hospitalier de l' Université de Montréal, without whose assistance, and supply of samples, this project never would have occurred. Further, I would like to thank my supervisor, Dr. Tracy Rogers for all of your assistance and guidance throughout this project; it has really meant a lot.

On a personal note, I would also like to acknowledge and thank Jenna Schall, Evonne Turner-Byfield, Patrick Bozek, Kathryn Campeau, Danielle Carrol, and Tracey Wilson, and all the others who have helped sustain me throughout this project – your friendship is more than I could ever have asked. Lastly, I would like to thank my parents, Douglas and Cheryl Smith, who held me up even when I was at my lowest.

*Nor have we herein barr'd your better wisdoms, which have freely gone with this affair along.  
For all, our thanks.*

– Claudius, *Hamlet*, Act I Scene 2 [Lines 14 – 16] (W<sup>m</sup> Shakespeare)

# Table of Contents

Acknowledgments.....	iii
Table of Contents .....	iv
List of Tables .....	viii
List of Figures .....	x
List of Appendices .....	xv
Chapter 1 Introduction .....	1
1.1 Purpose & Significance.....	1
1.2 Background.....	3
1.2.1 Theories of Death.....	3
1.2.2 Bone Composition .....	4
1.2.2.1 Osteoclasts.....	5
1.2.2.2 Osteopontin and Osteocalcin.....	9
1.2.3 Decomposition .....	13
1.2.3.1 Fresh .....	14
1.2.3.2 Bloat/Early Decay .....	15
1.2.3.3 Later Decomposition Stages.....	16
1.2.4 Methods for Assessing Decomposition .....	17
1.2.5 Bone Microstructural Diagenesis.....	19
1.2.5.1 Oxford Histological Index.....	20
1.2.5.2 Bioerosion Index .....	21
1.2.6 Laser Confocal Microscopy.....	22
1.2.7 Laser Scanning Confocal Microscopy <i>versus</i> Light Microscopy .....	26
1.2.8 Fixation, Staining, and Labeling.....	27
1.3 Context.....	29
Chapter 2 Histotaphonomy and Histochemical Foundations.....	30

2.1 Chapter Introduction .....	30
2.2 Use of laser-scanning confocal microscopy in the detection of diagenesis in bone (188).....	34
2.2.1 Introduction.....	34
2.2.2 Materials and Methods.....	36
2.2.3 Preparation and initial examination of all samples .....	37
2.2.3.1 Phase 1 sample and methodology.....	37
2.2.3.2 Phase 2 sample and methodology.....	41
2.2.4 Results.....	44
2.2.4.1 Phase 1 .....	44
2.2.4.2 Phase 2.....	50
2.2.5 Discussion & Conclusion.....	56
2.3 Effect of embalming on the preservation of osteopontin in bone.....	60
2.3.1 Introduction.....	60
2.3.2 Materials and Methods.....	63
2.3.3 Data Analysis .....	67
2.3.4 Results.....	68
2.3.5 Discussion.....	73
Chapter 3 Osteopontin and Osteocalcin Degradation as a Means of Establishing the Early Postmortem Interval.....	76
3.1 Chapter Introduction .....	76
3.2 Degradation of osteocalcin and osteopontin for use in postmortem interval estimation during the early postmortem period.....	78
3.2.1 Introduction.....	78
3.2.2 Materials and Methods.....	85
3.2.3 Results.....	91
3.2.3.1 Outliers .....	105

3.2.4	Discussion and Conclusion .....	125
Chapter 4	Osteocellular Degradation: Its Use in Calculating the Early Postmortem Interval.....	131
4.1	Chapter Introduction .....	131
4.2	Cellular degradation and migration in bone as a tool to investigate the postmortem interval .....	133
4.2.1	Introduction.....	133
4.2.1.1	Decomposition.....	133
4.2.1.1.1	Fresh .....	134
4.2.1.1.2	Bloat/Early Decay.....	135
4.2.1.2	Methods for Assessing the Postmortem Interval.....	136
4.2.1.3	Osteoclasts .....	138
4.2.2	Materials and Methods.....	142
4.2.3	Results.....	150
4.2.4	Discussion and Conclusion .....	157
Chapter 5	Conclusions .....	164
5.1	Combined Study Findings.....	164
5.2	Limitations and Future Projects .....	177
5.3	Reflections .....	178
5.4	Implications.....	181
References	.....	184
Appendices	.....	203
Appendix A	.....	203
Appendix B	.....	204
Appendix C	.....	207
Appendix D	.....	209
6.4.2	Use of Samples Approval from CHUM.....	211

6.4.3	Material Transfer Agreements .....	213
	Copyright Acknowledgements.....	216

## List of Tables

Table 1.2-1: Stages of Decomposition.....	15
Table 1.2-2: Oxford Histological Index.....	21
Table 2.2-1: Samples and stains for phase 1 study.....	41
Table 2.2-2: Samples and stains for phase 2 study.....	42
Table 2.2-3: Results of the phase 1 quantitative study.....	49
Table 2.2-4: Red/Green/Blue histogram means from the Phase 2 study.....	56
Table 2.3-1: Sample demographics for Ch. 2.3 including age and sex.....	67
Table 2.3-2: List of the mean pixel intensities and standard deviations for all samples.....	72
Table 2.3-3: Age and Sex Kruskal-Wallis H-test and Mann-Whitney U-test Results.....	72
Table 3.2-1: Ratio differences between the time groups.....	102
Table 3.2-2: Post Hoc Pairwise Tests.....	102
Table 3.2-3: Kruskal Wallis (Age) and Mann-Whitney U-test (Sex) Results.....	104
Table 3.2-4: Post Hoc Pairwise results for Kruskal-Wallis H-tests with both individual outliers removed and whole individuals removed.....	120
Table 4.2-1: Post Hoc Pairwise Results.....	152
Table 4.2-2: Post Hoc Pairwise Results with Individual Outliers Removed.....	154
Table 4.2-3: Post Hoc Pairwise Results with Whole Outliers Removed.....	156
Table 4.2-4: Results of the Kruskal-Wallis (Age) and Mann-Whitney U-test (Sex) results.....	157
Table 5.1-1: Post hoc pairwise results from combined Ch. 2.3 & Ch. 3.2 osteopontin mean intensity.....	167

Table 5.1-2: Post hoc pairwise results of combined Ch. 2.3 & Ch. 3.2 osteopontin standard deviation data. ....	168
Table 5.1-3: Post hoc pairwise combined Ch. 2.3 & Ch. 3.2 mean intensity results with individual outliers removed. ....	171
Table 5.1-4: Post hoc pairwise results of combined Ch. 2.3 & Ch. 3.2 osteopontin standard deviation data with individual outliers removed.....	171
Table 5.1-5: Post hoc pairwise results for mean intensity of combined Ch. 2.3 & Ch. 3.2 with whole outliers removed. ....	174
Table 5.1-6: Post hoc pairwise results for standard deviation of combined Ch. 2.3 & Ch. 3.2 with whole outliers removed. ....	175
Table 5.1-7: Combined (Ch. 2.3 & 3.2) osteopontin age and sex results. ....	176
Table 6.1-1: Sample demographic data for Ch. 3.2 & 4.2 .....	203
Table 6.2-1: Raw protein data.....	204
Table 6.3-1: Osteoclast count data.....	207

## List of Figures

Figure 1.2.1: Schematic of Minsky's confocal microscope .....	22
Figure 1.2.2: Schematic of a modern LSCM .....	26
Figure 2.2.1: Histogram of an unstained 5-year pig sample .....	40
Figure 2.2.2: Image of “Fresh” unstained pig bone sample.....	45
Figure 2.2.3: Image of 5-year unstained pig bone sample depicting diagenetic alteration .....	46
Figure 2.2.4: Grayscale image of “Fresh” pig bone with unknown cell highlighted.....	47
Figure 2.2.5: Red mean box plot.....	47
Figure 2.2.6: Green mean box plot. ....	48
Figure 2.2.7: Blue mean box plot.....	48
Figure 2.2.8: Scatter plot of Phase 1 means with outliers removed.....	50
Figure 2.2.9: Ratio of fluorescence intensity using unstained bone .....	51
Figure 2.2.10: Ratio of fluorescence intensity from the Clinical sample using toluidine blue.....	51
Figure 2.2.11: Ratio of fluorescence intensity from Apollonian sample using toluidine blue. ....	52
Figure 2.2.12: Image of Clinical iliac sample stained with toluidine blue .....	53
Figure 2.2.13: Image of Apollonian rib section stained with toluidine blue .....	54
Figure 2.2.14: Image of unstained section of femur .....	54
Figure 2.2.15: Image of femoral control stained with toluidine blue .....	55
Figure 2.2.16: Scatter plot of Phase 2 demonstrating the distribution of red, green, and blue means across the four groups with 2 outliers removed.....	55
Figure 2.2.17: Image of femoral cortex stained with Basic Fuchsin .....	57

Figure 2.3.1: Variation in unembalmed FIJI/ImageJ© histograms .....	70
Figure 2.3.2: Variation in embalmed sample FIJI/ImageJ© histograms .....	70
Figure 2.3.3: Plot of image pixel intensity and image standard deviation.....	70
Figure 2.3.4: Box plot of mean pixel intensity with outlier (#4) removed. ....	71
Figure 2.3.5: Box plot of pixel standard deviation data with 2 outliers removed.....	71
Figure 3.2.1: Osteopontin labeled cortical bone .....	91
Figure 3.2.2: Osteocalcin labeled bone.....	92
Figure 3.2.3: Osteocalcin fluorescence intensity over the four time-groups. ....	95
Figure 3.2.4: Osteocalcin pixel intensity group means.....	95
Figure 3.2.5: Osteocalcin pixel standard deviation.....	96
Figure 3.2.6: Line graph of individual postmortem osteocalcin mean intensity fluctuation. ....	96
Figure 3.2.7: Line graph of postmortem osteocalcin standard deviation fluctuation. ....	97
Figure 3.2.8: Osteopontin fluorescence intensity data.....	97
Figure 3.2.9: Osteopontin pixel intensity group means. ....	98
Figure 3.2.10: Osteopontin pixel intensity standard deviation. ....	98
Figure 3.2.11: Postmortem osteopontin mean intensity fluctuation. ....	99
Figure 3.2.12: Postmortem osteopontin standard deviation fluctuation. ....	99
Figure 3.2.13: OPN:OC ratio fluorescence data as a relationship of mean intensity to standard deviation.....	100
Figure 3.2.14. OPN:OC mean intensity data. ....	100
Figure 3.2.15: OPN:OC standard deviation data. ....	101

Figure 3.2.16: Postmortem OPN:OC mean intensity fluctuations.....	101
Figure 3.2.17: OPN:OC postmortem standard deviation fluctuations.....	102
Figure 3.2.18: Osteocalcin mean intensity with individual outliers removed. ....	109
Figure 3.2.19: Osteocalcin standard deviation with individual outliers removed. ....	109
Figure 3.2.20: Osteocalcin mean intensity with whole individuals removed. ....	110
Figure 3.2.21: Osteocalcin standard deviations with whole individuals removed. ....	110
Figure 3.2.22: Postmortem osteocalcin mean intensity fluctuations with individual outliers removed.....	111
Figure 3.2.23: Postmortem osteocalcin standard deviation fluctuations with individual outliers removed.....	111
Figure 3.2.24: Postmortem osteocalcin mean intensity fluctuations with whole individuals removed.....	112
Figure 3.2.25: Postmortem osteocalcin standard deviation fluctuations with whole individuals removed.....	112
Figure 3.2.26: Osteopontin mean intensity with individual outliers removed.....	113
Figure 3.2.27: Osteopontin standard deviations with individual outliers removed. ....	113
Figure 3.2.28: Osteopontin mean intensity with whole individuals removed. ....	114
Figure 3.2.29: Osteopontin standard deviations with whole individuals removed.....	114
Figure 3.2.30: Postmortem osteopontin mean intensity fluctuations with individual outliers removed.....	115
Figure 3.2.31: Postmortem osteopontin standard deviation fluctuations with individual outliers removed.....	115

Figure 3.2.32: Postmortem osteopontin mean intensity fluctuations with whole individuals removed.....	116
Figure 3.2.33: Postmortem osteopontin standard deviation fluctuations with whole individuals removed.....	116
Figure 3.2.34: OPN:OC mean intensity with individual outliers removed.....	117
Figure 3.2.35: OPN:OC standard deviations with individual outliers removed. ....	117
Figure 3.2.36: OPN:OC mean intensity with whole individuals removed. ....	118
Figure 3.2.37: OPN:OC standard deviations with whole individuals removed.....	118
Figure 3.2.38: Postmortem OPN:OC mean intensity fluctuations with individual outliers removed.....	119
Figure 3.2.39: Postmortem OPN:OC standard deviation fluctuations with individual outliers removed.....	119
Figure 3.2.40: Postmortem OPN:OC mean intensity fluctuations with whole individuals removed.....	120
Figure 3.2.41: Postmortem OPN:OC standard deviation fluctuations with whole individuals removed.....	120
Figure 4.2.1: Single slice unaltered image showing outer iliac table .....	148
Figure 4.2.2: Mask applied surrounding the cortical bone .....	148
Figure 4.2.3: Final analyzed image using only the cortical bone and peri- & endosteum.....	149
Figure 4.2.4: Osteoclastic degradation over the four time-groups (outliers included). ....	151
Figure 4.2.5: Postmortem osteoclast decrease (outliers included).....	151
Figure 4.2.6: Osteoclastic degradation with individual outliers removed .....	153
Figure 4.2.7: Postmortem osteoclast degradation with individual outliers removed.....	154

Figure 4.2.8: Osteoclastic degradation with whole outliers removed.....	155
Figure 4.2.9: Postmortem osteoclast degradation with whole outliers removed. ....	156
Figure 4.2.10: Perimortem sample with cellular material indicated with spheres.....	159
Figure 4.2.11: Early-postmortem sample.....	159
Figure 4.2.12: 7-day postmortem sample from same individual as Fig. 4.2.11.....	160
Figure 4.2.13: 14-day postmortem sample, from same individual as Figs. 4.2.11 and 4.2.12. ..	161
Figure 5.1.1: Scatter plot of Ch. 2.3 & Ch. 3.2 mean intensity and standard deviation. ....	166
Figure 5.1.2: Boxplot of combined Ch. 2.3 & Ch. 3.2 osteopontin mean intensity. ....	166
Figure 5.1.3: Boxplot of Ch. 2.3 & Ch. 3.2 osteopontin standard deviation intensity data.....	167
Figure 5.1.4: Scatter plot of combined Ch. 2.3 & Ch. 3.2 osteopontin mean intensity and standard deviation data with individual outliers removed.....	169
Figure 5.1.5: Boxplot of combined Ch. 2.3 & Ch. 3.2 osteopontin mean intensity data with individual outliers removed. ....	170
Figure 5.1.6: Boxplot of combined Ch. 2.3 & 3.2 osteopontin standard deviation data with individual outliers removed. ....	170
Figure 5.1.7: Scatter plot of combined Ch. 2.3 & Ch. 3.2 osteopontin mean intensity and standard deviation data with whole outliers removed. ....	173
Figure 5.1.8: Boxplot of combined Ch. 2.3 & Ch. 3.2 osteopontin mean intensity data with whole outliers removed.....	173
Figure 5.1.9: Boxplot of combined Ch. 2.3 & Ch. 3.2 standard deviation data with whole outliers removed.....	174
Figure 6.4.1: University of Toronto Human Research Ethics Protocol approval letter.....	209
Figure 6.4.2: University of Toronto Division of Anatomy sample approval letter .....	210

## List of Appendices

Appendix A: Final sample demographic data

Appendix B: Raw sample protein data

Appendix C: Raw sample cellular data

Appendix D: Ethics Approvals & Information, Material Transfer Agreement Information

# Chapter 1

## Introduction

### 1.1 Purpose & Significance

In forensic anthropology, the analysis and determination of the postmortem interval (PMI) of human remains is an important aspect in the reconstruction of the events surrounding the death of an individual. Understanding the PMI allows anthropologists and pathologists the ability to better reconstruct the death event by situating the incident and potential individuals around a temporal range. A common challenge posed by defense counsel, however, is to question if the stated “estimated postmortem interval” is correct, or if a later or early interval is more accurate. This is particularly true given that as time progresses postmortem, the less precise estimation becomes. Current methods of estimating PMI vary depending on the state of the remains and the ability to utilize certain anatomical features. Methods relying on histochemical techniques such as vitreous humor or gingival tissue are valid but for a span of around a week or less (1-5), while using bone utilizes weathering of bone and histological diagenetic processes, (6-10), but these methods have only been studied on dried elements after soft tissue decomposition has ended. During the decomposition process, PMI estimation has largely been limited to assessing the degree of decomposition and attempting to formulaically tie it to climatic conditions to arrive at an estimated window (11-13). Because of the vagueness in PMI estimation, particularly in cases where some time has passed between the estimated somatic death and the discovery of the remains, defense counsels often challenge the alleged guilt of their clients by arguing that timing of the crime is in error.

The purpose of this research was to develop a histochemical method of estimating postmortem interval (PMI) from bone in order to provide more accurate timing of events in the immediate postmortem period. The project had 3 main goals: 1) to determine the potential of fluorescence microscopy as a tool in PMI estimation; 2) to establish the postmortem interval during which these methods are most effective; and 3) to assess the feasibility of adapting this approach to generating an estimate of the postmortem interval (PMI), or time since death.

Current methods of establishing the postmortem interval vary depending upon the state of the remains, with contrasting degrees of precision (1-5, 11-13). These methodologies are used

with remains that are either in fresh or some stage of advanced decomposition, however their precision decreases as the time postmortem increases. Additionally, compounded with the time factor, microenvironmental and body habitus factors also play a role in the rate of decomposition, which widens the generated potential postmortem range (14, 15). Future methodologies in PMI estimation need to balance guarding against microenvironment and body habitus factors, while also adding precision as postmortem time progresses. This project examines whether it is possible to use fluorescent histological analyses as a potential tool for assessing the postmortem interval. Laser-scanning confocal microscopy (LSCM) was used to: 1) assess diagenetic changes through quantification of fluorescent channel changes; 2) quantify the degradation of the protein through quantifying fluorescence; and 3) quantifying the amount of osteoclasts present throughout the cortical structure in the perimortem versus postmortem samples.

This research aims to provide additional resources for establishing the true nature of estimating the postmortem interval during the early postmortem period, resulting in a more accurate theory of events. Clarity in event timing will ultimately permit stronger cases to be built against defendants or will reduce the number of potential miscarriages of justice that could occur if the true postmortem interval is in doubt. During the development of judicial cases multiple lines of evidence are explored and presented within courts of law. Among those lines of evidence is the presentation of an estimated time of death of the victim. However, a vague time since death due to the lack of precision can lead to the challenges which can potentially lead to one of two outcomes. The first would be a successful challenge where defence counsel secures an acquittal for a guilty defendant through the introduction of an artificial alibi. A worse miscarriage, however, would be an innocent defendant being found guilty due to the fact that the postmortem interval range was so wide that a true alibi could not have been adequately applied. The present research aims to explore potential new methodologies as tools for developing a more precise and accurate postmortem interval, particularly for those remains that are within a 14 day PMI window.

## 1.2 Background

### 1.2.1 Theories of Death

Death is a multifaceted phenomenon that is simultaneously clear cut and amorphous. Thanatology, the study of death, combines elements of philosophy, medicine, law, sociology, psychology, and anthropology (16). In ancient and pre-historic times humans were concerned with the metaphysical aspects of death. Evidence of humans pondering the question of “what is death,” can be seen since the dawn of humans (17). In the historic ancient times theories of death were as wide and varied as the present cultures and civilizations; many with religions based on the concept of death (17). By the classical period of the Ancient Greeks, the questions of death had evolved to classifying and examining how one died and its effects on the metaphysical afterlife (17). In the 17<sup>th</sup>-century Europe, at the heart of the scientific Renaissance, death started to be examined from a scientific framework. The study of death was transformed from focusing on the soul to focusing on the body, and the process of death and how that affected the individual in the afterlife. It was during this time that experimentation on the preservation of remains became a practice within the fledgling medical community (17).

The Oxford English Dictionary defines death as “...the permanent cessation of vital functions of a person, animal, plant, or other organism” (18). The question then shifts to “what are the vital functions?” In the early 1900’s this was defined as the absence or cessation of respiration and heartbeat. On December 3<sup>rd</sup>, 1967, an event challenged the definition and understanding of death when the first heart transplant took place. As the heart became a commodity used to treat the living, a new definition was needed to assess the condition of individuals whose vital functions were supported by mechanical means. A new definition of death was needed to include the cessation of neural functions – so called brain death (19). In 1968 a committee formed within Harvard Medical School to define brain death, determining that 4 tests should be used to establish when brain activity ceases, including conducting a cerebral angiography, electroencephalography, transcranial Doppler ultrasonography, and cerebral scintigraphy (19, 20). As a part of this commission, the committee set out to distinguish between an irreversible coma and persistent vegetative state (19).

The findings of the Harvard Committee on death were not without criticisms, however. In the 1980’s U.S. President Ronald Reagan tasked the President’s Commission for the Study of

Ethical Problems in Medicine and Biomedical and Behavioral Research (established in 1978 as part of Public Law 95-622 (21)) to tackle the criticisms of the Harvard Committee, and to legally define the concept of “death” (19). In 1981 the Commission proposed that a legislative act be formed with the definition that death is the cessation of either circulatory and respiratory functions, or the irreversible cessation of all brain activity (22). Further, as medical science progresses, the Commission argued that the definition of death, particularly as it relates to brain death, should be continuously studied and revised (19, 22).

The benefits of such definitions, particularly that of cardio-pulmonary death (CPD), is that they allow for a clear-cut “time of death.” If monitored, one can record the exact time at which the last heartbeat coupled with the last respiration takes place. The problem with such definitions is that they do not necessarily reflect the truth of death. The definitions establish the creation of an exact event, but the human body is not as integrated as such definitions dictate. Instead, it is organized into layers and systems, starting at the cellular level, then extending to tissues, organs, systems, and ultimately the integrated body. As such, the lack of oxygenation affects each tissue in a different way and at a different time. Cardio-pulmonary death (CPD) with intact neural functions (such as with a massive myocardial infarction) will cause the brain functions to terminate minutes post CPD (23), thus leading to somatic death (the cessation of neural, cardiac, and pulmonary activities). Muscles may not be active at this point, but necrosis of the skeletal muscles is not instantaneous following somatic death. In theory the same can be said for bone, where osteoclastic activity is present at extracellular necrotic bone (24-26), such as can be seen soon after breakage at the point of bone failure. Since death is not as clear cut as might be expected, this study was designed to determine at what point following somatic death the skeletal system finally reaches a terminal phase and experiences death. To achieve this aim, the focus is on determining which changes take place in bone in the days and weeks following somatic death using histochemical techniques, as well as when those changes occur. Understanding the processes that occur as bone dies, makes it possible to correctly interpret and reconstruct the events that took place at and around the time of death.

### 1.2.2 Bone Composition

Bone is divided into two constituent components that interact with one another to create stability and strength: the organic and inorganic matrices (27-29). The inorganic matrix of bone

is derived from a naturally occurring calcium-phosphate substance known as hydroxyapatite  $[\text{Ca}_{10}(\text{PO}_4)_6(\text{OH})_2]$ , and accounts for 60 – 70% of the bone's dry [defleshed] weight (27-29). Accounting for 30 – 40% of the remaining dry weight, the organic matrix is a complex cellular system consisting of branching Type I collagen fibers, with cross-links to aid in strength, and a small amount of Type V collagen, whose role is limited to fibrillogenesis (27).

### 1.2.2.1 Osteoclasts

Within this organic matrix is a complex cellular system that is used to maintain overall bone stability as various forces, including load, are enacted upon it. Among those cells are osteoblasts (responsible for mineralization among other tasks), osteocytes (responsible for regulating homeostasis through coordination with osteoblasts and -clasts), and osteoclasts (responsible for resorption among other tasks). Together, these three cells work in concert to generally maintain bone homeostasis, specifically within an element, but given the structure of the human skeleton, a variation within one element would naturally have a compensatory effect on other elements (30, 31).

Of the three cell types in questions, the present study focused on osteoclasts. Osteoclasts are multinucleated cells responsible primarily for resorption of bone matrices (30). The resorption process takes place when osteoclasts interacts with the inorganic matrices, the cell itself becomes polarized through matrix derived signals transmitted by the  $\alpha\beta3$ -integrin which creates a microenvironment between the cell and the bone matrix (32). This matrix becomes potentially acidic microenvironment by  $\text{H}^+$  adenosine triphosphate (ATP)ase-mediated extracellular transport of protons while the intracellular pH is maintained through an electroneutral  $\text{HCO}_3^-/\text{Cl}^-$  (32). As the  $\text{Cl}^-$  enters the cell it is released into the microenvironment by an ion channel coupled to the  $\text{H}^+$  ATPase creating an acidic environment (32). This then exposed the organic matrix of bone that is degraded by cathepsin-K (32).

Osteoclasts have multiple origins with each depending upon both the developmental stage of the individual, and the nature of the need of those osteoclasts. Beginning with embryonic development, osteoclastic cells arise from two generalized pathways: erythromyeloid progenitors (EMPs) which develop around embryonic day (E) 7- E7.5, and hematopoietic stem cells precursors (HSCs) around E10.5 (33). The EMPs are divided into two categories depending on developmental timing with early EMPs developing around E7 and then morphing into colony-

stimulating factor 1 receptor 1 (CSF1R)<sup>+</sup> yolk-sac macrophages which, by E8.25 with the yolk-sac vasculature connecting to the intraembryonic circulatory system, colonize the various organs. After this colonization, a second wave of EMPs (late EMPs) develop within the yolk-sac and migrate into the live to produce monocytes (33). By around E10.5, in the final waves of hematopoiesis, HSCs begin to emerge around the aorta-gonad-mesonephros region. At around E15.5 the EMPs, having developed into embryonic osteoclast precursors, begin the formation of the marrow cavity, which is then inhabited by both the residual EMP osteoclast precursors, as well as the HSC osteoclast precursors derived from the fetal liver (33). While both are known to exist long into adult-hood, at this stage the cells themselves remain progenitor cells with their final maturation and functionality having some overlap but generally being separated. Specifically, EMPs, while existing up to 6-months postnatally, and having some derivatives in fracture (*fx*) repair, are eventually replaced by HSCs both in bone maintenance and remodelling, as well as being engaged in the primary role of *fx* repair (33).

The transcription of the precursor cells to mature osteoclasts, mainly those of the HSC origin, start with the HSC differentiating into multipotent progenitors, which are then lineage-restricted, meaning that they have the ability to develop into any number of type of cell but then become limited in their ultimate trajectory (33). For osteoclastic precursors, the HSC multipotent progenitors develop into common myeloid progenitors (CMPs) that produce granulocyte/macrophage progenitors (GMPs) as well as common osteoclast/dendritic cell progenitors (MODPs), with dendritic cells (DCs) also serving as antigen-presenting cells or APCs (33). The MODPs develop into mature osteoclasts through interactions with receptor activators of nuclear factor-kappa B ligand (NF- $\kappa$ B, or RANKL), colony-stimulating factor 1 (CSF1 or M-CSF for macrophage) (34). Additionally, there is evidence to believe that in children, interleukin 3 receptor- $\alpha$  as well as a KIT protooncogene receptor tyrosine kinase (KIT)<sup>+</sup> may also have roles in the development of osteoclastic precursor cells into mature osteoclasts (35, 36).

Once the mature osteoclasts are developed, they are then engaged in the development of the bone through the normal processes of modelling and remodelling. Following the process of ossification, the bone is then modeled via osteoblasts (formative) or osteoclasts (resorptive) based on the strain and load placed on the bone (30). Localized strains when elevated beyond a threshold signal for formative modelling and new bone being applied, while those below the

threshold trigger resorptive modelling and bone being removed by osteoclasts (30). This process is continued until the strain is normalized, and the positioning of the bone is changed to align with the needed central axis; a process referred to as bone drift (30). While existent throughout life, in adults this process becomes less prominent except in the case of pathology (30). In addition to modelling, osteoclasts are also prominent in remodeling, as well which is more localized than the modeling process. Remodelling can take place throughout the bone element and is used in the repair of defects and replacement of existing bone matrix (30). As these osteoclasts, acting in concert with osteoblasts, are working with associated blood vessels in multicellular units (bone multicellular unit or BMUs), this process of remodelling is what gives rise to the concentric osteons and Haversian systems found within the human skeletal system (30).

In addition to the modelling and remodelling phases that are required for normal bone homeostasis, osteoclasts also play a pivotal role in  $f_x$  repair as well. Osteologically there are four stages of  $f_x$  healing beginning from the time of propagation (induction) to the terminal stage of remodeling (37-39). The time to traverse from the initial to the final stage can take months to years, with healing dependent upon the sex and age of the individual; the younger the individual, the faster the healing rate (37, 39). The fastest of the four stages, however, is the initial stage of induction (also referred to as the inflammation stage) (37, 39). This stage generally lasts a few weeks, beginning with the initial  $f_x$  and ending at the appearance of new bone (NBF) (37, 39, 40). Due to the vascular nature of bone, once it reaches the failure point, thousands of capillaries rupture leading to a massive hemorrhage (37-39). Within minutes of  $f_x$  propagation, the vasculature will undergo normal blood clotting procedures and a hematoma will develop (37). Osteoprogenitor cells located in the periosteum will migrate, convert the hematoma to granulation tissue and ultimately osteoid (37, 39, 40). More specifically, osteoclastic precursor cells are recruited to the  $f_x$  site from the blood stream and differentiate into mature osteoclasts following signals such as the receptor activator of nuclear factor Kappa-B ligand (RANKL), macrophage colony-stimulating factor (M-CSF), and cytokines such as tumor necrosis factor- $\alpha$  (TNF- $\alpha$ ) and others, all stemming from the hematoma (24, 41-43), processes similar to differentiation into mature osteoclasts in normal bone formation. In addition, high mobility mature osteoclast cells within the extravascular structure of the bone migrate to the  $f_x$  site, while additional cells (possibly splenic in origin) begin migrating through the vasculature (33,

44). Once the hematoma develops two processes initiate: inflammation of soft tissues and resorption of necrotic tissues (37, 39), although, as noted, research suggests osteoclasts respond immediately to  $f_x$  based on signaling from osteoblasts as well as hematoma formation (33, 44-46).

In the second stage of  $f_x$  repair, osteoclasts begin the resorption process by engaging in osteolytic activities (37, 39). Specifically, mature osteoclasts attach to the bone surface at the  $f_x$  site and form an irregular border, increasing the surface area for bone resorption. The osteoclasts then secrete hydrochloric acid and proteolytic enzymes such as cathepsin K to dissolve the hydroxyapatite and degrade the organic matrix (24, 42). Polarized histological and radiographic studies suggest that this activity begins following the formation of new capillary beds within the hematoma, and can be seen between 4 and 7 days post-injury (PI) (37, 39). At this point osteoblasts begin secreting new bone under the periosteum which has formed around the hematoma. This new bone formation, SPNBF or sub-periosteal new bone formation, can be seen around the fracture margins and is the marker for the start of the “soft callus,” third, stage (39).

In the third stage of  $f_x$  healing is the soft callus stage where the hematoma is replaced with a fibrous matrix that bridges the  $f_x$  line, and then the fibrous matrix is gradually replaced with primary woven bone (39). This occurs by the SPNBF expanding to bridge the  $f_x$  line while simultaneously the fibrous bridge disintegrates during a maceration process (39). Once the fibrous matrix has disintegrated, the fourth, “hard callus” stage begins where the  $f_x$  callus has fully bridged the  $f_x$  (39). It is during the hard callus stage that the inflammatory tissues have resorbed while osteoclasts remain relatively active, leading directly to the remodelling stage where the primary woven bone is converted to lamellar bone and then ultimately remodeled to the original contours via bone drift to meet the central axis of the bone (30, 39).

The last area of the osteoclast lifespan that requires attention is that of apoptosis and autolysis. Both apoptosis and autolysis are related to cell death, however they function in two vastly different ways. Apoptosis is the natural death of a cell at the end of its individual life-cycle, normally after the resorptive process (47, 48). While numerous receptors and processes go into osteoclastic apoptosis, according to Soysa and Alles (48) the prevailing theory on a molecular level is that tumor necrosis factors (TNFs), specifically TNF apoptosis-inducing ligand receptors (TRAIL-Rs) permeate the cell membrane or bind as a soluble receptor. These

TRAIL-Rs have been found to exist both in differentiated and precursor osteoclasts (48). Further, with the reduction of M-CSF, these can lead to an increase in the BH3-only Bcl family Bim protein, leading to cytokine withdrawal and ultimately apoptosis (48). However, while much is known regarding osteoclast apoptosis, very little has been published regarding its sister, autolysis. Autolysis, or “self-death,” is a form of cellular death that takes place when the molecular functions to sustain life have been disrupted, often through somatic death of the individual. In general, following somatic death, cells do not instantaneously undergo a process of autolysis, but rather undergo in a system by system manner. Decompositional studies have shown that smooth and serrated muscles undergo this change first, namely in the gut, but other organs quickly follow (49). However, turning to transplantation medicine one can get a rough estimate as to the process of autolysis of whole organs as hearts and lungs are recommended to be transplanted within 4 to 6 hours while kidney’s can last as long as 36 hours, though must be initiated within 24 hours after somatic death (50, 51). As viable cells are needed for the tissues and organs to function in the transplanted state, then it can be inferred that the cells can survive, with assistance from proper isolated conditions up to the recommended timeframe and even slightly beyond. That said, an examination of osteoclast autolysis through PubMed turned up no such results (52). However, again turning to transplantation medicine, under the right conditions bone tissue samples can be held and successfully transplanted up to 5 years after donation (51).

### 1.2.2.2 Osteopontin and Osteocalcin

Osteopontin (OPN) is an acidic glycosylated phosphoprotein with origins both within and external to the skeletal system including in some areas of both endothelial and epithelial cells, smooth muscle cells, and fibroblasts (53). In the skeletal system, osteopontin has origins from both osteoblasts and osteoclasts, indicating a significant role in the bone turnover process. It is predominately produced by osteoclasts where the primary function is the anchoring and regulation of osteoclasts to the bone matrix, and the anchoring of the type I collagen to the hydroxyapatite (28, 29, 54-60). Weighing between 44 and 75kDa per molecule, OPN is found in the extra cellular matrix. Due to its role in cytokine immune regulation, and soft tissue wound healing (61, 62), OPN can also be found in Haversian and Volkmann’s canals, particularly as OPN is entering the vessels and the blood stream (54, 55, 57). Further, because it has some genesis with osteocytes, OPN is also found in the lacunae as well. (54, 55, 57). External to the skeletal system OPN is also involved in a number of physiological processes including cancer

growth and metastasis, angiogenesis, as well as contributing to inflammation and tissue damage in individuals with autoimmune conditions (63-65).

As a significant non-collagenous protein component of the bone matrix, OPN is distributed throughout the bone matrix but is particularly concentrated in the regions undergoing active remodeling (66-68). It is involved in the regulation of hydroxyapatite crystal growth, inhibiting excessive mineralization and ensuring proper bone density and structure (66, 67, 69). OPN is also found at sites of bone resorption and cement lines, where it is secreted by osteoclasts to facilitate cellular attachment to the hydroxyapatite (55, 66). Additionally, OPN is present in the periosteum and endosteum, to facilitate bone growth and repair (66, 67, 69). In the periosteum, OPN contributes to the formation of new bone during growth and responds to bone injury, while in the endosteum, it plays a role in bone turnover and maintenance (67). Given the overconcentration of OPN at the periosteum and endosteum, the middle envelope is the best area of visualization for general levels of OPN.

In bone remodeling and mineralization, OPN contains the arginine-glycine-aspartate (RGD) sequence, which facilitates osteoclast adhesion by interacting with integrins such as  $\alpha v \beta 3$ . This is essential for cell attachment to the bone matrix and subsequently bone resorption (56, 58, 59, 63, 68, 70, 71). It modulates the secretion of enzymes such as cathepsin K (potassium) and matrix metalloproteinases (MMPs) which are necessary for matrix degradation (72). Additionally, OPN interacts with collagen through its phosphorylated regions and RGD sequence (54, 55, 58, 60, 69).

Osteocalcin (OC) is a  $\gamma$ -carboxylated protein produced almost exclusively in the skeletal system by osteoblasts, though also with genesis through osteocytes as well, generally in their role as trapped osteoblasts (73). More specifically, genesis is primarily found in osteoblasts for the purpose of bone remodeling regulation, while in osteocytes, OC is found to be more for mineralization and mechanosensation (74, 75). OC is approximately 5-6 kDa in molecular weight (57). Like, OPN, OC has physiological functions outside of the skeletal system including in glucose management and even fertility (69, 76-78). In bone, OC is primarily associated with the regulation of bone turnover as well as in the anchoring of the inorganic and organic matrices by binding to the OPN (28, 29, 54, 55, 57, 59, 60). Specifically, OC binds to hydroxyapatite crystals, contributing to the regulation of mineralization, and is distributed throughout the

mineral matrix with concentrations in newly formed bone (76, 79, 80). Being complementary with OPN, OC is responsible for remodeling, regulation of mineralization, and response to mechanical stress, and binds with OPN to secure hydroxyapatite to the collagen matrix. OC contains three  $\gamma$ -carboxyglutamic acid residues, which release calcium ions that are crucial for binding to hydroxyapatite (76, 79). The binding of OC to the hydroxyapatite regulates the size and shape of the mineral crystals that contribute to mineralization (54, 59, 77, 79, 81, 82). OC modulates the activity of both osteoblasts and osteoclasts by inhibiting excessive mineralization, which ensures that bone formation occurs in a controlled manner, thus preventing the development of overly dense and brittle bones (54, 78, 79, 82-84). OC acts as a signaling molecule, influencing osteoblast differentiation and activity through the expression of genes involved in bone matrix production and mineralization and thereby enhancing the overall bone formation process (54, 76, 79, 82, 84, 85). In OC-deficient mice, studies have shown subjects to have altered bone morphology and mechanical properties (83). When combined with OPN, both proteins respond to mechanical stress and adapt their functions accordingly. OPN is upregulated in response to mechanical strain, enhancing osteoclast-mediated resorption, while OC facilitates the repair and strengthening of bone through mineralization processes (54, 59).

In the process of binding hydroxyapatite and collagen, OC and OPN have distinct but complementary roles. OC binds directly to hydroxyapatite crystals through its  $\gamma$ -carboxyglutamic acid residues, which chelate calcium ions on the crystalline surface (54). This binding is crucial for the nucleation and growth of hydroxyapatite crystals within the collagen matrix. OC and OPN are known to interact with collagen, although the mechanisms differ. OC binds to specific sites on the collagen fibrils, stabilizing the mineral-collagen interface (54, 58, 59, 69, 85). While OPN and OC are both necessary for the function and stability of bone, the ratio between the two is difficult to ascertain. The ratio of OPN to OC can possibly vary from bone to bone, with normal bone having a OPN:OC ratio of 1:1.5 but expanding to a ratio of 1:13 in microfractures forming dilatational bands (29). Though not extensively studied in literature, it is possible that there are regional variabilities in this ratio of OPN:OC, more notably given the ratio of cortical and trabecular bone and the variability in the turnover activities of osteoclasts and osteoblasts in those bone types which are directly related to the deposition of osteopontin and osteocalcin respectively (73, 86, 87). Because of this, though it should be stressed limited studies have been conducted, it is plausible that bones, and bone regions, with a higher percentage of trabecular

bone may potentially have a differing ratio of OPN:OC than bones and regions with greater cortical bone; though no study has been found which directly measured the ratio of OPN:OC in trabecular vs. cortical bone, nor differing bones by anatomical region or bone load.

OC and OPN are, however, influenced through age and sex as influenced by hormones (hormonal sex). With age, OC levels change, reflecting alterations in bone turnover rates (88-90). In children and adolescents, osteocalcin levels are typically higher due to rapid bone growth and development, though as an individual ages OC levels generally decrease (88, 90). This decline is associated with reduced bone formation and an increased risk of osteoporosis and fractures. One study (89) demonstrated that serum osteocalcin levels were significantly higher in premenopausal women compared to postmenopausal women, indicating a decrease in bone formation post-menopause. Similarly, Szulc and Delmas (91) found that older men had lower OC levels compared to younger counterparts. OPN levels also exhibit age-dependent variations. OPN is upregulated in response to mechanical stress and micro-damage, both of which are more prevalent in younger, maturing bones (92, 93). Excessive OPN, through osteoclastic and osteocytic activity, can also contribute to pathological bone remodeling, including osteoporosis (94). One study conducted on young rats by Johnston and Buckley (92) indicated that OPN expression was elevated in younger bone, correlating with increased bone turnover, though stabilized after sexual maturity. This is matched by Du *et al.* (95) and Carvalho *et al.* (96) who found that there are lower levels of OPN (and OC in the case of Carvalho *et al.* (96)) in older bone, though the inverse is found in serum levels, specifically with menopausal women (97, 98). While any technique designed to estimate postmortem interval based on alterations from the antemortem OPN:OC ratio would therefore need to consider the individual's age and sex, it should be recognized that the literature is incongruent, with regards to age, as studies' results vary depending on whether bone or serum OPN or OC is measured.

Sex, as influenced by hormones (hormonal sex) plays an important role in OC and OPN production and regulation. Estrogen and testosterone regulate levels of OC (81, 88, 90, 98, 99). Estrogen has a protective effect by inhibiting bone resorption and maintaining OC levels. Estrogen deficiency post-menopause leads to a marked increase in OC and OPN levels, contributing to increased bone turnover and the development of osteoporosis among other pathological conditions (98, 100, 101). Similarly, in men, testosterone supports bone formation and OC production (98). Reduced testosterone levels can lead to decreased OC levels. Khosla

and colleagues (98) found that testosterone replacement in hypogonadal men significantly increased serum OC levels, thus highlighting the hormone's role in bone metabolism (99). OPN levels also show sex-specific differences influenced by hormonal changes (98). With OPN, estrogen suppresses the protein expression, thereby reducing bone resorption. This is expressed with postmenopausal women, who exhibit increased OPN levels, contributing to enhanced bone resorption (98). Conversely, testosterone appears to have a less direct effect on OPN levels but still contributes to overall bone metabolism (98).

Following somatic death, the complexes binding the OPN and OC along with the osteonectin (which binds to the Type III, Type VI, and Type V collagen) begin to degrade. One of the quantitative portions of this research assesses the differential degradation of OPN to OC. The role of OC in diagenesis has been reported in the osteoarcheological literature, but the lack of information regarding the role of OPN in diagenesis suggests that the two degrade at different rates with OPN decomposing faster than OC (102-105). In 2014, Boaks *et al.* (9) found that collagenous proteins degrade at a consistent rate in the natural environment. If the same holds true for the non-collagenous proteins, then mapping and quantifying the degradation of OC and OPN may help determine the postmortem interval (PMI) as well as the timing of a discontinuity in the bone. The sampling location is important due to the distribution of OPN and OC. Despite the concentrations of OPN in Haversian and Volkmann's canals and in cement lines, cortical bone is a preferred sampling location, given the variability in surface volume using trabecular bone. Its potential concentration in the periosteum and endosteum also suggest that the middle envelop of the cortical bone would be most consistent between individuals. Lastly, given the potential differences in OPN:OC ratio in weight-bearing and non-weight-bearing bones, due to the potential greater abundance of micro  $f_x$  and therefore dilatational bands (29), this study preferred samples be taken from non-weight-bearing bone regions such as the iliac crest. While there is limited cortical structure present, there is enough for visualisation using the modality selected.

### 1.2.3 Decomposition

Decomposition is a dual-phase process that occurs both intrinsically and extrinsically. Intrinsic decomposition occurs mainly at a cellular level and eventually extends into the extrinsic, which can be seen in the external soft-tissues and ultimately bone (15, 106-113). Both

intrinsic and extrinsic decomposition have been organized into various series (see Table 1.2-1) created to assist in establishing the PMI [also referred as time since death (TSD)] (11, 15, 112-117). While the basic categories of decomposition are addressed in the literature, these stages are not precise and have both overlapping and/or differing names for various sequences (117). In general, decomposition progresses as follows: fresh (intrinsic/autolysis), bloat, early decay, advanced decay, and finally skeletonization/mummification (112, 114-117).

### 1.2.3.1 Fresh

The first stage of decomposition shared by all of the sequences is “fresh” stage, which begins at the point of somatic death. Approximately 4 minutes postmortem, the cellular structure starts a process of autolysis, specifically within the smooth and followed by striated musculature, where lysosomes are released into the cytoplasm due to a decrease in intercellular pH levels (111). This decrease in pH level is the direct result of the deprivation of oxygen (O<sub>2</sub>) and adenosine-triphosphate (ATP) (49, 111, 112). Cell walls begin to deteriorate and the basement membranes/intracellular matrix begin to dissolve, resulting in the breakdown of the cellular and tissue structures (49, 111, 117, 118). Gill-King (49) characterized autolysis into two stages. Stage 1, or early, reversible, is the point at which localized individual cell death occurs, but the overall tissue may be spared. Stage 2, or late/irreversible, is noted when autolysis has progressed to the point where tissue necrosis can be seen microscopically as the absence of cell nuclei (49). Using these stages, Gill-King (49) organized tissue decomposition based on those tissues with a higher level of ATP; starting with the soft-muscle tissues of the digestive tract and vasculature, then the pulmonary structure, brain/nervous tissue, skeletal muscles, and lastly connective tissues. In bone, however, the intercellular matrix is predominantly inorganic rather than organic (27) and limited research has taken place demonstrating the effect of autolysis on the organic matrix of bone cells and tissue (10, 119-124). One of the aspects of the current research was to document and quantify the effects of intercellular autolysis on the organic matrix of bone and subsequent relationship to the inorganic matrix, specifically through the process of bone migration. It should be noted, however, like Cvetko *et al.* (125), previously active cells that demonstrated evidence of migration, may have been inactive at the time of imaging and analysis. Their presence would be quantified, but still may no longer be viable.

As the process of autolysis continues, the mortis triad (algor, livor, and rigor mortis) becomes established, the combination of which has been instrumental in determining approximate PMI (126-128). Livor mortis takes place when capillary beds throughout the body begin to rupture; 20 minutes postmortem, the gravitational pooling of the blood will cause the downward facing surface of the skin to exhibit a red to purple hue (112, 113, 127, 128). Once the intrinsic autolysis process has progressed to the irreversible Stage 2 and is multiplied to the wider tissue process, endogenous bacteria begin to initiate putrefaction, approximately 48 – 72 hours postmortem (49). During this stage, the digestive tract begins to break down, leading to the second universally accepted stage, the bloat/early decomposition stage (11, 110, 112, 114, 115).

**Table 1.2-1: Stages of Decomposition [as taken from Smith (129)]. The darker cells indicate later stages of decomposition.**

Rodriguez and Bass (116)	Galloway <i>et al.</i> (114)	Megyesi <i>et al.</i> (11)
Fresh	Fresh	Fresh
Bloated	Early Decomposition	Early Decomposition
Decay (Active)	Advanced Decomposition	Advanced Decomposition
Dry	Skeletonization Extreme Decomposition	Skeletonization

### 1.2.3.2 Bloat/Early Decay

Through the process of putrefaction, anaerobic bacteria become increasingly active, attacking what remains of the larger blood vessels and internal organs (15, 49, 112, 115). In soft-tissue decomposition, this results in the release of excess interstitial gasses and ultimately bloating of the body (11, 15, 110, 112, 114-116). During the later phases of this stage the intrinsic bacterial activity begins to slow, while the extrinsic activity begins to accelerate (15, 112, 114, 116). Extrinsic activity, such as arthropod oviposition and additional macrofaunal activity, occurs during the later phases of early decomposition, and can affect the physical decompositional process. Much is known regarding the extrinsic appearance of the remains during this stage, yet little is known regarding how bone is affected by the putrefactive and

internal decomposition processes (119). While it is believed that the process of autolysis and putrefaction effects decomposition of periosteal surfaces, there is limited research distinguishing the effects caused during the bloat/early decay stage and the later stages when bone is exposed to the elements. The present research contributes to this knowledge, focusing on changes that occur as a result of decomposition, and excluding changes that occur as a result of environmental deposition.

### 1.2.3.3 Later Decomposition Stages

The final two stages of decomposition are the advanced decomposition and skeletonization stages, both of which are generally dictated by extrinsic factors, rather than intrinsic (11, 15, 108, 114-116). During the advanced decompositional stage, bone becomes exposed at different rates throughout the body, with “skeletonization” being attained when most of the elements finally become exposed. The remaining soft tissues either disintegrate, undergo saponification, or begin a slow desiccation process and ultimately mummify, depending upon the environmental and arthropod activity (11, 15, 108, 114, 115, 129). Once skeletonization occurs, the remains could theoretically continue in this phase indefinitely. Like the previous stages, there are sub-stages defined by the appearance and texture of the bone. At this point the diagenetic process accelerates, with ultimate trajectories influenced by the surrounding environment (113). The first of the skeletonization sub-stages is the “initial skeletonization” phase, where some remaining soft-tissues may be present and the bones have a greasy texture to them (11, 15, 114, 115). Once the remaining soft-tissue has deteriorated, but the skeleton is still greasy, the remains are said to be in the second sub-stage, or “wet bone” stage (11, 15, 108, 114). It should be noted that there is limited consensus as to the presence of this stage in the literature, with some authors (108, 114) separating this stage, while others (11, 15) combine this stage with the final stage. The third and final stage is the “dry bone” stage, where the bones have dried out and now have a “wood-like,” and ultimately white appearance, depending upon the environment (11, 15, 108, 114, 115). Over time, if the remains continue to be exposed to the elements, the normal taphonomic processes will continue with the fate of the skeletal remnants depending upon the environmental conditions (15, 114, 130, 131).

#### 1.2.4 Methods for Assessing Decomposition

The methodologies to assess the postmortem interval varies depending on the degree estimated time postmortem and the degree of putrefaction, as methodologies have differing degrees of reliability based on time postmortem (132). According to Ruiz López and Partido Navadijo (132), pathological methodologies for assessing the postmortem interval can be divided into two categories based on the presence of putrefaction: early or late. These can be overlaid with anthropological categories with early being that of “fresh,” while the late is associated with the “bloat/early decay” (11, 114, 116, 129).

The methodologies for assessment of the early period can be divided into two main categories. One is based on gross body modifications following off of the mortis triad (algor, rigor, livor). Here, the assessment is a trinity of assessments which combines assessing the degree of temperature equilibrium with the surrounding environment (algor mortis), the contraction and relaxation of the musculature (rigor mortis), and the collapsing of the capillary beds settling, and setting of the blood at the gravitational lowest point of the body (livor mortis). However, the timings are more dependant on the surrounding environment and body habitus, and generally are considered less accurate, and after 72 hours are generally useless. The next set, however, is more micro in scale, based on histology, histochemistry, or going larger focused on organs rather than whole body (i.e. uterus or crystalline lens). These are also considered more accurate to PMI timing, especially after the initial 72 hour period. These early methodologies are rather germane to the present study because they are widely varied yet rarely last beyond 7 days while the present project extends to 14 days.

These micro-level pathological methodologies for postmortem interval estimation generally come in a few areas that are tested (132). The most common, and some of the more accurate testable areas is the assessment of potassium (K) in the vitreous humour within the eye, which increases approximately 1 mmol/l K for every 6.42 hours postmortem up to a maximum of just under 7 days (2), though this is age dependant and younger individuals (below the age of 18) exhibit a faster increase in K (1). Similar studies have also worked on levels of K in vitreous humour, as well as albumin, as a means of testing the postmortem interval, yet the maximum study dates are all less than 8 days with the exception of Zilg *et al.* (1) which lasted for 17 days (beyond the 14 day window of the present study) (2, 3, 132). In addition to the level of

potassium, a few early postmortem interval estimation methodology studies also have examined the degradation of cardiac proteins, specifically Troponin-C, a subunit of Troponin, which binds to the calcium leached from the myosin and actin within the cardiac muscle fibres, and Troponin-T, a subunit which acts as a stabilizer (133, 134). While studying different proteins, both Abd Elazeem *et al.* (133) and Kumar *et al.* (134) did come up with relatively similar conclusions regarding the degradation of the proteins over time reaching the lowest useful levels at around 50 hours postmortem. Additional markers for the early postmortem interval can be found in gingival tissues which begin to break down after 24 hours with a similar decrease in phosphatase while ammonia levels increases as the epithelial cells deteriorate (5). Further, the crystalline lenses within the eyes are known to demonstrate timed structural changes in the early postmortem period beginning at 48 hours postmortem and losing all structure and sphericity at 96 hours (135).

Once putrefaction has begun, however, the assessments of the postmortem interval, shift from a pathological assessment to a more anthropological one, and is largely based on the degree of decomposition, skeletal exposure, mummification (if present), and the degree of skeletal element degradation as a result of taphonomy and diagenesis. If soft tissue is still present, or the exposed skeletal elements are “wet” in appearance as a result of decompositional fluids or the elements still uniformly retaining a greasy texture, it is possible to tie that degree of decomposition to the accumulated climate to attain a rough estimate of the postmortem interval (11). One of the first to sort of standardize this process was Megyesi *et al.* (11) who developed a model for calculating the degree of decomposition based on a 35 point scale, with each region of the body (head/neck, trunk, limbs) is assessed. This is then entered into a formula to develop a potential set of accumulated degree days which can be compared to climactic data to establish a potential postmortem interval (11). However, there are limitations to this model, not the least of which is that the estimated postmortem interval range increases as the time postmortem increases (as accumulated degree days increases) and flaws in the base model (12, 13). Additionally, there are other climactic factors that effect the rate of decomposition including humidity (14, 108, 136-139), moisture (140, 141), presence of sun/shade (142), and others (15, 143-152) which are ignored in the Megyesi *et al.* (11) and Moffatt *et al.* (12) models that could either increase or slowdown the decompositional rate. However, while Megyesi *et al.* (11) and Moffatt *et al.* (12) established a measurable scale for the postmortem interval, much has been done which examines

the degree of decomposition as well skeletal taphonomy and ties it to gross timing, but not an exact postmortem scale (8, 14, 15, 108, 119, 130, 153, 154).

### 1.2.5 Bone Microstructural Diagenesis

To fully understand the postmortem destruction of bone, regardless of the postmortem timing, a histological understanding of diagenesis is needed. Immediately following somatic death, histochemical, and therefore potentially micro- and ultrastructural changes begin, and the organic-inorganic bone matrix interface degrade along with changes in the individual matrices. Bone microstructural diagenesis is the histological study of bone with particular focus on postmortem modification and preservation, especially that of bioerosion. These diagenetic changes are most likely ultrastructural in nature as well. The fact that bone undergoes microstructural changes following death was first observed accidentally by Wedl in 1864 (10). Wedl then began systematic experiments in an effort to recreate his initial observations, including the submersion and burial of defleshed bone and teeth, and was successful in his attempts particularly with the marine studies (10). In the late 1800's few others examined the postmortem modification of bone and teeth, leading to a dearth in the literature (10, 119). The next great wave of histotaphonomic studies came in the middle of the 20<sup>th</sup> Century with the works of Sognaes (155-158), Syssovena (159), Falin (160), and Marchiafava *et al.* (161) [as cited in Bell (10)].

In the 1950's Sognaes revived a long-since abandoned study of the postmortem taphonomic effect on teeth collected from across the globe and from differing time periods. During his studies he discovered that tiny "corkscrew" tunnels were found in the dental tissue, though the enamel exhibited no corkscrews. While he excluded the factor of time in the severity of the damage, Sognaes did postulate that the tunnels were created by microbial activity during the putrefactive stages of decomposition (10). This marks the first published theories that intrinsic decompositional process can produce microscopic damage to bone.

Around the same time that Sognaes was conducting his studies, Syssovena was postulating that macroscopic changes to bone could be seen microscopically (10). Using 196 teeth from individuals deceased no more than 10 years, Syssovena attempted to determine when the earliest postmortem changes could be observed, however he found that there was no obvious changes to the microstructure, arguing instead that postmortem alterations occurred well after

cardio-pulmonary death (10). In 1961, Falin, utilized Syssovena's original theory and applied it to various materials, including teeth finding the same corkscrew tunneling that was seen in Sognaes' studies (10). Over the next decade several additional studies followed Falin observing this same corkscrew tunneling in bone. In 1974, Marchiafara observed that a potential cause for the tunneling was fungal activity, particularly that of *Mucor fungus* (10).

Recent work has been more focused on specific causes of post-depositional alterations to bone with particular interest in newer technologies such as SEM and backscatter electron microscopy (BSM) (10, 119). In 2004 Jans and colleagues (121) broke from this pattern and attempted to distinguish between post-depositional and decompositional microbial attack using human and animal bone from 41 archaeological sites, examined under polarized light microscopy (LM). The authors were able to differentiate types of tunneling including bioerosion and acidic erosion in the bone slices but were unable to distinguish conclusively if the tunneling was from decompositional bacteria, or soil bacteria since both are similar (10, 119, 121). Much of the modern literature, particularly that from Lynne Bell and Miranda Jans, preeminent scholars in the area of microstructural diagenetic research, argue that the future of histotaphonomy should be in differentiating between decompositional and depositional alteration using a more controlled setting involving both traditional LM, SEM, and BSM (10, 119, 123). Current trends have also included LSCM as a useful tool in observing the diagenetic processes that alter bone, although its use has been limited to a few published studies (119, 162-164).

#### 1.2.5.1 Oxford Histological Index

In order to better quantify diagenetic changes over time, two different histological indices have been created: the Oxford Histological Index and the Bioerosion Index. Developed in 1995, the Oxford Histological Index (OHI) is a semi-quantitative methodology that scales the amount of bioerosion in bone based on microbial alteration (10, 119, 165). The OHI was originally created for histological analysis of archaeological bone, by Hedges *et al.* (165) and uses a scale of 0 to 5 based on the degree of diagenetic change (see Table 1.2-2). Although the scale is subjective in nature, the developers demonstrated that in a blind test multiple observers could agree within a single index number (165). While this method was created for use with LM, more recent studies have applied this same scale for use in SEM studies, demonstrating that the method works across different scales (10, 119).

**Table 1.2-2: Oxford Histological Index (OHI) [as taken from Hedges *et al.* (165)]**

<i>Index</i>	<i>% of intact bone</i>	<i>Description</i>
0	<5	No original features identifiable, other than Haversian canals
1	<15	Small areas of well-preserved bone present, or some lamellar structure preserved by pattern destructive foci
2	<33	Clear lamellate structure preserved between destructive foci
3	>67	Clear preservation of some osteocyte lacunae
4	>85	Minor amounts of destructive foci, generally well preserved
5	>95	Very well preserved, virtually indistinguishable from fresh bone

### 1.2.5.2 Bioerosion Index

The Bioerosion Index (BI) was developed by Turner-Walker and Syversen (166) for use with BSE/SEM. Unlike the OHI, the BI uses a formula rather than a table of pre-set indices, and takes demineralization, hypermineralization, and porosity into account (10, 119, 166). As the BI is formulaic rather than tabular, it can be considered more accurate and more quantitative than the OHI (10, 119), although it is still a semi-quantitative methodology in that the underlying parameters are subjectively assessed. The BI can be calculated using the following formula:

$$BI = \frac{d + h + p}{a} \times 100$$

where *d* is the total area of demineralized zones, *h* the hypermineralized zone, *p* the diagenetic porosity, and *a* the original bone left (166). To calculate the various zones, Turner-Walker and Syversen (166) utilised the imaging software Scion Image. Like the OHI, the BI was originally designed for archaeological bone as a means of detecting soil bioerosion (119, 166), however in 2004 Jans *et al.* (121) used BI in conjunction with microscopical focal destruction descriptions, as established by Hackett (167), to distinguish between depositional bioerosion and decompositional bioerosion, with some controversy.

## 1.2.6 Laser Confocal Microscopy

Developed in 1955 (patented in 1957) by Marvin Minsky, confocal microscopy can be considered an extension of LM (168, 169). Designed with the particular interest of observing biological events *in vivo*, the basic theory behind confocal imaging is that by reducing the amount of scattered light from the image via pinhole technology, one can produce a more detailed image down to the cellular and intracellular level (168-170). Minsky's microscope utilised a zirconium arc source to produce a pinhole of light that was focused on an objective lens, passing through the specimen, then through a second objective lens with a second pinhole and the same focus, or confocal, as the original. The light then strikes a low-noise photomultiplier which produces a signal proportional to the brightness of the pinhole light (see Fig. 1.2.1) (168, 169).

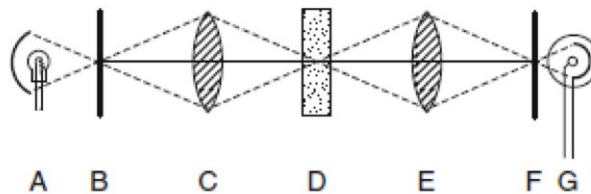


**Figure 1.2.1: Schematic of Minsky's confocal microscope. A point of light is produced by a zirconium arc (A) and passes through a primary pinhole (B). The light is then focused by an objective lens (C) onto and through the specimen (D). The light is then focused through a second objective lens (E) onto a second pinhole (F) and onto a low-noise photomultiplier (G) which produces a signal [used with permission from Paddock and Eliceiri (169: 12)]**

In the 1960's and 1970's, great advancements were made in video and laser technology, both of which have aided in improving the original Minsky microscope. In 1960 Theodore Harold Maiman announced the development of the first operational laser used for holography, and by 1966 G. W. Ellis began incorporating lasers in microscopy with a novel conventional light microscope that was able to split the beam (168). With his microscope, and using the principles of holography and lasers, three-dimensional (3D) microimaging became possible. However, the use of laser light in this manner also includes both the dirt and residue, as well as defects within the lens of a traditional light microscope, thus creating optical noise in the final imaging (168). While 3D imaging was not immediately available with Ellis' microscope, the use of laser light did allow for the advancement of polarized imaging. Laser lights are intense monochromatic light sources that can generate beams with a great degree of coherence (the

ability for beams to interfere causing increased amplitude). This coherence and intensity allowed for a greater amount of polarization, thus increasing the detail of the specimen in question (168).

In the early 1970's a team of engineers at Yale University married the first use of laser technology with confocal microscopy using an oscillated objective lens to scan the beam over the specimen. By the middle of the decade, Collin J. R. Sheppard and colleagues developed a laser illuminated confocal microscope and a novel specimen holder, which allowed for greater control, and thus greater resolution, along the z-axis (168). By the end of the decade, laser confocal microscopy had advanced to the point where a second photomultiplier tube was in use allowing for greater focus and intensity, and greater resolution (168). In the 1980's numerous groups were working to develop a stage-scanning confocal microscope, and by 1983 Nils Åslund and colleagues developed the first laser-scanning confocal microscope. This technology allowed for the imaging of thin optical scans free from out-of-focus fluorescent light (168).

The modern laser scanning confocal microscope uses acousto-optic tunable filters (AOTF) as a means of selecting excitation wavelengths of fluorophore probes. Advancing computer technology further allows for the movement of mirrors and lenses to collect and display the best image possible (169). With the development and aid of computer technology, modern LSCMs are able to project images using quantified microscopy; that is, in a given pixel the software calculates the light intensity in comparison to other pixels (169-171). This allows the operator to quantify the presence of a substance, immunoassay, protein, etc. in a given tissue/cell, with the understanding that the greater the quantity of a substance, the brighter it will fluoresce in a pixelated area. Thus, as pixelation resolution technology improves, with improvements in resolution and computing technology, the image resolution and quality will also improve.

While LSCM has been used for the localization of OPN and OC (29, 85, 96), for the purposes of quantification there are a limited number of studies, particularly with regards to the use of fluorescence as a protein proxy. Though LSCM does provide a great level of resolution, for the visualization of individual proteins, that resolution, nor magnification, is still not viable. Despite these limitations, LSCM was chosen as the optimum microscope due to its ability to be utilized in all three phases of this project, thereby limiting the number of instruments required for a potential overall usable PMI method. Additionally, there is a ubiquity to LSCM that is not available with imaging modalities with higher power; meaning that the probability of access is

greater with the potential methodology's end-users. The use of LSCM is also more viable on an affordability scale to the potential methodology's end-users. Lastly, though destructive, the processes required for LSCM visualization is less destructive than other methods used for protein quantification; a consideration that is a must for the realm of forensic sciences.

While LSCM has been in use for 30+ years as a means of examining biological events on a cellular level *in vivo*, its use on archaeological and anthropological bone histology and observation is still relatively novel. One of the first studies of bone in an archaeological context was conducted by Maggiano *et al.* (163, 164). The authors utilised LSCM to demonstrate the usefulness of the technology as a means of testing the presence and concentration of tetracycline (TC) in bone, as TC has an implication in the health and diet of past peoples. Maggiano *et al.* (163, 164) used samples from the Kellis 2 cemetery from the Dakhleh Oasis, Egypt with an approximate date of AD 100 – 400, along with modern elements from dog (*Canis familiaris*) and *S. scrofa* with selected fluorophore probes. The authors utilised LSCM as a means of conducting spectral analyses and fluorescence intensity. Looking at various regions of interest along the cortical bone of selected faunal and archaeological human remains, the authors were able to positively demonstrate that LSCM can be used with bone in both spectral and fluorescence intensity (163, 164). Further, the authors were able to demonstrate successful imaging of bone at both a 2D and 3D level (163, 164). Given the decay rate of the fluorophores, theoretically this technology could be used to calculate probable dating/PMI of archaeological bone, provided that the fluorophore has a predictable decay rate.

Poundarik and colleagues (29) conducted one of the first trauma studies of bone using LSCM, with a particular interest in the role of OC/OPN dilatational band formation in  $f_x$ , defence and its separation as a result of  $f_x$ . Osteocalcin and OPN work in combination as a means of coupling the noncollagenous hydroxyapatite to the collagenous fibers (29). Using LSCM and atomic force microscopy (AFM) Poundarik *et al.* (29) were able to detect the presence of OC and OPN in the microfractures ( $mf_x$ ) resulting from their controlled crack propagation test (29). Additionally the authors were also able to demonstrate some of the benefits of LSCM in visualizing the microstructures of bone, through the development of a 3D rendering of the microsurface of the bone to detect  $mf_x$ , though it should be noted that LSCM was primarily used for localization and not quantification of targeted proteins (29). Schmidt and colleagues (162) used white light confocal microscopy (WLCM) as a way of visualizing, quantifying, and

profiling cut marks of the surface of cortical bone. The authors cut various dried elements from a domestic cow (*Bos taurus*) then scanned the cut marks using WLCM as a means of spectral analysis on the surface of bone. Using mapping software, Schmidt and colleagues (162) were able to create a topographic 3D map of the surface of the bone with the ability to quantify the kerf patterns of the various cut marks, and were further able to accurately ascertain the profiles made by the different style blades used. By using a method similar to Schmidt and colleagues (162), this research aims to quantify and map the surface of the bone segments to determine if there is a microstructural variation between a perimortem  $f_x$  and a postmortem break.

In 2017, Capasso *et al.* (172) utilized LSCM to distinguish between archaeological remains and clinical remains using bone's natural autofluorescence. Their study was conducted in two parts: examining if the natural autofluorescence was the result of the bone mineral component or the collagen component and using that autofluorescence intensity to determine the date of the bone. The results of Capasso *et al.* (172) found that autofluorescence is not dependent on the presence of the mineral component, indicating that the mineral component can be used in examining the bone's autofluorescence. In addition, Capasso *et al.* (172) were able to demonstrate that the bone's natural autofluorescence decreases over time, likely due to the decreasing organic component. In 2018, Blouin *et al.* (173) published on the use of LSCM as a general tool used to image osteoblast/osteoclast, canalicular organization, and tetracycline labeling. Their results found that LSCM was a useful tool in the imaging of pre-osteoblastic formation, the three-dimensional imaging of canaliculi, and the registration of tetracycline; however their studies used mice models (173).

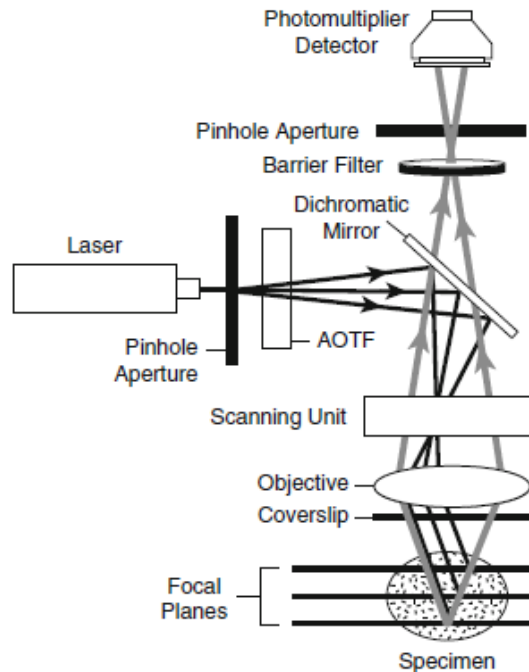


**Figure 1.2.2: Schematic of a modern LSCM. Laser light passes through a pinhole, attenuated through an AOTF, reflected by a dichromatic mirror and then passes to the scanning unit. Once scanned, the beam enters the back focal plane of the objective lens which focuses the light onto the specimen exciting fluorophores. Light from the fluorophores passes back through the objective lens and the scanning unit, through the dichromatic mirror, barrier filter, focused through a second pinhole and then received by the photomultiplier which is then projected by software as an image [used with permission from Paddock and Eliceiri (169: 16)]**

### 1.2.7 Laser Scanning Confocal Microscopy *versus* Light Microscopy

When comparing the information gleaned, laser scanning confocal microscopy bears many advantages to traditional light microscopy (LM). LSCM, with its greater axial resolution and multiple focal planes provides true three-dimensional imaging, allowing the researcher to visualize deep within the cell, or in the case of the present research, within the bone (168, 169, 174). LM lacks this capability thus only allowing for a two-dimensional image along a single focal plane. By utilizing the three-dimensional capabilities of LSCM, the present research is able to visualize and quantify the targeted cells and protein (via fluorescence) within the whole of a given sample rather than being limited to a surface view. Additionally, while epifluorescence microscopy is available within a subset of traditional LM, LSCM allows for the labeling of targeted materials (see 1.2.7.2) and visual isolation of that material by limiting and optimizing single channel fluorescence (168, 169, 174). This allows for the targeted material (cells or

proteins) to be isolated in the imaging process so that only the targeted material is captured. This will then allow for the ease of quantification of that material. Along those lines, LSCM also allows for the quantification of the power of that fluorescence by quantifying the intensity within each pixel (168, 169, 174). Lastly, through the dual focus (confocal) of light pathways eliminating of out of focus light, LSCM allows for greater resolution (down to  $\approx 254\text{nm}$ ), than traditional LM will allow (168, 169, 174). Though pixelization intensity quantification, and channel isolation is possible with other LM modalities, coupling this with the greater resolution of LSCM allows, this modality allows for better differentiation of targeted material and therefore more accurate quantification.

### 1.2.8 Fixation, Staining, and Labeling

Three common chemical processes are used in microscopy to better observe and quantify the microstructural and cellular components of bone: fixation, staining, and labeling. It is vital that a good fixative and staining/labeling protocol be established to maximize the data obtained (175). Given the time frame of this project, and the low survivability of the material, all samples were fixed at specific pre-determined postmortem time frames in an effort to arrest autolysis and microbial destruction [ $<48\text{-hrs}$ , 7-days, & 14-days postmortem] (162, 175-182). Just as there are varied ways of observing material on a microscopic scale, there are a varied number of ways in which to fix a particular sample, each one with its own risks and rewards (175, 176). The risks with any particular fixative range from health risks, such as mercury-based fixatives, to loss of data, as with alcohol based fixatives (176).

As LSCM can largely be considered a cross between LM and SEM (using LM principles, but with 3D axial, and surface resolution similar to SEM), the proper selection of a fixative agent must work with both forms of microscopy. According to Bacallao *et al.* (183), two common fixatives used with LSCM are glutaraldehyde, a fixative that is similar in properties to formalin, but uses a larger molecule, and formaldehyde (181-183). Because the resolution is much greater, glutaraldehyde is commonly used in SEM as a means of arresting autolysis (178, 181, 182). It maintains much of the same beneficial properties of 10% Neutral Buffered Formalin (NBF), a popular fixative agent in LM, but does not have some of the same artifact properties NBF has (178, 181, 182). It preserves the underlying crosslink proteins, thus maintaining the ultrastructure (178, 181, 182). However, the use of glutaraldehyde requires a complicated

protocol to both prepare the solution and the sample. Conversely, formaldehyde is considered more damaging to soft-tissue cultures but is less complicated to prepare and can be used by a third party (178, 181). Although considered more damaging to soft tissues, the use of formaldehyde in bone cultures has long been established and is less damaging to the organic matrix (175, 176, 178, 181). Given the limited risk of damage to the organic and inorganic matrices, the ease of use by third parties, and its use at the labs from which the samples were gathered, this project utilized a formaldehyde based fixative agent.

In order to best visualize the various physical and chemical structures found in bone, the sample should undergo an appropriate labeling protocol after fixation. While both staining and labeling highlight chemically targeted materials for analysis, staining is more for tissue-level analyses (such as various hard and soft tissues), while labeling is more on the protein and cellular level. As the use of bone and its constituent parts is still relatively novel in LSCM imaging, limited information on appropriate labels is available in the literature. Immunofluorescence staining was used by Poundarik *et al.* (29), who utilized basic fuchsin to stain the hydroxyapatite while protein-specific labels followed by a fluorescent secondary antibody (Alexa Fluor™(tm)) was used to label the OC and OPN differentially. While the exact staining methodology is not included in their published study, they do note that the samples were hydrated using PBS for 30 minutes and then stained with OPN and OC immunoassay antibodies at concentrations of 2 µg/mL for OPN and 10 µg/mL for OC, multiplex labelling yet imaging individually for OPN and OC (29). With regard to visualizing and quantifying osteoclast presence, Coxon (184) developed a second staining protocol using alendronate Alexa Fluor™(tm)-488 to observe and quantify *in vivo* human osteoclasts using LSCM. Alendronate Alexa Fluor™(tm)-488 operates with an excitation wavelength of 494 nm and an emission wavelength of 517 nm (184), thus allowing it to be received with a 488nm emission filter. This project followed the labeling protocols as established by Poundarik *et al.* (29) and Coxon (184). While Poundarik *et al.* (29) used a base stain of basic fuchsin combined with the use of two anti-antibodies for OC and OPN staining with the fluorophore Alendronate AF-488 for image fluorescence, the present study, through preliminary experimentation, found that the use of Alexa Fluor™(tm)-555 rather than Alexa Fluor™(tm)-488 allowed for the imaging of the various proteins at low laser power, while excluding the native hydroxyapatite which fluoresces at the same wavelength, but requiring more power and a larger pinhole aperture.

Additionally, with the use of Alendronate AF-488 label mixed with MitoTracker™ Red FM dye, osteoclast presence can be visualized and quantified. One of the benefits of LSCM is that it uses an algorithm based on light intensity as a means of generating an image. This intensity can then be used to quantify the presence of particular substances in a designated field of view. Using secondary software, such as Oxford Industries BitPlane™ Imaris® v.9 (185) and FIJI/ImageJ© (186) v.1.50i, it is possible to quantify the amount of three-dimensional objects such as cells and to quantify the abundance of materials such as proteins. Using the methodologies afforded by LSCM, it is hypothesized that a clear differentiation can be established between bone broken perimortem, and that damaged up to two weeks postmortem, as well as set the groundwork for establishing an accurate skeletal histochemical postmortem interval.

### 1.3 Context

This thesis is subdivided into three major parts comprising four papers: the use of LSCM in bone histoanalysis, as well as the differentia in OPN levels between unembalmed and embalmed samples; OPN and OC degradation as a means of determining postmortem interval; and osteoclast degradation as a means of establishing a postmortem interval. These four papers have been either published [Ch. 2.2 (187)] in the *Journal of Forensic Sciences* or will be submitted for publication in a number of academic journals including, *Journal of Forensic Medicine* [Ch. 2.3], *Forensic Science International* [Ch. 3.2], and *Forensic Anthropology* [Ch. 4.2]. Beyond publication, these various chapters have been presented at several academic conferences including the *American Academy of Forensic Sciences* [Ch. 2.2 & Ch. 4.2], the *Canadian Association of Biological Anthropology* [Ch. 2.3], and the *American Anatomical Association* [Ch. 3.2].

## Chapter 2

# Histotaphonomy and Histochemical Foundations

### 2.1 Chapter Introduction

The present thesis is divided into three major parts, each tackling a specific aspect of study. Part I (Ch. 2) is foundational, exploring the use of laser scanning confocal microscopy in postmortem investigations, both histotaphonomically and histochemically. The primary paper generated from this research was the “Use of laser scanning confocal microscopy in detection of diagenesis in bone” co-authored between Ashley Smith, Lelia Watamaniuk, and Tracy Rogers (187), and published in 2022 in the *Journal of Forensic Sciences*. For this paper, the primary author and researcher was Ashley Smith, while Lelia Watamaniuk provided samples and some editing and Tracy Rogers’ role was limited to editing the manuscript. The second part of this chapter (Ch. 2.3) was co-authored by Cassidy Ferguson, Ashley Smith, and Tracy Rogers, and will be submitted to *Forensic Science International* under the title “Effects of embalming in the preservation of osteopontin” in later 2025. For Ch. 2.3, Cassidy Ferguson and Ashley Smith served as co-primary researchers and authors while Tracy Rogers served in an editorial role.

Chapter 2.2 is a histotaphonomic paper that focuses primarily on establishing the use of laser scanning confocal microscopy as a means of distinguishing fresh bone from diagenetically altered bone. The paper used three sample groups, including domestic pig (*S. scrofa*) and two human groups. Ethics protocol was approved under the University of Toronto Research Ethics Board (Human Ethics Protocol #33324), with the porcine samples euthanized in June of 2011 under Boston University’s and Tufts University’s Institutional Animal Care & Use Committee protocols (117, 129, 188, 189). The study was conducted in two phases with the initial phase being a non-human study examining the difference in autofluorescence as a means to detect diagenesis using a fresh and 5-year old bone from a surface decomposition study (117). The second phase used human bone from a modern clinical sample and Apollonian rib bone from the 3<sup>rd</sup> – 5<sup>th</sup> Century B.C.E. Capasso *et al* (190) found that under laser scanning confocal microscopy, bone gives off a natural autofluorescence; that is, like most biological material, when bone is illuminated with a targeted wavelength, a specific yet different emission wavelength will be generated. In Capasso *et al* (190), the authors were using this

autofluorescence to distinguish archaeological bone from more recent forensic bone. Chapter 2.2 used a similar technique to distinguish two pig samples that would both be considered “forensic” (<75 years) and were only 5 years apart in terms of PMI. To quantify variability, Ch. 2.2 utilized a technique in histoanalysis that evaluates pixel intensity. When an image is taken using laser scanning confocal microscopy, depending on the bit-rate, a grey-scale image is generated with each pixel intensity being rated as 0 (black) – 255 (white) [8-bit] *or* 0 (black) – 65,535 (white) [16-bit]. Here it should be noted that as the research progressed, the knowledge and skills gained were applied; as information gleaned, it was applied to subsequent phases and chapters. For Ch. 2.2 an 8-bit analysis was run, but by Ch. 2.3 and subsequently a 16-bit process was used due to its greater image intensity resolution through a more accurate gradation of channel output.

In addition to the autofluorescence used in Ch. 2.2 phase 1, Ch. 2.2 also utilized a second phase which examined differences between modern human (forensic) controls and an archaeological sample from the 3<sup>rd</sup> – 5<sup>th</sup> Century B.C.E Apollonia. This portion of the study (Ch. 2.2.3.2 and Ch. 2.2.4.2) was to establish a protocol of using laser scanning confocal microscopy to map and quantify diagenesis. Here three groups were used including a stained ancient collection, stained modern controls, and unstained modern controls. As these samples all came from rib, ilia, and femur, the unstained and stained controls were used to verify that there was no difference in fluorescence between bone types, and that any difference was the result of diagenesis.

For both phases of Ch. 2.2 analyses were conducted on the mean pixel intensity as well as the standard deviation of that intensity. In this case the main analysis was on the mean pixel intensity as this provides the most accurate portrait of what is taking place within the bone’s hue. The standard deviation was also examined for each of the hues (red, green, and blue) as this metric would show the variation found within each hue value. Though novel, the theory for this methodology is that variation within each colour [Phase 1] or wavelength [Phase 2] would exist as a metric of diagenesis noting that as various exogenous agents (both biological and chemical/mineral) penetrate the cortical structure of the bone, the fluorescence reaction (with both stained and unstained elements) would vary. Non-diagenetically altered bone, with a specific biochemical make-up, would fluoresce in a particular manner, with targeted wavelengths emitting a range and degree of intensity. With the addition of exogenous agents to that bone, the

base chemical and biological structure is altered, and theoretically the range and intensity of the emitted wavelengths would alter as well.

The second paper of Chapter 2 was that of Ch 2.3. This manuscript was an additional foundational paper for this research in that it specifically examined the quantification of a target bone protein, namely osteopontin. The research was designed to examine the osteopontin differences between the main perimortem sample used for the present research from that of a sample derived from previously embalmed individuals as a means of determining if embalming plays a role in protein preservation. The study examined 9 iliac biopsy samples from 9 individuals, listed as “unembalmed,” and 7 iliac samples from 7 embalmed individuals. The study used a Mann-Whitney U-test to compare the medians for the image mean pixel intensity (16-bit) and pixel standard deviation. Introducing a new software program into the mix, Oxford Industries BitPlane™ Imaris® v.9 (185), this manuscript established the guidelines for the protein fluorescence portions of Ch. 3.2, as well as the protocols for cellular counts used in Ch4.2.

It should be noted that following Ch. 2.2 methodological changes were made to the imaging protocol of this project. Most notably, there was a change in the bit-per-pixel setting from 8-bits, which yield a greyscale intensity rating from 0 – 255, to 16-bits which yields a rating from 0 – 65,535. This allows for a much greater gradation in the image resolution and potentially more accurate results when analyzing for pixel intensity. Additionally, standardization was undertaken in the manner by which the images were taken, with a final protocol when imaging the proteins using a 40x objective for a total magnification of 400x/frame (utilizing a tile arrangement of 9 frames). While not affecting the results of Ch. 2.2, these new parameters did standardize the imaging of Ch. 2.3, 3.2, 4.2, and 5.1 and allow for more precise results. Further, there was progression within Ch. 2.2 as well, specifically with the methodology of the image quantification. In Phase 1 in Ch. 2.2. an RGB methodology was used as described above, but after completion of that pilot study, a more accurate methodology was found using the emission channels rather RGB (used in Phase 2 of Ch. 2.2). Emission channels were subsequently used in all subsequent chapters (Ch. 3, 4, and 5). Furthermore, upon retrospection, there were some methodological protocols there were selected that, while not necessarily in error, would have been better standardized if alternatives were used. In particular, the use of a third element in Ch. 2.2 Phase 2 (femoral controls). While these controls served their purpose and demonstrated that the variations seen between the Apollonian sample and the Clinical

sample were more likely derived from diagenesis and not as a result of elemental differences, similar aims could have been achieved using methodologies such as cortical masking. This would have allowed the direct comparison of bone surface to bone surface without the addition of a third, confounding element. However, given the fact that the results of the study found the stained femoral controls more closely mirrored that of the Clinical sample, while the bone structure of ilia is more in line with ribs than femora suggests that the wavelength variation was more likely than not diagenetic in origin.

## 2.2 Use of laser-scanning confocal microscopy in the detection of diagenesis in bone (187)

### 2.2.1 Introduction

Much of the histological work that has been conducted in forensic anthropology to date has been limited to the use of polarized light microscopy (191), although technologies such as scanning electron microscopy (SEM) (178, 192), and specialized staining of samples for histopathological analyses have also been employed (193). The present study focuses on the use of an underutilized tool in osteological analysis: laser scanning confocal microscopy (LSCM). Using non-human and human bone samples, we examined the value, strengths, and drawbacks of employing LSCM for various histo-osteological analyses, or the analysis of bone at a microscopic level. In particular, the purpose of this research is to examine the usefulness of LSCM in the detection of diagenesis, and bone protein presence and quantification. By detecting bone protein presence and quantification, theoretically one could calculate its degradation and develop a more accurate post-mortem interval in highly decomposed and skeletonized remains.

Developed in 1955 (patented in 1957) by Marvin Minsky, confocal microscopy can be considered an extension of light microscopy (168, 169). Designed with the particular interest of observing biological events *in vivo*, the basic theory behind confocal imaging is that by reducing the amount of scattered light from the image via pinhole technology, one can produce a more detailed image down to the cellular and intracellular level (168-170). Minsky's microscope utilized a zirconium arc source to produce a pinhole of light that was focused on an objective lens, passing through the specimen, then through a second objective lens with a second pinhole and the same focus, or confocal, as the original. The light then strikes a low-noise photomultiplier which produces a signal proportional to the brightness of the pinhole light (168, 169).

In the 1960's and 1970's, great advancements were made in video and laser technology, both of which have aided in improving the original Minsky microscope. In 1966 G. W. Ellis began incorporating lasers in microscopy with a novel conventional light microscope that was able to split the beam (168). With this microscope, three-dimensional (3D) microimaging became possible. By 1983 laser and scanning technology had progressed and Nils Åslund and

colleagues were able to develop the first laser scanning confocal microscope. This technology allowed for the imaging of thin optical scans free from out-of-focus fluorescent light (168).

The modern laser scanning confocal microscope uses acousto-optic tunable filters (AOTF) as a means of selecting excitation wavelengths of fluorophore probes. Advancing computer technology further allows for the movement of mirrors and lenses to collect and display the best image possible (169). With the development and aid of computer technology, modern LSCM is able to project images using quantified microscopy; that is, in a given pixel the software calculates the light intensity in comparison to other pixels (169-171). This allows the operator to quantify the presence of a substance, immunoassay, cells, etc. in a given tissue, with the understanding that the greater the quantity of a substance, the brighter it will shine in a pixelated area. Further aiding this methodology, as pixelation technology improves with the advancement in resolution and computing technology, the generated image resolution and quality will also improve.

While LSCM has been in use for 30+ years as a means of examining biological events on a cellular level *in vivo*, its use on archaeological and anthropological bone histology, particularly forensic anthropological bone histology is still relatively novel. One of the first studies of bone in an archaeological context using LSCM was conducted by Maggiano and colleagues (163, 164). They (163, 164) utilised LSCM to demonstrate the usefulness of the technology as a means of testing the presence and concentration of tetracycline (TC) in bone, as TC has an implication in the health and diet of past peoples. Looking at various regions of interest along the cortical bone, the authors were able to positively demonstrate that LSCM can be used to visualize bone using both spectral and fluorescence intensity (163, 164).

Poundarik *et al* (29) conducted one of the first trauma studies of bone using LSCM with a particular interest in the role of osteocalcin/osteopontin (OC/OPN) dilatational band formation in fracture ( $f_x$ ) defence, and band separation as a result of fracture energy. Using LSCM and atomic force microscopy (AFM) Poundarik *et al* (29) were able to detect the presence of OC and OPN in the microfractures ( $mf_x$ ) resulting from their controlled crack propagation test (29). Schmidt *et al* (162) used white light confocal microscopy (WLCM) as a way of visualizing, quantifying, and profiling cut marks of the surface of cortical bone. Using mapping software, Schmidt *et al* (162) were able to create a topographic 3D map of the surface of the bone with the ability to quantify

the kerf patterns of the various cut marks, and were further able to accurately ascertain the profiles made by the different style blades used.

In 2017, Capasso *et al* (172) utilized LSCM to distinguish between archaeological remains and clinical remains using bone's natural autofluorescence. Their study was conducted in two parts: examining whether the natural autofluorescence was the result of the bone mineral component or the collagen and using the autofluorescence intensity to determine the date of the bone. They found that it is not necessary to de-mineralize the bone prior to assessing autofluorescence, as had been done previously, and that the mineral component can be used in examining the bone's autofluorescence (172). In addition, Capasso *et al* (172) were able to demonstrate that the bone mineral's natural autofluorescence decreases over time, likely due to the decreasing organic components (172). In 2018 Blouin *et al* (173) published on the use of LSCM as a general tool used to image osteoblasts/osteoclasts, canalicular organization, and tetracycline labeling. They found that LSCM was a useful tool in the imaging of pre-osteoblastic formation, the three-dimensional imaging of canaliculi, and the registration of tetracycline in mice models (173).

While the results of the previous studies found that LSCM can be a useful tool in bone research, they are limited in scope and, with the exception of Capasso *et al* (172), have not been tested for forensic applications. This paper introduces a variety of applications of LSCM in forensic anthropological research, including differentiating between "Fresh" and 5-year-old bone, and detecting and mapping diagenetic alterations. This research opens the door to future work in which three-dimensional models of targeted materials can be used to detect and map pathological, traumatic, or diagenetic events by specifically demonstrating the utility of LSCM in histo-osteological analysis.

## 2.2.2 Materials and Methods

This research was divided into two phases. The first was designed to establish how LSCM could be used to evaluate the presence or absence of proteins and cells, as well as to develop a framework for studying diagenesis in relation to the loss of these organic materials. The presence of autofluorescence under various wavelengths was used to distinguish diagenetically altered bone from "Fresh" bone. The second phase involved using toluidine blue to map diagenetic alteration in human bone.

### 2.2.3 Preparation and initial examination of all samples

All samples were embedded in methyl methacrylate, sectioned, and polished to approximately 10 $\mu$ m. Samples were imaged using a Carl Zeiss™ LSM 800® laser scanning confocal microscope. Methyl methacrylate was chosen as the embedding medium given its widespread acceptance in reflected light and SEM histology, and its low optical noise component (194). Multiple image parameters, including wavelength, pinhole, depth of z-stack, and gain, were utilized to maximize image quality. All samples were imaged initially using all four lasers, including the 405nm, 488nm, 543nm, and 633nm wavelengths ( $\lambda$ ), producing one image per wavelength. If the wavelength did not register an image, then it was eliminated from a particular analysis. In this manner, the number of lasers could be systematically reduced to maximize image visibility. Excitation wavelength transmissions were set to literature recommended standards (169), and the master gain and offsets were adjusted per section to optimize the image. Emission wavelengths were also adjusted to literature recommended standards (169). Individual wavelengths were turned off, both in imaging and post-imaging, to isolate targeted materials. Images were then analyzed using Fiji® imaging software (195), Carl Zeiss™ Zen 2 Core® imaging software (196), and the on-board Carl Zeiss™ LSM 800® image capture software. It should be noted that in both Phase 1 and Phase 2, this study did not mask and exclude negative areas within the cortical structure including Haversian, Volkmann's, micro-*f*<sub>x</sub>, and other areas that otherwise would appear as black spaces. As a result, a retrospective limitation is that samples with an excess of negative spaces could artificially depress the individual and grouped wavelengths thus effecting the overall results.

#### 2.2.3.1 Phase 1 sample and methodology

A sample of 23 pig (*Sus scrofa*) bone samples extracted from the ilium and humerus of 6 individuals, divided equally between “commercial/fresh” and “5-Year,” were used to assess the overall ability of LSCM to detect proteins and cellular structures, as well as to determine if diagenetic alterations could be imaged using histochemical techniques. Thirteen of the samples, from 6 individuals originated from a sub-arial (surface) deposition decompositional study conducted at Boston University (Boston, MA), examining the effect of trauma on the rate of decomposition, using purpose-bred pigs euthanized following approved methods (captive-bolt) by the Institutional Animal Care and Use Committee (IACUC) at Tufts University School of Veterinary Medicine (117, 129, 188). The bones were left on the surface for 2 years. Upon

completion of the original study, the samples were packaged in brown paper bags and stored for 3 years, allowing the organic materials to continue decomposition at a reduced rate. These were designated the “5-Year” sample (see Appendix D: 6.4.3 for Material Transfer Agreements). An additional 10 samples from 5 individuals were collected from a commercial butcher and were designated as the “Fresh” sample. The individual bones were collected a few days postmortem and embedded within a week of death.

In order to detect diagenetic alteration all four wavelengths of the LSCM were individually utilized and examined at all three levels of magnification (400x, 640x, 1000x). Samples from all were examined unstained ( $n=20$ ) and then staining was applied to  $n=11$  (see Table 2.2-1). While the endosteal surface also demonstrates diagenetic changes, this portion of the study only focused on the periosteal surface. Multiple fields of view along the periosteal edge were selected for imaging, because it was anticipated that environmental degradation, or taphonomic processes would impact the periosteal surface first. The images from the individual wavelengths that exhibited fluorescence at a given level magnification were subsequently combined into a single stacked image using Carl Zeiss™ Zen 2 Core® imaging software (69 images total). Differences in fluorescence between the 5-Year and Fresh bone were examined by importing the grey-scale channel images produced for each sample into Fiji® and converting them into RGB, with the colours of the channels arbitrarily set by the author to closely mirror the wavelength to the visible spectrum. Fiji® was then used to count the number of red, green, and blue pixels on each image (195). The intensity of fluorescence was analyzed using colour values. Fiji® begins with a greyscale image and scores each pixel on the image from 0-255, where 0 equals black and 255 equals white, then converts to individual RGB colour bands (red, green, or blue). The most intense fluorescence, therefore, scores 255 (see Fig. 2.2.1 for an example of the histogram output). The mean colour-value, calculated as the mean pixel value across the entire image, was input into SPSS® (197). Each sample included over 100,000 data points. For the histograms and analyses used, the colours displayed were arbitrarily set to particular emission wavelengths from the specific laser excitations using the default colouration ascribed by the Carl Zeiss™ LSM800. In post-processing of the images generated using ImageJ© (186), the 4 individual colourized channels were compressed into a single stacked and flattened image, removing the data from the individual wavelengths (405nm, 488nm, 555nm, 643nm), transforming the image into a standard photograph. A red/green/blue analysis was done

on these images with the visual colours (and therefore the histogram analyses) being retroactively associated to their original Zeiss™ wavelength colourations. More specifically the red histogram bar corresponds to the 643nm and 555nm lasers as these were default red and orange in the initial imaging, the green colour corresponds to 488nm and the blue to the 405nm, again for similar reasons. An ANOVA was therefore conducted for the red, green, and blue means of the unstained images in order to ascertain statistical differences between the two sample groups (Fresh vs 5-Year). For the purposes of this experiment the  $H_0$  was the  $p>0.05$  indicating that there was no statistically significant difference between the subject groupings while  $H_1$  would be  $p\leq 0.05$  indicating a significant difference. The average voxel volume was  $0.795\mu\text{m}^3$ , with the average  $x$ - and  $y$ -axis being  $\approx 900\mu\text{m}$  at 1024 pixels, and the  $z$ -axis being  $\approx 25.75\mu\text{m}$  with 25 optical slices with a interval of  $1.03\mu\text{m}$ , and the voxel volume calculated using the following formula:

$$d^x = \frac{FOV^x}{Matrix^x}$$

$$d^y = \frac{FOV^y}{Matrix^y}$$

$$d^z = \frac{FOV^z}{\#ofSlices}$$

$$Voxel\ Volume\ \mu\text{m}^3 = d^x \times d^y \times d^z$$

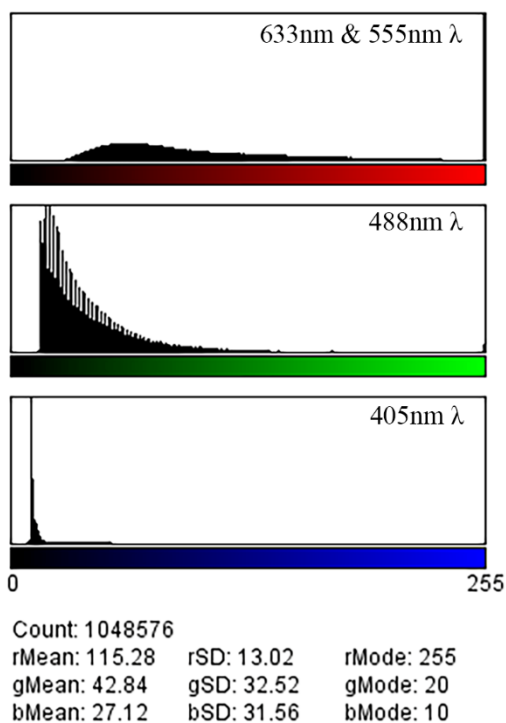


**Figure 2.2.1: Histogram of an unstained 5-year pig sample. The red hue is associated with both the 633nm and 555nm wavelengths, while the green is associated with the 488nm wavelength and blue is associated with the 405nm wavelength.**

In order to differentiate the inorganic from organic components of bone, three different stains were tested. Six (5-Year,  $n=3$  and Fresh,  $n=3$ ) of the 23 samples were stained with Basic Fuchsin, which adheres to the mineral component of bone and fluoresces at the 543nm wavelength (Table 2.2-1). Hematoxylin and Eosin (HE) stain was also used on three samples as it has been shown to be useful in traditional light microscopy of bone. HE also fluoresces with LSCM, but the combination of LSCM bone imaging and HE stain created a photo bleaching effect. As a result, these samples were excluded from further analysis and are not included in the results. Nine were left unstained for comparison.

**Table 2.2-1: Samples and stains for phase 1 study.**

	<b>Basic Fuchsin</b>	<b>Hematoxylin &amp; Eosin</b>	<b>AF488/SlowFade Gold</b>	<b>Remained Unstained</b>	<b>Total</b>
<i>5-Year samples</i>	3	2	2	6	13
Ilium	1	1	1	2	5
Humerus	2	1	1	4	8
<i>Fresh samples</i>	3	1	3	3	10
Ilium	1	1	1	1	4
Humerus	2	0	2	2	6

Five of the samples (5-Year samples,  $n=2$  and Fresh samples,  $n=3$ ) were labeled with Alexa Fluor™(tm) 488 pre-mixed with SlowFade Gold and examined using LSCM at 405nm, 543nm at 640x magnification for fluorescence of cells, in order to determine if this protocol is as effective as the approach taken by Capasso and colleagues (13). The stacked images from the two wavelengths were imported into Fiji/ImageJ<sup>®</sup>. Areas of cellular fluorescence were manually highlighted and counted using the object count feature in Fiji/ImageJ<sup>®</sup>. A Fisher's Exact Test was completed to determine if there was a difference between the bone age (fresh vs. 5-Year) and cell count. This was then repeated with the cell count standardized by bone volume using the formula as set down by Parfitt *et al.* (198) which calculates osteoclast number/Total Volume as  $\text{mm}^3$ . It should be noted, however, that the Parfitt *et al.* (198) formula is based osteoclast numbers, and the present study is using it on unspecified cells.

### 2.2.3.2 Phase 2 sample and methodology

A total of 13 human samples from 13 individuals were used to establish a protocol for detecting diagenesis in human bone, including samples of femora, ilia, and rib sections (Table 2.2-2). The Clinical sample consists of iliac biopsy samples representing modern living individuals obtained from the Centre Hospitalier de l'Université de Montréal (Montréal, QC). While informed that the samples were devoid of pathological conditions by the CHUM laboratory, the reason for their collection was not disclosed to the primary researcher and the laboratory personnel have since moved on to different positions. The Apollonian sample from approximately 7 individuals dates from 5<sup>th</sup>-2<sup>nd</sup> century BCE and consists of ribs derived from a sub-surface deposition (see Appendix D: 6.4.3 for Material Transfer Agreements). This sample

was designated as “Apollonian”. A modern femoral cadaveric “control-style” sample obtained from the University of Toronto Division of Anatomy was used to determine if differences observed between the ilia and ribs could be the result of anatomical variation between bones, rather than differences in the age/time period of the bones. If the stained imaging results mirrored that of the clinical ilia versus that of the ribs rather than being different in and of itself, this would indicate that variation between the ilia and rib would be more related to diagenesis than actual bone variation. As age and sex of the Apollonian sample were not known given the fragmentary nature of the remains, and the fact that they made up a majority of the study population, the collection of age and gross anatomical sex were not recorded for any individual. While diagenesis may affect elements differently, this study was primarily concerned with staining differentiation. Ethics protocol approval was granted from the University of Toronto Research Ethics Board (Toronto, ON, Human Protocol #33324) for use of all samples (see Appendix D)<sup>1</sup>.

**Table 2.2-2: Samples and stains for phase 2 study.**

<b>Sample Location</b>	<b>Element</b>	<b>Stain</b>	<b>Number</b>
Clinical	Ilium	Toluidine Blue	<i>n</i> =4
Apollonian (5 <sup>th</sup> -2 <sup>nd</sup> century BCE)	Rib	Toluidine Blue	<i>n</i> =7
Modern Femoral Control	Femur	Toluidine Blue	<i>n</i> =1
Modern Unstained Control	Femur	Unstained	<i>n</i> =1

All samples, except one modern femoral section, were stained with Toluidine Blue. Toluidine Blue has been shown to highlight the mineral components of bone under light microscopy. The initial plan was to test whether or not Toluidine Blue could similarly enhance the mineral aspect of bone using LSCM. When testing this sample, differences were observed between the Apollonian and Clinical samples, leading to further exploration of diagenetic alteration. In order to ascribe differences between the samples to diagenesis, confounding factors

---

<sup>1</sup> For CHUM Use of Samples, ethics approval, and Material Transfer Agreement information see Appendix D.

such as anatomical region, and quantity of stain were considered. One unstained femoral cross-section was imaged to obtain a baseline of natural autofluorescence of unstained cortical bone. One stained femoral control provided a point of comparison to the stained rib and iliac samples to ensure that differences in bone anatomy and physiology did not produce differential staining capable of impacting the degree of fluorescence, independent of the degree of diagenesis.

All samples were imaged at both 400x and 640x magnification. The entire ilium and rib sections were tile imaged; meaning that the entire bone was imaged at the specified level of magnification and each field of view was “stitched” together automatically by the software. Only the antero-medial section of the femoral controls was imaged, although all three compartments from periosteal through to the endosteal surface were tile imaged.

For each wavelength, the presence or absence of an excited fluorophore at a given pixel can be detected. The number of excited pixels per image was calculated using the Carl Zeiss™ LSM 800® Image Capture software. The results for each sample type (Clinical vs Apollonian) were then averaged in Microsoft™ Excel® (199). To examine degree of diagenesis a similar approach was taken from Ch. 2.2.3.1 (Phase 1) where each wavelength intensity was calculated in a combined stacked RGB image, as well as individually<sup>2</sup>. By assessing individually, a more accurate representation of each wavelength is presented, with the absence of blending of wavelengths as seen in Phase 1. Additionally, it should be noted that for Phase 2, the 555nm emission wavelength as used in Phase 1 was altered to a 543nm emission wavelength, and the arbitrary colours assigned to each wavelength by default settings as set by the Carl Zeiss® LSM800™ Zen capture software was altered as well with the 543nm changing from orange to red, and 633nm changing from red to blue. Each sample consisted of over 100,000 points, therefore a one-way ANOVA of the means was conducted in IBM's™ SPSS® (197). A Bonferroni post-hoc test was not conducted as there were less than two individuals in the three categories tested. For the purposes of this experiment the  $H_0$  was the  $p>0.05$  indicating that

---

<sup>2</sup> Unfortunately, a data loss including loss of the original .czi images and the original data spreadsheets precludes their inclusion in this paper.

there was no statistically significant difference between the subject groupings while  $H_I$  would be  $p \leq 0.05$  indicating a significant difference.

## 2.2.4 Results

### 2.2.4.1 Phase 1

The results of the ANOVA comparing the RGB fluorescence of the Fresh vs 5-Year bone were significant in the red and blue means, ( $p=0.004, f_l=3.571$  [red];  $p=0.010, f_l=8.379$  [blue]), while the green mean yielded no significant difference ( $p=0.560, f_l=0.353$ ). This is unsurprising as the green fluoresced at similar colour values in both sample groups, while the red visually appeared in only the 5-Year sample through a qualitative analyses of the images. In addition, the Fresh sample yielded smaller colour-value ranges with lower means, standard deviations, and modes, but higher average pixel counts at the wavelength modes.

There were also qualitative differences in the histochemical properties between the 5-Year pig bone and the Fresh bone, at all levels of magnification, in both the unstained and Basic Fuchsin stained samples. Using the  $405nm$  and  $633nm$  lasers it was possible to fluoresce both the organic components and bone mineral structure of the Fresh and 5-Year bone, although more pixels exhibited fluorescence in the Fresh bone. We can determine this because Basic Fuchsin fluoresces the mineral component at the  $405nm$  and  $543nm$  wavelengths (thus appearing red in colour), while fluorescing the organic component at the  $633nm$  wavelength (appearing more green). When converted to RGB, the unstained 5-Year bone included red/yellow pixels in greater numbers, in addition to the green and blue pixels, whereas the Fresh bone registered mainly green/blue pixels (Fig. 2.2.2). The Fresh samples registered a higher colour-value mean, standard deviation, and mode for the green and blue colours (RGB) on the combined image produced by using the  $405nm$ ,  $488nm$ , and  $633nm$  wavelengths, than the 5-Year sample. The difference in the wavelength registrations of the  $488nm$ ,  $543nm$ , and  $633nm$  channels between the Fresh and 5-Year samples are indicative of some diagenetic variation in the samples. While this variation was true for all channels, only the  $555nm$  (which correlates with the red colour) mean ANOVA analyses yielded a significant difference with a  $p=0.004$ . This suggests that the  $555nm$  (red) wavelength was fluorescing the diagenetic alterations (Fig. 2.2.3). Overall, the Fresh samples were more uniform in colour visually and did not generate a significant difference in the green ( $488nm$ ) wavelength only. The diagenetically altered (5-Year) samples registered a

wider range of wavelength values and higher wavelength value means, wider standard deviations, and higher modes, but lower mean pixel counts at those modes. Upon reanalysis of the sample results, several potential outliers appeared. A  $z$ -score analysis was conducted on the three colour means yielding outliers in the red and green channels and the ANOVAs reanalyzed. That said, once removed, the interpretation of the ANOVAs did not change, though the significance of the red channel ANOVA rose to  $p=0.028$  ( $f=6.003$ ), and the green channel to  $p=0.567$  ( $f=0.342$ ). However, though a reanalysis of the ANOVA did *not* yield any change, when graphing and analyzing the individual means generated, specifically with the outliers removed, what was noted was that the pattern of colour variation changed. While a qualitative analysis of the images demonstrated more, and concentrated red areas with the 5-Year samples that were lacking in the Fresh samples, the individual means and a scatter plot of those means demonstrates that the red channel was the largest channel generated for both sample groups, followed by the green channel and then the blue (see Table 2.2-3, Fig 2.2.8). The difference, however, as seen in Fig 2.2.8, is in the proportions, with the red channel registering higher in the 5-Year sample, and while the red channel was the highest in the Fresh sample as well, the green channel registered more equidistant in the Fresh sample than in the 5-Year sample. Though the green channel was higher in the 5-year sample group than the Fresh, it appears it was overshadowed by the red channel given the amount of the red channel in comparison to the green.

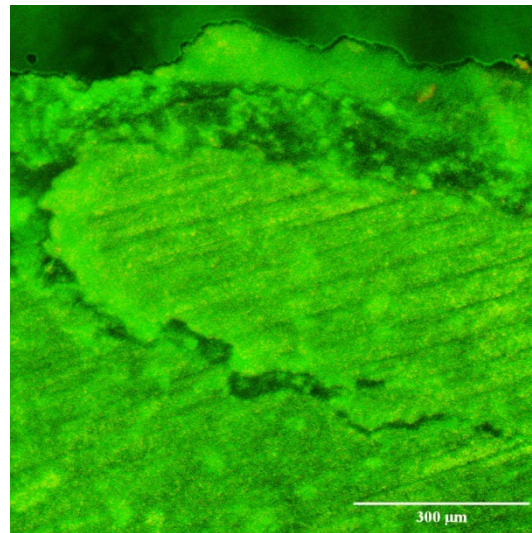


**Figure 2.2.2: Image of “Fresh” unstained pig bone sample (640x magnification). All four channels (405nm, 488nm, 555nm, 633nm) represented. Scale bar is 300 $\mu$ m.**

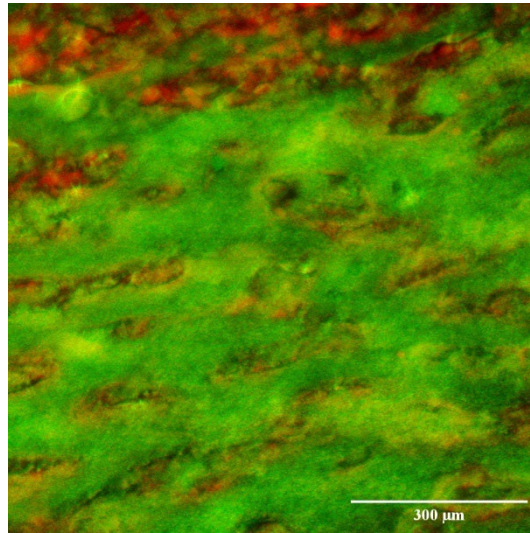


**Figure 2.2.3: Image of 5-year unstained pig bone sample depicting diagenetic alteration (640x magnification). All four channels (405nm, 488nm, 555nm, 633nm) represented. Scale bar is 300 $\mu$ m.**

Using the 405nm laser, and the AF488/Slow-Fade Gold samples, cells were visible in the Fresh bone (Fig. 2.2.4), while the 5-Year samples yielded no presence of cells and were generally devoid of 405nm fluorescence. The 405nm wavelength was ascribed to cell presence as the image results were similar qualitatively to Blouin *et al* (173). Although 633nm wavelength produced fluorescence in all samples, it was brighter and more common in the Fresh sample group, demonstrating that the collagen content was higher in this sample. Fisher's Exact Test confirmed what is evident in Table 2.2-3; there is a strong negative association between cell count and postmortem interval ( $p < 0.001$ ). This test was also run to a standardized bone volume with  $p < 0.001$ . Lastly, given the small sample size in both phase 1 and phase 2 of the paper, a power and Eta squared ( $\eta^2$ ) effect size analyses were run with the results being a power of 0.389 and an effect sizes ranging from 0.166 [red mean], 0.019 [green mean], to 0.318 [blue mean] (a large effect size being considered at or above 0.13) indicating that there was a strong possibility of achieving a correct result.

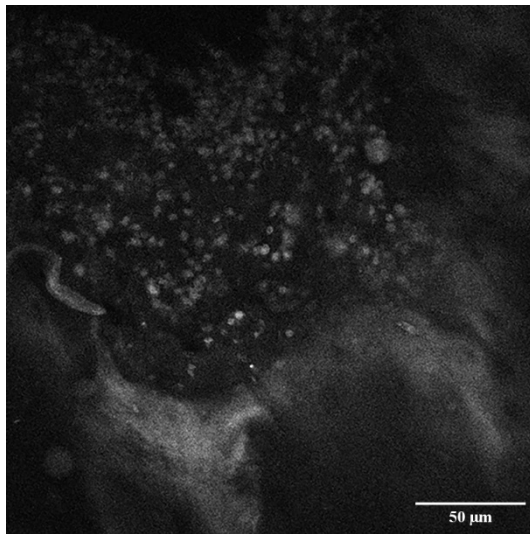


**Figure 2.2.4: Grayscale image of “Fresh” pig bone with unknown cell highlighted present (640x magnification). Imaged with 555nm wavelength. Scale bar is 50μm.**

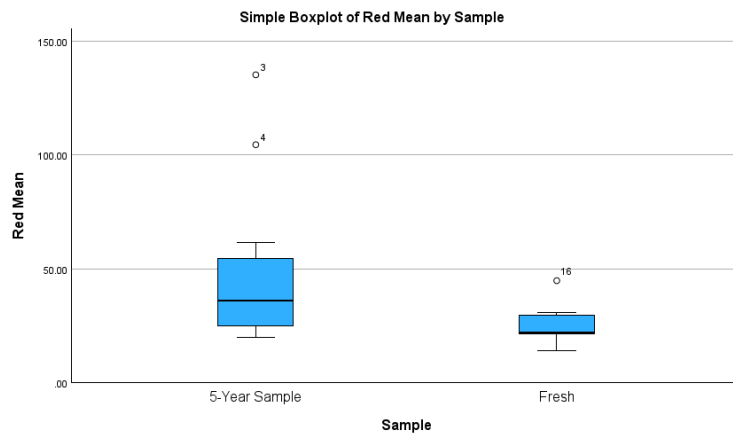


**Figure 2.2.5: Red mean box plot.**

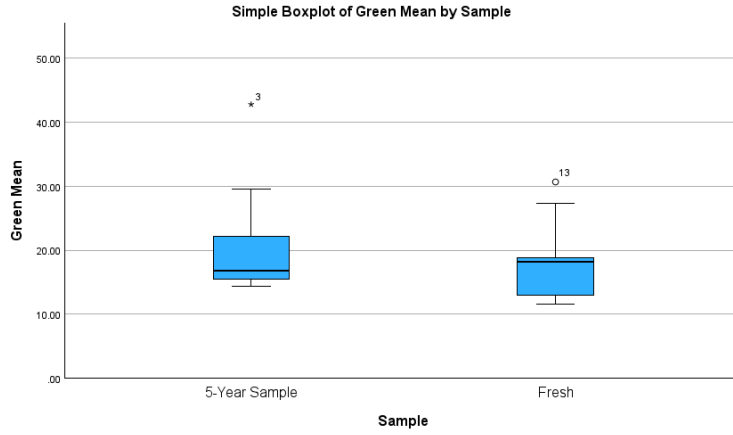


**Figure 2.2.6: Green mean box plot.**

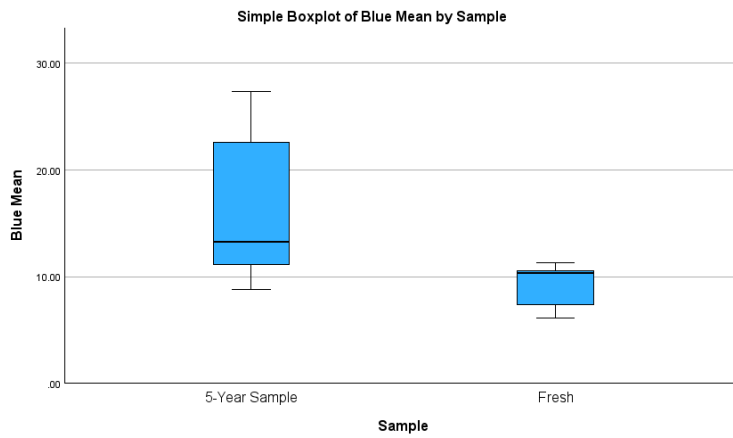


**Figure 2.2.7: Blue mean box plot.**

**Table 2.2-3: Results of the phase 1 quantitative study. In this table the green samples are left unstained, red are stained with Basic Fuchsin, and yellow labeled with Alexa Fluor™(tm)488 with SlowFade Gold. Please note all samples were imaged unstained prior to treatment, and the Red/Green/Blue values presented are from the unstained calculations. Also note the H&E samples were excluded due to photobleaching.**

Sample	Cell Count	Cell Count per mm <sup>3</sup>	Red Mean	Red StDev	Red Mode	Green Mean	Green StDev	Green Mode	Blue Mean	Blue StDev	Blue Mode
5-Year	0	0	28.95	7.69	21	16.81	3.34	15	11.5	8.53	10
5-Year	0	0	36.21	6.96	34	21.18	2.57	21	26.7	22.06	12
5-Year	0	0	135.2	66.76	254	42.81	24.83	36	25.4	28.89	12
5-Year	0	0	104.5	35.43	128	29.61	18.58	26	27.4	32.86	11
5-Year	0	0	19.99	5.18	17	14.4	6.94	14	10.74	7.27	8
5-Year	0	0	40.1	23.1	29	16.52	2.66	15	13.28	9.53	11
5-Year	0	0	29.97	18.58	17	23.21	15.42	15	10.57	5.24	10
5-Year	0	0	21.27	3.94	20	16.75	1.03	16	11.94	5.32	11
5-Year	0	0	61.65	55.89	22	18.13	10.57	14	13.53	8.26	13
5-Year	0	0	20.25	9.48	17	14.35	12.05	13	8.82	1.16	8
5-Year	0	0	47.18	34.17	17	14.43	3.84	13	19.71	20.5	8
Fresh	24	0.8718	30.6	7.48	29	18.85	7.51	17	11.26	9.71	10
Fresh	24	0.8718	13.94	8.63	10	30.68	3.65	29	6.13	3.42	6
Fresh	24	0.8718	22.92	7.41	20	17.14	3.73	16	10.42	6.92	10
Fresh	30	1.0898	22.13	6.19	18	12.47	0.67	12	10.55	9.06	6
Fresh	27	0.9808	44.78	32.65	25	27.28	26.85	15	10.89	8.96	9
Fresh	27	0.9808	21.53	4.47	19	18.27	1.65	17	7.16	4.68	7
Fresh	27	0.9808	29.5	11.38	24	18.71	7.02	16	9.1	6.21	9
Fresh	15	0.5449	19.92	5.85	17	12.99	1.55	12	7.4	1.85	7
Fresh	15	0.5449	22.08	9.33	17	11.62	0.65	12	10.32	10.09	7

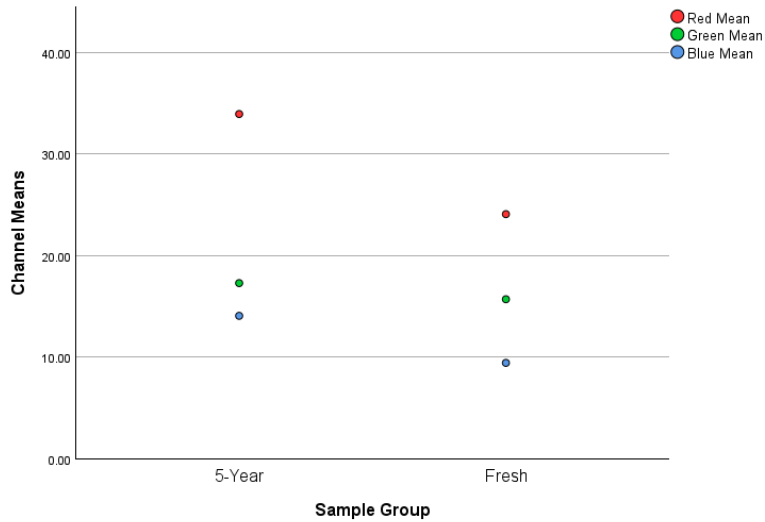


**Figure 2.2.8: Scatter plot of Phase 1 means with outliers removed.**

### 2.2.4.2 Phase 2

In Phase 2, all of the stained samples (Clinical and Apollonian) registered on the 543nm 633nm wavelength, though there was variation between these two sample groups. Meanwhile the Unstained Control had minimal registration on these wavelength. The Clinical samples registered higher on the 543nm wavelength, while the Apollonian sample registered higher on the 633nm wavelength ( $\bar{x}=38.303$ ) for the Clinical sample at the 633nm;  $\bar{x}=74.071$  for the Apollonian sample) (Fig. 2.2.9 – 2.2.11). Note that the colour of the various bars on graphs mirror the colours used during the arbitrary colouration of the greyscale imaging of the microscope. The setting used was a secondary default of the LSM800 and though used in error in comparison to Ch. 2.2.3.1, the variations seen are true in the sense that they are calculated from the greyscale and not the colouration. This variation in wavelength ratios altered the colour-value of the samples, causing the Clinical samples to appear more violet in colour and the Apollonian samples to appear more blue (Fig. 2.2.12 & 2.2.13), but not the channel values. For the Apollonian sample, focalized registration on the 405nm and 488nm wavelengths (Fig. 2.2.13) and thicker mineralization around the Haversian canals were also evident. Additionally, a one-way ANOVA was run between the clinical, diagenetic, and two control groups to test if there was a difference in the means of the four channel's differing mean fluorescence and standard deviations.

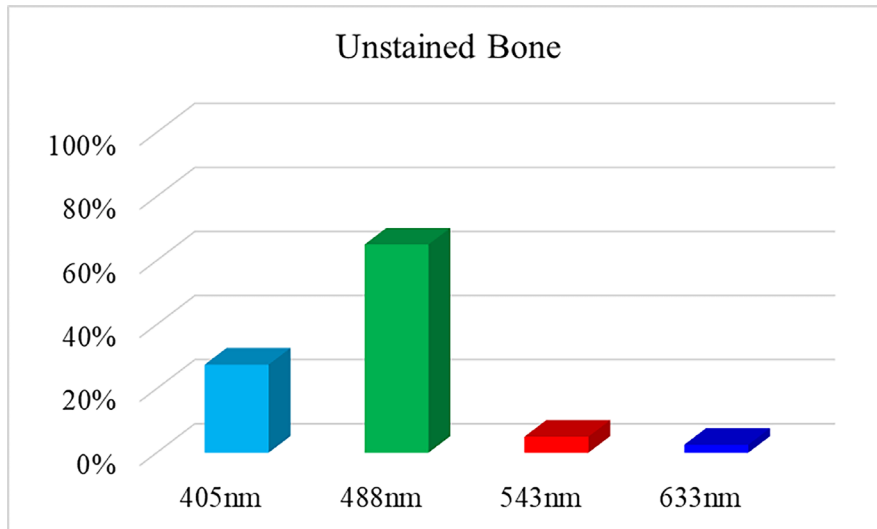


**Figure 2.2.9: Ratio of fluorescence intensity using unstained bone. The colours correspond to the colours used on the generated greyscale image.**

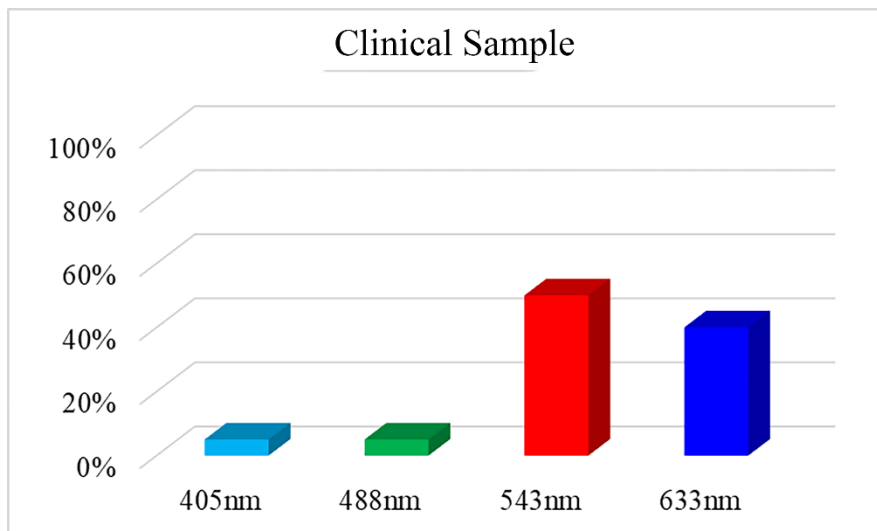


**Figure 2.2.10: Ratio of fluorescence intensity from the Clinical sample using toluidine blue.**

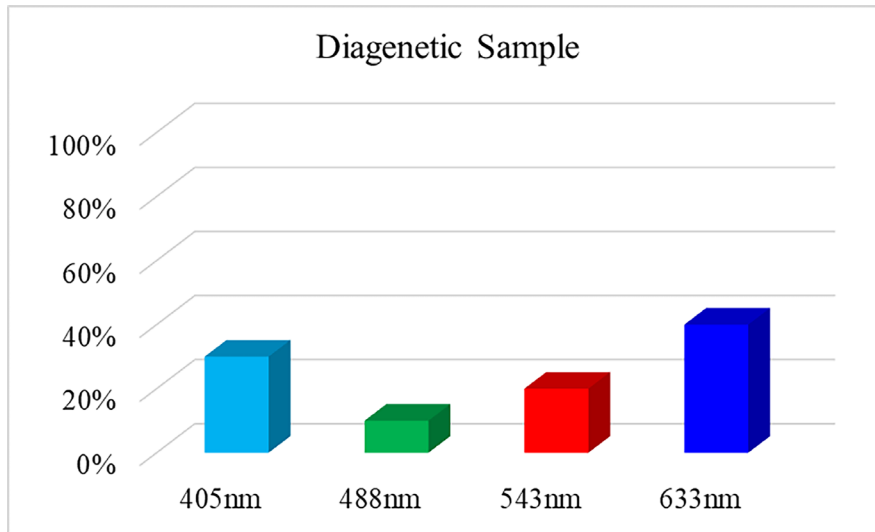


**Figure 2.2.11: Ratio of fluorescence intensity from Apollonian sample using toluidine blue.**

The results of the ANOVA test indicate that there was a significant difference between the Apollonian (rib) and Clinical (iliac) samples in the 488nm wavelength ( $p=0.016, f=8.411$ ). In contrast to the Apollonian and Clinical bones stained with toluidine blue, which register on the 543nm and 633nm wavelengths (Fig. 2.2.12 & 2.2.13), unstained bone registers on the 405nm and 488nm wavelengths (Fig. 2.2.14). For the Apollonian bone, localized areas of diagenetic alteration are registering on the 405nm and 633nm wavelengths, particularly at the margins where they appear more green and turquoise in colour (Fig. 2.2.13). The modern femoral control stained using the same protocols, registered similarly to the iliac Clinical samples thus eliminating bone location as a factor of wavelength registration (Compare Fig 2.2.11 & 2.2.12).

When examining the ANOVAs from a standpoint of a red/green/blue analysis, there was a significant difference in the green channel ( $p=0.011, f=6.732, \eta^2=0.692$ ), while the red channel demonstrated no significant difference ( $p=0.671, f=0.532, \eta^2=0.151$ ). The blue channel returned a mixed result with this phase, however. Initially a non-significant result was returned with  $p=0.115 (f=2.623, \eta^2=0.466)$ , though two outliers were present, including one in the blue channel and once removed, the significance changes to  $p=0.015 (f=6.564, \eta^2=0.711)$ . The second outlier was found in the red channel which had an Apollonian individual that was found to be low. Once removed, the results of the ANOVA increased to  $p=0.708 (f=0.475, \eta^2=0.151)$ . However, while these results indicate that there is a probably a variation in the 405nm, 643nm, and especially the 488nm (green) wavelengths, these ANOVA results do include the unstained and

stained femoral controls, the former of which would naturally push the 405nm and particularly the 488nm wavelengths. This can be seen especially when one examines the scatter graph (Fig. 2.2.15) in which with the unstained femoral control the channel with the highest registration is green, which is the channel of the lowest registration in clinical and stained femoral control and middle channel in the Apollonian sample. With the femoral controls removed, and comparing just the clinical and the Apollonian samples there is again a significant difference in both the green and blue means ( $p=0.042, f=5.605, \eta^2=0.384$  [green];  $p=0.025, f=7.182, \eta^2=0.444$  [blue]), but not in the red mean ( $p=0.888, f=0.21, \eta^2=0.002$ ). When the two Apollonian outliers are removed the overall results do not change though the numbers do. Specifically, the blue mean changes to  $p=0.003$  ( $f=17.733, \eta^2=0.689$ ) and the red mean changes to  $p=0.713$  ( $f=0.146, \eta^2=0.018$ ). See Fig. 2.2.16 and Table 2.2-4. The results of these tests, particularly with the femoral controls removed, indicate that the Apollonian samples have a higher registration of the blue, and especially the green channels, than that of the clinical samples (see Fig. 2.2.16). Finally, a power analyses was performed with the results of the power analysis being 0.757 suggesting a strong possibility of achieving a true result.

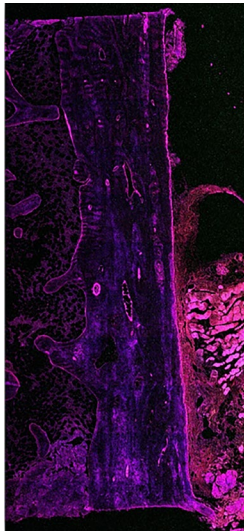


**Figure 2.2.12: Image of Clinical iliac sample stained with toluidine blue at 400x magnification per frame, using 60 frames. All four channels (405nm, 488nm, 543nm, 633nm) represented.**

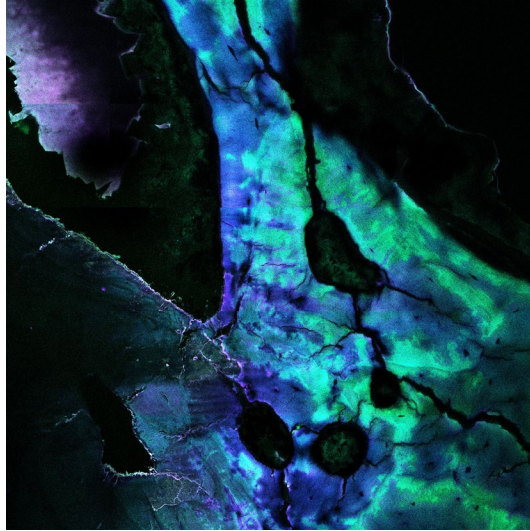


**Figure 2.2.13: Image of Apollonian rib section at 640x magnification per frame using 9 frames, stained with toluidine blue. Of important note is the turquoise/green staining around the edges demonstrating registration of the 405nm and 488nm wavelengths. The turquoise/green colour represents 488nm and 405nm, while the blue and purple colour represents the 543nm and 633nm.**

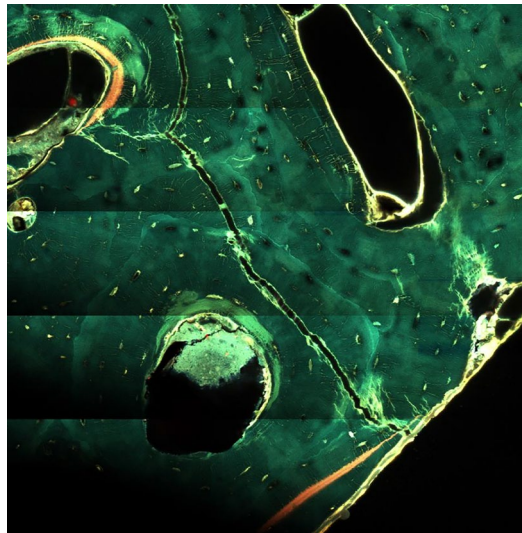


**Figure 2.2.14: Image of unstained section of femur at 640x magnification per frame using 25 frames. All four channels (405nm, 488nm, 543nm, 633nm) represented.**

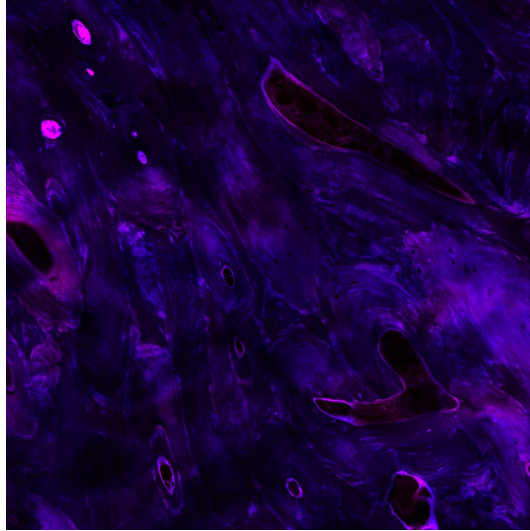


**Figure 2.2.15: Image of femoral control at 640x magnification per frame using 25 frames, stained with toluidine blue demonstrating a close registration of wavelengths to that of the Clinical iliac samples. All four channels (405nm, 488nm, 543nm, 633nm) represented.**

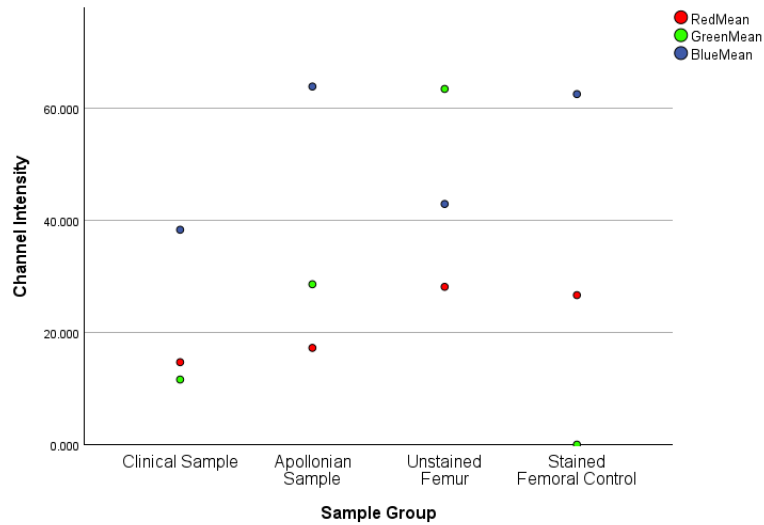


**Figure 2.2.16: Scatter plot of Phase 2 demonstrating the distribution of red, green, and blue means across the four groups with 2 outliers removed. Note: the colour of the dots correspond to the red, green, and blue means calculated from the histograms.**

**Table 2.2-4: Red/Green/Blue histogram means from the Phase 2 study.**

<b>Sample</b>	<b>Red Mean</b>	<b>Green Mean</b>	<b>Blue Mean</b>
Clinical Sample	4.540	9.450	42.145
Clinical Sample	7.919	15.121	45.071
Clinical Sample	1.979	7.890	18.110
Clinical Sample	44.349	13.942	47.885
Apollonian Sample	12.769	16.855	57.398
Apollonian Sample	20.326	34.025	128.805
Apollonian Sample	18.325	17.129	65.024
Apollonian Sample	15.731	14.632	58.288
Apollonian Sample	4.248	29.962	74.946
Apollonian Sample	18.801	54.363	66.319
Apollonian Sample	20.606	39.955	72.154
Unstained Femur	28.130	63.407	42.900
Stained Femoral Control	26.651	0.000	62.485

## 2.2.5 Discussion & Conclusion

There are many tools that can be used to ascertain the mineral make-up of bone. From SEM to  $\mu$ CT, researchers can develop a 3D bone model in greater resolution. This research has demonstrated that laser scanning confocal microscopy can be a valuable method of examining the microstructure of bone on a histological level. Researchers can use techniques to differentially stain the non-mineral portions of bone, deselect the 543nm wavelength and then preferentially image the organic over the inorganic, or *vice versa* (Fig. 2.2.16). These steps could prove useful when examining the collagenous portions of bone, various proteins, and even bone cells. Overall, laser scanning confocal microscopy has demonstrated a usefulness in examining histological samples of bone that other modalities may miss, such as protein quantification along the *z*-axis of a sample. When dealing with decomposition and diagenesis, using this modality and quantifying protein degradation, theoretically researchers can develop a more accurate post-mortem interval, particularly with highly decomposed and skeletonized remains.

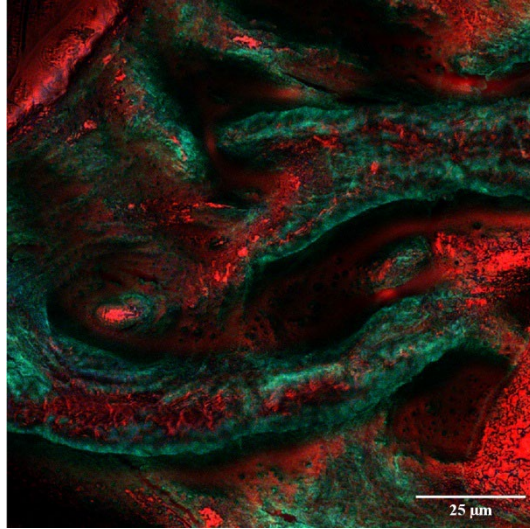


**Figure 2.2.17: Image of femoral cortex stained with Basic Fuchsin at 640x magnification per frame using 9 frames, demonstrating the interaction between collagen and mineral substructure. All four channels (405nm, 488nm, 543nm, 633nm) represented. Scale bar is 25μm.**

Visualizing the mineral and nonmineral component of bone was most effective for all samples using Basic Fuchsin. The combination of Hematoxylin and Eosin stains, which are regularly used in traditional light microscopy and have been shown to fluoresce and work with LSCM (179, 200), were tested in this analysis, but they could not be used because the fluorescence blended with the autofluorescence of bone creating a photo-bleaching effect.

Phase 1 demonstrated that LSCM can be used to differentiate bone diagenetic alteration, and that protein and organic material can be highlighted. Specifically, the 5-year samples fluoresced with greater intensity on all channels, and more so on the red channel (633nm and 555nm  $\lambda$ ), compared to the fresh samples. Both qualitative and quantitative differences in the mineral, collagenous, and protein quality were evident between the two study samples. The Fresh sample group visually appeared more green with no visible red hue (despite registration on the RGB histogram), while the 5-Year sample exhibited red hues along the periosteal margins, with wider colour-value (0-255) ranges, and no cellular fluorescence. In other words, the Fresh samples were of a brighter, more uniform green while the 5-Year sample had distinct patches of a clearly and boldly red areas indicating diagenetic incursion.

When searching for diagenetic alteration in human bone, LSCM was found to be a useful tool to visualize focalized changes in the diagenetically altered bone. This project found

diagenetic incursions into the cortices and Haversian canals of the various individual samples, but we were unable to determine if this alteration is mineral or biological in nature. Additional differential staining should aid in this distinction, and further study along these lines is recommended. The focalized fluorescence registered on the same wavelength for both the unstained bone as well as the toluidine blue stained bone, but it must be mentioned that it is not just the registration that is relevant. Rather, it is the ratio of registration that is important. Unstained bone registers predominately on the  $488\text{nm}$  wavelength, with some  $405\text{nm}$  registration and negligible registration at the  $543\text{nm}$  and  $633\text{nm}$  wavelengths, producing an overall green colour. Meanwhile the toluidine blue Clinical registered almost exclusively on the  $543\text{nm}$  and  $633\text{nm}$  wavelengths, with a higher proportion of  $543\text{nm}$  than  $633\text{nm}$ , retaining an overall blue-purple colour. Diagenetic bone however registers focally on all four wavelengths, with more at the  $405\text{nm}$  and the most at  $633\text{nm}$ , resulting in a pure-blue colour when the stacked image is converted to RGB in Fiji<sup>®</sup>. Thus, we can eliminate uneven staining as the reason for the wavelength differences.

There are some drawbacks to using LSCM, however. First of all, the equipment is expensive. To defray such costs, cross-departmental, cross-agency collaboration is highly recommended. In addition to the costs, LSCM imaging can be time consuming, depending on the features and image quality one wishes to obtain. Parts of this project utilized a tile-image  $z$ -stack, which combines multiple images throughout the sample along the  $z$ -axis and overlapping images across  $x/y$ -axes of the sample to develop a wider field of view. This, however, can take over an hour to develop a quality image, depending on sample thickness and size. Lastly, the set-up is not universal across samples; each slide must be adjusted for various sample parameters, such as pin-hole set-up and master/laser gains, which adds time to the analysis and limits the degree of standardization that is possible.

While there are some drawbacks to LSCM, the benefits are significant. Laser scanning confocal microscopy allows for higher resolution than traditional light microscopy, thus allowing more clarity of targeted materials. It is therefore possible to isolate and quantify target materials such as proteins in a sample. Assuming that bone proteins degrade in a predictable pattern, given environmental conditions, by quantifying the degradation of bone proteins in a sample, one could create a more accurate post-mortem interval in a highly decomposed or early skeletonized set of remains, though more research is needed on this topic. Further, though not addressed

specifically in this research, by isolating wavelengths one can generate more detailed microstructural examinations including analyzing for pathological indicators and bone lesions, which can affect the microstructural processes. In other words, one can visualize the effects of lesions on the microstructural level, isolating specific components, at higher magnification, resolution, and in a three-dimensional plain. Additionally, one can research with greater accuracy the effects of soil and other factors in the taphonomic processes. Lastly, LSCM can allow for greater opportunities in histo-osteological examinations including the mapping of a histological sample along the  $z$ -axis, including mapping  $mf_x$  and histotaphonomic processes.

This research demonstrates that it is possible to visualize diagenetic changes in bone using LSCM with specific stains. By combining the results of histochemical changes (as seen in phase 2), with an assessment of protein degradation (as seen in phase 1), it may be possible to develop a more accurate post-mortem interval estimate, particularly in the early “skeletonized” postmortem period. Further, by mapping out chemical diagenesis in bone, researchers can locate and focus their analyses on unaffected bone, thus avoiding potential confounding results arising from diagenesis. Although diagenesis and the presence of proteins can be visualized using traditional light microscopy, LSCM grants both greater resolution and clarity than light microscopy. With regard to diagenetic alterations, traditional light microscopy tends to focus on bone mineral destruction (165, 166). In contrast, this research demonstrates that LSCM can be used to detect histochemical changes in bone beyond mineral destruction, though more research is needed to distinguish between environmental and biological changes. Understanding protein degradation is also greatly enhanced using LSCM, where the targeted material can be isolated and counted with greater accuracy.

Further research is being conducted to determine if the diagenetic changes detected through the use of LSCM have a mineral or biological origin. Further, as different soils effect bone taphonomy in different ways, it would theoretically be possible to determine if remains have been moved by examining their diagenetic signature. Lastly, additional studies will explore the time frame required before such changes can be detected.

## 2.3 Effect of embalming on the preservation of osteopontin in bone

### 2.3.1 Introduction

The process of embalming to preserve human tissue after an individual has passed away involves chemicals such as formaldehyde, methanol, sodium borate, sodium nitrate, glycerin, water, dyes, and other detergents (201, 202). Embalming fluid infiltrates the body through major blood vessels and may be introduced through major organs and/or body cavities (202). Resulting from this, the blood in the body is either washed out completely or diluted by the embalming fluid (202). Formalin, the most commonly used embalming fluid, works efficiently for short-term preservation of soft tissue primarily during funerary practices (201, 202). Formalin has been shown to be beneficial in preserving tissue without deterioration in room-temperature conditions for longer time periods, but no study has assessed whether the fluid, through the embalming process, goes deep enough into the hard tissues of bone through the vasculature to preserve the organic materials such as proteins and cells (203). While other studies have attempted to assess the effect of embalming preservation on the mechanical properties (tensile strength, compressive strength, bending strength, etc.) of bone, this study will assess the effect of embalming fluid on the preservation of the bone protein, osteopontin (204).

Bone histology is an area that studies the microscopic tissues of bones as the proteins, cells, and hard tissues looking at the structure, morphology, size, rate of production, and growth and remodeling (203). This study focuses on the organic matrix of bone, specifically the acidic glycosylated phosphoprotein osteopontin, and its ability or inability to resist degradation post-embalming (202). Previous research has found that embalming fluid affects the amino groups in the protein polypeptide chain as it may combine with the formaldehyde to form a formylated protein, which then increases the amount cross-linking between collagenous fibers (204). The increased amount of cross-linking aids in the bone's mechanical structure, specifically the bone's strength (9, 205). The bone's ability to crack (breakage without the elastic properties, similar to a tree branch) rather than fracture (breakage with the elastic properties), relies on this collagen component (9, 29, 205).

Osteopontin (OPN) is a protein found in the bone's organic matrix that contributes to bone strength, bone matrix cohesion, and matrix toughness. It is a relatively long-lasting protein

with respect to its ability to avoid degradation, compared to other bone proteins responsible for aiding in the mechanical structure of bone (29). OPN acts as a form of bone glue in the sense that it has the ability to resist cracking and/or crack propagation (29). Osteopontin and osteocalcin work together to increase the collagenic links within the extra cellular matrix in bone to prevent the bone from fracturing, by bonding together to adhere the hydroxyapatite to the type I collagen (9, 29, 57, 59, 60, 205). By assessing the pixel intensity of osteopontin in a bone sample, one can assess the general amount of osteopontin and determine whether the bone remains structurally integral (9, 29, 205). The first areas of bone to lose collagenous proteins are the endosteal and periosteal regions largely due to the bone deposition and resorption functions that occur at these regions, and the presence of large amounts of osteoblasts and osteoclasts in these regions (30, 31, 56). Due to the differences in protein degradation by bone envelope, the samples used in this study were extracted from individuals who had undergone the full six-month process of embalming <sup>1</sup> to ensure that if there is an effect on bone, it would be present by that time (201, 204).

Estimating the postmortem interval based on loss of OPN may be affected by embalming fluid because it may preserve the bone from protein degradation and keep it at the same state as it was at the time of embalming, preventing any analysis on the time period of degradation since death (9, 29, 205, 206). As individuals age, the presence of osteopontin in their body increases, often as a result of mechanical stress and micro-damage (68, 92). If research into methods of age estimation using OPN levels are being considered, then it is important to know whether embalmed bone can be used. The potential preservation of osteopontin through embalming may alter age estimations, producing an estimate younger than the biological age (92, 119). In contrast, fractography studies may benefit from the preservation of osteopontin proteins. The fracture and/or trauma pattern that occurred during the perimortem or antemortem time period may also be affected by the preservation of osteopontin due the preservation of the bands that bind osteopontin and osteocalcin together (29). If these bands remain intact due to the

---

<sup>1</sup> While the actual process of embalming takes moments for the fluid exchange, it takes approximately 6-months for such embalming to have an effect throughout the whole of the body, preserving it enough for use in anatomical study.

preservation of osteopontin, a fracture will not progress, and the original state of trauma can be assessed (29). Similarly, fracture studies can make use of bone that has been embalmed as the bone will continue to respond as if in the early perimortem period due to the preservation of proteins.

Of the many microscopy modalities, confocal microscopy is the most beneficial for the scope of this research as it allows for the visualisation of the presence of proteins to be viewed using a fluorophore probe and fluorescence imaging (178). The pixel intensity can be viewed to directly correlate to protein presence and can be compared across all of the samples. It should be noted that the resolution of a confocal microscope is not fine enough to detect individual protein molecules, as the closest it can get is  $\approx 254\text{nm}$ . Therefore, with this paper, what is being visualized is the level of proteins through fluorescence intensity as a method of quantifying protein abundance as OPN is only between 44 – 75 kDa.<sup>2</sup>

The purpose of this research is to determine whether or not the normal embalming process for donated human cadavers affects the degradation of OPN. The fixed biopsy samples in this study attempted to represent the level of OPN in living bone, however, there was no validation using an unembalmed, unfixed fresh sample. These are designated the unembalmed sample. The embalmed sample was examined at 6 months post-embalming, giving the process time to penetrate and preserve the OPN if embalming does have an effect on OPN preservation, or for the OPN to begin degrading if embalming does not have an affect on OPN preservation. This research is significant because it is the first to address osteopontin and the microscopic effects of embalming fluid on human bone. Many other researchers use unembalmed samples in their studies and it has become the unspoken gold standard in forensic anthropology (9, 29, 205). If embalming fluid preserves the osteopontin in bone, then remains that have been embalmed could be included in forensic anthropological research that pertains to age estimation and fractography/trauma studies, but should be excluded from taphonomy and PMI studies (49, 92,

---

<sup>2</sup> In this case, protein size is listed by molecular weight over physical length as molecular weight (or Daltons) provides a more accurate representation and standardization of general size.

119, 178). The hypothesis of this project is that embalming fluid would have an effect on osteopontin preservation and, by extension, protein intensity.

### 2.3.2 Materials and Methods

This study used adult, human bone samples provided by the University of Toronto's Division of Anatomy through the Willed-Body Donation Program, as well as biopsy samples ( $\approx 10\text{mm}^3$ ) collected from living individuals through the Centre Hospitalier de l'Université de Montreal (CHUM) <sup>3</sup>. In this case, the biopsy sample is acting as a proxy for a bone collected from a deceased individual as it was fixed shortly after the sample was taken. Ethics protocol approval for this project was obtained from the University of Toronto Research Ethics Board (Human Research Protocol #33324 [see Appendix D]) <sup>4</sup>. Samples were stored in a restricted and locked laboratory with identifying information segregated on an external hard drive held off site. There were nine samples from the CHUM donation, and seven samples of embalmed bone from the University of Toronto. The embalmed samples derived from individuals whose remains underwent a full blood replacement procedure with 10% formalin solution. Individuals of all ages, combined sexes, and no known previous pathological conditions were accepted (see Table 2.3-1). The six-month-embalmed samples were chosen for this research due to accessibility, and to ensure the full effects of embalming had occurred on the tissue (201-204). The nine samples from CHUM were collected from live individuals and fixed at collection. The CHUM samples did not go through the process of embalming, as they were collected from living individuals so that the base line state of the histological condition of these samples could be compared to the histological state of the recently deceased individuals' samples. This allows them to be

---

<sup>3</sup> To conform to protocols established under U of T Protocol #33324 to protect the anonymity of the subjects, limited information was agreed to be collected. This was limited to the control number, age, sex, and date of death (for the postmortem individuals only). While it was requested and verbally assured from both CHUM and the U of T Division of Anatomy that the individuals did not have any pathological conditions, the presence of any pathological conditions were masked from the primary researcher per the ethics protocol. The CHUM pathology verification was given on 15 February 2018, while the U of T verification was given during sample harvesting. Since 2021, both of the researchers at the CHUM laboratory have moved to different positions, and the primary researcher is no longer able to access the subjects' pathological conditions.

<sup>4</sup> For CHUM Use of Samples, ethics approval, and Material Transfer Agreement information see Appendix D.

compared to the embalmed samples as a replicate of individuals who had yet to go through the embalming process. The embalmed samples were derived from the left iliac crest. The harvesting of embalmed samples followed the appropriate morgue standards and procedures and samples were provided to the authors with limited soft tissue present.

Once received, the embalmed samples were labeled in separate jars and each underwent a serial dehydration process of an ethyl alcohol solution of 95% for three days followed by a 100% solution for four days (176, 179, 183, 207). After each embalmed sample had been dehydrated, it was embedded in methyl methacrylate (MMA), as it is optically neutral (does not fluoresce) and more infiltrates the sample better than epoxy resin (176). However, MMA can affect the penetrative power of antibodies and they can be damaged in the embedding process. Due to this, labeling took place post thin sectioning, with as thin a section as possible and with an extended incubation period (208, 209).

After the MMA was activated and the samples were successfully embedded, the glass container was broken off and the sample was rinsed to remove any remaining glass particulates. Excess MMA was trimmed using a hand saw and then sanded down to create a smooth surface. Thin sections were created using a Struers® Accutom-100™ with thin sections mounted to slides using non-UV cyanoacrylate. One slice was taken from each sample, and the smallest attainable slice size for this research was ~100µm. This is in comparison to the CHUM samples which were pre-sectioned and mounted with a slice thickness of 15µm. The embalmed (UofT) slices were adhered to slides with their associated sample ID number and then each slice was hand-sanded using 60-grit sandpaper and then polished with 200-grit sandpaper, for 7 of the embalmed samples only. The final slice thickness for each embalmed sample was approximately 100µm, and 15µm for the unembalmed samples, which were pre-prepared prior to shipment<sup>5</sup>. Final slice thickness was immaterial with regards to imaging depth only as the depth of the slice in imaging (the z-axis) was standardized to 12.75µm (0.25µm slice interval).

---

<sup>5</sup> CHUM samples were fixed using a serial dehydration protocol and likewise embedded in MMA prior to thin-sectioning. The dehydration and embedding procedure used for the embalmed sample, while founded in literature, followed the CHUM protocol as provided by the laboratory.

All slices were hydrated and sterilized in a phosphate buffer solution and left to incubate for 30 minutes (210-212). Each slice was then labeled with five mL of osteopontin monoclonal primary antibody and was left to incubate for an additional 30 minutes (210-212). The slides were then labeled with 10 $\mu$ L of Alexa Fluor™(tm) 555 secondary antibody label (211-215). One sample (#12) was stained with basic fuchsin base stain on the hydroxyapatite prior to the phosphate buffer solution, and a goat anti-rabbit Alexa Fluor™ 488 as a means of determining if basic fuchsin would isolate the hydroxyapatite during the imaging process. Although this process worked, it was determined that using Alexa Fluor™ 555 instead of 488 could achieve the same end without requiring the additional step of staining with basic fuchsin. Consequently only #12 was imaged using Alexa Fluor™ 488, while the rest of the sample used Alexa Fluor™ 555. A comparison of the resulting pixel intensity (Table 2.2-3) demonstrated that the 488nm specimen was not an outlier and that the only difference between it and the other specimens was the channel used to detect the fluorescence (488nm instead of 555nm). The process of primary and secondary antibody tagging works by way of the osteopontin monoclonal antibody adhering to the native osteopontin in the bone; with the Alexa Fluor™ adhering to the primary antibody. It is the Alexa Fluor™ that fluoresces for visualization (211-214). As Alexa Fluor™ 555 is photosensitive, the slides were covered to block out any interfering light source while drying (211, 212, 215, 216). A cover slip was adhered to each slice after 48 hours using a Fluoromount™ aqueous mounting medium, a non-fluorescent mounting medium (215).

Each sample was examined using a Carl Zeiss® LSM-800 laser scanning confocal microscope as it provides a three-dimensional visualization of the sample with the highest resolution possible (162). Each sample was imaged following a similar set of parameters on the 555nm emission (561nm excitation) <sup>6</sup> wavelength, with a pinhole size  $\approx$ 20 $\mu$ m, power of 0.1%, 16-bit resolution, 400x magnification, a scan area of 447 $\mu$ m x 447 $\mu$ m, and a z-stack containing 50 optical slices (0.25 $\mu$ m slice thickness with an image thickness of 12.75 $\mu$ m) (168). These parameters allowed for the visualization of the protein material without capturing the hydroxyapatite and other material in the sample. The average voxel volume was 0.00155 $\mu$ m<sup>3</sup>,

---

<sup>6</sup> One sample was imaged using the 488nm excitation/emission wavelength as it was labeled with Alexa Fluor™ 488 over 555.

calculated by obtaining the voxel volume from each individual image. The voxel volume was calculated using the following formulae:

$$d^x = \frac{FOV^x}{Matrix^x}$$

$$d^y = \frac{FOV^y}{Matrix^y}$$

$$d^z = \frac{FOV^z}{\#ofSlices}$$

$$Voxel\ Volume\ \mu m^3 = d^x \times d^y \times d^z$$

The calculations were compared against the formulae for scaling per pixel in Zen Blue® (217) and comparing the calculated voxel amount [ $Matrix^x \times Matrix^y \times \#of\ slices$ ] with the voxel count in BitPlane® Imaris™ v. 9 (185). Oxford Industries BitPlane™ Imaris® v.9 (185) calculates the voxel (3- dimensional pixels) intensity, by combining the z-stack images, using a 16-bit scale (derived from the grey-scale original images) from 0 – 65,535 with 0 being black (no object) to 65,535 being pure white (or brightness saturation) (218). Care was taken to ensure that the images were as close in generalized regions (specifically the middle envelope) as possible throughout all samples, though individualization of the sampling process prohibited an exact match. The mean pixel intensity generated from the fluorophores bonded to the osteopontin proteins were assessed in ImageJ® through histograms that capture the pixel intensity throughout the 50 slice stack (162, 163, 168, 169, 187). The mean light intensity of the pixels correlates directly to the protein material abundance in the bone sample (162, 163, 168, 169, 187). As a result, the more pixels registered will increase the mean pixel intensity of the image as a whole, i.e. images with a higher mean pixel intensity can indicate a sample with higher protein abundance.

**Table 2.3-1: Sample demographics for Ch. 2.3 including age and sex.**

Sample #	Sample Group	Age	Sex	Sample #	Sample Group	Age	Sex
	Embalmed	87	Male	9	Unembalmed	52	Male
2	Embalmed	89	Female	10	Unembalmed	53	Male
3	Embalmed	64	Male	11	Unembalmed	52	Male
4	Embalmed	83	Female	12	Unembalmed	50	Male
5	Embalmed	91	Male	13	Unembalmed	57	Male
6	Embalmed	94	Male	14	Unembalmed	30	Male
7	Embalmed	82	Male	15	Unembalmed	51	Male
8	Unembalmed	57	Male	16	Unembalmed	47	Male

### 2.3.3 Data Analysis

The variables were not normally distributed due to the small sample size. Variables examined included the embalmed pixel intensity and unembalmed pixel intensity, along with their standard deviations. The standard deviation was collected in this study as a means of examining the variation in pixel intensity within each individual, the hypothesis being that the embalmed sample group would demonstrate a significantly smaller level of variation than the unembalmed. This is due to the fact that if embalming does not penetrate to the level of preserving osteopontin, it therefore will allow the protein to degrade. Further, due to the small sample size, a power and effect analysis was conducted to determine the ability to get a true test result.

To ensure that age and sex were not confounding the results of the comparison between embalmed and unembalmed bone, initial statistical tests were conducted. As osteopontin is predominately produced by osteoclasts which diminish with age yet also upregulate as a response to micro-cracks and damage as an age response, a Kruskal-Wallis H-test was run to determine if pixel intensity would be affected by age variation (using age groups divided by lustrums) using the unembalmed and embalmed sample both pooled and independently. Additionally, a Mann-Whitney U-test was conducted for assigned sex but was limited to the embalmed sample group only as that was the only group with a heterogenous group.

Overall, the main test statistic was a Mann-Whitney U-test which was employed to assess whether embalming affected the level of osteopontin intensity. The null hypothesis ( $H_0$ ) would be rejected if  $p > 0.05$  indicating there is no significant difference between pixel intensity (and by extension, amount of OPN) in the embalmed versus unembalmed sample. All statistics were performed using IBM's™ SPSS® v.29 (219) statistical software. The samples were then labeled 1-16 to anonymize the identity of the individuals.

### 2.3.4 Results

The results for the Mann-Whitney U-tests comparing the medians of the pixel intensities between the embalmed and unembalmed samples indicated that there is no significant difference in intensity (and by extension the amount of OPN present) ( $p = 0.071$ ;  $U=6.000$ ;). Given the small sample size a power analysis was conducted with a result of 0.200 and a Cliff's  $\delta$  effect size was conducted with a large result of 0.756 (large being above 0.60) indicating that while there is a low probability of detecting a true variance given the sample size, there is a large significant variance in the samples. Despite the lack of statistical significance, a visual qualitative examination of the images themselves suggested otherwise. The unembalmed fixed samples from CHUM displayed bright images suggesting an abundance of proteins using BitPlane™ Imaris® v.9 (185). In comparison, the embalmed samples showed minimal fluorescence indicating far fewer proteins were present to bind with the antibody and Alexa Fluor™(tm) in the temporal colour codes used in this analysis. Using z-scores [ $z=(x - \mu)/\sigma$ ] in IBM™ SPSS® v.29 (219) to detect outliers, one outlier was present in the embalmed sample, Individual #4 (Table 2.3-2). Individual #4 exhibited an intensity greater than 4000, compared to the next highest value in the embalmed sample of 1170.47. Two additional individuals, #'s 11 and 12, appear in the raw numbers to be outliers, however, did not register as true outliers using the z-score. With the Mann-Whitney U-test re-run with the outlier removed, the results do indicate a significant difference in both the mean pixel intensity and pixel standard deviation with  $p=0.018$  ( $U=7.000$ ) and  $p<0.001$  ( $U=0.000$ ) respectively (see Figs. 2.3.3 – 2.3.5), with the results of the power and effect analyses being 0.356 and 0.953 respectively.

Artifact imaging is a fact in histological and fluorescence analysis and may be at issue in this study. Though attempts were made to limit artifacts, the complete elimination of artifacts is largely impracticable; only mitigating their impact on, and interpretation of the results. In this

particular study, while the raw numbers indicate saturation, which may indicate the presence of artifacts, the saturation being seen across all samples may likewise be natural and biological in nature. To ensure that these potential artifacts are not placing any undue influence on the results, a statistical scan for outliers was conducted with those that registered being removed. Others could be argued to be outliers, and therefore artifactual in nature, however, the self-same statistical analysis did not classify them as such, instead marking them within the “upper whisker” of a generate box plot.

The protein intensities exhibited a wide range of variation, with a level of ~5000 pixel intensity between the lowest and highest intensity in the unembalmed/fixed samples (Fig. 2.3.1 and 2.3.2). While there was no statistically significant difference between the mean pixel intensities of the embalmed and unembalmed samples, a Mann-Whitney U-test of the standard deviations did return a significant variation ( $p=0.005$ ) with the embalmed sample producing a lower amount of pixel variation than the unembalmed sample (2001.2175 vs 4137.4164). This metric, however, demonstrates that there was merely a difference in the pixel variation within each image.

When testing between age cohort based on lustrums, the results of the Kruskal-Wallis H-test found that there was no significant difference in the mean pixel intensity when pooled ( $p=0.682$ ,  $H=1.500$ ,  $\eta^2=0.5$ ) and standard deviation ( $p=0.956$ ,  $H=0.321$ ,  $\eta^2=0.631$ ). Further, when testing between sex the pooled results of the Mann-Whitney U-test again found no significant difference with  $p=1.000$  for both the mean pixel intensity ( $U=5.000$ ,  $\delta=0.945$ ) and mean standard deviation ( $U=6.000$ ,  $\delta=1.134$ ). When examining within each subject group, the unembalmed age cohort based on lustrums Kruskal-Wallis H-test was not significant for both mean intensity and standard deviation, while the embalmed sample group was likewise not significant at for the mean pixel intensity and for the standard deviation. The results of the embalmed between sex Mann-Whitney U-test for both mean intensity and standard deviation was likewise found to be not significant (see Table 2.3-3). These results combined suggests that for this cohort neither age nor sex had an effect on the results of osteopontin degradation and that the differences seen are more likely related to postmortem time passage. It should be noted, however, that for the Mann-Whitney U-test regarding sex, the distribution of males and females is so out of balance and the  $n$  within the female cohort small, the non-significant results were as

expected, and can be considered a major limitation of the test. As a result, a similar study with a more robust cohort may find that sex does have an impact on the overall results.

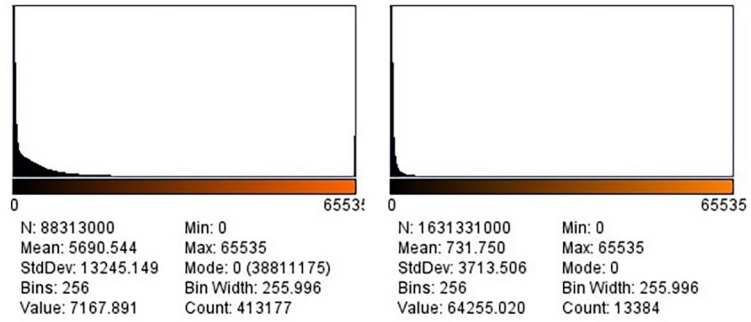


**Figure 2.3.1: Variation in unembalmed sample #12 (left) and sample #10 (right) FIJI/ImageJ© histograms showing mean pixel intensity. Generated from a 488nm (#12) 555nm (#10) wavelength image.**

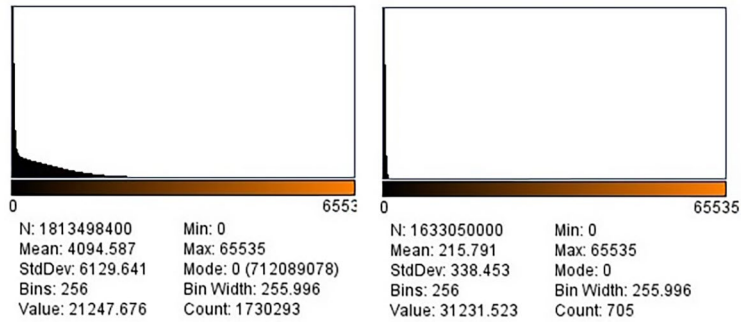


**Figure 2.3.2: Variation in embalmed sample #4 (left) and sample #2 (right) FIJI/ImageJ© histograms showing mean pixel intensity. Generated from a 555nm wavelength image.**

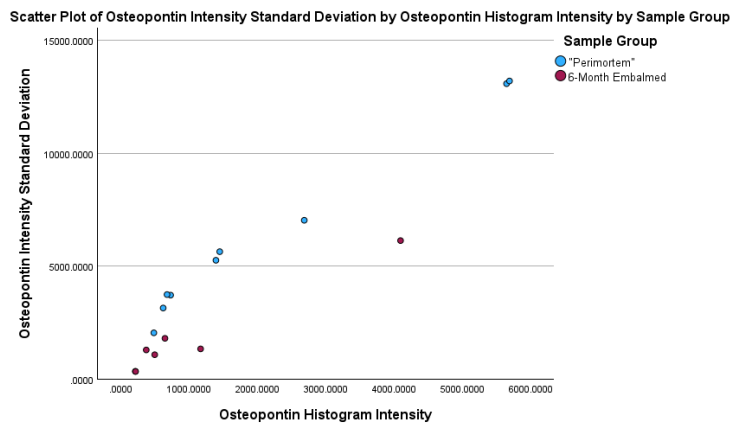


**Figure 2.3.3: Plot of image pixel intensity and image standard deviation.**

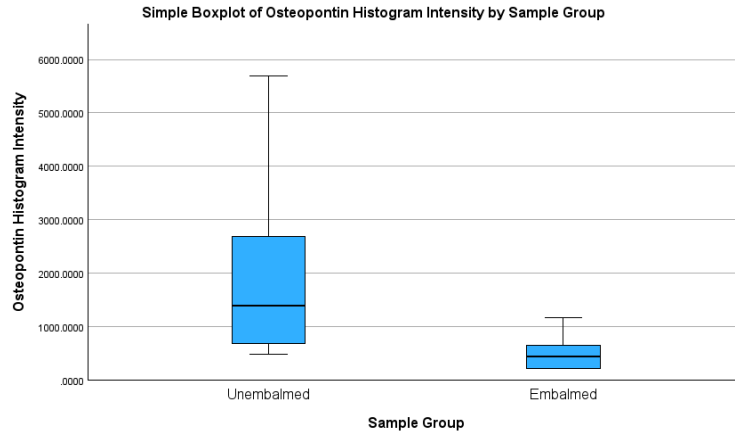


**Figure 2.3.4: Box plot of mean pixel intensity with outlier (#4) removed.**

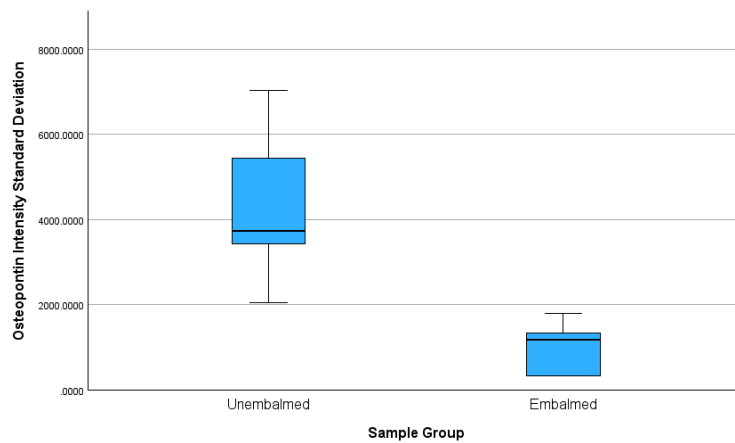


**Figure 2.3.5: Box plot of pixel standard deviation data with 2 outliers removed.**

**Table 2.3-2: List of the mean pixel intensities and standard deviations for all samples**

Sample #	Sample Group	Pixel Intensity	Standard Deviation
1	Embalmed	649.2130	1800.4500
2	Embalmed	215.7910	338.4530
3	Embalmed	1170.4700	1333.0800
4	Embalmed	4094.5900	6129.6400
5	Embalmed	499.3930	1075.2000
6	Embalmed	375.3850	1286.1600
7	Embalmed	219.3820	332.6280
8	Unembalmed	1450.2800	5638.8300
9	Unembalmed	2686.6000	7029.5900
10	Unembalmed	731.7500	3713.5100
11	Unembalmed	5645.0307	13079.7323
12	Unembalmed	5688.0800	13199.4000
13	Unembalmed	486.4790	2044.3200
14	Unembalmed	623.1890	3142.8530
15	Unembalmed	679.5180	3739.1900
16	Unembalmed	1394.5600	5257.8600

**Table 2.3-3: Age and Sex Kruskal-Wallis H-test and Mann-Whitney U-test Results.**

	Test		<i>p</i> -Value	<i>H/U</i> -Stat	$\eta^2$ /Cliff's $\delta$
Age	Mean Pixel Intensity	Embalmed	<i>p</i> =0.682	<i>H</i> =1.500	$\eta^2$ =0.3
		Unembalmed	<i>p</i> =0.430	<i>H</i> =2.760	$\eta^2$ =0.048
	Standard Deviation	Embalmed	<i>p</i> =0.956	<i>H</i> =0.321	$\eta^2$ =0.536
		Unembalmed	<i>p</i> =0.430	<i>H</i> =2.760	$\eta^2$ =0.048
Sex	Mean Pixel Intensity	Embalmed	<i>p</i> =1.000	<i>U</i> =5.000	$\delta$ =1.581
		Unembalmed		N/A	
	Standard Deviation	Embalmed	<i>p</i> =1.000	<i>U</i> =6.000	$\delta$ =1.897
		Unembalmed		N/A	

### 2.3.5 Discussion

The results of this study found no significant difference between the medians of osteopontin pixel intensities in the embalmed and unembalmed/fixed samples occurred, indicating that the pixel intensities remain the same when all samples are included. When the single outlier (Sample #4) is removed from the analyses, then a clear and significant difference between the sample groups (embalmed vs unembalmed) emerges.

Overall, however, given the results of this study, it is suggested that more research be conducted to determine if embalmed remains can be considered the same as unembalmed remains with respect to their histochemical condition. Qualitatively a variation was seen suggesting that embalming does not affect the amount of proteins found in a sample, which was borne out through the Mann-Whitney U-tests with the single outlier of Sample #4 removed. Laser scanning confocal microscopy does not allow for the visualization of individual proteins as the average voxel volume ( $0.0015\mu\text{m}^3$ ) is much larger than the size of an osteopontin protein (44 – 75 kDa). While the current standard practice in forensic anthropological research is to use only unembalmed remains, this research suggests that forensic anthropologists may possibly include the use of embalmed remains in research that requires histochemical degradation (postmortem interval studies, etc.), as qualitatively there is no effect from the embalming fluid that would alter the bone condition, or their results. Potential areas of benefit include cadaver studies, where donor bodies can be further researched at the histological level with no concern about osteological impact of the embalming process. This may extend the use of cadaver donors in future research.

This research does have some limitation, largely given its small sample size. A future study would benefit from a larger sample size, with more optical slices imaged and processed from each sample to potentially account for the inter-sample variation in pixel intensity. Different stages of embalming may be beneficial for the assessment of protein degradation, as well as a comparison between degradation of unembalmed and embalmed samples at the same time intervals, as it is possible that embalming fluid retards the rate of degradation of proteins in human bone in comparison to unembalmed human bone samples but does not halt the process entirely.

The ability to examine the amount of protein directly, rather than to approximate the amount indirectly through fluorescence intensity is hampered by the limitations of LSCM. This research originally included a count feature; however, it was noted that the voxel volume size was much larger than the individual proteins, and the calculated wavelength resolution (0.241) would prevent the discernment of individual proteins in the image. Using the count function there was statistically significant variation between the sample groups in terms of the amount of proteins, but it is unclear how the proteins were grouped and counted by the AI. In addition to the inability to count individual proteins, a number of confounding variables were introduced including variation in age and sex which are known to influence the OPN levels in healthy bone (89, 91, 98). While this project did not find a difference in the amount of protein present in embalmed vs unembalmed bone, the limited sample size could be masking an effect. To account for these variables, it is recommended that biochemical assay tests and animal models be used to reconstruct this project, with respect to pixel intensity, and an actual protein count. By using such models, particularly with mice, the confounding variables of age and sex can be accounted for, along with other variables such as overall health of the subject. This would give a much more accurate representation of the individual OPN levels and the degradation between the two subject groups.

In addition to these confounding variables, the issue of potential artifacts is present within this study. Prior to this research, a number of pilot studies were conducted to determine the best approach limit artifacts (193, 220-223). While steps were taken to follow standard protocols to minimize artifacts, it is not always possible to eliminate them altogether. As the appearance of artifacts can mirror true and targeted biological material, one has to examine the macro vs the micro (whole cortical image vs  $447\mu\text{m}^2$  image). In this case, the projections on the micro are found within the macro image (see Ch. 3.2.4, Figs. 3.2.1 & 3.2.9). If potential artifacts are purely artifactual in nature, then they would be seen in both the embalmed *and* unembalmed sample producing a random outcome because both samples were labelled at the same time. There was no way for an artifact to have produced a systematic bias resulting in a patterned outcome. Given the qualitative and quantitative variation between the two subject groups, the results suggests that the effects of artifacts are limited (i.e., that variation exists despite any potential artifacts). This variation between the two subject groups suggests that the material

being imaged are more likely than not targeted biological material (natural) rather than artifactual.

Saturation, also, may indicate the presence of artifacts. It should be noted that saturation was present in all cases, but only one individual was statistically determined to be an outlier and removed (individual #4). Once removed, a statistical difference was found between the embalmed and unembalmed groups, suggesting that if artifacts are being counted to a significant degree, their effect was limited to a single case, and had a masking effect hiding a true difference between the two subject groups, rather than creating a pseudo-variation between them. However, the mere presence of universal saturation in all samples is suggestive of a methodological failure within the study. Again, with the use of animal models, and a greater number of subjects, it would be possible to better identify, quantify, and correct for artifacts introduced via labelling.

An additional factor that may be at play is the escape depth, or diffusion of light through the sample, differential between the unembalmed and embalmed sample groups. In this case, the unembalmed sample had a total thickness of 15 $\mu$ m while the embalmed was 100 $\mu$ m. While the laser penetrative power on LSCM through a sample is between 100-200 $\mu$ m (224), the thickness difference between the sample groups would potentially allow for more light, and therefore greater fluorescence intensity, to pass through the thinner, unembalmed sample, than the thicker, embalmed sample.

Overall, however, with all considered, this study has demonstrated that it might be possible to use embalmed remains in histochemical studies within the field of forensic anthropology, and indeed skeletal biology, and anatomy, specifically if one examines the qualitative results. By using embalmed cadaveric remains, once intended for the use of gross anatomical study, scientists will be able to increase the number of subjects that can be used in studies that rely on organic histological degradation. Thus, the contribution of these donors can be even more impactful than originally anticipated.

## Chapter 3

# Osteopontin and Osteocalcin Degradation as a Means of Establishing the Early Postmortem Interval

### 3.1 Chapter Introduction

While Chapter 2 focused on the histotaphonomy and foundations of this research, Chapter 3 focus on evaluating the potential to use proteins as a means of establishing a postmortem interval. Chapter 3 consists of a potential journal article, “Degradation of osteocalcin and osteopontin and its potential use in developing a postmortem interval in early skeletonized remains,” by Ashley Smith and Tracy Rogers, and will be submitted to the *Journal of Forensic Medicine* by the end of 2025.

The following manuscript specifically examines the degradation of two bone proteins as a means of determining their use in developing a more accurate postmortem interval. Bone is largely comprised of an inorganic component (hydroxyapatite  $[Ca_{10}(PO_4)_6(OH)_2]$ ) and an organic component (Type I and Type V collagen, proteins, and various cells) (27). Similar to Ch. 2.3, this research focused on an acidic glycosylated phosphoprotein known as osteopontin, coupled with the addition of the  $\gamma$ -carboxylated protein, osteocalcin. These two proteins bind the inorganic and the organic matrices of bone. In brief (with a fuller explanation within the manuscript) osteocalcin, produced predominately by osteoblasts, connects the hydroxyapatite to the osteopontin, produced by predominately by osteoclasts, which in turn binds to the Type I collagen (28).

The purpose of the following manuscript was to determine if the degradation of osteocalcin and osteopontin can be used to develop a more accurate postmortem interval for human remains in advanced states of tissue decomposition through to early skeletonization. While osteocalcin is largely present in skeletonized remains, extending long into the archaeological (> 50,000 years) time periods (102-105), very little research has been conducted in osteopontin degradation, which is more closely associated with binding to the organic matrix. This manuscript specifically examines the degradation of osteocalcin and osteopontin fluorescence, and the

independent variation between them over a set time frame ranging from “perimortem” to 14-days postmortem using mean pixel intensity, as well as through the ratio of mean pixel intensity between OPN:OC.

In order to assess the variation, two main sample groups were utilized including a perimortem group derived from bone biopsies <sup>1</sup>, and a postmortem group derived from cadaveric remains with a postmortem interval of  $\approx 48$  hours before collection and processing. With this postmortem sample group, immediately upon collection 1/3 of the sample (hereafter noted as early-postmortem (labelled in the experiment as XXXX.1 where XXXX represents in donated individual cadaver number) was removed and fixed, while the remaining 2/3 was allowed to decompose. After a 7-day period post cardiopulmonary death of the donor, an additional 1/3 was removed and fixed (7-day postmortem or XXXX.2), with the remaining 1/3 fixed 14-days postmortem (14-day postmortem or XXXX.3). It should be noted that for anonymizing purposes, the individual 3- & 4-digit donor number was converted to 1 – 18. While the anonymized number is presented in this thesis, the researcher still maintains the original donor number. After labeling and imaging using the 16-bit setting, analysis included the pixel intensity data, focusing primarily on mean pixel intensity and the standard deviation. The use of pixel intensity theoretically allows for the quantification of protein material with the idea being that as negative space means no targeted material, the greater the mean pixel intensity the more target material present.

---

<sup>1</sup> Data including the reason for biopsy collection, demographic data beyond age, and additional sample information from the biopsies were collected and maintained by the staff at CHUM. However, in the recent years, those who were employed within the lab and engaged by the primary researcher of this present project have left and access to that information has since been terminated.

## 3.2 Degradation of osteocalcin and osteopontin for use in postmortem interval estimation during the early postmortem period

### 3.2.1 Introduction

Of all the analyses conducted by a forensic anthropologist, none is as challenging as the determination of the postmortem interval (PMI), due to the many factors that play a role in the decomposition and degradation of the soft tissues and skeleton. The purpose of this paper is to assess the feasibility of using degradation of osteocalcin and osteopontin to estimate the postmortem interval (PMI) for early skeletonized human remains using immunofluorescent labelling and confocal microscopy.

The clock of the postmortem interval begins the second the cardio-respiratory systems cease to function – the point of somatic death. In general, as oxygen is no longer passing through the system, the cells are deprived of metabolic support and begin to die, breaking down capillary beds, organs, and overall organ systems. While a base view of the concept suggests that this is an instantaneous process, the presence of transplant medicine suggests that the breakdown of organ systems post somatic death is a more gradual process. In a general sense, this breakdown is the natural process we term “decomposition.” Decomposition is a dual-phase process that occurs both intrinsically and extrinsically, normally beginning in the intestinal tract. Intrinsic decomposition occurs mainly at a cellular level and includes processes such as cell lysis and bacteria migrating from the gut. Extrinsic decomposition is that which can be seen externally and has contributing factors such as insect infestation and scavenging, which are dependent on environmental factors. Eventually intrinsic decomposition extends into the extrinsic decomposition, which can be seen in the external soft-tissues and ultimately bone (15, 106-113). Both intrinsic and extrinsic decomposition have been organized into various stages to assist in establishing the PMI (11, 15, 112-116, 225). While there are several progression charts, and slight variations in names and descriptions, decomposition generally progresses as follows: fresh (intrinsic/autolysis), bloat, early decay, advanced decay, and finally skeletonization/mummification (112, 114-116, 225).

The first stage of decomposition shared by all of the sequences is the “fresh” stage, which begins at the point of somatic death. Approximately 4 minutes postmortem, some cellular

structures throughout the body (and particularly within the gut) start a process of autolysis where lysosomes are released into the cytoplasm due to a decrease in intercellular pH levels (111). This decrease in pH level is the direct result of the deprivation of oxygen (O<sub>2</sub>) and adenosine-triphosphate (ATP) (49, 111, 112). Cell walls begin to deteriorate and the basement membranes/intracellular matrix begin to dissolve, resulting in the breakdown of the cellular and tissue structures (49, 111, 118, 225). Gill-King (49) characterized autolysis into two stages. Stage 1, or early, reversible, is the point at which localized individual cell death occurs, but the overall tissue may be spared. Stage 2, or late/irreversible, is noted when autolysis has progressed to the point where tissue necrosis can be seen microscopically as the absence of cell nuclei (49). Using these stages, Gill-King (49) organized tissue decomposition in order from tissues with a higher level of ATP to those with lowest levels; starting with the soft-muscle tissues of the digestive tract and vasculature, then the pulmonary structure, brain/nervous tissue, skeletal muscles, and lastly connective tissues. In bone, however, the intercellular matrix is predominantly inorganic rather than organic (27), and limited research has demonstrated the effects of autolysis on the inorganic matrix of bone cells and tissue (10, 119-124).

As the process of autolysis continues, the mortis triad (algor, livor, and rigor mortis) becomes established, the combination of which has been instrumental in determining approximate PMI in the early postmortem period (from minutes to 72 hours) (126-128). After 48 – 72 hours postmortem, the digestive tract begins to break down, leading to the second universally accepted stage, the bloat/early decomposition stage (11, 49, 110, 112, 114, 115). Through the process of putrefaction, anaerobic bacteria become increasingly active, attacking what remains of the larger blood vessels and internal organs (15, 49, 112, 115). In soft-tissue decomposition, this results in the release of excess interstitial gasses and ultimately bloating of the body (11, 15, 110, 112, 114-116). During the later phases of this stage the intrinsic bacterial activity begins to slow, while the extrinsic activity begins to accelerate (15, 112, 114, 116). Extrinsic activity, such as arthropod oviposition and additional macrofaunal activity, occurs during the later phases of early decomposition, and can affect the physical decompositional process. Much is known regarding the extrinsic appearance of the remains during this stage (119).

The final two stages of decomposition are advanced decomposition and skeletonization, both of which are generally dictated by extrinsic factors, rather than intrinsic (11, 15, 108, 114-

116). During the advanced decompositional stage, bone becomes exposed at different rates throughout the body, with “skeletonization” being attained when most of the elements finally become exposed. The remaining soft tissues either break down entirely, undergo saponification, or begin a slow desiccation process and ultimately mummify, depending upon the environmental and arthropod activity (11, 15, 108, 114, 115, 129). Once skeletonization occurs, the remains could theoretically continue in this phase until the skeletal elements either weather and disintegrate or fossilize, depending on the conditions.

Like the previous stages, there are sub-stages defined by the appearance and texture of the bone. At this point the diagenetic process (taphonomic processes that effect the alteration of bone postmortem, which can include biological and chemical [mineral] alterations) accelerates, with ultimate trajectories influenced by the surrounding environment (113). The first of the skeletonization sub-stages is the “initial skeletonization” phase, where some remaining soft-tissues may be present and the bones have a greasy texture (11, 15, 114, 115). Once the remaining soft-tissue has deteriorated, but the skeleton is still greasy, the remains are said to be in the second sub-stage, or “wet bone” stage (11, 15, 108, 114). It should be noted that there is limited consensus as to the presence of this stage in the literature, with some authors (108, 114) recognizing this stage as a unique phase, while others (11, 15) combine this stage with the final outcome. The third and final stage is “dry bone”, where the bones have dried out and now have a “wood-like,” and ultimately white appearance, depending upon the environment (11, 15, 108, 114, 115). Over time, if the remains continue to be exposed to the elements, the normal taphonomic processes will continue, with the fate of the skeletal remnants depending upon the environmental conditions including ultimately either the destruction or preservation of the bone (15, 114, 130, 131).

Over the years, several attempts have been made to scientifically associate the degree of extrinsic decomposition to a particular PMI. One of the most utilized methods has been that of Megyesi and colleagues (11), where the authors calculated total body decomposition scores (TBS), defined as the degree of decomposition scored in regions of the body then added together, and linked the TBS to accumulated degree days. To determine the PMI, one calculates the known environmental temperatures backwards through time (also known as accumulated degree days) and then using a specific formula one can use these accumulated degree days and the TBS to calculate the PMI (11). While it provides some guidance to estimating PMI, the method omits

other important factors in the decompositional process. Humidity, soil pH, insect, carnivore/rodent, and avian activity, and even UV access, as well intrinsic factors such as body habitus can impact decomposition (14, 225).

The longer it is from the time of somatic death, the less accurate the postmortem interval becomes as greater variation in external factors come into play, such as body habitus, environment, clothing, and other factors. Skeletonization is even more problematic as bone can remain in an unaltered state for years prior to discovery. While many approaches to PMI estimation are in use, most rely on a degree of taphonomic activity. Whether that activity is subaerial, marine, or subsurface, the bones will degrade in a semi-predictable pattern, although most research in PMI estimation involves subaerial weathering (130, 131, 154, 226). By noting the degree of bone degradation and comparing it to documented research, the amount of bone degradation can be linked to a potential number of months and years postmortem (130, 154). This tends to be a rough approach, resulting in a potential PMI range of years or even decades. Ultraviolet light, precipitation, and temperature fluctuations, such as the freeze-thaw cycle, can all play a role in the speed of the bones' decomposition and destruction (154). Microbial and chemical agents from the soil attack bone and degrade it from inside the bone matrix; a process known as diagenesis (119, 187). Thus, when calculating the PMI from skeletal remains, there are numerous factors to consider, and the end result is semi-accurate, broad range.

Bone is divided into two constituent components that interact with one another to create stability and strength: the organic and inorganic matrices (27-29). The inorganic matrix of bone is derived from a naturally occurring calcium-phosphate substance known as hydroxyapatite  $[\text{Ca}_{10}(\text{PO}_4)_6(\text{OH})_2]$ , and accounts for 60 – 70% of the bone's dry weight (27-29). Accounting for 30 – 40% of the remaining dry weight, the organic matrix is a complex system consisting of cellular structures, coupled with branching Type I collagen fibers, with cross-links to aid in strength, and a small amount of Type V collagen, whose role is limited to fibrillogenesis (27). A complex in the extra cellular matrix is made up of two non-collagenous proteins: an acidic glycosylated phosphoprotein known as osteopontin, and a  $\gamma$ -carboxylated protein, osteocalcin. Together they connect the inorganic and organic matrices of bone (28, 29, 55, 57, 60).

The present study was designed to evaluate the potential of improving postmortem interval estimates based on the degradation of osteocalcin [OC] and osteopontin [OPN]. While any bone

protein can be selected in assessing cellular degradation, osteocalcin and osteopontin were specifically chosen given their importance in binding the organic to the inorganic components of bone. It should be noted that given the size of the protein molecules and the resolution of the microscope ( $\approx 254\text{nm}$  at the  $555\text{nm}$  wavelength), plus the voxel size of the images, the goal is not to examine individual proteins, but rather to assess the overall amount and degradation of these proteins using fluorescent labelling of antibodies that bind to the proteins.

Osteopontin is an acidic glycosylated phosphoprotein with origins both within and external to the skeletal system including in some areas of both endothelial and epithelial cells, smooth muscle cells, and fibroblasts (53). In the skeletal system, osteopontin has origins from both osteoblasts and osteoclasts, indicating a significant role in the bone turnover process, as well as some origins from osteocytes. It is predominately produced by osteoclasts where the primary function is the anchoring and regulation of osteoclasts to the bone matrix, and the anchoring of the type I collagen to the hydroxyapatite (28, 29, 55-60). Weighing between 44 and 75kDa per molecule (63), OPN is found in the extra cellular matrix. Due to its role in cytokine immune regulation, and soft tissue wound healing (61, 62), OPN can also be found in Haversian and Volkmann's canals, particularly as OPN enters the vessels and the blood stream (55, 57). Further, because it has some genesis with osteocytes, OPN is also found in the lacunae (55, 57). External to the skeletal system OPN is also involved in a number of physiological processes including cancer growth and metastasis, angiogenesis, as well as contributing to inflammation and tissue damage in individuals with autoimmune conditions (63-65).

As a significant non-collagenous protein component of the bone matrix, OPN is distributed throughout the bone matrix but is particularly concentrated in the regions undergoing active remodeling (66-68). It is involved in the regulation of hydroxyapatite crystal growth, inhibiting excessive mineralization and ensuring proper bone density and structure (66, 67, 69). OPN is also found at sites of bone resorption and cement lines, where it is secreted by osteoclasts to facilitate cellular attachment to the hydroxyapatite (55, 66). Additionally, OPN is present in the periosteum and endosteum, to facilitate bone growth and repair (66, 67, 69). In the periosteum, OPN contributes to the formation of new bone during growth and responds to bone injury, while in the endosteum, it plays a role in bone turnover and maintenance (67). Given the overconcentration of OPN at the periosteum and endosteum, the middle envelope is the best area of visualization for general levels of OPN.

In bone remodeling and mineralization, OPN contains the arginine-glycine-aspartate (RGD) sequence, which facilitates osteoclast adhesion by interacting with integrins such as  $\alpha\text{v}\beta\text{3}$ . This is essential for cell attachment to the bone matrix and subsequently bone resorption (56, 58, 59, 63, 68, 70, 71). Further, it modulates the secretion of enzymes such as cathepsin K (potassium) and matrix metalloproteinases (MMPs) which are necessary for matrix degradation (72). Additionally, OPN interacts with collagen through its phosphorylated regions and RGD sequence (55, 58, 60, 69).

Osteocalcin (OC) is a  $\gamma$ -carboxylated protein produced almost exclusively in the skeletal system by osteoblasts, though also with genesis through osteocytes as well, generally in their role as trapped osteoblasts (73). More specifically, OC genesis is primarily produced by osteoblasts for the purpose of bone remodeling regulation, while in osteocytes, OC is found to be more for mineralization and mechanosensation (74, 75). OC is approximately 5-6 kDa in molecular weight (57). Like, OPN, OC has physiological functions outside of the skeletal system including in glucose management and even fertility (69, 76-78). In bone, OC is primarily associated with the regulation of bone turnover as well as in the anchoring of the inorganic and organic matrices by binding to the OPN (28, 29, 55, 57, 59, 60). Specifically, OC binds to hydroxyapatite crystals, contributing to the regulation of mineralization, and is distributed throughout the mineral matrix with concentrations in newly formed bone (76, 79, 80). Being complementary with OPN, OC is responsible for remodeling, regulation of mineralization, and response to mechanical stress, and binds with OPN to secure hydroxyapatite to the collagen matrix. OC contains three  $\gamma$ -carboxyglutamic acid residues, which release calcium ions that are crucial for binding to hydroxyapatite (76, 79). The binding of OC to the hydroxyapatite regulates the size and shape of the mineral crystals that contribute to mineralization (54, 59, 77, 79, 81, 82). OC modulates the activity of both osteoblasts and osteoclasts by inhibiting excessive mineralization, which ensures that bone formation occurs in a controlled manner, thus preventing the development of overly dense and brittle bones (54, 78, 79, 82-84). OC acts as a signaling molecule, influencing osteoblast differentiation and activity through the expression of genes involved in bone matrix production and mineralization and thereby enhancing the overall bone formation process (76, 79, 82, 84, 85). In OC-deficient mice, studies have shown subjects to have altered bone morphology and mechanical properties (83). When combined with OPN, both proteins respond to mechanical stress and adapt their functions accordingly. OPN is upregulated in response to

mechanical strain, enhancing osteoclast-mediated resorption, while OC facilitates the repair and strengthening of bone through mineralization processes (93, 94).

In the process of binding hydroxyapatite and collagen, OC and OPN have distinct but complementary roles. OC binds directly to hydroxyapatite crystals through its  $\gamma$ -carboxyglutamic acid residues, which chelate calcium ions on the crystalline surface (54). This binding is crucial for the nucleation and growth of hydroxyapatite crystals within the collagen matrix. OC and OPN are known to interact with collagen, although the mechanisms differ. OC binds to specific sites on the collagen fibrils, stabilizing the mineral-collagen interface (58, 59, 69, 85). While OPN and OC are both necessary for the function and stability of bone, the ratio between the two is difficult to ascertain. The ratio of OPN to OC can possibly vary from bone to bone, with normal bone having a OPN:OC ratio of 1:1.5 but expanding to a ratio of 1:13 in microfractures forming dilatational bands (29). Though not extensively studied in literature, it is possible that there are regional variabilities in this ratio of OPN:OC, more notably given the ratio of cortical and trabecular bone and the variability in the turnover activities of osteoclasts and osteoblasts in those bone types which are directly related to the deposition of osteopontin and osteocalcin respectively (73, 86, 87). Because of this, though it should be stressed limited studies have been conducted, it is plausible that bones, and bone regions, with a higher percentage of trabecular bone may potentially have a differing ratio of OPN:OC than bones and regions with greater cortical bone; though no study has been found which directly measured the ratio of OPN:OC in trabecular vs. cortical bone, nor differing bones by anatomical region or bone load. Given this discrepancy, the present study focused on one consistent site with reduced load: the iliac crest.

This study assessed the differential degradation of osteopontin to osteocalcin with the goals of 1) establishing if confocal microscopy could be utilized as a modality to assess for protein detection and quantification in relation to its combined use with other target materials (namely osteoclasts and histotaphonomy), thus allowing for a unified modality, and 2) to establish whether or not OPN degrades at a rate distinct from OC such that the assessment of the target protein degradation may be useful for estimating early PMI. The role of osteocalcin in diagenesis has been reported in the osteoarchaeological literature, but the lack of information regarding the role of osteopontin in diagenesis suggests that the two degrade at different rates, with osteopontin decomposing faster than OC (102-105). In 2014, Boaks and colleagues (9) found that collagenous proteins degrade consistently. If the same holds true for the non-

collagenous proteins, then mapping and quantifying the degradation of osteopontin and osteocalcin can be useful in establishing the early postmortem interval (PMI) from days to weeks.

### 3.2.2 Materials and Methods

Two research groups were established. The “perimortem” group was derived from iliac biopsies taken from living people, which were fixed soon after harvesting<sup>2</sup>. These samples were the same as the “unembalmed” samples found in Ch. 2.3.2 and acted as a proxy for true perimortem fractures, which are produced during the processes leading to death. Because the tissues were fixed at the time of harvesting, the levels of OPN and OC will be as close to cell death as is possible to obtain. The postmortem group consist of iliac segments  $\approx 2.5\text{cm} \times 2.5\text{cm}$  gathered from recently ( $<48\text{hr}$  but  $>18\text{hrs}$ ) deceased individuals. The perimortem group was harvested and processed (fixed using formalin and embedded in methyl methacrylate) by the Department of Pathology, Laboratory of Bone Histomorphometry, Centre Hospitalier de l' Université de Montréal (CHUM) in Montréal, QC (biopsy size  $10\text{mm}^3$ ). The postmortem sample group was harvested by the Division of Anatomy at the University of Toronto in Toronto, ON, with processing of the segments conducted by the first author following the CHUM practice as closely as possible in both fixation and embedding. With regards to fixation and embedding protocols, an internal document noting the process was provided to the first author (discussed below). The only variation in the difference between the processing of the two samples was limited to the initial timing from harvesting to fixation as well as the final sample thickness which varied from  $15\mu\text{m}$  for the CHUM perimortem samples and  $\approx 100\mu\text{m}$  for the U of T postmortem samples. While the effect depth (laser penetrative depth before diffusion) variation

---

<sup>2</sup> To conform to protocols established under U of T Protocol #33324 to protect the anonymity of the subjects, limited information was agreed to be collected. This was limited to the control number, age, sex, and date of death (for the postmortem individuals only). While it was requested and verbally assured from both CHUM and the U of T Division of Anatomy that the individuals did not have any pathological conditions, the presence of any pathological conditions were masked from the primary researcher per the ethics protocol. The CHUM pathology verification was given on 15 February 2018, while the U of T verification was given during sample harvesting. Since 2021, both of the researchers at the CHUM laboratory have moved to different positions, and the primary researcher is no longer able to access the subjects' pathological conditions.

between the samples could be an issue given the stark differences, this can be mitigated by the fact that the effective effect depth is between 100 – 200 $\mu\text{m}$  and the  $z$ -axis depth imaged was standardized to  $\approx 12.75\mu\text{m}$  for all samples.

Ethics protocols were approved by the University of Toronto Research Ethics Board, Protocol #33324<sup>3</sup> (see Appendix D). Samples were stored in a restricted and locked laboratory with identifying information segregated on an external hard drive held off site. The total sample size is 18, from 18 individuals, including 9 perimortem samples from 9 individuals (CHUM sample) and 9 post-mortem samples from 9 individuals (U of T sample), with the perimortem grouping ranging in age from 30 to 57 years and all being assessed as males through gross anatomy. The postmortem sample ranged in age from 70 to 108 years and consisted of 5 male and 4 female individuals. The date of death was also recorded but not provided to protect anonymity, however no other demographic data such as ancestry (race), stature, weight, and body mass index were recorded.

In order to assess changes in the levels of osteocalcin and osteopontin over time, the postmortem samples were sectioned and fixed at different points in time. After harvesting from the cadaver, 1/3 of each 2.5cm<sup>2</sup> segment was cut using a manual bone saw. This smaller segment was then immediately (within 1 hour) placed in a small jar with a 40% solution of formaldehyde to arrest protein and cellular degradation, and was subsequently labeled “early postmortem”, while the remaining 2/3 segment was reserved in a separate, empty but sealed jar. Because the timing varied slightly between death and donation, a consistent time could not be maintained between death and harvesting, thus the “early postmortem” period includes variable times up to 48 hours post somatic death. After a 7-day period following cardiopulmonary death, irrespective of harvesting date and time, the unfixed segment was cut in half using the same parameters as noted above, with one part being fixed in the solution and labeled as 7-day postmortem, and the remaining part left unfixed and again placed in a sealed jar. After yet another 7-day period (14 days following cardiopulmonary death, irrespective of harvesting date

---

<sup>3</sup> For CHUM Use of Samples, ethics approval, and Material Transfer Agreement information see Appendix D.

and time), the remaining segment was fixed in the 40% formaldehyde solution to arrest biological activity including protein and cellular degradation and labeled as 14-days postmortem. It should be noted that a 14-day time window was arbitrarily chosen due practical considerations related to the sectioning and fixation, as well as to its ability to discern potential significant differences over the time period. Following a 4-day fixation soak, the samples were then dried using a successive alcohol immersion protocol including in 95% ethyl alcohol for 7 days, and then 7 days in anhydrous alcohol. The samples were then soaked in methyl methacrylate (MMA) prior to embedding using manufacture recommended guidelines. MMA was selected as the mounting medium as it is optically neutral forgoing the photobleaching effect of epoxy resin. However, MMA can affect the penetrative power of antibodies which can be damaged in the embedding process. To address this potential problem, labeling took place post thin sectioning, with as thin a section as possible ( $\approx 100\mu\text{m}$ ) and with an extended incubation period following recommended practices (208, 209).

After segments were fully embedded and the medium allowed to dry, the segments were then mounted on glass slides and cut and polished using a Struers® Accutom-100™ to a final thickness of  $100\mu\text{m}$ . While the CHUM samples were  $\approx 15\mu\text{m}$ , numerous mechanical and technical issues with the Struers® Accutom-100™ prevented thinner sectioning and grinding without destruction of the samples. Two samples were produced per segment group: one for osteocalcin labeling and one for osteopontin labeling. The result was two samples (one OPN and one OC) per time period from 18 individuals over 4 time periods, for a total sample size of 72 for both OPN and OC combined, or 36 per protein (18 perimortem [CHUM], 18 postmortem-48hr, 18-7-day, and 18-14-day [UofT]).

After the preparation phase of the samples was complete, the samples went through similar labelling protocols to highlight either osteocalcin or osteopontin. Two specimens from each individual were isolated after thin-sectioning, in order to highlight for osteocalcin and osteopontin following protocols as listed for immunofluorescent labeling with Thermo Fisher Scientific™ (210, 227). The bone sections were hydrated and sterilized in phosphate buffer solution (PBS) for 30 minutes then labeled with an Osteocalcin Polyclonal Antibody (Thermo Fisher™) ( $\approx 2\mu\text{L}/\text{sample}$ ), or Osteopontin Monoclonal Antibody (Thermo Fisher™) per manufacturer's instructions ( $\approx 2\mu\text{L}/\text{sample}$ ). These were then allowed to incubate for 30 minutes before being rinsed in phosphate buffer solution (PBS). After rinsing, a secondary antibody of

goat anti-mouse IgG, Alexa Fluor™ 555 (Thermo Fisher™) was applied per manufacture’s instructions to both the OC and OPN samples (211-215). These samples were then allowed to incubate for a second period of 30 minutes before being rinsed in PBS, air dried for 24-48 hours following Thermo Fisher™ recommendation, and a glass coverslip being applied using Fluoromount™ aqueous mounting medium (Sigma Aldrich) (211, 212, 215, 216).

Imaging of the samples was completed on a Carl Zeiss™ LSM-800® laser scanning confocal microscope housed with the Department of Biology, University of Toronto – Mississauga, Mississauga, ON. The osteocalcin and osteopontin samples were imaged using the 40x oil-objective, for a total magnification of 400x per frame. Acquisition parameters were set at 2048 pixels x 2048 pixels per frame and 16 bits per pass. This allows for excellent resolution and has a much larger gradient when examining the pixel intensity (0 [black, no material] – 65,535 [white, full intensity] v 0 – 255). Samples were imaged using the 561nm excitation/555nm emission wavelength channel, with parameters for the laser power, pinhole, and master-gain adjusted per sample for optimization and to minimize image capture saturation. In general, the power was adjusted to approximately 0.2% with a pinhole of 32µm, and a master-gain of approximately 650V. A z-stack of 50 optical slices (≈0.25µm slice thickness; 12.75µm image thickness) was created going through the visible sample, and a tile-set was created that yielded a field of view of 447.23µm x 447.23µm (3 frames x 3 frames). The average voxel volume was 0.00155µm<sup>3</sup>, calculated by obtaining the voxel volume from each individual image. The voxel volume was calculated using the following formulae:

$$d^x = \frac{FOV^x}{Matrix^x}$$

$$d^y = \frac{FOV^y}{Matrix^y}$$

$$d^z = \frac{FOV^z}{\#ofSlices}$$

$$Voxel\ Volume\ \mu m^3 = d^x \times d^y \times d^z$$

The calculations were compared against the formulae for scaling per pixel in Zen Blue® (217) and comparing the calculated voxel amount [ $Matrix^x \times Matrix^y \times \#ofSlices$ ] with the voxel count in BitPlane® Imaris™ v. 9 (185).

For this project the middle envelope was selected for imaging as the periosteum and the endosteum have a naturally higher level of osteopontin which would inflate the OPN numbers. By selecting the middle envelope, the periosteum and endosteum are excluded so mainly those proteins used in the binding of the organic and inorganic matrices are imaged. It should be noted that negative space areas, such as Haversian and Volkmann canals, were not masked away due to the inability to layer multiple masks through an image stack with Imaris, thus allowing their inclusion in the image analyses. This would result in those samples with fewer negative spaces registering a higher overall pixel intensity as more fluoresced pixels would be registered.

Image analysis was conducted using Oxford Industries BitPlane™ Imaris® v9 (185). Imaris is a high-power software program that allows visualization and quantification without crashing due to lack of memory; a common issue found with FIJI/ImageJ® (186). The analysis examined pixel intensity gathered from the complete specimen image, rather than single slices, using the statistics and proprietary algorithms generated in Imaris (185) from the unaltered images. These data were collected because the Alexa Fluor™(tm) 555 only attaches to the target protein, thus only the protein will fluoresce. As 16-bit imaging was utilized, the software classified the mean pixel intensity and standard deviation on a scale of 0 – 65,535. The theory is that the greater the amount of target material, the higher on the intensity scale it will fluoresce. While complete standardization of image parameters such as pinhole, power, gain, etc. would be optimal, rigidity in this instance would invite over saturation and under-capture of targeted materials as each individual sample has some unique properties. While post-capture processing and analyses did find saturation in all images, care was taken to optimize rather than standardize image capture to minimize saturation during the capture process. BitPlane™ Imaris® (185) was used in preference to FIJI/ImageJ® (186) due to the fact that FIJI/ImageJ® (186) frequently crashed due to image size and lack of computational memory.

Statistics were run using IBM™ SPSS® v28 (219), specifically the mean pixel intensity and standard deviation using a Kruskal-Wallis Independent Samples H-test to determine if there was a difference between the perimortem, and postmortem groups, as well as a Spearman correlation analysis, to determine if intensity fluctuations correlated to segment timing (perimortem, postmortem-48hr, -7-day, -14-day). Additionally, a Friedman repeated measures test was run on the postmortem sample groups only, to determine if there was a significant variation over time in the postmortem group. Additionally, post hoc analyses were run to

determine if any variation seen existed within all groups or was limited to between specific time groups. Lastly, due to the potential presence of outliers, the above mentioned tests were run with any outliers removed. The nature of an outlier is not always clear, as it could result from an artifact on a specific slide in a particular time period in a particular test, or it could be something inherent to the person that would affect multiple time periods. For this reason, two tests were conducted for the outliers. The first test removed the outlier only from the time period that demonstrated the effect, i.e. if Individual X was an outlier in only the OPN mean intensity 14-day period, then Individual X was removed only from the OPN mean intensity 14-day analysis. The second test removed that same Individual X from all OPN tests entirely, in case they were impacting the results in a less obvious way in other time periods.

The standard deviation was used as a secondary metric to determine if there was a difference in the variability of pixel intensity found within each image and grouping. This metric is generated due to the fact that the primary metric (mean pixel intensity) accounts for variation within the image as each pixel produces a different intensity level. While relying on mean pixel intensity could be used as a solitary metric, questions would arise as to the variability within each sample image as a mean was generated rather than a hard point. It is hypothesized that for OPN the variability in both mean pixel intensity and pixel intensity standard deviation would be variable and even decrease as the postmortem interval increased because the protein will have degraded naturally. With OC there should be no significant differences in the means between the 4 time groups in either the mean pixel intensity nor the standard deviation due to the fact that as postmortem interval increases OC maintains its presence even through decomposition and diagenesis. Given the sample size and non-normality in the distributions, non-parametric tests were utilized. The K-W H Test was chosen to determine if there was a statistically significant difference in the means between the various time groups with  $H_0$  being supported if  $p > 0.05$  meaning that there was no significant difference between the time groups, and  $H_1$  being accepted if  $p \leq 0.05$  meaning that there was a significant difference between the time groups. Additionally, because this project compared ordinal with scale data, the Spearman rho correlation was selected as it would be able to determine if those differences had a linear relationship. Finally, given the small sample size for this project, a power and eta-squared ( $\eta^2$ ) effect size analyses were conducted, with Cliff's  $\delta$  calculated for the Mann-Whitney U-tests used to calculate the effect of sex.

It was hypothesized that there would be a significant and predictable decrease in the amount fluorescence of the osteopontin-labeled samples as time progressed due to the natural decomposition of the organic matrix of the bone and the subsequent protein (OPN), while the osteocalcin-labeled complexes would remain more static because OC has been shown to decompose very slowly over time (102, 103, 105). In addition to the individual changes in the levels of OPN and OC, ratio changes were calculated between OPN:OC using both the mean pixel intensity and standard deviation data.

### 3.2.3 Results

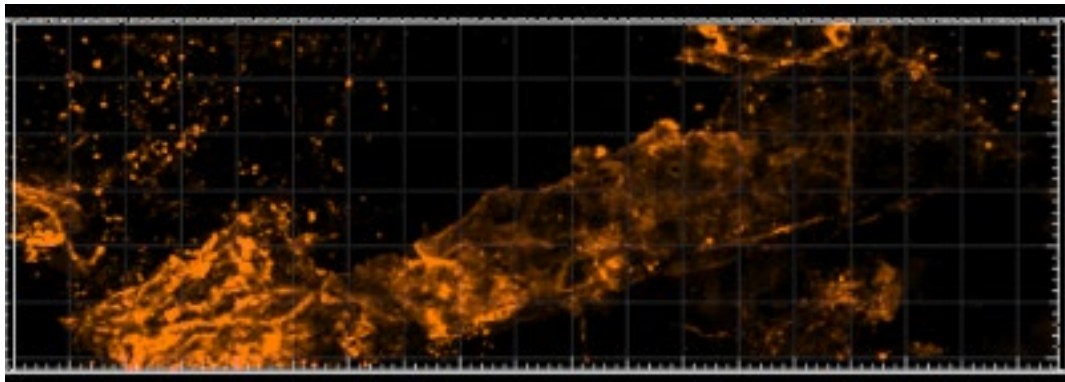


**Figure 3.2.1: Osteopontin labeled cortical bone (Sample #3). In this image the distribution of OPN is as expected following the literature - across the bone section with higher concentrations at cement lines and Haversian canals. Image was taken at 400x total magnification per frame, using 1,314 frames to obtain a 3.07mm x 9.26mm total image size; 50 optical slices with a depth of 100 $\mu$ m compressed from a 3D image.**

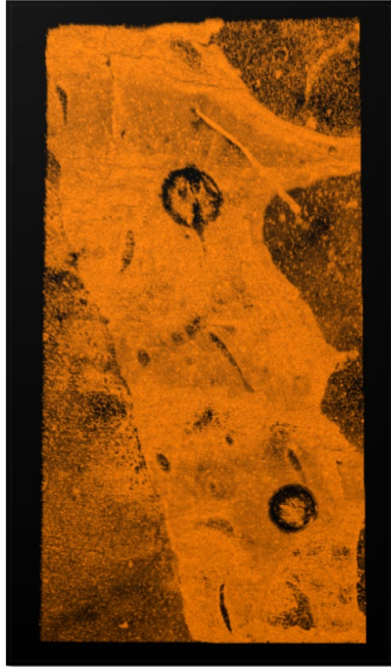


**Figure 3.2.2: Osteocalcin labeled bone (Sample #4).** In this image the OC is distributed as expected according to literature, throughout the cortical extra cellular matrix. Image was taken at 400x total magnification per frame, using 135 frames to obtain a 1.23mm x 2.37mm total image size; 50 optical slices with a depth of 15 $\mu$ m stacked from a 3D image.

Overall, the results of this study found no significant difference in the fluorescence mean intensity ( $p=0.373$ ) nor the standard deviation of that intensity ( $p=0.339$ ) (Fig. 3.2.3 – 3.2.7) in the osteocalcin portion of this study over the four time groups. The results of the power analyses being 0.119 for the intensity and 0.269 for the standard deviation while the results of the  $\eta^2$  effect sizes were 0.004 for the intensity and 0.011 for the standard deviation indicating a low effect size. Further, there was no significant correlation to time in either the mean intensity at  $r=0.007$  ( $p=0.967$ ), or the standard deviation at  $r=-0.041$  ( $p=0.841$ ). Additionally, the results of the Friedman test demonstrated no significant difference between the postmortem groups with a  $p=0.459$ , and the ranking fluctuating across the time groups. These results, coupled with the means and distribution as seen in Fig. 3.2.4 & 3.2.5 suggest that while there is some measure of stability between the four time groups as it relates to osteocalcin, in reality, there is a measurable deal of variability that spans with and between the groups leading to a sense of temporal stability (Figs. 3.2.3 – 3.2.7).

Meanwhile, on a gross scale, there was a degradation (to the  $\alpha=0.05$  level) in the osteopontin labeled samples over time (Fig. 3.2.9 & 3.2.10). The results of the tests on the

fluorescence mean intensity and standard deviations (Fig. 3.2.9 – 3.2.10) of the osteopontin demonstrated significant results in both the K-W ( $p=0.035$ ,  $H=8.620$  for mean intensity and  $p=0.007$ ,  $H=12.129$  for standard deviations) and the correlations ( $r=-0.466$ ,  $p=0.004$  for the mean intensity, and  $r=-0.519$ ,  $p=0.001$  for the standard deviation), while the time group means demonstrated a clear degradation as time increased postmortem (Fig. 3.2.9). The results of the power and  $\eta^2$  effect analyses demonstrated a moderate to strong result with power results being 0.563 for the mean intensity and 0.840 for the standard deviation with the  $\eta^2$  effect sizes being 0.176 for the mean intensity and 0.285 for the standard deviation respectively, indicating a large effect size, demonstrating a greater chance of obtaining a true result. However, the results of the post hoc analyses and the Friedman test indicate that the difference may only be limited to between the perimortem vs postmortem rather than between the individual time groups. With regards to the post hoc analyses (see Table 3.2-2 ), the only significant pairwise results for the mean intensity are between the perimortem group and the 7-day group ( $p=0.011$ ), and between the perimortem and the 14-day postmortem ( $p=0.12$ ). Meanwhile, for the standard deviation post hoc analysis, the only significant pairwise results are again perimortem/7-day postmortem ( $p=0.006$ ) and perimortem/14-day postmortem ( $p=0.002$ ). Additionally, the results of the Friedman test confirm that there was no significant variation between the postmortem groupings with  $p=0.895$ . That said, the mean rank with the Friedman test did demonstrate a decrease over the 3 postmortem groups (2.11, 2.00, and 1.89 respectively). The cumulative results of this data suggests that while there may not be a *significant* decrease between the means of the time groups, a declination does exist. However, an analysis of the line graphs generated from the postmortem osteopontin studies (Figs. 3.2.11 – 3.2.12) demonstrated that, though a slight pattern may be present in the mean, several individuals do not follow any pattern.

Though ratio data is complicated as noted, it was calculated by examining the difference between the different time groups (Table 3.2-1). The results of this study did not find an overall decline in the ratio of OPN:OC in either the mean intensity, standard deviations, or in the range. Universally there was a declination in the ratio from the perimortem group to the early postmortem and between the 7-day postmortem and the 14-day, but from the early-postmortem to the 7-day, there was an increase in the ratio. This, however, can be explained by the declination in the osteocalcin between these two groups, despite the OC demonstrating no real pattern of declination over time suggesting stability. A Kruskal-Wallis H-test was run for the

calculated ratio between both the mean intensity and standard deviation as a ratio of OPN:OC with neither demonstrating a significant result (mean intensity  $p=0.185$ ,  $H=4.832$ , standard deviation  $p=0.090$ ,  $H=6.504$ ). The results of the  $\eta^2$  effect size for both tests was 0.057 and 0.110 respectively, indicating a moderate effect size with regards to the standard deviation analysis but a weaker effect with regards to the mean intensity. Additionally, as no significant result was seen in the larger Kruskal Wallis H-test, the post hoc analyses as well found no significant difference between any paired group. Furthermore, the results of the Friedman test also demonstrated no significant difference between the different postmortem groupings with  $p=0.459$  for the mean intensity and standard deviation, with the largest mean rank falling on the 7-day postmortem group at 2.33 for both mean intensity and standard deviation, then early postmortem, then 14-day postmortem. See figs. 3.2.13 – 3.2.17.

When accounting for age at death (as defined by lustrum given the dispersal) and its effect on the difference in pixel intensity for osteopontin and osteocalcin the results of the Kruskal-Wallis indicate there is no significant difference with either protein in the mean pixel intensity or pixel standard deviation (Table 3.2-3). Similarly, sex also failed to return a significant result using Mann-Whitney U test with respect to osteopontin and osteocalcin pixel intensity or pixel standard deviation (Table 3.2-3). That said, it should be noted that the perimortem sample was younger in age and all male, while the postmortem sample is derived from an older sample that was divided more equally between males and females (though there was one more male than female). Further, for the Mann-Whitney U-test regarding sex, the distribution of males and females is so out of balance and the  $n$  within the female cohort small, the non-significant results were as expected, and can be considered a major limitation of the test. As a result, a similar study with a more robust cohort may find that sex does have an impact on the overall results.

See Appendix A for sample demographic data and Appendix B for raw data for both the osteopontin and osteocalcin mean pixel intensities and pixel intensity standard deviations.

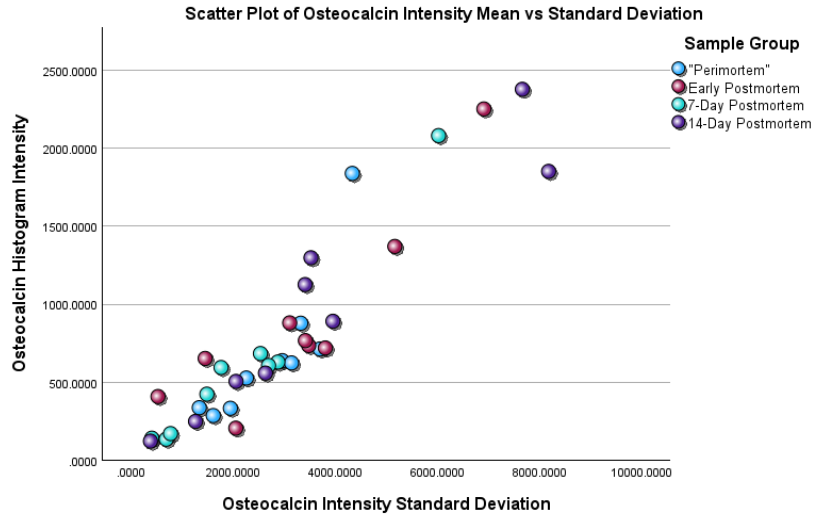


Figure 3.2.3: Osteocalcin fluorescence intensity over the four time-groups.

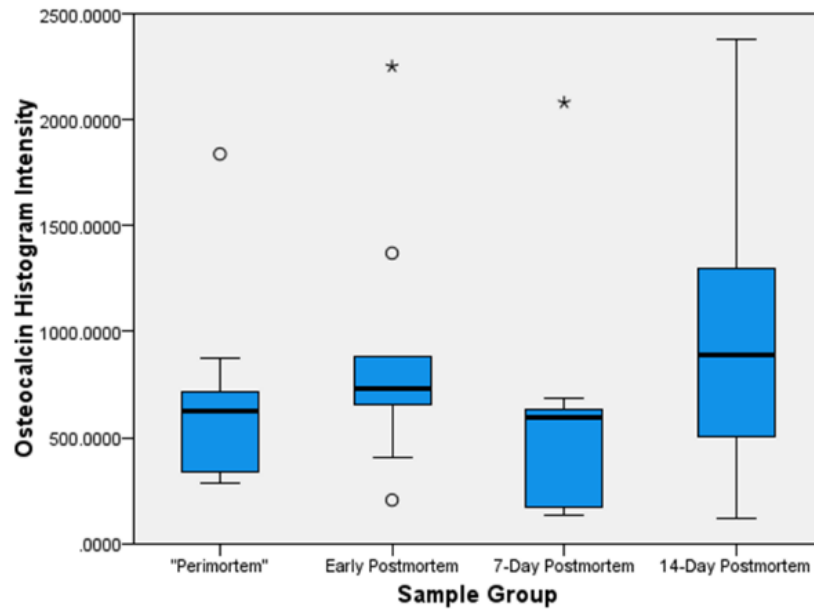
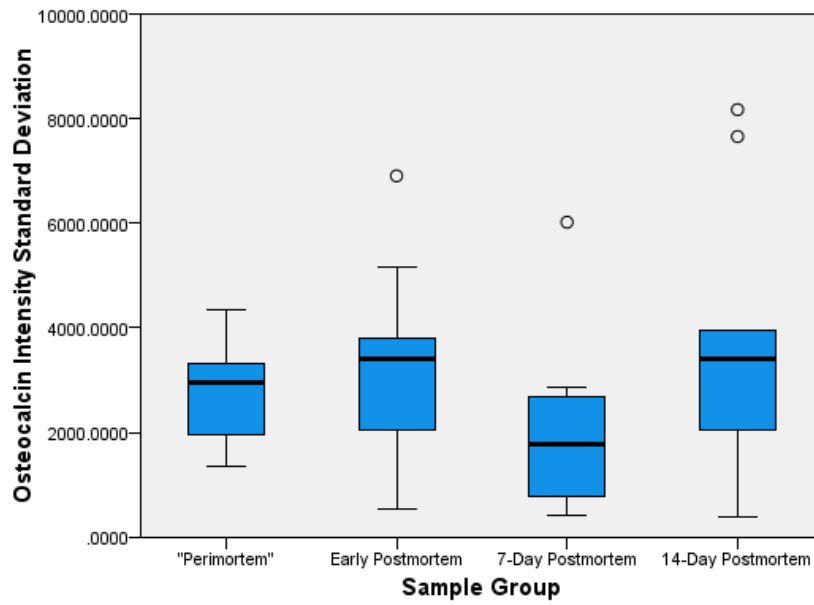
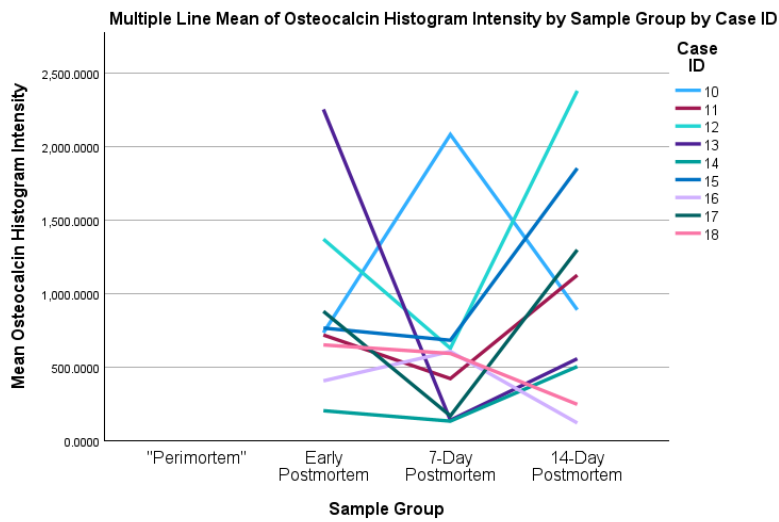


Figure 3.2.4: Osteocalcin pixel intensity group means.



**Figure 3.2.5: Osteocalcin pixel standard deviation.**



**Figure 3.2.6: Line graph of individual postmortem osteocalcin mean intensity fluctuation.**

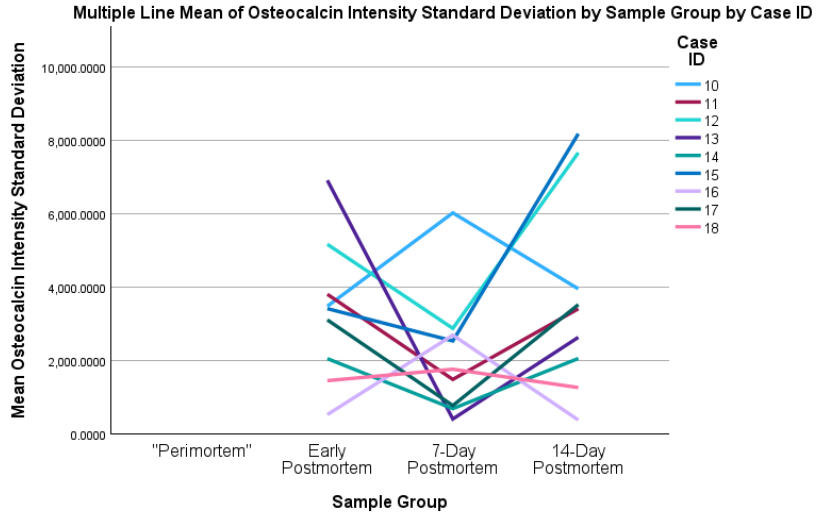


**Figure 3.2.7: Line graph of postmortem osteocalcin standard deviation fluctuation.**

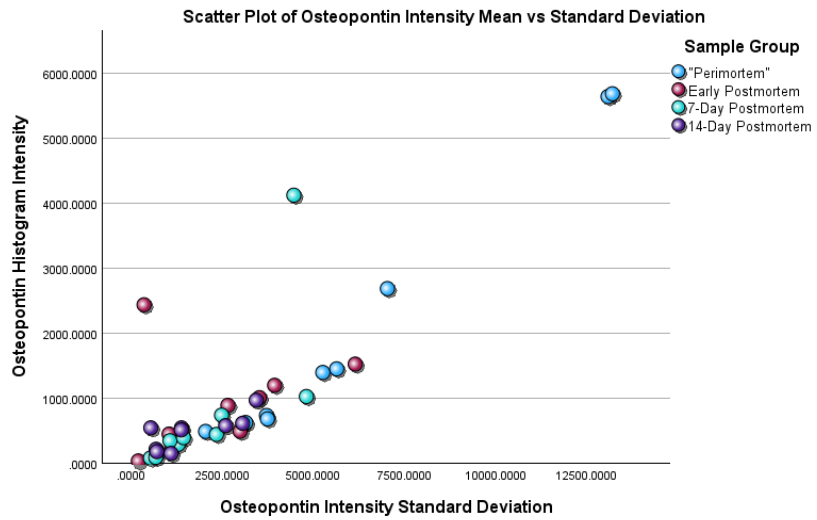


**Figure 3.2.8: Osteopontin fluorescence intensity data.**

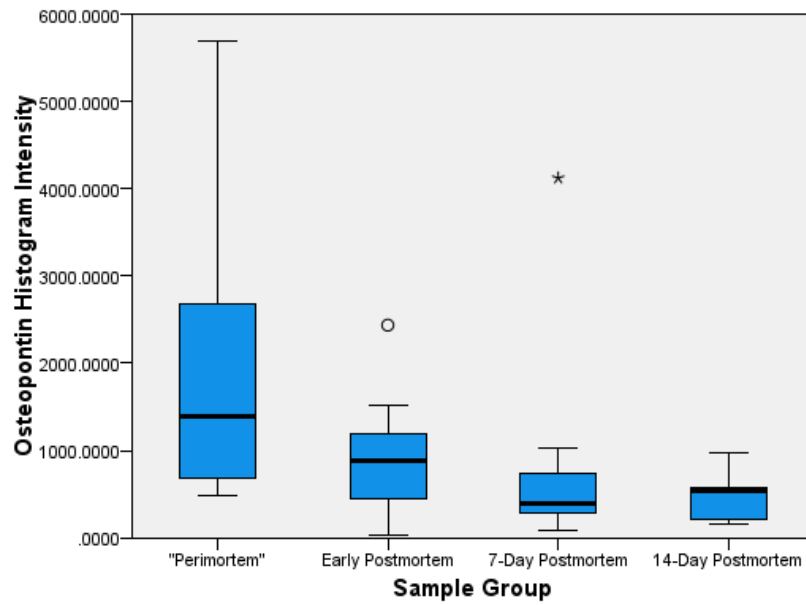


Figure 3.2.9: Osteopontin pixel intensity group means.

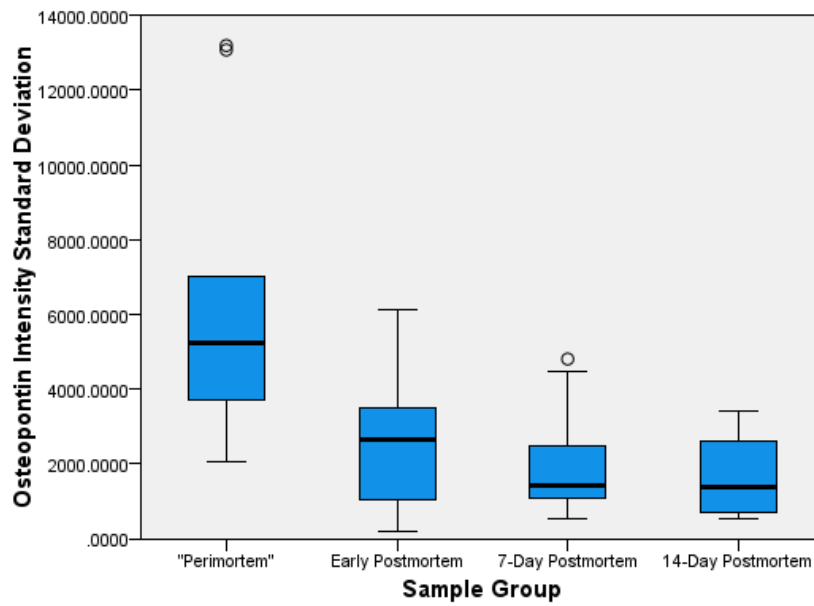
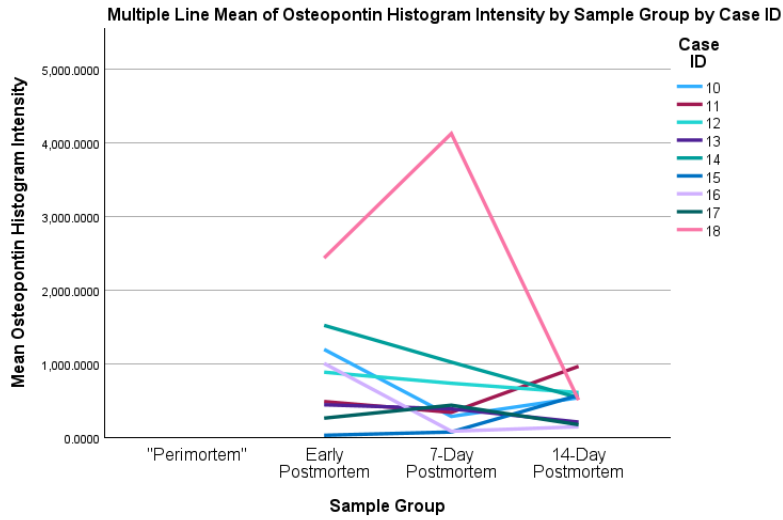
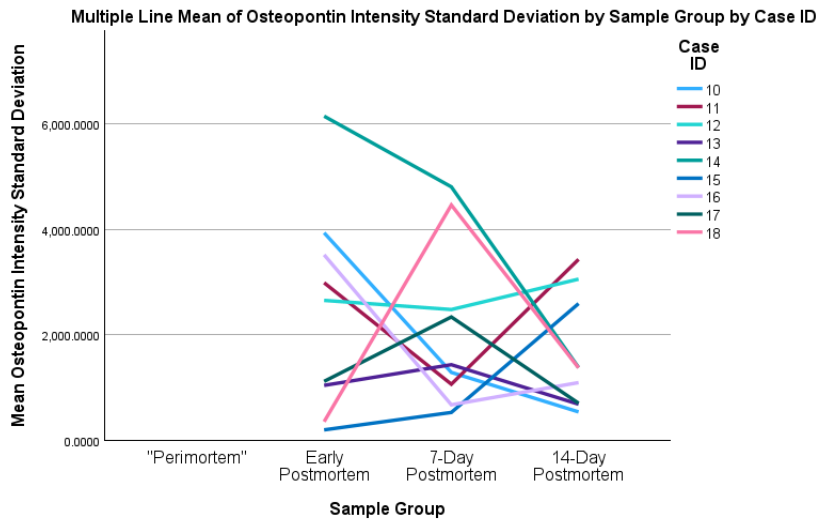


Figure 3.2.10: Osteopontin pixel intensity standard deviation.



**Figure 3.2.11: Postmortem osteopontin mean intensity fluctuation.**



**Figure 3.2.12: Postmortem osteopontin standard deviation fluctuation.**

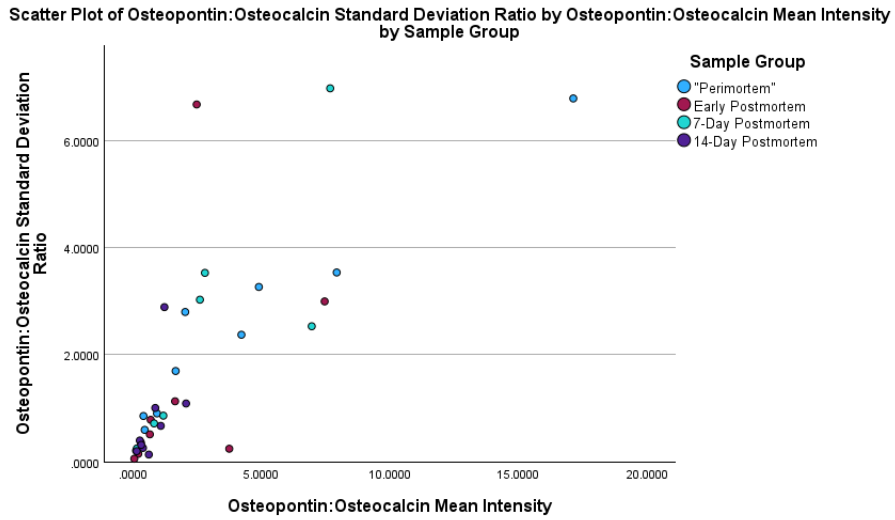


**Figure 3.2.13: OPN:OC ratio fluorescence data as a relationship of mean intensity to standard deviation.**

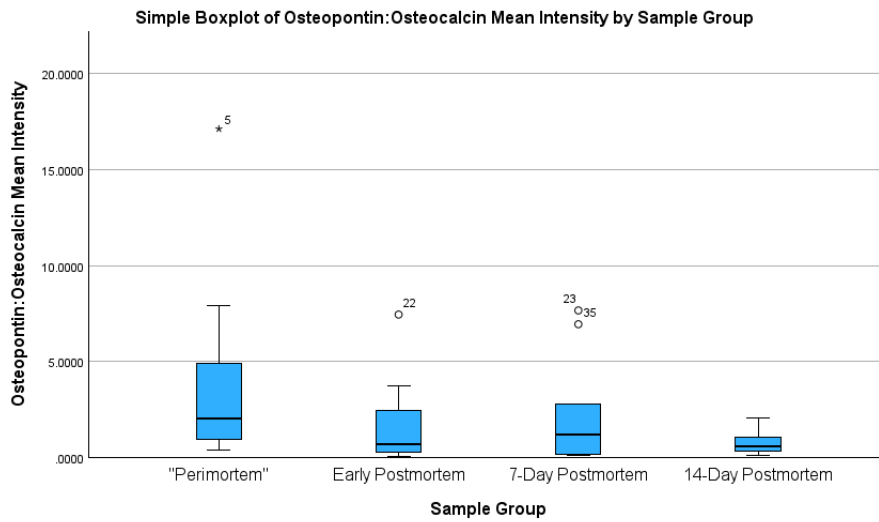


**Figure 3.2.14. OPN:OC mean intensity data.**

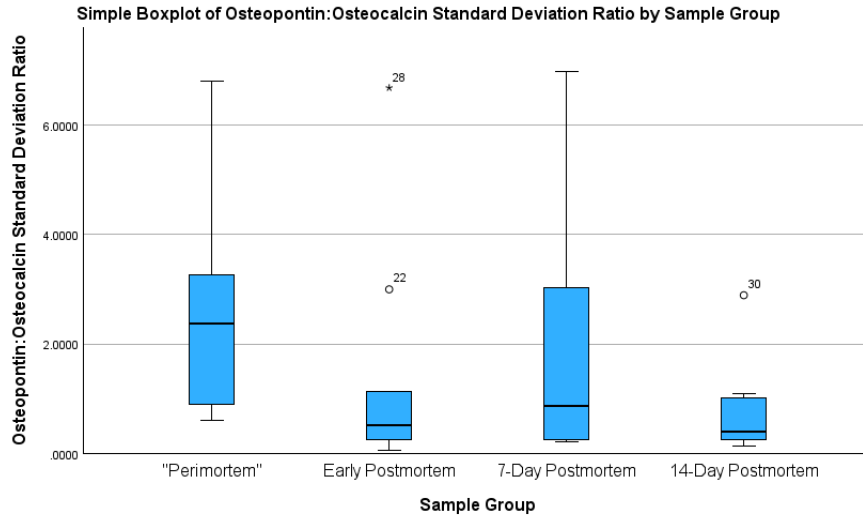


**Figure 3.2.15: OPN:OC standard deviation data.**

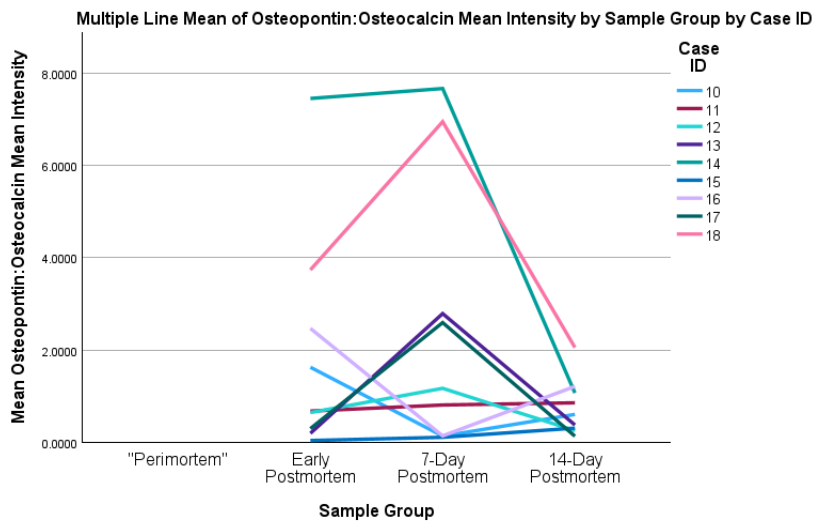


**Figure 3.2.16: Postmortem OPN:OC mean intensity fluctuations.**

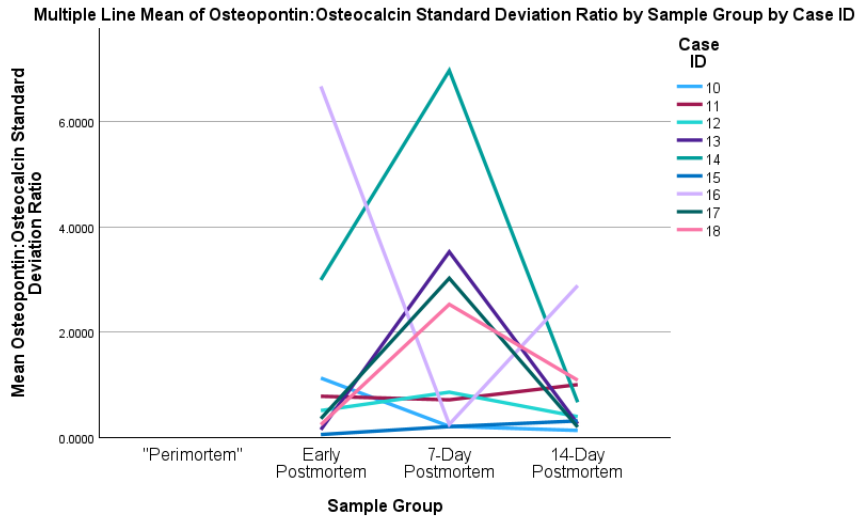


Figure 3.2.17: OPN:OC postmortem standard deviation fluctuations.

Table 3.2-1: Ratio differences between the time groups.

	OPN:OC Mean Intensity	OPN:OC Std. Dev.	Range
Perimortem	4.40:1	2.535:1	1.86:1 - 6.93:1
Early-Postmortem	1.91:1	1.435:1	0.47:1 – 3.34:1
7-Day Postmortem	2.48:1	2.035:1	0.45:1 – 4.52:1
14-Day Postmortem	0.766:1	0.775:1	0.008:1 – 1.54:1

Table 3.2-2: Post Hoc Pairwise Tests

Test	Sample 1-Sample 2	Test Statistic	Std. Error	Std. Test Statistic	Sig.	Adj. Sig. <sup>a</sup>
Osteocalcin Mean Intensity	7-Day Postmortem-"Perimortem"	4.667	4.967	0.940	0.347	1.000
	7-Day Postmortem-14-Day Postmortem	-7.111	4.967	-1.432	0.152	0.913
	7-Day Postmortem-Early Postmortem	8.000	4.967	1.611	0.107	0.643
	"Perimortem"-14-Day Postmortem	-2.444	4.967	-0.492	0.623	1.000
	"Perimortem"-Early Postmortem	-3.333	4.967	-0.671	0.502	1.000
	14-Day Postmortem-Early Postmortem	0.889	4.967	0.179	0.858	1.000
	7-Day Postmortem-"Perimortem"	6.444	4.967	1.298	0.194	1.000

<b>Test</b>	<b>Sample 1-Sample 2</b>	<b>Test Statistic</b>	<b>Std. Error</b>	<b>Std. Test Statistic</b>	<b>Sig.</b>	<b>Adj. Sig.<sup>a</sup></b>
Osteocalcin Mean Standard Deviation	7-Day Postmortem-Early Postmortem	7.778	4.967	1.566	0.117	0.704
	7-Day Postmortem-14-Day Postmortem	-7.778	4.967	-1.566	0.117	0.704
	"Perimortem"-Early Postmortem	-1.333	4.967	-0.268	0.788	1.000
	"Perimortem"-14-Day Postmortem	-1.333	4.967	-0.268	0.788	1.000
	Early Postmortem-14-Day Postmortem	0.000	4.967	0.000	1.000	1.000
	Osteopontin Mean Intensity	14-Day Postmortem-7-Day Postmortem	0.222	4.967	0.045	0.964
Osteopontin Mean Standard Deviation	14-Day Postmortem-Early Postmortem	5.556	4.967	1.119	0.263	1.000
	14-Day Postmortem-"Perimortem"	12.667	4.967	2.550	0.011	0.065
	7-Day Postmortem-Early Postmortem	5.333	4.967	1.074	0.283	1.000
	7-Day Postmortem-"Perimortem"	12.444	4.967	2.506	0.012	0.073
	Early Postmortem-"Perimortem"	7.111	4.967	1.432	0.152	0.913
	OPN:OC Mean Intensity	14-Day Postmortem-7-Day Postmortem	2.111	4.967	0.425	0.671
14-Day Postmortem-Early Postmortem		3.333	4.967	0.671	0.502	1.000
14-Day Postmortem-"Perimortem"		15.667	4.967	3.154	0.002	0.010
7-Day Postmortem-Early Postmortem		1.222	4.967	0.246	0.806	1.000
7-Day Postmortem-"Perimortem"		13.556	4.967	2.729	0.006	0.038
Early Postmortem-"Perimortem"		12.333	4.967	2.483	0.013	0.078
OPN:OC Mean Intensity		14-Day Postmortem-Early Postmortem	3.333	4.967	0.671	0.502

Test	Sample 1-Sample 2	Test Statistic	Std. Error	Std. Test Statistic	Sig.	Adj. Sig. <sup>a</sup>
	14-Day Postmortem-7-Day Postmortem	4.889	4.967	0.984	0.325	1.000
	14-Day Postmortem-"Perimortem"	10.667	4.967	2.148	0.032	0.190
	Early Postmortem-7-Day Postmortem	-1.556	4.967	-0.313	0.754	1.000
	Early Postmortem-"Perimortem"	7.333	4.967	1.477	0.140	0.839
	7-Day Postmortem-"Perimortem"	5.778	4.967	1.163	0.245	1.000
OPN:OC Mean Standard Deviation	14-Day Postmortem-Early Postmortem	1.667	4.967	0.336	0.737	1.000
	14-Day Postmortem-7-Day Postmortem	6.111	4.967	1.230	0.219	1.000
	14-Day Postmortem-"Perimortem"	11.556	4.967	2.327	0.020	0.120
	Early Postmortem-7-Day Postmortem	-4.444	4.967	-0.895	0.371	1.000
	Early Postmortem-"Perimortem"	9.889	4.967	1.991	0.046	0.279
	7-Day Postmortem-"Perimortem"	5.444	4.967	1.096	0.273	1.000

Each row tests the null hypothesis that the Sample 1 and Sample 2 distributions are the same. Asymptotic significances (2-sided tests) are displayed. The significance level is .050.

<sup>a</sup>. Significance values have been adjusted by the Bonferroni correction for multiple tests.

**Table 3.2-3: Kruskal Wallis (Age) and Mann-Whitney U-test (Sex) Results**

Test			<i>p</i> -Value	<i>H</i> / <i>U</i> -Stat	$\eta^2$ /Cliff's $\delta$	
Osteopontin	Mean Pixel Intensity	Age	Perimortem	<i>p</i> =0.430	<i>H</i> =2.760	$\eta^2$ =0.048
		Age	Early Postmortem	<i>p</i> =0.302	<i>H</i> =6.044	$\eta^2$ =0.348
		Age	7-Day Postmortem	<i>p</i> =0.724	<i>H</i> =2.844	$\eta^2$ =0.719
		Age	14-Day Postmortem	<i>p</i> =0.387	<i>H</i> =5.244	$\eta^2$ =0.081
		Age	Perimortem	<i>p</i> =0.430	<i>H</i> =2.760	$\eta^2$ =0.048
	Standard Deviation	Age	Early Postmortem	<i>p</i> =0.387	<i>H</i> =5.244	$\eta^2$ =0.081
		Age	7-Day Postmortem	<i>p</i> =0.721	<i>H</i> =2.867	$\eta^2$ =0.711
		Age	14-Day Postmortem	<i>p</i> =0.628	<i>H</i> =3.467	$\eta^2$ =0.511
		Age	Perimortem	<i>p</i> =0.334	<i>H</i> =3.400	$\eta^2$ =0.080
		Age	Early Postmortem	<i>p</i> =0.176	<i>H</i> =7.667	$\eta^2$ =0.889
Osteocalcin	Mean Pixel Intensity	Age	7-Day Postmortem	<i>p</i> =0.484	<i>H</i> =4.467	$\eta^2$ =0.178

Osteopontin	Standard Deviation	Age	14-Day Postmortem	$p=0.254$	$H=6.578$	$\eta^2=0.526$
			Perimortem	$p=0.339$	$H=3.360$	$\eta^2=0.072$
			Early Postmortem	$p=0.319$	$H=5.867$	$\eta^2=0.289$
			7-Day Postmortem	$p=0.484$	$H=4.467$	$\eta^2=0.178$
			14-Day Postmortem	$p=0.302$	$H=6.044$	$\eta^2=0.348$
	Mean Pixel Intensity	Sex	Early Postmortem	$p=0.556$	$U=13.000$	$\delta=2.907$
			7-Day Postmortem	$p=0.111$	$U=17.000$	$\delta=3.801$
			14-Day Postmortem	$p=1.000$	$U=10.000$	$\delta=2.236$
			Early Postmortem	$p=1.000$	$U=11.000$	$\delta=2.460$
			7-Day Postmortem	$p=0.190$	$U=16.000$	$\delta=3.578$
Osteocalcin	Standard Deviation	Sex	14-Day Postmortem	$p=0.556$	$U=13.000$	$\delta=2.907$
			Early Postmortem	$p=0.286$	$U=5.000$	$\delta=1.118$
			7-Day Postmortem	$p=0.111$	$U=3.000$	$\delta=0.671$
	Mean Pixel Intensity	Sex	14-Day Postmortem	$p=0.730$	$U=8.000$	$\delta=1.789$
			Early Postmortem	$p=0.413$	$U=6.000$	$\delta=1.342$
			7-Day Postmortem	$p=0.190$	$U=4.000$	$\delta=0.894$
			14-Day Postmortem	$p=0.413$	$U=6.000$	$\delta=1.342$

### 3.2.3.1 Outliers

When conducting an analysis such as the present study, the existence of outliers will develop. The question becomes how to address those outliers in the analyses that ensue. With the present study, two methods are presented depending on the theory behind the cause of the outliers. The first is the removal of the individual outlier from the test statistic that is being measured. That is, if Individual X is found to be an outlier in 7-day postmortem mean intensity, then that sample is removed from just the 7-day postmortem mean intensity. This is useful if the prevailing theory is that the outlier is a result of artifacts found only within that sample, and not a more biological explanation found within the individual. The second option would be the removal of Individual X from all osteopontin related tests rather than just the one area to which they are an outlier. Here the prevailing theory would be that the individual rather than the sample is the cause of being an outlier. At issue with the present study are two considerations when making a decision as to which route to take. The first is that the removal of excessive individuals due to being an outlier in a single metric would artificially limit a sample pool that is already limited in scale. The second, however, is that when reviewing the outliers in question, numerous were found to be in multiple categories (i.e. Individual X was an outlier in both the 7-day *and* 14-day). At this point it becomes a judgement as to whether the cause is due to artifacts or is biological in nature. For the present study, to account for both situations, analyses were run

with the outliers removed from the individual test, as well as the second set of analyses run with the whole of the individual removed from that particular protein. For example, if Individual X was found to be an outlier in the 7-day postmortem OPN mean intensity, the analyses were run once with Individual X removed from just the 7-day postmortem OPN mean intensity, and then a second time with that individual removed from *all* OPN tests. In order to determine where the outliers existed, a *z*-score analysis [ $z=(x - \mu)/\sigma$ ] was run for all test categories.

With the outliers removed either on an individual group bases, or from the whole test, the results of the osteocalcin analyses mirror that of the initial analyses. With outliers removed from individual test groups, the results of the Kruskal Wallis H-test found no significant difference between the four time groups in either the mean intensity ( $p=0.231$ ,  $H=4.300$ ) or standard deviation ( $p=0.510$ ,  $H=2.316$ ) (see Figs. 3.2.18 – 3.2.21). For both the  $\eta^2$  was 0.046 and 0.022 respectively, suggesting a low effect size. When examining with the outlier individuals removed from all osteocalcin groups, the results were again not significant with the results of the Kruskal-Wallis H-test being  $p=0.581$  ( $H=1.959$ ) and  $p=0.436$  ( $H=2.724$ ) for both the mean intensity and standard deviation respectively, and an effect size of  $\eta^2=0.055$  and 0.014 respectively. The results of the post hoc analyses for the osteocalcin studies, examining both the individual group, and whole group removal found no significant difference between any pair (see Table 3.2-4). Further, the results of the Friedman tests also demonstrated no significant difference between the postmortem groups, with  $p=0.311$  for the mean intensity with the individual outliers removed,  $p=0.819$  for the standard deviation,  $p=0.236$  for the mean intensity with the individual removed from all OC tests, and  $p=0.459$  for the standard deviation. Additionally, with all tests, the mean ranks demonstrate no pattern, though consistently the 7-day postmortem group summed the lowest. See Figs. 3.2.22 – 3.2.25.

The results of the osteopontin test also mirrored the analysis with all samples included, when both the individual outliers are removed as well as when whole individuals are removed from all OPN studies. On an individual basis, the results of the Kruskal-Wallis H-test found a significant difference between the four time groups in both the mean intensity ( $p=0.015$ ,  $H=10.536$ ) and the standard deviation ( $p=0.025$ ,  $H=9.310$ ) (see Figs. 3.2.26 & 3.2.27). The results of the  $\eta^2$  effect test was 0.251 and 0.218 indicating a large effect size with this test. When whole individuals are removed, the results of the Kruskal-Wallis H-tests again found a significant difference between the four time groups with  $p=0.034$  ( $H=8.675$ ) for the mean

intensity and  $p=0.011$  ( $H=11.208$ ) for the standard deviation (Figs. 3.2.28 & 3.2.29). The effect size for these tests were  $\eta^2=0.236$  and  $0.342$  respectively, again indicating a large effect size with this test.

These results aside, an analysis of the post hoc pairwise tests suggests that, while a significant difference does exist between the time groups, this difference is more limited to perimortem/later-postmortem rather than between each individual group (see Table 3.2-4). The post hoc tests with both the individual outliers removed as well as with the whole individuals removed indicate that for the mean intensity the only significant difference is between the perimortem/7-day postmortem pair ( $p=0.003$ ,  $H=2.971$  [individual];  $p=0.005$ ,  $H=2.827$  [complete removal]), and the perimortem/14-day postmortem pair ( $p=0.010$ ,  $H=2.580$ [individual];  $p=0.035$ ,  $H=2.122$  [complete removal]). These results suggest that while degradation does exist, some time is needed from baseline before that degradation becomes significant. While sample composition may be a factor in generating the trend, when compared to the results with the outliers included, the similarities in the results between the tests suggests that the significance in the differences in the means starting at the 7-day postmortem time period is more likely due to degradation than sample composition.

In addition to the Kruskal Wallis H-test and subsequent post hoc analyses, a series of Friedman repeated measures tests were also run for the osteopontin mean intensity and standard deviation, with both the individual outliers removed and the whole individuals removed. The results of the Friedman tests found no significant difference between the various postmortem groups on any level. With the individual outliers removed the results were  $p=0.233$ , and  $p=1.000$  for the mean intensity and standard deviation respectively, and  $p=0.368$  and  $p=0.867$  respectively with the whole individual removed. When comparing the results of the osteopontin tests with both the inclusion and the exclusion of the outliers, particularly with the outliers removed in any fashion, the cumulative results suggest a pattern might be present, but that such a pattern takes time postmortem to become present. However, a review of the line graphs generated (Figs. 3.2.30 – 3.2.33) demonstrates that no such true pattern exists with this data set, particularly with regards to the 7-day postmortem group which, while demonstrating an overall decline, also has a number individuals with a rise at this time period.

When it comes to the ratio of OPN:OC, a more complicated picture arose. Only one Kruskal-Wallis H-test found a significant result: that of the standard deviation ratio with only the individual outliers removed. All of the other tests were found to be not significant. Specifically, the results of the OPN:OC standard deviation ratio was  $p=0.012$  ( $H=10.925$ ,  $\eta^2=0.273$ ). However, here again an analysis of the post hoc pairwise results indicate that only two significant pair differences existed, this time between the perimortem/early postmortem ( $p=0.005$ ,  $H=2.818$ ) and the perimortem/14-day postmortem ( $p=0.007$ ,  $H=2.675$ ). With all other tests, the results were not significant, with the mean intensity being  $p=0.200$  ( $H=4.636$ ) with individual outliers removed and  $p=0.112$  ( $H=5.982$ ) with the whole individuals removed, while the standard deviation with whole individuals removed was  $p=0.403$  ( $H=2.982$ ). The  $\eta^2$  effect size test results for the previous three were  $\eta^2=0.058$ ,  $0.110$ , and  $0.0007$  suggesting that only the OPN:OC mean intensity ratio whole individuals removed had a moderate effect size, while the remaining two had a weak effect size. When examining the post hoc pairwise analyses of these three tests as well, no pair was found to have a significant result (see. Table 3.2-4).

In addition to the Kruskal-Wallis H-test and post hoc analysis, Friedman repeated measures tests were run on the ratio calculations, again both mean intensity and standard deviations, as well as with both the individual outliers removed and with the whole individuals removed. The results of the Friedman tests found no significant results within any of the four tests. For the OPN:OC mean intensity with both the individual outliers removed and whole individuals removed, the results of the Friedman test was  $p=1.000$  respectively, with the mean rank remaining the same across the board. With regards to the standard deviation the results were  $p=0.819$  with the individual outliers removed and  $p=0.717$  with whole individuals removed. The mean rank showed no real pattern in the latter, but with individual outliers removed, there was a steady degradation of 0.20 in the mean rank from 2.20 in the early postmortem to 1.80 in the 14-day postmortem. See Figs. 3.2.32 – 3.2.41.

When taken as a complete whole, the simplified results of this study indicate that there is no real pattern in the fluorescence of osteocalcin through the time groups, while osteopontin indicates a possible degradation, though that degradation only appears significant when compared to the perimortem group and only registers as significant once the 7-day postmortem period begins. As for the ratio between osteopontin to osteocalcin fluorescence, there does not appear to be any pattern detected either with all of the samples present or with outliers removed

in any fashion. There is a significant difference found in the OPN:OC standard deviation, but analyses of the post hoc results indicate no real pattern in that difference. When the irregular distribution of osteocalcin fluorescence is considered as part of the OPN:OC ratio, the interchange between the early-postmortem and 7-day postmortem groups appear to be the area where OPN:OC ratio data becomes unreliable as a metric.

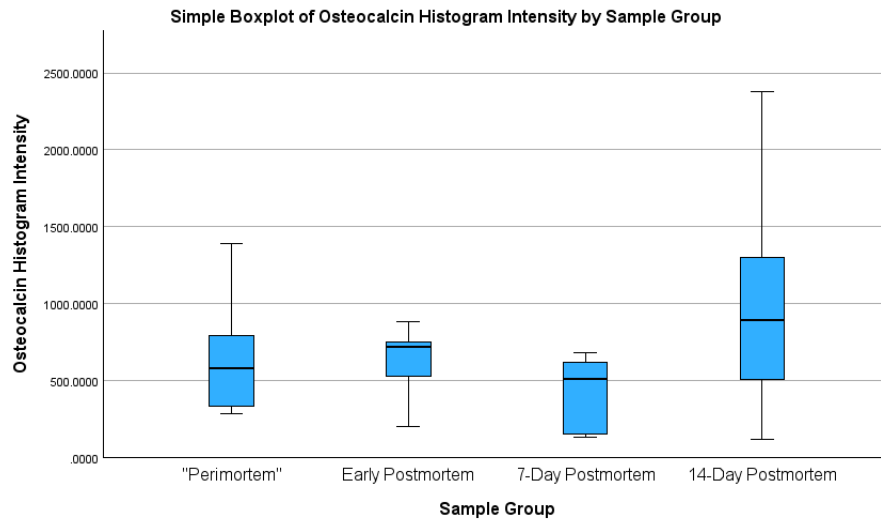


**Figure 3.2.18: Osteocalcin mean intensity with individual outliers removed.**

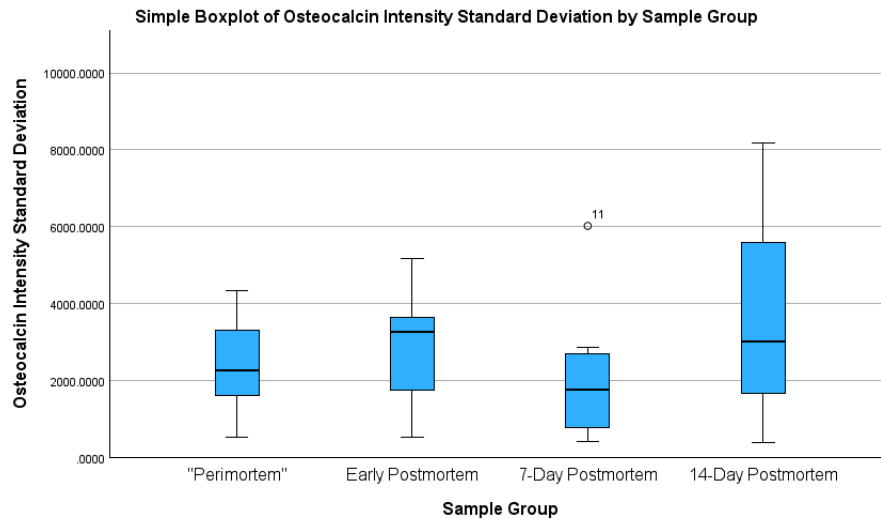


**Figure 3.2.19: Osteocalcin standard deviation with individual outliers removed.**

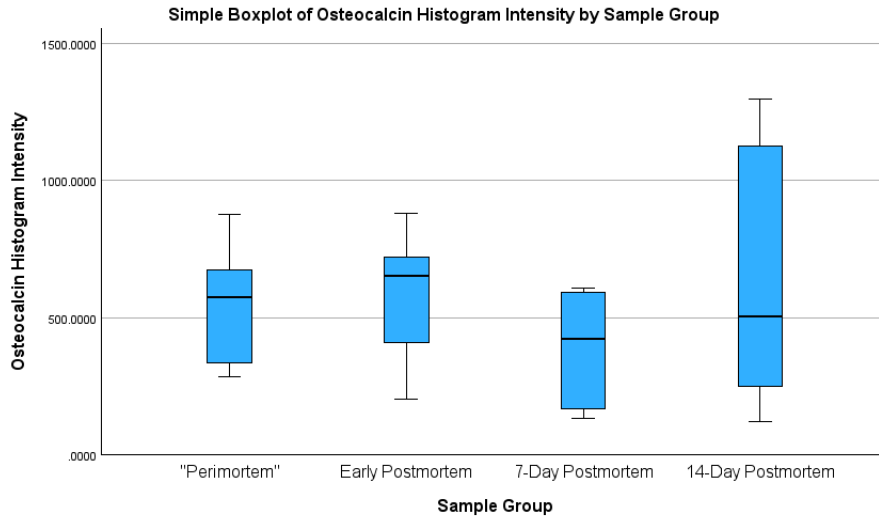


**Figure 3.2.20: Osteocalcin mean intensity with whole individuals removed.**

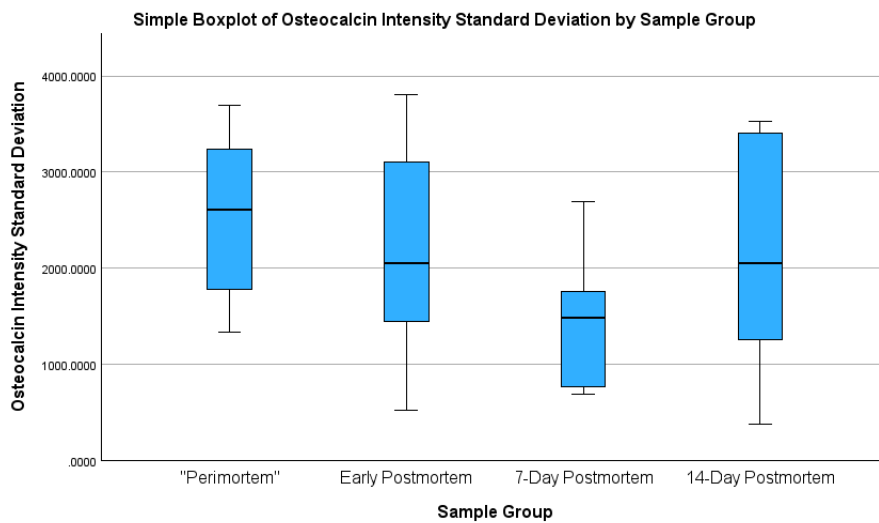


**Figure 3.2.21: Osteocalcin standard deviations with whole individuals removed.**

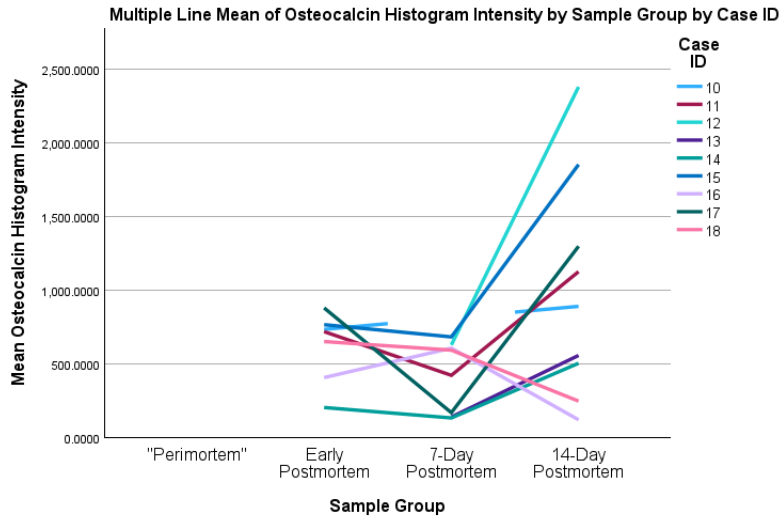


**Figure 3.2.22: Postmortem osteocalcin mean intensity fluctuations with individual outliers removed.**

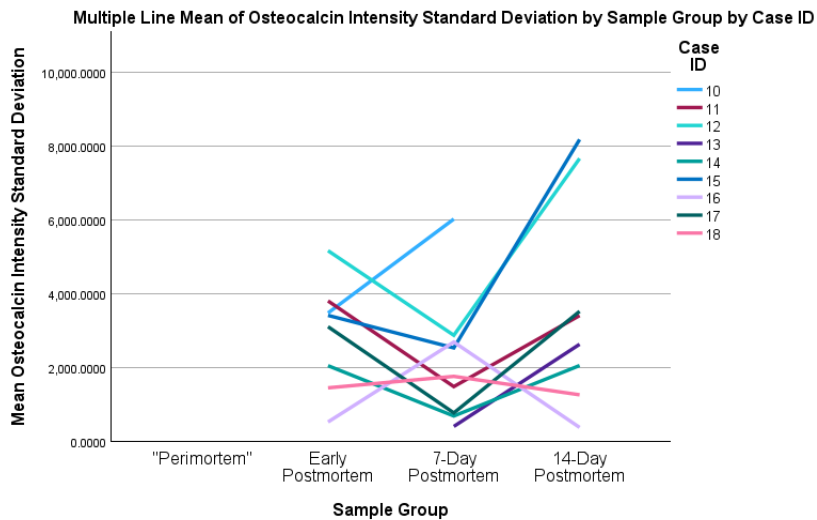


**Figure 3.2.23: Postmortem osteocalcin standard deviation fluctuations with individual outliers removed.**

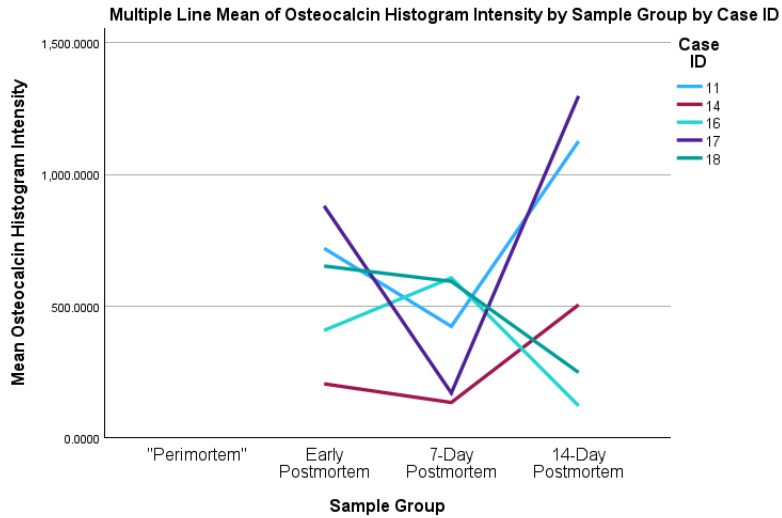


**Figure 3.2.24: Postmortem osteocalcin mean intensity fluctuations with whole individuals removed.**

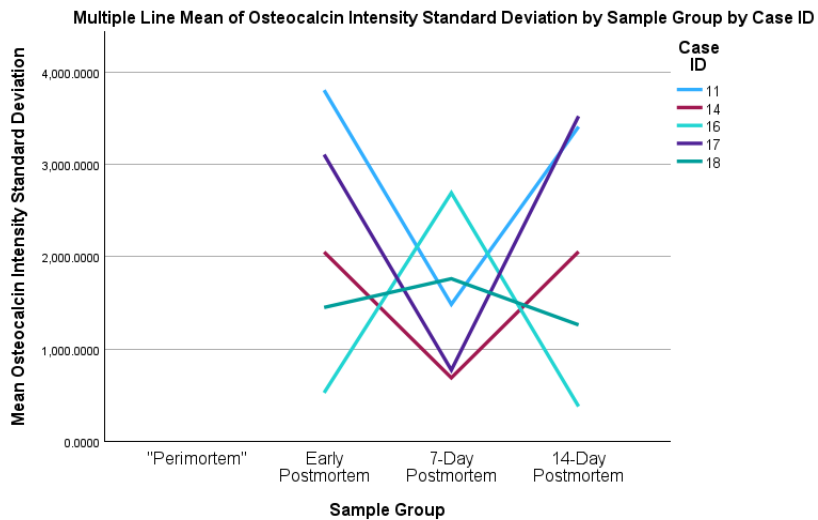


**Figure 3.2.25: Postmortem osteocalcin standard deviation fluctuations with whole individuals removed.**

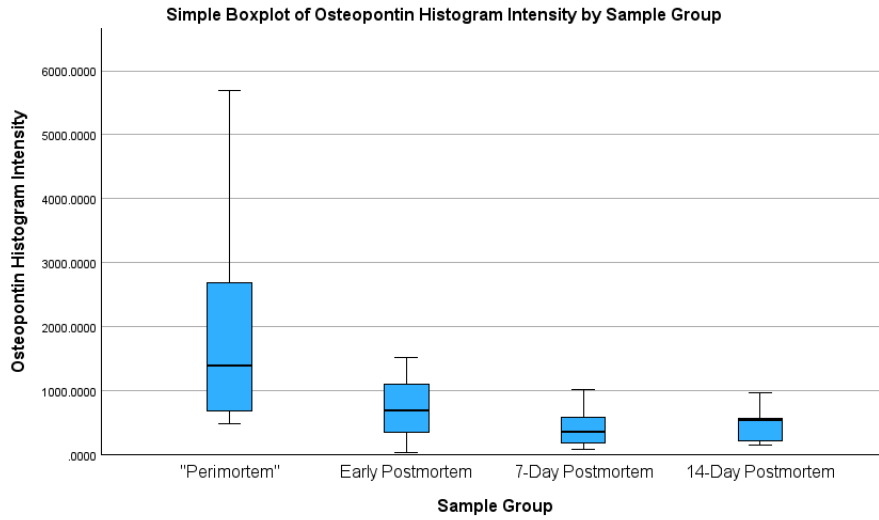


**Figure 3.2.26: Osteopontin mean intensity with individual outliers removed.**

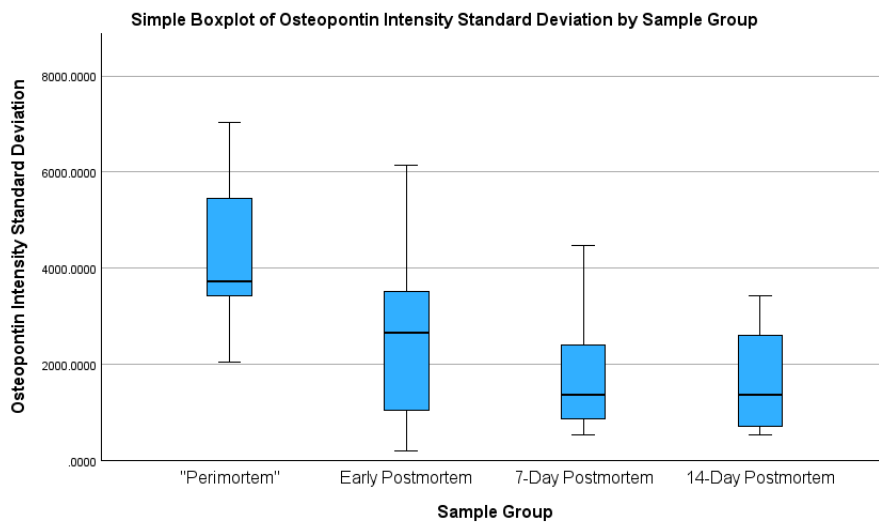


**Figure 3.2.27: Osteopontin standard deviations with individual outliers removed.**

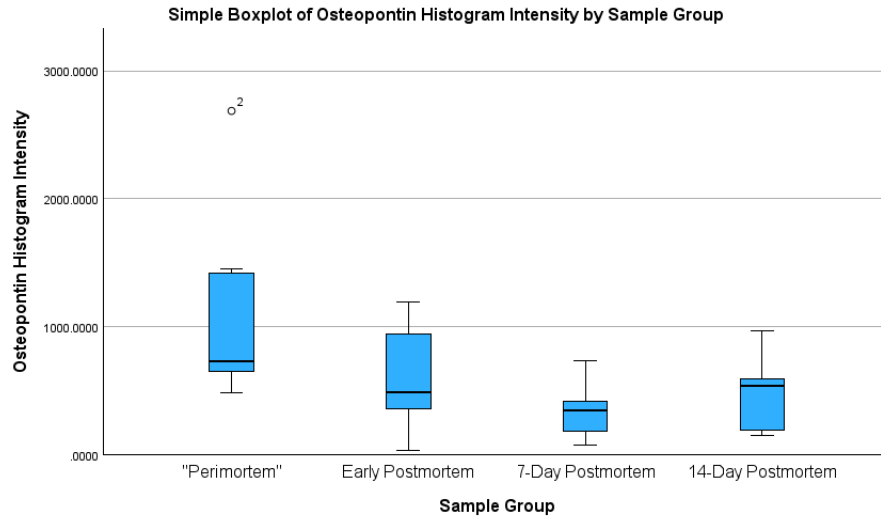


**Figure 3.2.28: Osteopontin mean intensity with whole individuals removed.**

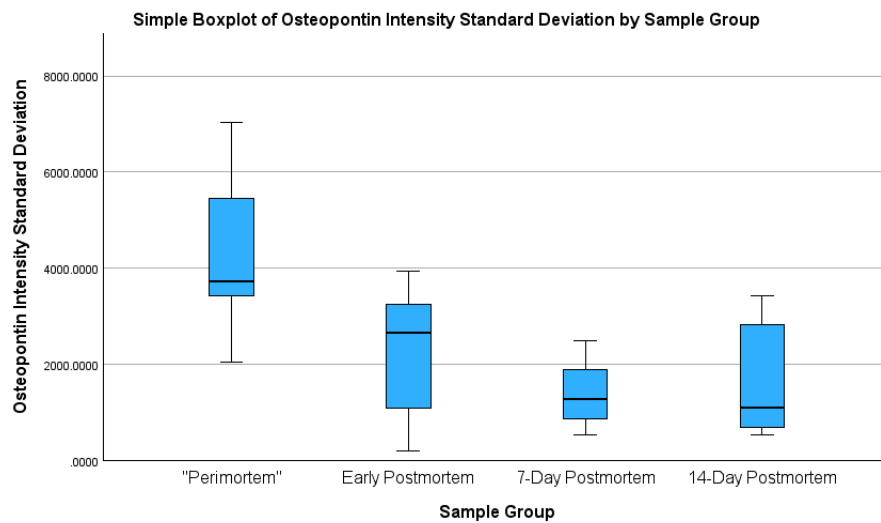


**Figure 3.2.29: Osteopontin standard deviations with whole individuals removed.**

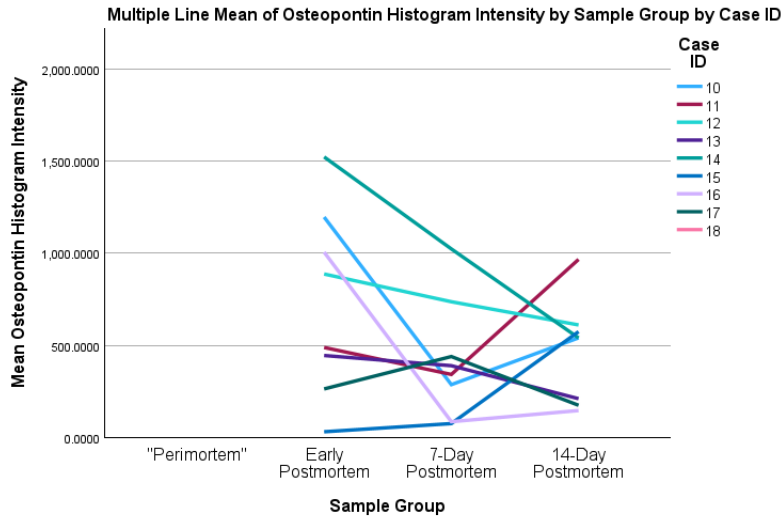


**Figure 3.2.30: Postmortem osteopontin mean intensity fluctuations with individual outliers removed.**

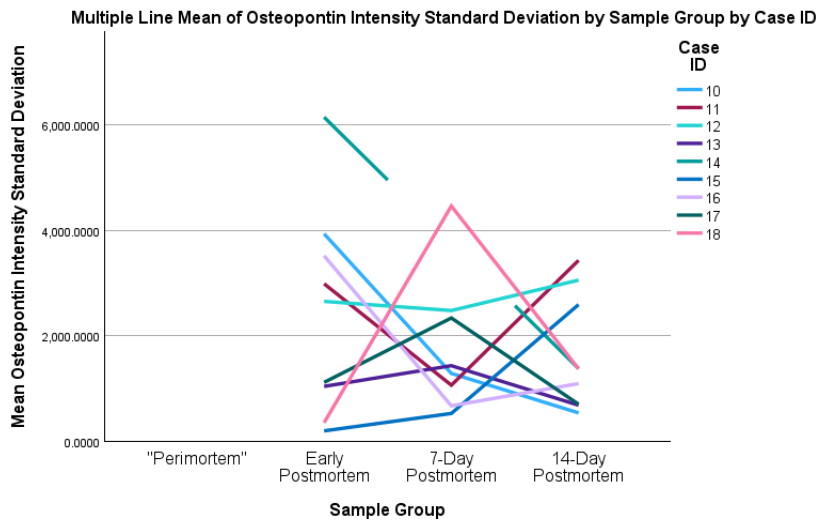


**Figure 3.2.31: Postmortem osteopontin standard deviation fluctuations with individual outliers removed.**

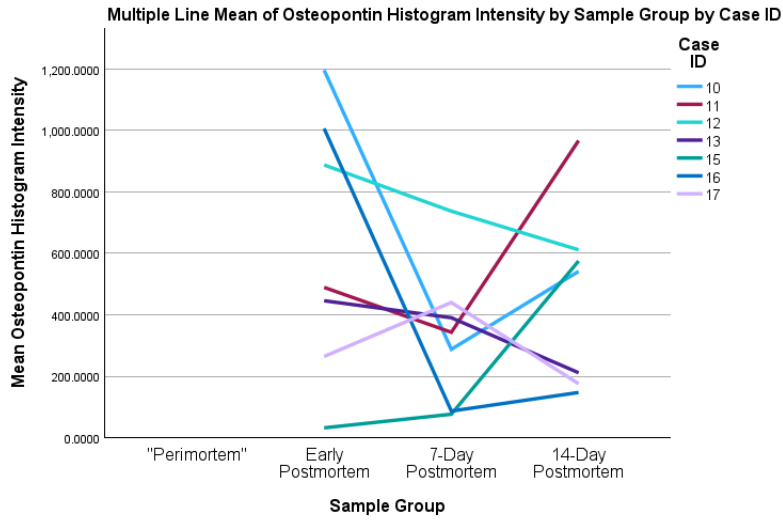


**Figure 3.2.32: Postmortem osteopontin mean intensity fluctuations with whole individuals removed.**

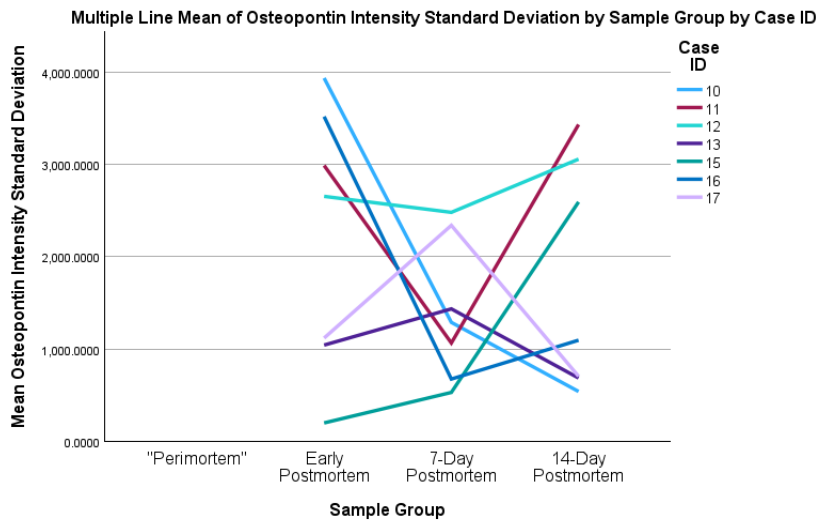


**Figure 3.2.33: Postmortem osteopontin standard deviation fluctuations with whole individuals removed.**

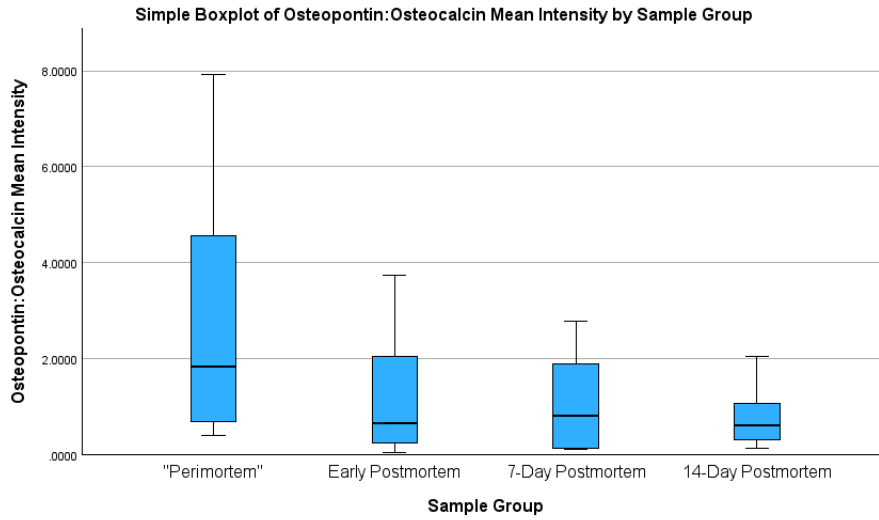


**Figure 3.234: OPN:OC mean intensity with individual outliers removed.**

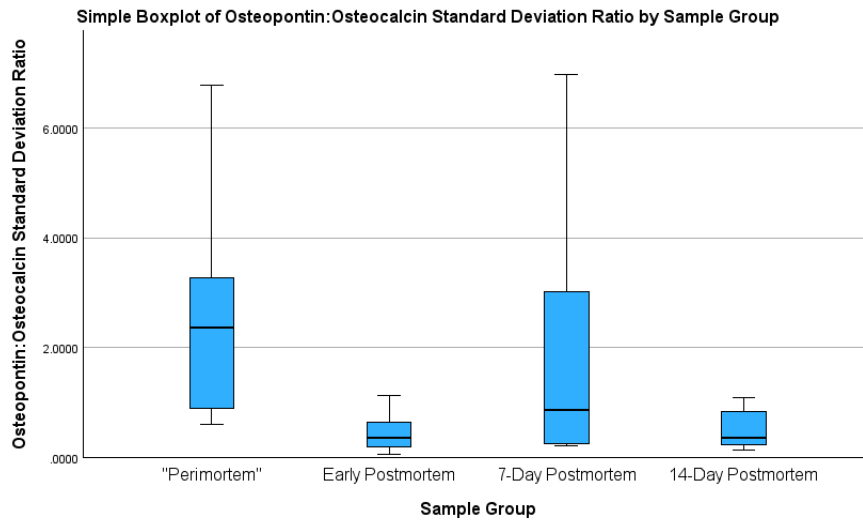


**Figure 3.235: OPN:OC standard deviations with individual outliers removed.**

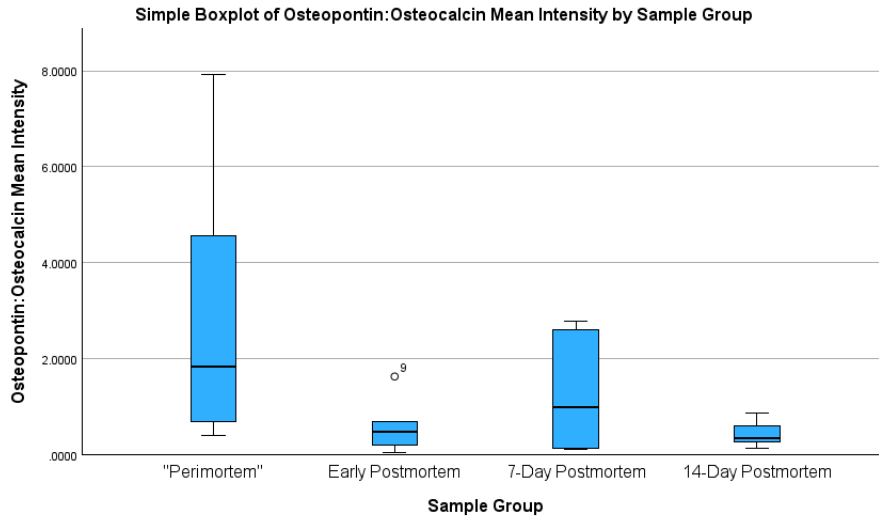


**Figure 3.2.36: OPN:OC mean intensity with whole individuals removed.**

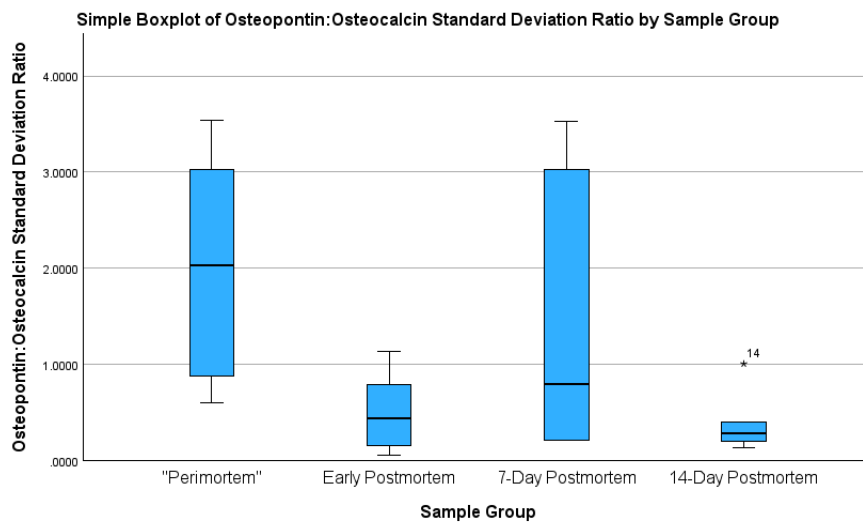


**Figure 3.2.37: OPN:OC standard deviations with whole individuals removed.**

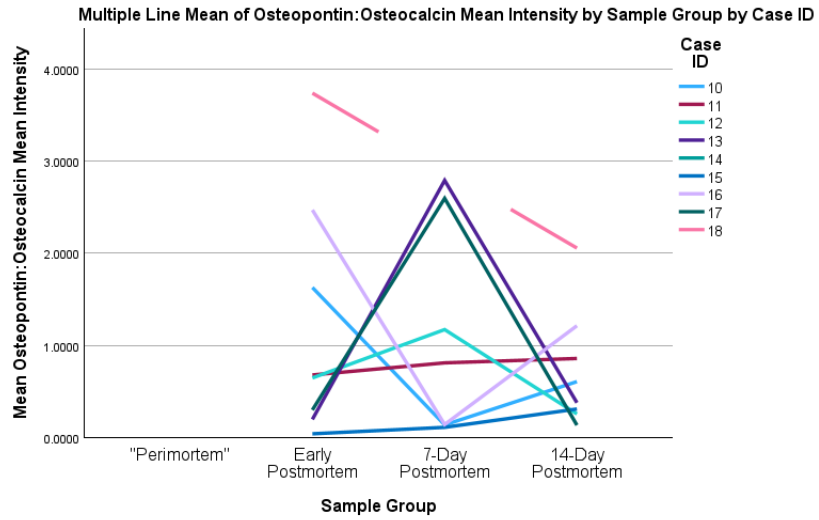


**Figure 3.2.38: Postmortem OPN:OC mean intensity fluctuations with individual outliers removed.**

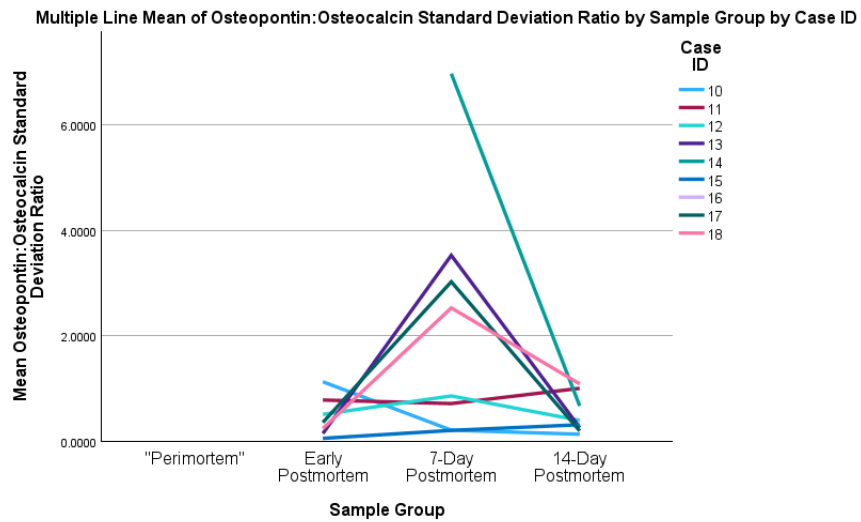


**Figure 3.2.39: Postmortem OPN:OC standard deviation fluctuations with individual outliers removed.**

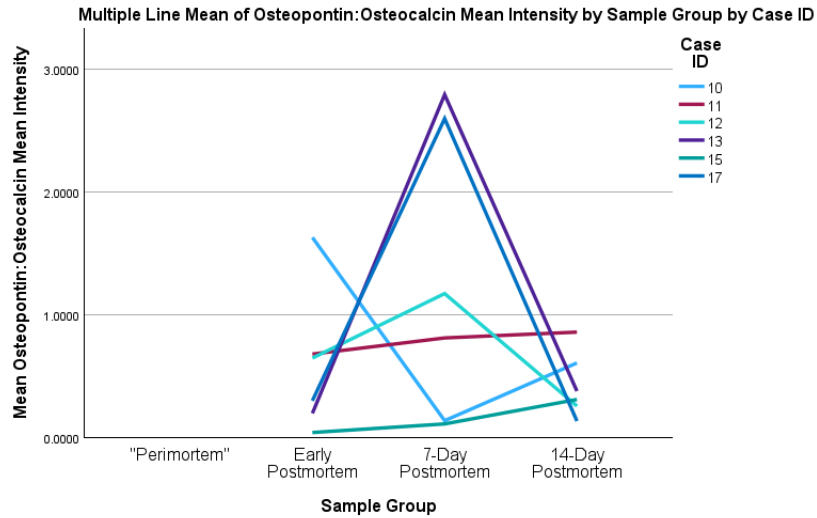


**Figure 3.2.40: Postmortem OPN:OC mean intensity fluctuations with whole individuals removed.**

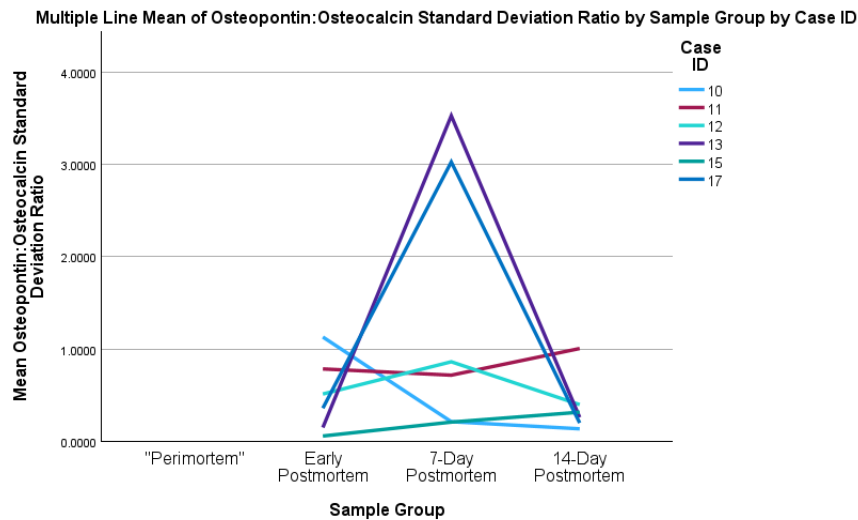


**Figure 3.2.41: Postmortem OPN:OC standard deviation fluctuations with whole individuals removed.**

**Table 3.2-4: Post Hoc Pairwise results for Kruskal-Wallis H-tests with both individual outliers removed and whole individuals removed.**

Test	Sample 1-Sample 2	Test Statistic	Std. Error	Std. Test Statistic	Sig.	Adj. Sig. <sup>a</sup>
Osteocalcin Mean Intensity Individual Outliers Removed	7-Day Postmortem-"Perimortem"	3.875	4.690	0.826	0.409	1.000
	7-Day Postmortem-Early Postmortem	7.893	4.855	1.626	0.104	0.624

Test	Sample 1-Sample 2	Test Statistic	Std. Error	Std. Test Statistic	Sig.	Adj. Sig. <sup>a</sup>
	7-Day Postmortem-14-Day Postmortem	-9.083	4.558	-1.993	0.046	0.278
	"Perimortem"-Early Postmortem	-4.018	4.855	-0.828	0.408	1.000
	"Perimortem"-14-Day Postmortem	-5.208	4.558	-1.143	0.253	1.000
	Early Postmortem-14-Day Postmortem	-1.190	4.727	-0.252	0.801	1.000
Osteocalcin Standard Deviation Individual Outliers Removed	7-Day Postmortem-"Perimortem"	5.667	4.694	1.207	0.227	1.000
	7-Day Postmortem-Early Postmortem	6.611	4.839	1.366	0.172	1.000
	7-Day Postmortem-14-Day Postmortem	-6.611	4.839	-1.366	0.172	1.000
	"Perimortem"-Early Postmortem	-0.944	4.839	-0.195	0.845	1.000
	"Perimortem"-14-Day Postmortem	-0.944	4.839	-0.195	0.845	1.000
	Early Postmortem-14-Day Postmortem	0.000	4.979	0.000	1.000	1.000
	Osteocalcin Mean Intensity Whole Individuals Removed	7-Day Postmortem-14-Day Postmortem	-4.000	4.290	-0.933	0.351
7-Day Postmortem-"Perimortem"		4.350	3.867	1.125	0.261	1.000
7-Day Postmortem-Early Postmortem		5.600	4.290	1.306	0.192	1.000
14-Day Postmortem-"Perimortem"		0.350	3.867	0.091	0.928	1.000
14-Day Postmortem-Early Postmortem		1.600	4.290	0.373	0.709	1.000
"Perimortem"-Early Postmortem		-1.250	3.867	-0.323	0.746	1.000
Osteocalcin Standard Deviations Whole Individuals Removed	7-Day Postmortem-14-Day Postmortem	-4.000	4.290	-0.933	0.351	1.000
	7-Day Postmortem-Early Postmortem	4.200	4.290	0.979	0.328	1.000
	7-Day Postmortem-"Perimortem"	6.375	3.867	1.649	0.099	0.595

Test	Sample 1-Sample 2	Test Statistic	Std. Error	Std. Test Statistic	Sig.	Adj. Sig. <sup>a</sup>
	14-Day Postmortem-Early Postmortem	0.200	4.290	0.047	0.963	1.000
	14-Day Postmortem-"Perimortem"	2.375	3.867	0.614	0.539	1.000
	Early Postmortem-"Perimortem"	2.175	3.867	0.563	0.574	1.000
Osteopontin Mean Intensity Individual Outliers Removed	7-Day Postmortem-14-Day Postmortem	-2.264	4.839	-0.468	0.640	1.000
	7-Day Postmortem-Early Postmortem	6.250	4.979	1.255	0.209	1.000
	7-Day Postmortem-"Perimortem"	14.375	4.839	2.971	0.003	0.018
	14-Day Postmortem-Early Postmortem	3.986	4.839	0.824	0.410	1.000
	14-Day Postmortem-"Perimortem"	12.111	4.694	2.580	0.010	0.059
	Early Postmortem-"Perimortem"	8.125	4.839	1.679	0.093	0.559
Osteopontin Standard Deviation Individual Outliers Removed	14-Day Postmortem-7-Day Postmortem	0.278	4.699	0.059	0.953	1.000
	14-Day Postmortem-Early Postmortem	3.222	4.558	0.707	0.480	1.000
	14-Day Postmortem-"Perimortem"	13.349	4.873	2.739	0.006	0.037
	7-Day Postmortem-Early Postmortem	2.944	4.699	0.627	0.531	1.000
	7-Day Postmortem-"Perimortem"	13.071	5.004	2.612	0.009	0.054
	Early Postmortem-"Perimortem"	10.127	4.873	2.078	0.038	0.226
Osteopontin Mean Intensity Whole Individuals Removed	7-Day Postmortem-14-Day Postmortem	-3.143	4.397	-0.715	0.475	1.000
	7-Day Postmortem-Early Postmortem	5.857	4.397	1.332	0.183	1.000

Test	Sample 1-Sample 2	Test Statistic	Std. Error	Std. Test Statistic	Sig.	Adj. Sig. <sup>a</sup>	
	7-Day Postmortem- "Perimortem"	12.429	4.397	2.827	0.005	0.028	
	14-Day Postmortem-Early Postmortem	2.714	4.397	0.617	0.537	1.000	
	14-Day Postmortem- "Perimortem"	9.286	4.397	2.112	0.035	0.208	
	Early Postmortem- "Perimortem"	6.571	4.397	1.495	0.135	0.810	
Osteopontin Standard Deviations Whole Individuals Removed	7-Day Postmortem- 14-Day Postmortem	-1.857	4.397	-0.422	0.673	1.000	
	7-Day Postmortem- Early Postmortem	4.857	4.397	1.105	0.269	1.000	
	7-Day Postmortem- "Perimortem"	13.571	4.397	3.087	0.002	0.012	
	14-Day Postmortem-Early Postmortem	3.000	4.397	0.682	0.495	1.000	
	14-Day Postmortem- "Perimortem"	11.714	4.397	2.664	0.008	0.046	
	Early Postmortem- "Perimortem"	8.714	4.397	1.982	0.047	0.285	
OPN:OC Mean Intensity Individual Outliers Removed	14-Day Postmortem-7-Day Postmortem	0.794	4.727	0.168	0.867	1.000	
	14-Day Postmortem-Early Postmortem	1.347	4.558	0.296	0.768	1.000	
	14-Day Postmortem- "Perimortem"	8.847	4.558	1.941	0.052	0.314	
	7-Day Postmortem- Early Postmortem	0.554	4.855	0.114	0.909	1.000	
	7-Day Postmortem- "Perimortem"	8.054	4.855	1.659	0.097	0.583	
	Early Postmortem- "Perimortem"	7.500	4.690	1.599	0.110	0.659	
	OPN:OC Standard Deviation	Early Postmortem- 14-Day Postmortem	-1.161	5.004	-0.232	0.817	1.000

Test	Sample 1-Sample 2	Test Statistic	Std. Error	Std. Test Statistic	Sig.	Adj. Sig. <sup>a</sup>
Individual Outliers Removed	Early Postmortem-7-Day Postmortem	-8.286	4.873	-1.700	0.089	0.534
	Early Postmortem-"Perimortem"	13.730	4.873	2.818	0.005	0.029
	14-Day Postmortem-7-Day Postmortem	7.125	4.699	1.516	0.129	0.776
	14-Day Postmortem-"Perimortem"	12.569	4.699	2.675	0.007	0.045
	7-Day Postmortem-"Perimortem"	5.444	4.558	1.194	0.232	1.000
OPN:OC Mean Intensity Whole Individuals Removed	14-Day Postmortem-Early Postmortem	0.833	4.416	0.189	0.850	1.000
	14-Day Postmortem-7-Day Postmortem	5.000	4.416	1.132	0.258	1.000
	14-Day Postmortem-"Perimortem"	10.250	4.131	2.481	0.013	0.079
	Early Postmortem-7-Day Postmortem	-4.167	4.416	-0.944	0.345	1.000
	Early Postmortem-"Perimortem"	9.417	4.131	2.280	0.023	0.136
	7-Day Postmortem-"Perimortem"	5.250	4.131	1.271	0.204	1.000
	14-Day Postmortem-Early Postmortem	1.333	4.416	0.302	0.763	1.000
OPN:OC Standard Deviations Whole Individuals Removed	14-Day Postmortem-7-Day Postmortem	6.500	4.416	1.472	0.141	0.846
	14-Day Postmortem-"Perimortem"	11.458	4.131	2.774	0.006	0.033
	Early Postmortem-7-Day Postmortem	-5.167	4.416	-1.170	0.242	1.000
	Early Postmortem-"Perimortem"	10.125	4.131	2.451	0.014	0.085
	7-Day Postmortem-"Perimortem"	4.958	4.131	1.200	0.230	1.000

Test	Sample 1-Sample 2	Test Statistic	Std. Error	Std. Test Statistic	Sig.	Adj. Sig. <sup>a</sup>
------	-------------------	----------------	------------	---------------------	------	------------------------

Each row tests the null hypothesis that the Sample 1 and Sample 2 distributions are the same. Asymptotic significances (2-sided tests) are displayed. The significance level is .050.

<sup>a</sup>. Significance values have been adjusted by the Bonferroni correction for multiple tests.

### 3.2.4 Discussion and Conclusion

The overall results of this study indicate that the use of protein degradation in bone may be a viable mode of calculating the early postmortem interval in skeletal remains (within 14-days postmortem), but its usability and reliability is rather complicated. The best variable for this purpose would be degradation of osteopontin, which exhibited a negative correlation with time, resulting in generally lower OPN fluorescence as time progressed. However, an analysis of the post hoc results, both with and without the outliers, indicates that the only significant difference is between the later time groups (7-day and 14-day postmortem) and the perimortem. There was no significant degradation between the postmortem groups. This suggests that a degradation occurs, but that some time must pass before that degradation becomes significant. Additionally, it cannot be ignored that when examining the individual fluctuations of the postmortem groups using the line graphs, there was no real pattern, suggesting that individualizing factors may be at play as well. This individualization becomes even grater with the osteocalcin studies which lack significant variance in pixel intensity and no correlation with pixel intensity over time. While this suggests that the amount of osteocalcin in the bone is stable, the range within each time group, suggests that pixel intensity is highly dependent on the individual. However, with a larger sample size, it is possible that with the wide variations between time groups would even out and demonstrate the same stability that is found in archaeological literature (102-105).

However, in addition to the base osteopontin and osteocalcin studies, the results of a study of the ratio between OPN:OC mean intensity and standard deviation indicates that protein fluorescence intensity would not be a good marker for assessing the postmortem interval. When examining the results both with and without the outliers, there does not appear to be any real significant results save for in some of the pairwise post hoc tests (see Table 3.2-3 and 3.2-4). Despite there being no real significant differences between each group, when examining the box plot of the mean intensity with individual outliers removed, there does appear to be a superficial degradation as time progresses. Further, the range of intensity found within each group

decreases as well. That said, this is the only area in which a pattern appears present. Of greater interest is that, outside of the mean intensity with individual outliers removed, there is a universal pattern of a decrease between the perimortem and early-postmortem, a sharp increase from early-postmortem to 7-day postmortem, and then a sharp decline from 7-day postmortem to 14-day postmortem. When examining factors to account for this pattern, the obvious is that it mirrors that of the osteocalcin, suggesting that the pattern of OPN:OC is being driven by the OC changes. If a larger sample size levels-out the fluctuations in osteocalcin ranges, it is possible that the OPN:OC may follow a similar track.

When comparing the samples based on sex there was no significant difference in either the osteopontin or the osteocalcin with regards to mean pixel intensity or pixel standard deviation. Even when controlling for sex using a 1:1 perimortem/postmortem cohort (all males, 5 perimortem and 5 postmortem), with the outliers removed from consideration, similar results are obtained using the Kruskal-Wallis H-test demonstrating no significant difference. The results of the osteocalcin K-W H-test were  $p=0.722$  ( $H=1.331$ ;  $\eta^2=0.104$ ) for the mean intensity and  $p=0.589$  ( $H=1.880$ ;  $\eta^2=0.07$ ) for the standard deviation. The osteopontin results did demonstrate a significant difference when controlling for sex with results reflecting that of the K-W H-tests when assessing for time groups. The osteopontin results were  $p=0.036$  ( $H=8.531$ ;  $\eta^2=0.346$ ) for the mean intensity and  $p=0.015$  ( $H=10.451$ ;  $\eta^2=0.466$ ).

Similarly, age at death, broken down into lustrums did not have a significant variance with osteopontin or osteocalcin. When combined, this suggests that factors such as sex and age, as well as other physiological factors related to the individual may not play a major role in the base protein fluorescence intensity with this sample. That said, further research is necessary due to the relatively small sample size, the unequal representation of sexes (males to females 3.5:1) coupled with the unequal distribution of sexes between the sample groups (perimortem all male, postmortem 5 male to 4 female), and the age disparity between the groups with the perimortem group being younger in comparison to the postmortem group.

One area of concern regarding the imaging of the protein fluorescence is in the area of artifact identification. Artifacts, such as those created through embedding, staining, labeling, mounting, and even imaging itself are an inevitable part of anatomical histology. This project,

like that of the field of histology, attempted to limit such artifacts. The question remains, however, as to what impact they may have on the results.

With regards to this study, a dimension for examination of artifacts is the temporal declination of the objects being fluoresced. For the osteocalcin samples, this is problematic in origin in that there is no temporal decrease; a phenomenon mirrored by existing literature (103, 105). Osteopontin, in this study on the other hand, does show a temporal declination, however slight, even when the outliers are removed. With the outliers included, the arithmetic mean of the four time groups declines over time with a 2.4% decrease from the perimortem to the early-postmortem, an expanded decline of an additional 60.3% moving to the 7-day postmortem, with an additional 43.1% decline at the 14-day postmortem group. With this study, the samples were prepped, embedded, cut, and labeled in such a manner that allowed for overlap of the various time groups (i.e., 14-day sample of one individual may have been processed at the exact same time as the 7-day of another, and the early-postmortem of yet another), thus preventing a systematic presence of artifacts. If an artifact had been created during this process it would have affected multiple slices that would have impacted the data randomly, not systematically. If artifacts were being counted in such a way that would have an impact on the results of this study, then no temporal declination would be seen. Further, if there is a limited impact of artifacts on the osteopontin slides, then one can infer that a similar impact would be also be seen on the osteocalcin, as both were prepared simultaneously.

However, there is an issue with this particular study. While OPN degradation was seen, there was also a number of outliers that had to be removed from the sample groups. Two methods for outlier removal could be used based on the theoretical cause of the outliers. If the cause was artifactual by nature, then it should be limited to a single group (i.e., Individual X OPN mean intensity 7-day postmortem only). If the cause was more biological, then that outlier would be seen across a number of groups. In this study a mix was seen, hence both methodologies of treating outliers was utilized. With regard to artifacts, however, this is suggestive that artifacts did have some effect on the results of this study, but exactly what that effect was is difficult to ascertain. Specifically, when examining the osteopontin mean intensity K-W H-test results, the significance  $\alpha$  decreases as outliers are removed (from  $p=0.035$  to  $p=0.015$ ) suggesting that the artifacts may be having a masking effect. This is further supported by the fact that of the four osteopontin outliers, all were of a higher value than the mean, rather

than any being lower. Further, it should be noted that the osteocalcin sample exhibited more outliers than osteopontin. These were seen more across multiple time groups, hinting at a biological origin, but artifacts cannot be ruled out. Given the irregular pattern of the osteocalcin mean intensity and standard deviation, it is possible that artifacts are a contributing factor. Since it appears that artifacts may be playing a sort of masking role with osteopontin, it may also be so with osteocalcin. Since the samples for osteocalcin were prepared at the same time as the osteopontin, the presence of artifacts may be the cause of the fluctuations between the sample groups, masking an otherwise true pattern. If artifacts could be isolated and removed from the imaging, in both the osteopontin and osteocalcin sample, it may hold true that mean pixel intensity significantly decreases over time with osteopontin, and osteocalcin will appear steady.

One must also consider that even though there was a declination seen, however slight, there was no real discernible pattern. While a majority of the samples did follow a projected path of declination, even when examining the postmortem line graphs (see Fig 3.2.11, 3.2.30, & 3.2.32) a few did not. This few were enough to demonstrate that no real pattern exists. However, the cause for this lack of patterning is unknown. While it is possible that it could be a biological phenomenon, the more probable cause is artifacts are at play with these samples. However, these particular samples were not of sufficient strength to warrant being labelled an “outlier” and thus were retained within the study.

In addition to the presence of artifacts, one must also take into account the effect depth, or light penetration depth, with regards to the present study. While an effective sample effect depth is between 100 $\mu$ m -200 $\mu$ m, the difference in sample thickness between the perimortem [CHUM] samples and the postmortem [UofT] samples cannot be ignored. In this study, the perimortem samples were thin-sectioned to 15 $\mu$ m while the postmortem were at 100 $\mu$ m (at the lower range for maximum effect depth). This issue was mitigated somewhat by only imaging  $\approx$ 12.75 $\mu$ m along the  $z$ -axis on all samples. However, light is diffused throughout the entire sample, and therefore thinner sections would allow for a greater amount of light to pass through. While the  $z$ -axis depth was standardized, the laser and imaging levels (power, gain, offset, etc.) were adjusted for each individual sample to maximize data quality and limit image capture saturation, it is possible that the variation of fluorescence intensity was due to the perimortem [CHUM] samples being thinner to begin with. That said, the image capture settings were adjusted in a manner which would have limited capture saturation which would have been more present in the thinner

perimortem samples, and the fact that the range for the perimortem samples for all tests (OPN and OC mean intensity and standard deviation) overlapped with the early-postmortem group, which was thicker, suggests that the effect depth effect may be minimal.

The assessment of PMI for remains that are partially to completely skeletonized, during the early postmortem interval, is particularly challenging. The soft tissue may have degraded to a point that analyses of the tissue becomes obsolete and the taphonomic processes affecting bone may not have begun in earnest. The results of this study indicate that histochemical analyses may theoretically assist with establishing a more accurate postmortem interval. To transform the current study into a viable methodology for estimating PMI, more research is needed to establish several factors including, establishing baseline osteopontin level pixel intensity levels in living populations while incorporating the variation across demographics and bone element type, all while limiting the impact of artifacts. Further, research should be conducted into the relationship of pathologies on osteocalcin and osteopontin on base fluorescence as well. That said, there are several potential confounding variables related to the overall assessment of PMI that may impact this method. As this method was conducted in a controlled environment, issues such as external temperature and humidity, which are a major factor in soft tissue decomposition, may prove to be a variable in the decomposition of osteopontin and osteocalcin as well. Additionally, similar to humidity, the effects of moisture on the bone, known to alter the rate of soft tissue decomposition, may also have an effect on the bone proteins. Lastly, while this study was conducted with the bones excised from the body, which would mimic compound fractures that break the skin, it is unknown exactly what effect exposure to air has on the overall decomposition of these proteins.

One significant limitation to this study is the relatively small number of individuals, and therefore samples, used. As a result, a power and eta-squared ( $\eta^2$ ) and Cliff's  $\delta$  effect size analyses were conducted for the osteocalcin and osteopontin mean intensity and image standard deviations, as well as the ratio between OPN:OC. The results of those analyses were conflicting in that the osteocalcin results demonstrated a small power and  $\eta^2$  effect size while the osteopontin results demonstrated a high power and  $\eta^2$  effect size. This suggests that while there was very little variation in the osteocalcin, there was also a small chance for obtaining a "true" result. Conversely, for the osteopontin there was a large power and  $\eta^2$  effect size suggesting that there is a greater chance of obtain a "true" result.

With all of that said, this study was able to determine some significant results with limitations and caveats, and while more research is needed, has shown to be a potentially viable start to the use of protein degradation in the assessment of the postmortem interval in the early period of skeletonization when other, more established PMI methods are not viable. However, while protein degradation does have some potential, use of the laser scanning confocal microscope in assessing those levels should be limited until a better understanding is found between the relationship of protein fluorescence and quantification.

# Chapter 4

## Osteocellular Degradation: Its Use in Calculating the Early Postmortem Interval

### 4.1 Chapter Introduction

Chapter 4 addresses the issue of postmortem interval timing, though, where Chapter 3 utilized protein degradation as a means of assessing the postmortem interval, Chapter 4 uses the decrease of bone cells. Chapter 4 consists of a potential journal article, “Cellular degradation in bone as a tool to investigate the postmortem interval” by Ashley C. Smith and Tracy Rogers and will be submitted to *Forensic Anthropology* in late 2025. For this particular manuscript, Ashley C. Smith served as the primary researcher and author while Tracy Rogers edited the manuscript and was the research supervisor.

The following manuscript examined the postmortem degradation of osteoclasts in samples over various time frames, similar to Ch. 3.2. One of the more difficult aspects of a forensic investigation is the assessment of the postmortem interval. This becomes particularly difficult after the mortis triad (rigor, livor, and algor) window of 72 hours, as the loss of the triad of reliable markers means that accuracy and precision in the PMI estimate increases the further away (temporally) from somatic death one gets. The following manuscript examined the use of osteoclasts and their successive decrease over time as a potential tool for examining the postmortem interval. While this thesis aims to use both Ch. 3 and Ch. 4 as collective tools, operating under the forensic axiom that preferences utilization of multiple methodologies, Ch. 4, like Ch. 3, is presented independently. That said, it should be noted that the individuals used in Ch. 3 are the exact same individuals used in Ch. 4, therefore Individual #, age, sex, etc. are identical, only the methodology and what is being examined has varied.

In order to best understand the nature of osteoclast presence and abundance, and their potential use as a means of assessing the postmortem interval, Ch. 4.2 discusses several areas of knowledge including the current understanding of the decompositional process, methods for assessing the postmortem interval, and the derivation & differentiation, functionality, and apoptosis of osteoclasts. Specifically, with regards to osteoclasts themselves, this manuscript focuses on the process by which osteoclasts engage in the resorptive process, how they form and

differentiate from embryonic cells, how they develop and function with regards to fracture repair, and their ultimate death at the end of the resorptive process.

For the study portion, the following manuscript used their presence within an iliac sample, and through a serial repeated measure, compared against an independent perimortem group derived from biopsy samples, and assessed its potential usefulness in establishing the postmortem interval. The two main sample groups were a perimortem group made up of surgically removed biopsy samples gathered from CHUM, and a postmortem group obtained from the Division of Anatomy from the University of Toronto, derived from cadaveric remains and collected approximately 24-hours postmortem. A series of postmortem sections were obtained from the U of T individuals, fixed at set times following the cardio-pulmonary death of the individual with the 1<sup>st</sup> section fixed upon receipt of the remains (<48 hours postmortem), the 2<sup>nd</sup> at the 7-day mark following cardio-pulmonary death (regardless of the time of receipt of the individuals), and at the 14-day mark post cardio-pulmonary death (again regardless of the time of receipt). After fixation, thin-sectioning, labeling, and imaging, analyses were conducted to assess for the number of osteoclasts present in each sample. The number of osteoclasts present was standardized by bone volume using the formula as outlined by Parfitt *et al.* (198). A series of statistical analyses were run including a Kruskal-Wallis H-test, Spearman Rho correlation test, Friedman repeated measure test (on the postmortem samples only), and these were followed up with a Kernel Ridge Regression analysis to determine if there was an element of predictability to the results. Additionally, as outliers were present, these were removed in two different fashions with the tests re-run and the results presented. It was hypothesized that there would be a marked and significant decline in the abundance of osteoclasts as the time groups progressed.

## 4.2 Cellular degradation and migration in bone as a tool to investigate the postmortem interval

### 4.2.1 Introduction

One of the more difficult analyses forensic anthropologists and pathologists are tasked with is the assessment of the postmortem interval (PMI). This analysis is vital for the accurate reconstruction of the events surrounding the death of an individual, and the administration of justice should criminal actions be raised. A common challenge posed by defense counsel is to question the time of death. By posing if a later or earlier postmortem interval is more accurate, counsel can then raise the culpability of their client, suggesting potential alibies for the now contested postmortem interval. This challenge to the postmortem interval estimate arises because of the issue that as time progresses postmortem from somatic death, the less precise the estimation becomes. Current methods in forensic anthropology and pathology PMI estimation begins with a trinity of assessments based on blood settling (livor mortis), contraction and subsequent relaxation of muscles (rigor mortis), and the fluctuation of the body temperature to equilibrium with ambient temperatures (algor mortis). Combined this is the known as the mortis triad and is accurate within a 72 hour window. However, after this window, the estimation of PMI shifts to an examination on a degree of soft tissue decomposition, which decreases in precision as time progresses postmortem. The purpose of the following study was to assess if the quantification of osteoclasts and their degradation over a 14-day postmortem period would hold potential as a tool for assessing the postmortem interval within that time period.

#### 4.2.1.1 Decomposition

When an individual dies, their remains undergoes a process known as decomposition. By understanding the process of decomposition, one can develop an estimate of the postmortem interval. However, as the process progresses, the precision of that estimate decreases as the timing to attain selected benchmarks, such as transitional decompositional stages, or to achieve various total body scores in relation to accumulated degree days *sensu* Megyesi *et al.* (11) and Moffatt *et al.* (12) widens.

Decomposition is a dual-phase process that occurs both intrinsically and extrinsically. Intrinsic decomposition occurs mainly at a cellular level and eventually extends into the

extrinsic, which can be seen in the external soft-tissues and ultimately as exposed and weathered bone (15, 106-113). Decomposition can be broken down into various stages based on degree, and while the basic categories of decomposition are addressed in the literature, these stages are not precise and have both overlapping and/or differing names for various sequences [see Ch. 1.2.6.1; Table 1.2-1] (11, 114, 116, 117, 129). In general, decomposition progresses as follows: fresh (intrinsic/autolysis), bloat, early decay, advanced decay, and finally skeletonization/mummification (112, 114-117).

Given that the present study is examining the degradation of the cells (e.g. osteoclasts) as a potential tool for assessing the postmortem interval, and that the parameters of this study is examining within the first 14 days postmortem, the only stages of import are the "fresh" and "bloat/early decay."

#### 4.2.1.1.1 Fresh

The first stage of decomposition shared by all of the sequences is "fresh" stage, which begins at the point of somatic death. Approximately 4 minutes postmortem, the cellular structure starts a process of autolysis, specifically within the smooth musculature and followed by striated musculature, where lysosomes are released into the cytoplasm due to a decrease in intercellular pH levels (111). This decrease in pH levels is the direct result of the deprivation of oxygen (O<sub>2</sub>) and adenosine-triphosphate (ATP) (49, 111, 112). Cell walls begin to deteriorate and the basement membranes/intracellular matrix begin to dissolve, resulting in the breakdown of the cellular and tissue structures (49, 111, 117, 118). Gill-King (49) characterized autolysis into two stages. Stage 1, or early, reversible, is the point at which localized individual cell death occurs, but the overall tissue may be spared. Stage 2, or late/irreversible, is noted when autolysis has progressed to the point where tissue necrosis can be seen microscopically as the absence of cell nuclei (49). Using these stages, Gill-King (49) organized tissue decomposition based on those tissues with a higher level of ATP; starting with the soft-muscle tissues of the digestive tract and vasculature, then the pulmonary structure, brain/nervous tissue, skeletal muscles, and lastly connective tissues. In bone, however, the intercellular matrix is predominantly inorganic rather than organic (27) and limited research has taken place demonstrating the effect of autolysis on the organic matrix of bone cells and tissue (10, 119-124). That said, similar to Cvetko *et al.*

(125), while cells may be imaged and show evidence of previous activity such as evidence of migration, at the time of imaging they may be quantified yet still inactive and no longer viable.

As the process of autolysis continues, the mortis triad (algor, livor, and rigor mortis) becomes established, the combination of which has been instrumental in determining approximate PMI (126-128). Livor mortis takes place when capillary beds throughout the body begin to rupture; 20 minutes postmortem, the gravitational pooling of the blood will cause the downward facing surface of the skin to exhibit a red to purple hue (112, 113, 127, 128). Once the intrinsic autolysis process has progressed to the irreversible Stage 2 and is multiplied to the wider tissue process, endogenous bacteria begin to initiate putrefaction, approximately 48 – 72 hours postmortem (49). During this stage, the digestive tract begins to break down, leading to the second universally accepted stage, the bloat/early decomposition stage (11, 110, 112, 114, 115).

#### 4.2.1.1.2 Bloat/Early Decay

Through the process of putrefaction, anaerobic bacteria become increasingly active, attacking what remains of the larger blood vessels and internal organs (15, 49, 112, 115). In soft-tissue decomposition, this results in the release of excess interstitial gasses and ultimately bloating of the body (11, 15, 110, 112, 114-116). During the later phases of this stage the intrinsic bacterial activity begins to slow, while the extrinsic activity begins to accelerate (15, 112, 114, 116). Extrinsic activity, such as arthropod oviposition and additional macrofaunal activity, occurs during the later phases of early decomposition, and can affect the physical decompositional process. Much is known regarding the extrinsic appearance of the remains during this stage, yet little is known regarding how bone is affected by the putrefactive and internal decomposition processes (119). Given that smooth and striated musculature deterioration accelerates due to a weakening of the structures over the slowing of bacterial activity, it can be hypothesized that the organic matrix within the skeletal structure itself will begin its deterioration. Furthermore, and specific to the present study, cell deterioration, including that of osteoclasts should become more pronounced. Therefore, where in the fresh stage, like Cvetko *et al.* (125), inactive cells could still be imaged, in this stage of decomposition,

cells should begin the process of deteriorating, with their countable numbers noticeably decreasing.

#### 4.2.1.2 Methods for Assessing the Postmortem Interval

The methodologies to assess the postmortem interval varies depending on the degree estimated time postmortem and the degree of putrefaction, as methodologies have differing degrees of reliability based on time postmortem (132). According to Ruiz López and Partido Navadijo (132), pathological methodologies for assessing the postmortem interval can be divided into two categories based on the presence of putrefaction: early or late. These can be overlaid with anthropological categories with early being that of “fresh,” while the late is associated with the “bloat/early decay” (11, 114, 116, 129).

The methodologies for assessment of the early period can be divided into two main categories. One is based on gross body modifications following off of the mortis triad (algor, rigor, livor). Here, the assessment is a trinity of assessments which combines assessing the degree of temperature equilibrium with the surrounding environment (algor mortis), the contraction and relaxation of the musculature (rigor mortis), and the collapsing of the capillary beds settling, and setting of the blood at the gravitational lowest point of the body (livor mortis). However, the timings are more dependant on the surrounding environment and body habitus, and generally are considered less accurate, and after 72 hours are generally useless. The next set, however, is more micro in scale, based on histology, histochemistry, or going larger focused on organs rather than whole body (i.e. uterus or crystalline lens). These are also considered more accurate to PMI timing, especially after the initial 72 hour period. These early methodologies are rather germane to the present study because they are widely varied yet rarely last beyond 7 days while the present project extends to 14 days.

These micro-level pathological methodologies for postmortem interval estimation generally come in a few areas that are tested (132). The most common, and some of the more accurate testable areas is the assessment of potassium (K) in the vitreous humour within the eye, which increases approximately 1 mmol/l K for every 6.42 hours postmortem up to a maximum of just under 7 days (2), though this is age dependant and younger individuals (below the age of 18) exhibit a faster increase in K (1). Similar studies have also worked on levels of K in vitreous humour, as well as albumin, as a means of testing the postmortem interval, yet the maximum

study dates are all less than 8 days with the exception of Zilg *et al.* (1) which lasted for 17 days (beyond the 14 day window of the present study) (2, 3, 132). In addition to the level of potassium, a few early postmortem interval estimation methodology studies also have examined the degradation of cardiac proteins, specifically Troponin-C, a subunit of Troponin, which binds to the calcium leached from the myosin and actin within the cardiac muscle fibres, and Troponin-T, a subunit which acts as a stabilizer (133, 134). While studying different proteins, both Abd Elazeem *et al.* (133) and Kumar *et al.* (134) did come up with relatively similar conclusions regarding the degradation of the proteins over time reaching the lowest useful levels at around 50 hours postmortem. Additional markers for the early postmortem interval can be found in gingival tissues which begin to break down after 24 hours with a similar decrease in phosphatase while ammonia levels increases as the epithelial cells deteriorate (5). Further, the crystalline lenses within the eyes are known to demonstrate timed structural changes in the early postmortem period beginning at 48 hours postmortem and losing all structure and sphericity at 96 hours (135).

Once putrefaction has begun, however, the assessments of the postmortem interval, shift from a pathological assessment to a more anthropological one, and is largely based on the degree of decomposition, skeletal exposure, mummification (if present), and the degree of skeletal element degradation as a result of taphonomy and diagenesis. If soft tissue is still present, or the exposed skeletal elements are “wet” in appearance as a result of decompositional fluids or the elements still uniformly retaining a greasy texture, it is possible to tie that degree of decomposition to the accumulated climate to attain a rough estimate of the postmortem interval (11). One of the first to sort of standardize this process was Megyesi *et al.* (11) who developed a model for calculating the degree of decomposition based on a 35 point scale, with each region of the body (head/neck, trunk, limbs) is assessed. This is then entered into a formula to develop a potential set of accumulated degree days which can be compared to climactic data to establish a potential postmortem interval (11). However, there are limitations to this model, not the least of which is that the estimated postmortem interval range increases as the time postmortem increases (as accumulated degree days increases) and flaws in the base model (12, 13). Additionally, there are other climactic factors that effect the rate of decomposition including humidity (14, 108, 136-139), moisture (140, 141), presence of sun/shade (142), and others (15, 143-152) which are ignored in the Megyesi *et al.* (11) and Moffatt *et al.* (12) models that could either increase or

slowdown the decompositional rate. However, while Megyesi *et al.* (11) and Moffatt *et al.* (12) established a measurable scale for the postmortem interval, much has been done which examines the degree of decomposition as well skeletal taphonomy and ties it to gross timing, but not an exact postmortem scale (8, 14, 15, 108, 119, 130, 153, 154).

The present study was designed to staddle both the early and late postmortem interval methodologies by examining the declination of osteoclasts. While the present study was designed to address practical and ethical considerations with the skeletal elements removed from the corporal remains (see Ch. 4.2.3), given that osteoclasts within the boney structures are encapsulated by several layers of biological material including bone, connective tissue, and musculature, the theory is that this should protect, if not the viability, the visibility and presence.

#### 4.2.1.3 Osteoclasts

Within this organic matrix is a complex cellular system that is used to maintain overall bone stability as various forces, including load, are enacted upon it. Among those cells are osteoblasts (responsible for mineralization among other tasks), osteocytes (responsible for regulating homeostasis through coordination with osteoblasts and -clasts), and osteoclasts (responsible for resorption among other tasks). Together, these three cells work in concert to generally maintain bone homeostasis, specifically within an element, but given the structure of the human skeleton, a variation within one element would naturally have a compensatory effect on other elements (30, 31).

Of the three cell types in questions, the present study focused on osteoclasts. Osteoclasts are multinucleated cells responsible primarily for resorption of bone matrices (30). The resorption process takes place when osteoclasts interacts with the inorganic matrices, the cell itself becomes polarized through matrix derived signals transmitted by the  $\alpha\beta3$ -integrin which creates a microenvironment between the cell and the bone matrix (32). This matrix becomes potentially acidic microenvironment by  $H^+$  adenosine triphosphate (ATP)ase-mediated extracellular transport of protons while the intracellular pH is maintained through an electroneutral  $HCO_3^-/Cl^-$  (32). As the  $Cl^-$  enters the cell it is released into the microenvironment by an ion charged coupled to the  $H^+$  ATPase crating an acidic environment (32). This then exposed the organic matrix of bone that is degraded by cathepsin-K (32).

Osteoclasts have multiple origins with each depending upon both the developmental stage of the individual, and the nature of the need of those osteoclasts. Beginning with embryonic development, osteoclastic cells arise from two generalized pathways: erythromyeloid progenitors (EMPs) which develop around embryonic day (E) 7- E7.5, and hematopoietic stem cells precursors (HSCs) around E10.5 (33). The EMPs are divided into two categories depending on developmental timing with early EMPs developing around E7 and then morphing into colony-stimulating factor 1 receptor 1 (CSF1R)+ yolk-sac macrophages which, by E8.25 with the yolk-sac vasculature connecting to the intraembryonic circulatory system, colonize the various organs. After this colonization, a second wave of EMPs (late EMPs) develop within the yolk-sac and migrate into the live to produce monocytes (33). By around E10.5, in the final waves of hematopoiesis, HSCs begin to emerge around the aorta-gonad-mesonephros region. At around E15.5 the EMPs, having developed into embryonic osteoclast precursors, begin the formation of the marrow cavity, which is then inhabited by both the residual EMP osteoclast precursors, as well as the HSC osteoclast precursors derived from the fetal liver (33). While both are known to exist long into adult-hood, at this stage the cells themselves remain progenitor cells with their final maturation and functionality having some overlap but generally being separated. Specifically, EMPs, while existing up to 6-months postnatally, and having some derivatives in fracture (*fx*) repair, are eventually replaced by HSCs both in bone maintenance and remodelling, as well as being engaged in the primary role of *fx* repair (33).

The transcription of the precursor cells to mature osteoclasts, mainly those of the HSC origin, start with the HSC differentiating into multipotent progenitors, which are then lineage-restricted, meaning that they have the ability to develop into any number of type of cell but then become limited in their ultimate trajectory (33). For osteoclastic precursors, the HSC multipotent progenitors develop into common myeloid progenitors (CMPs) that produce granulocyte/macrophage progenitors (GMPs) as well as common osteoclast/dendritic cell progenitors (MODPs), with dendritic cells (DCs) also serving as antigen-presenting cells or APCs (33). The MODPs develop into mature osteoclasts through interactions with receptor activators of nuclear factor-kappa B ligand (NF- $\kappa$ B, or RANKL), colony-stimulating factor 1 (CSF1 or M-CSF for macrophage) (34). Additionally, there is evidence to believe that in children, interleukin 3 receptor- $\alpha$  as well as a KIT protooncogene receptor tyrosine kinase (KIT)<sup>+</sup>

may also have roles in the development of osteoclastic precursor cells into mature osteoclasts (35, 36).

Once the mature osteoclasts are developed, they are then engaged in the development of the bone through the normal processes of modelling and remodelling. Following the process of ossification, the bone is then modeled via osteoblasts (formative) or osteoclasts (resorptive) based on the strain and load placed on the bone (30). Localized strains when elevated beyond a threshold signal for formative modelling and new bone being applied, while those below the threshold trigger resorptive modelling and bone being removed by osteoclasts (30). This process is continued until the strain is normalized, and the positioning of the bone is changed to align with the needed central axis; a process referred to as bone drift (30). While existent throughout life, in adults this process becomes less prominent except in the case of pathology (30). In addition to modelling, osteoclasts are also prominent in remodeling, as well which is more localized than the modeling process. Remodelling can take place throughout the bone element and is used in the repair of defects and replacement of existing bone matrix (30). As these osteoclasts, acting in concert with osteoblasts, are working with associated blood vessels in multicellular units (bone multicellular unit or BMUs), this process of remodelling is what gives rise to the concentric osteons and Haversian systems found within the human skeletal system (30).

In addition to the modelling and remodelling phases that are required for normal bone homeostasis, osteoclasts also play a pivotal role in  $f_x$  repair as well. Osteologically there are four stages of  $f_x$  healing beginning from the time of propagation (induction) to the terminal stage of remodeling (37-39). The time to traverse from the initial to the final stage can take months to years, with healing dependent upon the sex and age of the individual; the younger the individual, the faster the healing rate (37, 39). The fastest of the four stages, however, is the initial stage of induction (also referred to as the inflammation stage) (37, 39). This stage generally lasts a few weeks, beginning with the initial  $f_x$  and ending at the appearance of new bone (NBF) (37, 39, 40). Due to the vascular nature of bone, once it reaches the failure point, thousands of capillaries rupture leading to a massive hemorrhage (37-39). Within minutes of  $f_x$  propagation, the vasculature will undergo normal blood clotting procedures and a hematoma will develop (37). Osteoprogenitor cells located in the periosteum will migrate, convert the hematoma to granulation tissue and ultimately osteoid (37, 39, 40). More specifically, osteoclastic precursor

cells are recruited to the  $f_x$  site from the blood stream and differentiate into mature osteoclasts following signals such as the receptor activator of nuclear factor Kappa-B ligand (RANKL), macrophage colony-stimulating factor (M-CSF), and cytokines such as tumor necrosis factor- $\alpha$  (TNF- $\alpha$ ) and others, all stemming from the hematoma (24, 41-43), processes similar to differentiation into mature osteoclasts in normal bone formation. In addition, high mobility mature osteoclast cells within the extravascular structure of the bone migrate to the  $f_x$  site, while additional cells (possibly splenic in origin) begin migrating through the vasculature (33, 44). Once the hematoma develops two processes initiate: inflammation of soft tissues and resorption of necrotic tissues (37, 39), although, as noted, research suggests osteoclasts respond immediately to  $f_x$  based on signaling from osteoblasts as well as hematoma formation (33, 44-46).

In the second stage of  $f_x$  repair, osteoclasts begin the resorption process by engaging in osteolytic activities (37, 39). Specifically, mature osteoclasts attach to the bone surface at the  $f_x$  site and form an irregular border, increasing the surface area for bone resorption. The osteoclasts then secrete hydrochloric acid and proteolytic enzymes such as cathepsin K to dissolve the hydroxyapatite and degrade the organic matrix (24, 42). Polarized histological and radiographic studies suggest that this activity begins following the formation of new capillary beds within the hematoma, and can be seen between 4 and 7 days post-injury (PI) (37, 39). At this point osteoblasts begin secreting new bone under the periosteum which has formed around the hematoma. This new bone formation, SPNBF or sub-periosteal new bone formation, can be seen around the fracture margins and is the marker for the start of the “soft callus,” third, stage (39).

In the third stage of  $f_x$  healing is the soft callus stage where the hematoma is replaced with a fibrous matrix that bridges the  $f_x$  line, and then the fibrous matrix is gradually replaced with primary woven bone (39). This occurs by the SPNBF expanding to bridge the  $f_x$  line while simultaneously the fibrous bridge disintegrates during a maceration process (39). Once the fibrous matrix has disintegrated, the fourth, “hard callus” stage begins where the  $f_x$  callus has fully bridged the  $f_x$  (39). It is during the hard callus stage that the inflammatory tissues have resorbed while osteoclasts remain relatively active, leading directly to the remodelling stage where the primary woven bone is converted to lamellar bone and then ultimately remodeled to the original contours via bone drift to meet the central axis of the bone (30, 39).

The last area of the osteoclast lifespan that requires attention is that of apoptosis and autolysis. Both apoptosis and autolysis are related to cell death, however they function in two vastly different ways. Apoptosis is the natural death of a cell at the end of its individual life-cycle, normally after the resorptive process (47, 48). While numerous receptors and processes go into osteoclastic apoptosis, according to Soysa and Alles (48) the prevailing theory on a molecular level is that tumor necrosis factors (TNFs), specifically TNF apoptosis-inducing ligand receptors (TRAIL-Rs) permeate the cell membrane or bind as a soluble receptor. These TRAIL-Rs have been found to exist both in differentiated and precursor osteoclasts (48). Further, with the reduction of M-CSF, these can lead to an increase in the BH3-only Bcl family Bim protein, leading to cytokine withdrawal and ultimately apoptosis (48). However, while much is known regarding osteoclast apoptosis, very little has been published regarding its sister, autolysis. Autolysis, or “self-death,” is a form of cellular death that takes place when the molecular functions to sustain life have been disrupted, often through somatic death of the individual. In general, following somatic death, cells do not instantaneously undergo a process of autolysis, but rather undergo in a system by system manner. Decompositional studies have shown that smooth and serrated muscles undergo this change first, namely in the gut, but other organs quickly follow (49). However, turning to transplantation medicine one can get a rough estimate as to the process of autolysis of whole organs as hearts and lungs are recommended to be transplanted within 4 to 6 hours while kidney’s can last as long as 36 hours, though must be initiated within 24 hours after somatic death (50, 51). As viable cells are needed for the tissues and organs to function in the transplanted state, then it can be inferred that the cells can survive, with assistance from proper isolated conditions up to the recommended timeframe and even slightly beyond. That said, an examination of osteoclast autolysis through PubMed turned up no such results (52). However, again turning to transplantation medicine, under the right conditions bone tissue samples can be held and successfully transplanted up to 5 years after donation (51). With the present study, the aim is to assess the presence, if not the viability of osteoclasts following somatic death, and measure the degradation of their abundance for use as a potential tool in the assessment of the postmortem interval.

#### 4.2.2 Materials and Methods

For this project, two sample groups were established: a “perimortem” group consisting of bone biopsies from human ilia, and a postmortem group derived from ilia from donated

cadaveric remains. The perimortem group was collected, fixed, and processed by the Department of Pathology, Laboratory of Bone Histomorphometry, Centre Hospitalier de l'Université de Montréal (CHUM) in Montréal, QC from still living human individuals, through pathologic study<sup>1</sup> (biopsy size 10mm<sup>3</sup><sup>2</sup>). This group acted as a proxy for perimortem breaks. By using such elements, we can mirror somatic death as the cardio-pulmonary functions to the section of bone would have stopped upon harvesting. The postmortem sample group was harvested from cadaveric remains donated through the Willed-Body Donation Program by the Division of Anatomy at the University of Toronto in Toronto, ON. Processing of these segments were conducted by the first author following the methodology as established by the CHUM for fixation and embedding, as described in a provided methodology form (discussed below). For this project, the samples included 9 postmortem and 9 perimortem samples for a total of 18 individuals and were the same as the individuals in Ch. 3.2, with the perimortem also being the same as the “unembalmed” sample group from Ch. 2.3. The perimortem sample had ages ranging from 30 to 57 years and were all male, while the postmortem sample ranged from 80 to 108 years and consisted of 5 male and 4 female individuals (see Appendix A for sample demographics). The dates of death was recorded but are withheld per anonymity protocols. Other demographic data such as ancestry (race), stature, weight, and body mass index as well as other factors were collected by CHUM and the University of Toronto’s Division of Anatomy respectively but were not released nor recorded by the primary researcher for this project for ethics and anonymity protocols. Ethics protocol approval was granted by the University of

---

<sup>1</sup> To conform to protocols established under U of T Protocol #33324 to protect the anonymity of the subjects, limited information was agreed to be collected. This was limited to the control number, age, sex, and date of death (for the postmortem individuals only). While it was requested and verbally assured from both CHUM and the U of T Division of Anatomy that the individuals did not have any pathological conditions, the presence of any pathological conditions were masked from the primary researcher per the ethics protocol. The CHUM pathology verification was given on 15 February 2018, while the U of T verification was given during sample harvesting. Since 2021, both of the researchers at the CHUM laboratory have moved to different positions, and the primary researcher is no longer able to access the subjects’ pathological conditions.

<sup>2</sup> While biopsy size is generally calculated by diameter of trephine plus depth, in this case the samples came pre-prepared on slides and the biopsy size was calculated using the sample provided.

Toronto Research Ethics Board, Human Protocol #33324<sup>3</sup> (see Appendix D). Samples were stored in a restricted and locked laboratory with identifying information segregated on an external hard drive held off site. As osteoclast numbers vary with age (228-230), a Kruskal-Wallis test was run within each sample group (perimortem, early-postmortem, 7-day postmortem, & 14-day postmortem) with age groups separated by lustrums.

The sample preparation including harvesting, sectioning, fixation, embedding, and thin-sectioning all mirrored Ch. 3.2.2. To assess the degradation of osteoclasts over time, the postmortem samples were sectioned and fixed at weekly intervals. Harvesting of samples took place upon the Division of Anatomy receiving the donor's remains (occurring <48 hours post cardiopulmonary death but >18 hours post cardiopulmonary death). Immediately after harvesting (within 1 hour), 1/3 of each segment was cut using a manual bone saw, fixed, and dehydrated in a serial fashion. The smaller segment was fixed separately with a 40% solution of formaldehyde to arrest cellular degradation and labeled as "early-postmortem", while the remaining 2/3 segment was reserved in a separate, empty but sealed jar to continue decomposing. Given the extended temporal variability between the time of the donor's cardiopulmonary death and the time of collection, it was recognized that this early-postmortem grouping would have the widest range in cellular abundance. The remaining postmortem samples, however, were standardized to the time of the donor's cardiopulmonary death irrespective of the time of harvesting and collection. Additionally, while air can inhibit cellular life, given ethical or moral practicalities of using human remains, in a controlled environment, it is difficult to mirror and investigate cellular degradation using a closed fracture, repeated collection methodology in cadaveric remains, particularly given that the donor's remains were to be used for anatomical instruction and therefore were scheduled for embalming post sample harvesting. While not ideal, the present methodology allowed for sample use while maximizing the donor's final wishes regarding their earthly remains.

---

<sup>3</sup> Regarding CHUM Use of Samples, ethics approval, and Material Transfer Agreement information see Appendix D.

After a 7-day period following subject cardiopulmonary death, irrespective of the time of the larger sample harvesting and collection, the unfixed segment was cut again using the same parameters as noted above, with one part then being fixed in the solution and labeled as “7-day postmortem” with the remaining part left unfixed. After yet another 7-day period (14 days following subject cardiopulmonary death), the remaining segment was fixed in the 40% formaldehyde solution to arrest biological activity and labeled as “14-day postmortem”. It should be noted that the 14-day time window was arbitrarily chosen given the limitations of the harvested sample size and complexities of the sampling and thin-sectioning process, coupled with the hypothesis that after the 14-day mark there would be limited noticeable cellular data.

After a 4-day fixation soak, all samples were serially dried using an alcohol dehydration process, including 95% ethyl alcohol for 4 days, followed by 4 days in anhydrous alcohol. The samples were then soaked in methyl methacrylate (MMA) prior to embedding using manufacture recommended guidelines. MMA was selected as the mounting medium as it is optically neutral forgoing the photobleaching effect of epoxy resin. However, MMA can affect the penetrative power of the labels which can be damaged in the embedding process. Due to this, labeling took place post thin sectioning, and an extended incubation period (208, 209).

After segments were fully embedded and the medium allowed to dry, the segments were then mounted on glass slides, and cut and polished using a Struers<sup>®</sup> Accutom-100<sup>™</sup> to a final thickness of 100 $\mu$ m then labeled following the method established by Coxon (184). The samples were initially incubated for 15 minutes in a solution of pH neutral phosphate buffer solution (PBS) with a 0.5% (v/v) Triton X-100 (Thermo Fisher<sup>™</sup>) (184). They were then labeled with a solution of 10% bovine serum mixed with 100 $\mu$ L of MitoTracker<sup>™</sup> Red FM Dye (Thermo Fisher<sup>™</sup>) and PBS and allowed to incubate for 1 hour (184). After an hour the samples were then secondarily labeled with goat anti-rabbit IgG Alexa Fluor<sup>™</sup> 488, giving good contrast to the MitoTracker<sup>™</sup>, and allowed to dry for an additional hour in a dark room (216). The remaining Alexa Fluor<sup>™</sup> 488 was then rinsed away in PBS and the samples were allowed to air dry completely for 24-48 hours before a glass coverslip was affixed using Fluoromount<sup>™</sup> aqueous mounting medium (Sigma Aldrich) (215).

Imaging was conducted using the Carl Zeiss<sup>™</sup> LSM-800<sup>®</sup> laser scanning confocal microscope housed with the Imaging Facility, Department of Biology at the University of

Toronto – Mississauga, Mississauga, ON. Samples were imaged using the 10x air objective, for a total of 100x magnification per frame. As the whole of the cortical table per sample was needed for imaging, a tile set was created using the “stake” feature with points being noted around the desired sample area. Given the individual variation in size between each sample, the overall tile set varied from sample to sample. To achieve three-dimensionality a z-stack of 10 slices was used throughout the tile set, with a z-depth of 12.75µm per sample. The z-depth was standardized to 12.75µm to account for the difference in overall sample slice thickness between the CHUM and the University of Toronto samples. The use of 10 optical slices allows for some depth without drastically increasing the time used to take the sample. Acquisition parameters were set at a frame size of 2048 pixels x 2048 pixels for higher resolution at 16 bits, thus allowing for more of a gradient in pixel intensity with each pass. The average voxel volume was 0.012µm<sup>3</sup>, calculated by obtaining the voxel volume from each individual image. That said, unlike Ch. 3.2 where the image size was more standardized, given the variability in the cortical sizes (and therefore the X/Y tile size) of each sample, the average is reported rather than each individual. The voxel volume was calculated using the following formulae:

$$d^x = \frac{FOV^x}{Matrix^x}$$

$$d^y = \frac{FOV^y}{Matrix^y}$$

$$d^z = \frac{FOV^z}{\#ofSlices}$$

$$Voxel\ Volume\ \mu m^3 = d^x \times d^y \times d^z$$

The calculations were compared against the formulae for scaling per pixel in Zen Blue® (217) and comparing the calculated voxel amount [ $Matrix^x \times Matrix^y \times \#ofSlices$ ] with the voxel count in BitPlane® Imaris™ v. 9 (185).

While the sample preparation allowed for imaging on the 405nm, 488nm, and 561nm excitation wavelengths, multiple-channel imaging exponentially increases the timing required for a single image. To account for this a single channel was selected, 561nm, which when used with MitoTracker™ Red FM Dye, allows for an emission registration of 555nm. Given the parameters used this allowed for the imaging of the cellular material without the overlaying

hydroxyapatite within the cortical sections masking the cellular material. While individual settings such as laser power, pinhole size, and master gain were adjusted per sample, in general the laser power was approximately 1.5% with a pinhole of 150 $\mu\text{m}$ , and a master gain of 700V, while unlabeled hydroxyapatite requires a power setting of approximately 4% and a pinhole of around 350-450  $\mu\text{m}$ . The variations in settings were required to ensure a constant image fluorescence and quality, limiting “hot spots” and potential “dead spots.” The settings for this research allowed for the visualization of items labeled with the MitoTracker™ while not being high enough to image the native hydroxyapatite (187).

Image analysis was conducted using Oxford Industries BitPlane™ Imaris® v9 (185). Imaris® v9 is similar in base functionality to that of the open-source software FIJI/ImageJ® v.1.50i (186), however it is more powerful and does not crash as often as FIJI/ImageJ® v.1.50i when dealing with large-sized image files, as were generated for this project (approximately 2GB per image). Additionally, Imaris® allows for the isolation and subsequent analyses of specific areas in a 3-dimensional array. For the present project, a mask feature was utilized to isolate the cortical element from surrounding soft tissue and marrow, while ensuring that the periosteum and endosteum remained within the mask (Fig. 4.2.1 – 4.2.3). After the mask was created, a spot counter was run to count the various voxel groups within the image. The spot counter feature in Imaris® v. 9 is similar to the object and voxel counter functions in FIJI/ImageJ® v.1.50i. A base size of 50 $\mu\text{m}^3$  was established, towards the lower end (16%) of size for an osteoclast (231, 232), with a quality rating of 10% utilized. This means that the artificial intelligence program within the software calculates those voxels that fall within the top 10% regarding quality of continuity and thus most likely to be cellular material. The number of osteoclasts present, the total volume within the masked area, and the number of osteoclasts per  $\text{mm}^3$  of bone were then inputted into IBM™ SPSS® v.28 (219). The latter metric was used to standardize the osteoclast count following the formula as set out by Parfitt *et al.* (198) using the formula  $\text{OCL\#} / \text{Total Volume}$ .

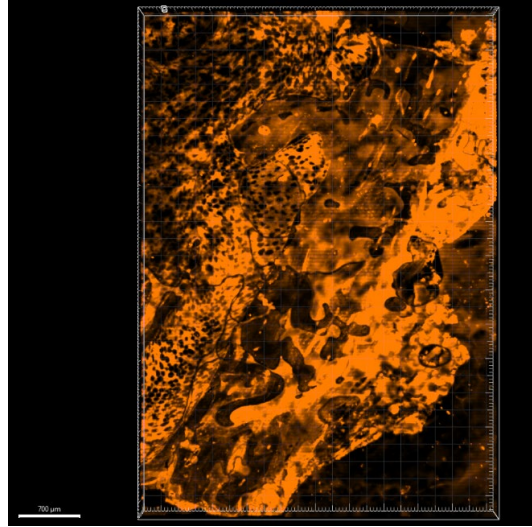


**Figure 4.2.1: Single slice (slice 6) unaltered image showing outer iliac table with adhering soft tissue and marrow, scanned using the 555nm emission wavelength. In this image the break margin is located on the bottom of the image with the periosteum to the image right. There is a large patch of non-cortical bone that is highlighted at the 555nm wavelength, however, given the high fluorescence of soft tissue, this was expected and therefore the reason for its masking and exclusion.**

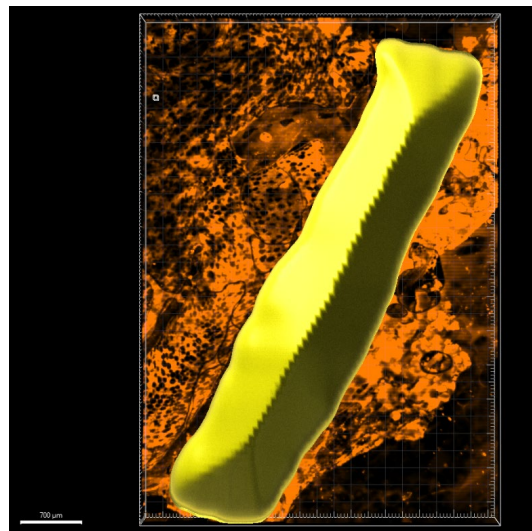


**Figure 4.2.2: Mask applied surrounding the cortical bone and the surrounding peri- and endosteum thus excluding the adhering soft-tissue and marrow.**

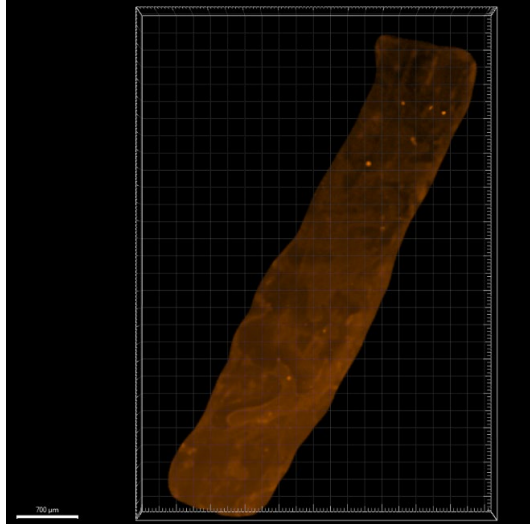


**Figure 4.2.3: Final analyzed image using only the cortical bone and peri- & endosteum. Note: image is of Slice 1 of 6 in comparison to Slice 6 of 6 used in the Figs. 4.2.1 and 4.2.2.**

A Shapiro-Wilk test was conducted for both cellular count and location as a means for testing normality using IMB™ SPSS® v.28 (219). Finding non-normality, a Kruskal-Wallis H Test was run to determine if there was a difference between the perimortem group and the three postmortem groups with respect to the standardized cellular counts. More specifically, the K-W test was selected as it would be able to distinguish if there was a statistically significant difference between count means of the 4 time groupings (perimortem, early-, 7-day-, 14-day postmortem), with the hypotheses being that  $H_0$  would be  $p > 0.05$  indicating that there is no significant difference while  $H_1$  would be that  $p \leq 0.05$  indicating that there was a significant difference. A Spearman rho correlation analysis was conducted to determine if postmortem timing correlated with abundance with a confidence interval set at 95%. This model was selected as it would determine a linear relationship between the ordinal data (the time groupings) and the scale data such as cell abundance exists. Further, a Kernel Ridge Regression (KRR) was run to determine the observed cell count changes can be associated to time groupings and if there is an element of predictability in any change in the cell counts. For the KRR, a Chi<sup>2</sup> model was selected, with an  $\alpha = 1.000$  and a  $\gamma = 1.000$ , due to the limited sample size within each time group (e.g. 9). Lastly, power and  $\eta^2$  effect size analyses were also conducted given the limited sample size to determine the detectability of any true effects. It was hypothesized that there would be a significant correlated and predictable decrease in the osteoclast abundance as the postmortem time progressed, with an almost negligible abundance count by the 14-day postmortem group.

### 4.2.3 Results

Overall, the results of this study found that there was a marked decrease in cellular abundance as the postmortem period increased. There was an 80% decrease in osteoclast number from the perimortem group to the 14-day postmortem group (Fig. 4.2.4). The differences between each time period is nonlinear; with a marked decrease of 71.5% between the perimortem group and the early postmortem group, compared to 55% between early postmortem and 7 days, then 51% decrease between 7- and 14-days postmortem. The results of this declination in cell counts are recorded in Appendix C with the raw counts as well as the counts standardized by volume as outlined by the osteoclast number (formerly osteoclast index) in Parfitt *et al.* (198), though the statistical results are only from the standardized data. The standardization is derived by dividing the number of counted osteoclasts by the total volume of the sample written as  $\text{mm}^3$  [OCL#/TV]. The results of the Kruskal-Wallis H test were significant ( $p < 0.001$ ;  $H = 27.376$ ), with a strong negative correlation ( $r = -0.880$ ,  $p < 0.001$ ). Given the small sample size, power and eta-squared ( $\eta^2$ ) effect analyses were conducted results demonstrating a strong power size with 0.993 and a  $\eta^2$  effect size of 0.762. These results indicate a large probability of achieving a true result with the Kruskal-Wallis H-test.

In addition to the main Kruskal-Wallis H-test, a post hoc analysis was conducted along with a Friedman test was conducted to determine if there were significant differences between the subject groups, both as a result of the test as a whole (K-W H-test) and on a repeated measures basis with just the postmortem groups. The results of the post hoc pairwise analysis found that there was a significant difference 3 of the 6 pairs; specifically, the perimortem – 7-day postmortem ( $p = 0.003$ ;  $H = 3.020$ ), perimortem – 14-day postmortem ( $p < 0.001$ ;  $H = 4.877$ ), and 7-day postmortem – 14-day postmortem ( $p < 0.001$ ;  $H = 3.691$ ) (see Table 4.2-1). This suggests that there becomes a significant difference in the trajectory of degradation of osteoclasts, but that this becomes significant at the 7-day postmortem period. That said, the results of the Friedman repeated measures test does indicate a significant difference between the postmortem groups ( $p < 0.001$ ) (see Fig. 4.2.5). The mean rank of the Friedman test also indicates a pattern with the sums decreasing equally from 3 with the early-postmortem group to 1 with the 14-day postmortem group. Lastly, a Kernel Ridge Regression was run testing association and predictability. The results of the KRR  $\chi^2$  was  $r^2 = 0.752$ , meaning that 75.2% of the variation between the time groups can be explained by the progression of time postmortem. Therefore,

any assessment in a future time, the osteoclast count would have a 75% chance of falling within the predicted trendline.

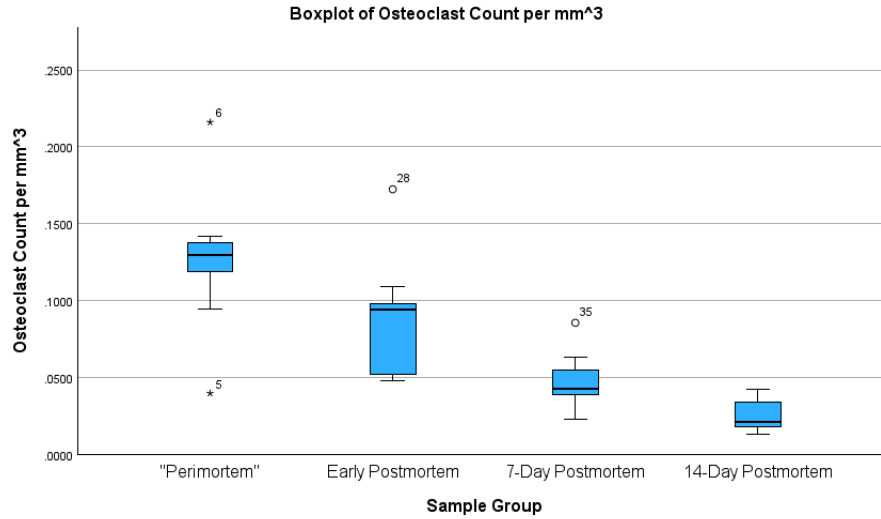


**Figure 4.2.4: Osteoclastic degradation over the four time-groups (outliers included).**

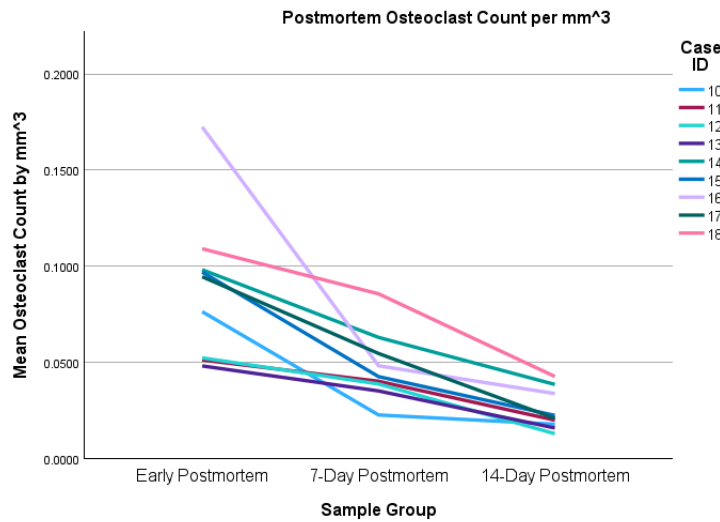


**Figure 4.2.5: Postmortem osteoclast decrease (outliers included).**

**Table 4.2-1: Post Hoc Pairwise Results**

Sample 1-Sample 2	Test Statistic	Std. Error	Std. Test Statistic	Sig.	Adj. Sig. <sup>a</sup>
14-Day Postmortem-7-Day Postmortem	9.222	4.967	1.857	0.063	0.380
14-Day Postmortem-Early Postmortem	18.333	4.967	3.691	<0.001	0.001
14-Day Postmortem-"Perimortem"	24.222	4.967	4.877	<0.001	0.000
7-Day Postmortem-Early Postmortem	9.111	4.967	1.834	0.067	0.399
7-Day Postmortem-"Perimortem"	15.000	4.967	3.020	0.003	0.015
Early Postmortem-"Perimortem"	5.889	4.967	1.186	0.236	1.000

Each row tests the null hypothesis that the Sample 1 and Sample 2 distributions are the same.

Asymptotic significances (2-sided tests) are displayed. The significance level is .050.

<sup>a</sup>. Significance values have been adjusted by the Bonferroni correction for multiple tests.

That said, in an analysis such as this study, outliers can be present. The question arises, however, in how to address those outliers. With the present study, two methods are presented depending on the theory behind the cause of the outliers. If the outlier is believed to be artifactual in nature, rather than being more biological, then a removal of that single outlier from that statistic would be pursued. That is, if Individual X is found to be an outlier in the 7-day postmortem group, then that sample is removed from just the 7-day postmortem. If, however, there is a more biological reason for the outlier, a second option would be the removal of Individual X from all postmortem groups rather than just the one which they are an outlier. For the present study, to account for the possibility of both situations, analyses were run with the outliers removed from the individual test, as well as the second set of analyses run with the whole of the individual removed. For example, if Individual X was found to be an outlier in the 7-day postmortem group, the analyses were run once with Individual X removed from just the 7-day postmortem group, and then a second time with that individual removed from *all* groups. In order to determine where the outliers existed, a z-score analysis [ $z=(x - \mu)/\sigma$ ] was run.

The results of the Kruskal-Wallis H-test and Spearman Rho correlation tests with individual outliers removed mirror that with the outliers in place. The results of the Kruskal-Wallis H-test found a significant difference between the four groups ( $p<0.001$ ;  $H=27.056$ ;  $\eta^2=0.859$ ), while the results of the Spearman Rho correlation test demonstrating a strong negative correlation ( $r=-0.934$ ;  $p<0.001$ ). These results indicate that there is a significant degradation trend in the osteoclast count (when standardized by volume) over the four time groups (see Fig. 4.2.6). Similar to the Kruskal-Wallis test with the outliers included, the post hoc

analysis with the individual outliers excluded found three out of six pairs in which a significant difference exists. However, the exact pairs differ in this case. Here the three groups which yielded significant differences perimortem – 7-day postmortem ( $p=0.002$ ;  $H=3.163$ ), the perimortem – 14-day postmortem ( $p<0.001$ ;  $H=4.929$ ), and the early-postmortem – 14-day postmortem ( $p<0.001$ ;  $H=3.388$ ) (Table 4.2-2). These results, though varied from that with the outliers included, also hint that there is a significant trend in the decline of osteoclast counts, but that the significance becomes noticeable around the 7-day postmortem level. Additionally, the results of the Friedman repeated measures tests found a significant results ( $p<0.001$ ), with the ranks, again, showing a equal and patterned decrease with the early-postmortem having a mean rank sum of 3 and the 14-day postmortem at 1 (Fig. 4.2.7). These results show that, even with the individual outliers removed, there is a significant decrease in the number of osteoclasts over time after death. Further, the results of the Kernel Ridge Regression  $\text{Chi}^2$  yielded a significant result with an  $r^2=0.853$ . This indicates that with the individual outliers removed now 85.3% of the variation between the time groups can be assessed to time postmortem. Moreover, this adds an element of predictability, indicating that there is an 85% chance than any future assessment would be demonstrate that the osteoclast number would fit within the trend line.

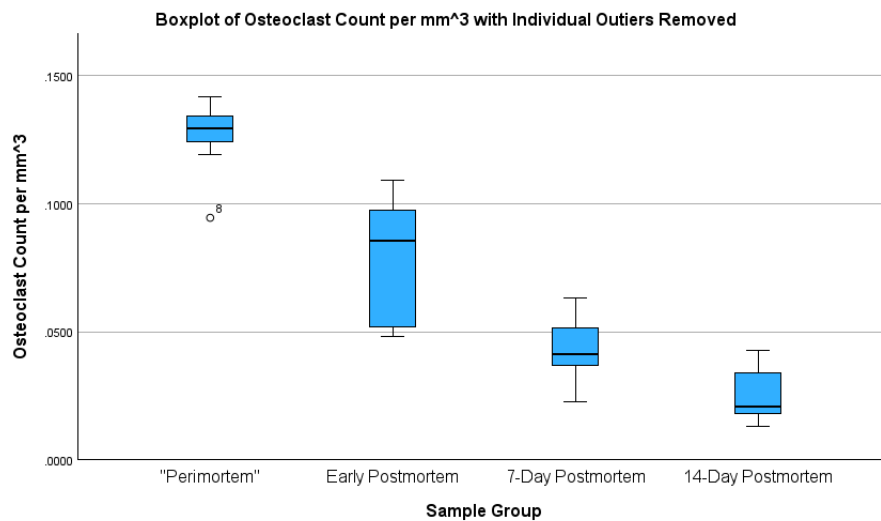


**Figure 4.2.6: Osteoclastic degradation over the four time groups with individual outliers removed. Note the removal of outliers produced even more outliers.**

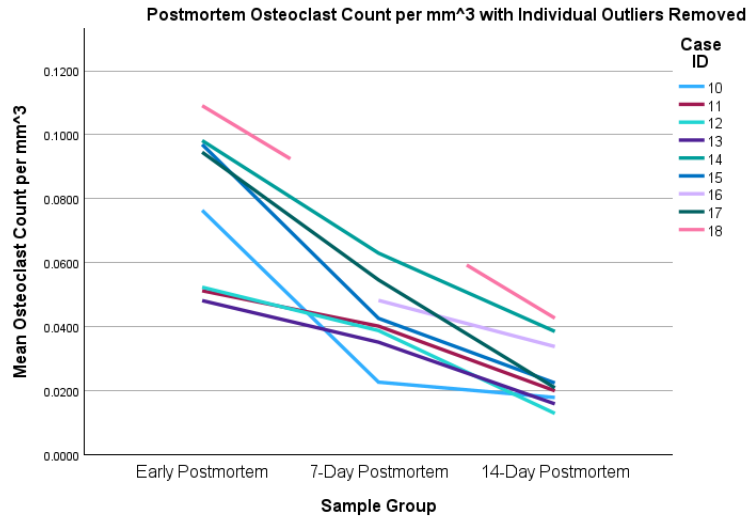


**Figure 4.2.7: Postmortem osteoclast degradation with individual outliers removed.**

**Table 4.2-2: Post Hoc Pairwise Results with Individual Outliers Removed.**

Sample 1-Sample 2	Test Statistic	Std. Error	Std. Test Statistic	Sig.	Adj. Sig. <sup>a</sup>
14-Day Postmortem-7-Day Postmortem	7.944	4.558	1.743	0.081	0.488
14-Day Postmortem-Early Postmortem	15.444	4.558	3.388	0.001	0.004
14-Day Postmortem-"Perimortem"	23.302	4.727	4.929	<0.001	<0.001
7-Day Postmortem-Early Postmortem	7.500	4.690	1.599	0.110	0.659
7-Day Postmortem-"Perimortem"	15.357	4.855	3.163	0.002	0.009
Early Postmortem-"Perimortem"	7.857	4.855	1.618	0.106	0.634

Each row tests the null hypothesis that the Sample 1 and Sample 2 distributions are the same.

Asymptotic significances (2-sided tests) are displayed. The significance level is .050.

<sup>a</sup>Significance values have been adjusted by the Bonferroni correction for multiple tests.

When removing whole individuals from the tests rather than from individual groups when they appear as outliers, again similar results are found. Here the results of the Kruskal-Wallis H-test found a significant difference between the four time groups with  $p < 0.001$  ( $H = 23.977$ ;  $\eta^2 = 0.874$ ). Similarly, the results of the Spearman Rho correlation found a strong negative correlation ( $r = -0.941$ ;  $p < 0.001$ ). These results also indicate that there is a strong, patterned degradation in the osteoclast number over the time periods (Fig. 4.2.8). Like with the outliers included, and with the outliers excluded on the individual level, the post hoc results also found three of six pairs having a significant difference. These pairs were the same as with the individual outliers removed with the significant pairs being perimortem – 7-day postmortem

( $p=0.002$ ;  $H=3.087$ ), perimortem – 14-day postmortem ( $p<0.001$ ;  $H=4.711$ ), and early-postmortem – 14-day postmortem ( $p=0.003$ ;  $H=2.957$ ) (Table 4.2-3). These results are suggestive that a difference does exist, but that difference truly becomes significant at the 7-day postmortem period. Further, the results of the Friedman repeated measures test found a significant difference ( $p<0.001$ ) between the three postmortem time groups with the whole individual outliers removed, with the mean rank sums again declining in an equal and patterned rate with early-postmortem having a rank score of 3 and the 14-day postmortem having a mean rank score of 1 (Fig. 4.2.9). When assessed collectively, the results of these analyses indicate that there was a significant and measured declination in the number of osteoclasts over the four time groups as time progresses postmortem. Additionally, and similar to the analyses with the individual outliers removed, the results of the Kernel Ridge Regression  $\text{Chi}^2$  were significant at  $r^2=0.853$  meaning that 85.3% of the differences between the groups can be attributed to the time postmortem. Furthermore, there is an element of predictability, as these results indicate that there is an 85% probability that a future assessment of osteoclast degradation will find that the osteoclast count would fall within the trend line.

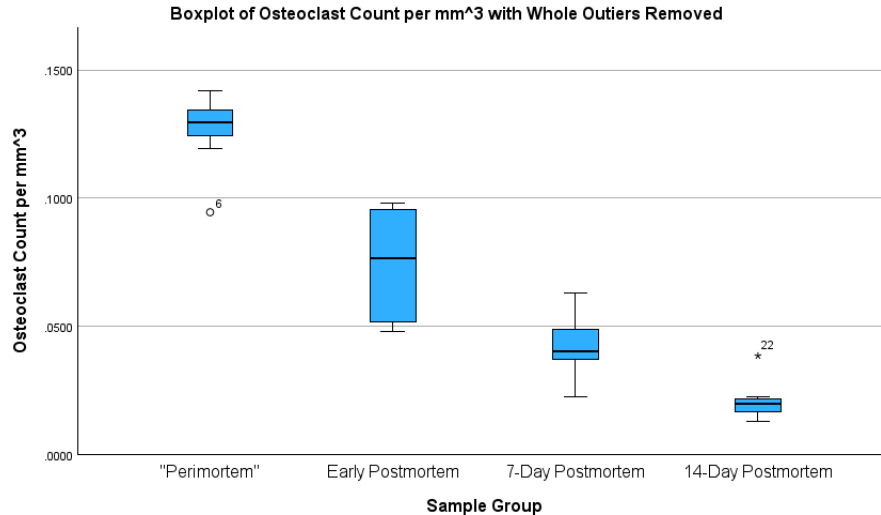


**Figure 4.2.8: Osteoclastic degradation over the four time groups with whole outliers removed. Note the removal of outliers produced more outliers.**

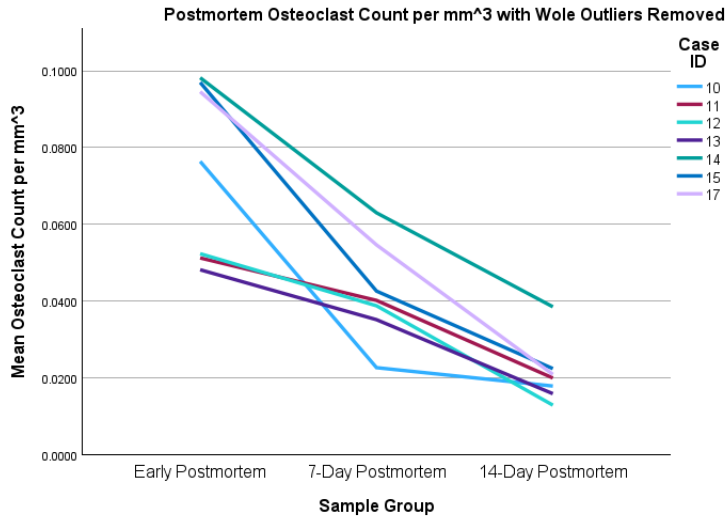


**Figure 4.2.9: Postmortem osteoclast degradation with whole outliers removed.**

**Table 4.2-3: Post Hoc Pairwise Results with Whole Outliers Removed.**

Sample 1-Sample 2	Test Statistic	Std. Error	Std. Test Statistic	Sig.	Adj. Sig. <sup>a</sup>
14-Day Postmortem-7-Day Postmortem	7.143	4.397	1.624	0.104	0.626
14-Day Postmortem-Early Postmortem	13.000	4.397	2.957	0.003	0.019
14-Day Postmortem-"Perimortem"	20.714	4.397	4.711	<0.001	0.000
7-Day Postmortem-Early Postmortem	5.857	4.397	1.332	0.183	1.000
7-Day Postmortem-"Perimortem"	13.571	4.397	3.087	0.002	0.012
Early Postmortem-"Perimortem"	7.714	4.397	1.754	0.079	0.476

Each row tests the null hypothesis that the Sample 1 and Sample 2 distributions are the same.

Asymptotic significances (2-sided tests) are displayed. The significance level is .050.

<sup>a</sup>. Significance values have been adjusted by the Bonferroni correction for multiple tests.

As age and sex can influence osteoclastic abundance, a Kruskal-Wallis ANOVA (age) and a Mann-Whitney U-test (assigned sex) were run to test for significant differences. The results of the Kruskal-Wallis H-test, with age cohorts divided by lustrum, found that there was no significant difference in any of the segregated time groups. Similarly, sex had no significant variation between the groupings with the Mann-Whitney U-test (Table 4.2-4). Additionally, to verify sex, a Kruskal-Wallis H-test was run using a 5 vs 5 all male comparison (with outliers removed) was run with the results finding that there was no significant difference ( $p < 0.001$ ;  $H = 16.189$ ;  $\eta^2 = 0.824$ ). While age and sex may have an effect on the number of active osteoclasts within an individual, the results of these studies demonstrated that with this study cohort, neither

age nor sex played a significant role in the number of osteoclasts present in the sample, and that the degradation seen is more likely than not related to time progressing beyond somatic death. However, it should be noted that for the Mann-Whitney U-test regarding sex, the distribution of males and females is so out of balance and the  $n$  within the female cohort small, the non-significant results were as expected and can be considered a major limitation of the test. As a result, a similar study with a more robust cohort may find that sex does have an impact on the overall results.

**Table 4.2-4: Results of the Kruskal-Wallis (Age) and Mann-Whitney U-test (Sex) results.**

	Test	$p$ -Value	$H/U$ -Stat	Cliff's $\delta/\eta^2$
Age	Perimortem	$p=0.385$	$H=3.040$	$\eta^2=0.008$
	Early Postmortem	$p=0.427$	$H=4.911$	$\eta^2=0.029$
	7-Day Postmortem	$p=0.683$	$H=3.111$	$\eta^2=0.630$
	14-Day Postmortem	$p=0.395$	$H=5.178$	$\eta^2=0.060$
Sex	Early Postmortem	$p=1.000$	$U=11.000$	$\delta=2.460$
	7-Day Postmortem	$p=0.111$	$U=17.000$	$\delta=3.801$
	14-Day Postmortem	$p=0.190$	$U=16.000$	$\delta=3.578$

#### 4.2.4 Discussion and Conclusion

The results of this study have found that it is clear that cellular data is potentially a good metric for establishing the postmortem interval. Whether one includes or excludes, in any fashion, the present outliers, the results of this study have shown a clear and marked decline in the number of counted osteoclasts from the perimortem group to the 14-day postmortem group. Further, that decline can be exponentially marked as the raw number of cells dropped from group to group as time progressed postmortem, with a stronger decrease at each time jump. With this particular study those jumps started as a 71.5% decrease from the perimortem to the early-postmortem, which then increased to a 55% decrease between the early- and 7-day postmortem, and finally a 51% decrease from the 7-day to the 14-day postmortem time groups. However, while there was a marked decrease in the raw counts from group to group, when standardized by bone volume, the mean cell count drops decreased to 58.6%, 57.3%, and 49.99% respectively, and the post hoc analyses only found a significant difference at the 7-day postmortem mark.

There was no significant difference in any post hoc pairwise analyses between the perimortem – early-postmortem pairing.

When one examines the boxplots of the various analyses (outliers included, individual outliers excluded, whole outliers excluded), it is clear that the time grouping with the greatest amount of range is that of the early-postmortem. With this, a potential confounding variable may be at play which has an impact on the results and implications of the present study. As noted in Materials and Methods (Ch. 4.2.3) there was a temporal range in the time between the cardiopulmonary death of the individual and the receipt of the corporal remains by the Division of Anatomy at the University of Toronto, ranging from 24 – 48 hours. As a result, for the initial collection of the postmortem sample, there was a variable time range post-cardiopulmonary death that was translated into the early-postmortem group. This time variability was removed and standardized in the other two postmortem groupings (7-day and 14-day postmortem) as they were timed *not to* collection, but to the donor's cardiopulmonary death. The result of this is that the early-postmortem group is the only group with a temporal variability, and, in general, being so close to cardiopulmonary death, those donors who were received closer to the time of cardiopulmonary death (and therefore an earlier sample harvesting time), would potentially have a greater abundance of osteoclasts than those which were received at a longer time from the donor?

Additionally, for practical considerations of this study, the samples were held in an extracorporeal environment (i.e., held within sealed jars); there is a question of cellular survival in an atmospheric environment. Boyce *et al.* (41) and Blair *et al.* (233) have shown osteoclastic damage and reduced resorptive properties when outside of a humidified low-oxygen environment, such as a corporeal environment. However, in this particular case, there were practical considerations that had to have been taken into account, namely that the remains from which the postmortem samples were derived came from individuals scheduled for chemical embalming, as the donors wished their remains to be used in anatomical instruction. Though the exposure to an atmospheric environment may have aided in the demise of cellular abundance, by examining other aspects of autolytic activity as a result of decomposition, one cannot discount a natural degradation as a result of PMI as well. Future studies, however, should account for the cellular environment, and use of animal models as a proxy would assist in separating the degradation as a result of atmospheric necrosis from decompositional autolysis.

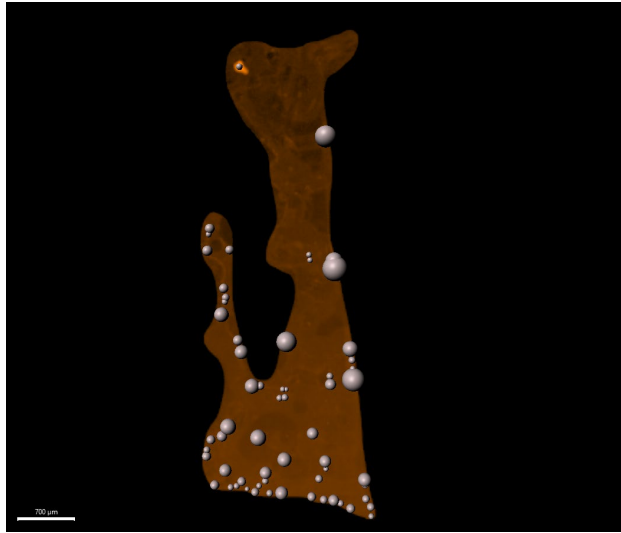


**Figure 4.2.10: Perimortem sample with cellular material indicated with spheres. Note: The image is generated from the 1st slice, while the calculations are through the whole of the sample. The relative size of the spheres is based on the algorithmic average pixel intensity found within each sphere rather than the anatomical size of the object calculated.**

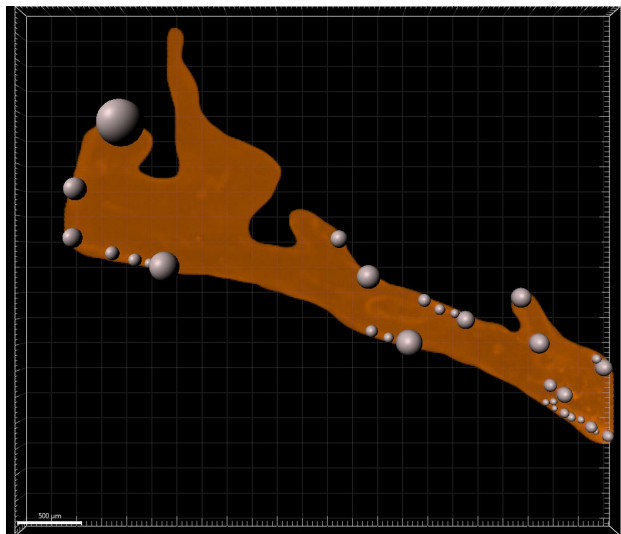


**Figure 4.2.11: Early-postmortem sample.**

Overall, however, the present study was able to determine that cellular degradation has potential to be an excellent method to determine the postmortem interval in remains in the early (2-week) postmortem period. The results of this study found that there was a significant decrease in osteoclasts over time and, as the time frame expands, that decrease becomes more marked. Between the perimortem and the early postmortem grouping the decrease is 71.5% but

by 7 days that decrease increases by an additional 55%. Between 7 days and 14 days there is an additional 51% decrease. Further, the results of the Kernel Ridge Regression analyses was suggestive that there was an element of predictability in the results with  $\approx 75.2\% - 85.3\%$  of the variation in the samples can be explained by the time postmortem. This would mean that when assessing the postmortem interval through the use of osteoclast number, there would be a probability of 75% – 85% that the count would fall within the predicted trend line. That said, however, given the low sample size, the potential influence of age and sex (though that influence was not detected in this sample cohort), and the various environmental factors, more research is needed prior to a viable deployable model is created for use is assessing the postmortem interval with osteoclast counts. However, this study has shown that the potential is present for such a model to be created following further research,

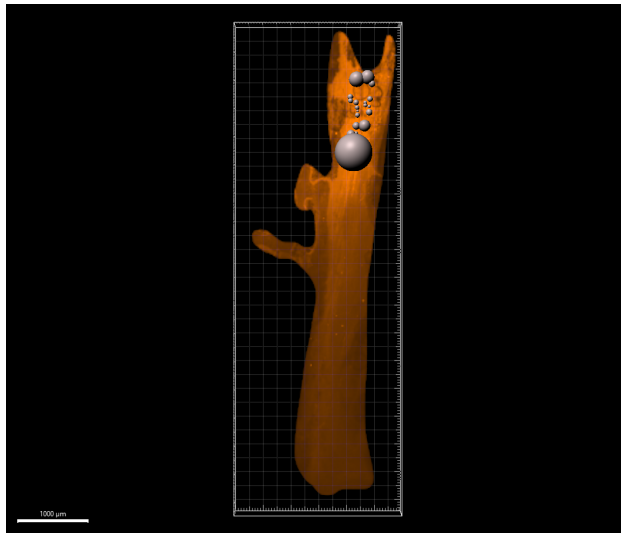


**Figure 4.2.12: 7-day postmortem sample from same individual as Fig. 4.2.11.**

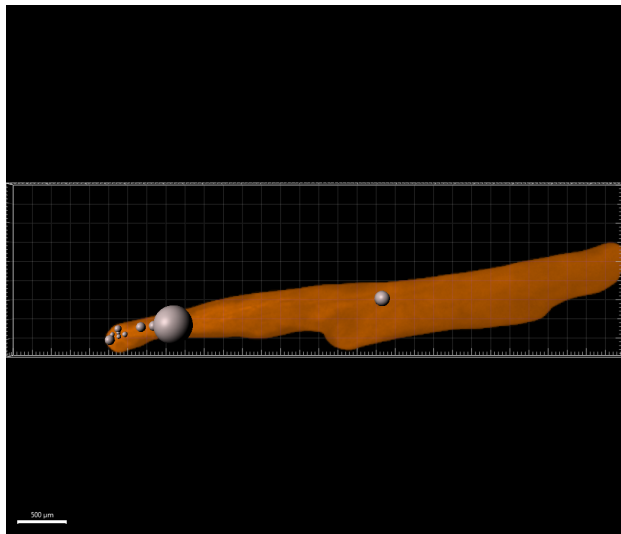


**Figure 4.2.13: 14-day postmortem sample, from same individual as Figs. 4.2.11 and 4.2.12.**

That said, one does have to consider the individual variation that could be present when considering the use of osteoclast as a measure of determining the postmortem interval. While this study did not find that age was a significant factor, previous studies have demonstrated that age can affect osteoclast abundance and activity (234). For this study the perimortem and the postmortem groups are significantly different by age with the age cohorts not even overlapping, but when the entire cohort was divided grouped by lustrum and cellular abundance examined within each time group, no significant difference was found. This lack of significance within the postmortem group in particular is indicative that the variation in osteoclast abundance within the postmortem subset is due to the timing rather than age. In addition to age, the overall health of the individual could also serve as a variable affecting the abundance of osteoclasts in a bone sample. That said, when calculating the number of cells by volume of a cortical iliac sample, noting some overlap between the groups, the average number of cells in a perimortem sample should be close to 0.126 cells per  $\text{mm}^3$  of bone, dropping to 0.042 cells per  $\text{mm}^3$  of bone at 7-days postmortem and then finishing at 0.021 cells per  $\text{mm}^3$  of bone 14-days following cardiopulmonary death. This number with regards to the perimortem sample is low compared to published literature, however, it should be noted that very few articles could be found noting an actual hard count of cells, with the closest being that of Gruber *et al.* (235) which calculated 0.96 ( $\pm 0.4$ ) osteoclasts per  $\text{mm}^2$  of bone. However, two issues arise when comparing the Gruber *et al.* (235) piece with the present study, namely that the authors were examining for cell activity in postmenopausal women, and that the authors were calculating  $\text{mm}^2$  where the present study

examines mm<sup>3</sup> of bone. Additionally, most remaining literature is limited to mice studies with no human correlation.

There were some limitations for this study that should be noted and should be addressed with further research. To begin, due to the effects of the COVID-19 pandemic and the freeze on anatomical donations, the sample size was only 18 individuals, with only 9 having any individual analysis beyond single imaging. That said, while this project was a histological study in methodology, this project, and its sample size in more in line with soft-tissue human decompositional research (236, 237). Moreover, power and  $\eta^2$  effect size analyses were conducted which demonstrated a moderate to large chance of obtaining a true result. Additionally, there was variation in age of the samples, but when examining the difference between the major groups (peri- and postmortem), age was not found to be significant. This study was also heavily biased towards males, with the whole of the perimortem group being male. However, when accounting for assigned sex using a Mann-Whitney U-test, this again was not found to be a significant factor. Though age and sex were not found to be significant with this study, however, given the limited sample size of this study, this is a limiting factor, and a more robust study may find that both age and sex do have a significant impact on the overall results. One also has to consider the use of biopsies as a proxy for perimortem fractures. This process creates a ring-like fracture which could cause osteoclastic travel in a 360° pattern within the sample. Further, such samples cause a complete removal from the body habitus thus eliminating means of osteoclasts and progenitor cells from outside the sample from attending to the wound site and resorbing the necrotic bone at the fracture margin. It should be noted that this study was conducted in a controlled environment, and that external environmental factors may have an effect of both cellular migration postmortem and cellular degradation.

Given the ethical and practical nature of studying such physiological activities in a controlled environment, animal studies (preferably mice) would be required to better understand these processes. The use of animal models would also allow for the control of confounding factors found within the present study, such as age and osteological sex; all known to affect osteoclastic levels. The use of animal studies would also allow for a control of additionally health and physiological factors, time factors such as time since death and time to fixation. And finally, the use of animal models would allow for an expansion of the total number of subjects per group.

One of the more difficult tasks when assessing skeletal remains in a forensic context is the assessment of the postmortem interval, particularly as time progresses beyond somatic death. Several methods used that yield high levels of accuracy and precision in the pathological world, drop their accuracy and precision as time progresses and lose their usefulness after around 7 days postmortem (1-5). The results of this study have found that the assessment of osteoclastic presence may be a good marker for the calculation of a postmortem interval. This research suggests that higher osteoclast count over 0.1 per mm<sup>3</sup> of bone, it is indicative of remains, including bone, being closer to somatic death, though if the count is lower (<0.02 cells per mm<sup>3</sup> of bone) then one is at 2 weeks or longer postmortem. This study examined up to 2 weeks post mortem, and while the approach works within a 2-week time frame, with the rate of decrease, it is possible that if there are no osteoclasts present, the PMI could be beyond 4 weeks. This was calculated in that the cell count appears to divide approximately 50% - 60% at every measurable turn. Between the perimortem – early-postmortem/early-postmortem – 7-day postmortem, the drop was approximately 60% (58% and 57% respectively), while between the 7-day and 14-day postmortem the decrease is approximately 50%. If projected, by 21-day postmortem the calculable cell count should be estimated at 0.01/mm<sup>3</sup>, while after that the count could be estimated as negligible. As such, while additional methodologies may be augmented for deaths occurring after approximately one month post-cardiopulmonary death, this study has shown that it would be a potentially useful tool in assessing the postmortem interval for remains with an estimated postmortem interval of less than one month.

## Chapter 5 Conclusions

### 5.1 Combined Study Findings

The results of this study have demonstrated multiple ways in which anthropologists could employ histological and histochemical variables to assess the postmortem interval of skeletal remains within the early postmortem period. This study examined the degradation of proteins (osteopontin and osteocalcin) and the postmortem degradation of osteoclasts.

Histotaphonomically, when examining animal bone (specifically *S. scrofa*), there is a significant difference in the pixel histograms depicting colour intensities between the 5-year sample and the fresh sample. This suggests that by using laser scanning confocal microscopy it is possible to assess whether a bone is from an individual who died more or less recently, which is particularly useful when gross taphonomic features may not be present on the bone. This study was also able to demonstrate that laser scanning confocal microscopy could be used to map diagenetic alterations within bone. Such information is valuable when examining bone histologically for evidence of pathological and traumatic changes because it allows the investigator to exclude or focus on diagenetic regions for the assessment.

This study was also able to demonstrate that cellular degradation occurs at a statistically significant rate suggesting these processes could be used to generate formulae for estimating the PMI. With regards to protein degradation, and specifically osteopontin degradation, the results were a bit more complicated. While there was a significant difference between the time groups, a closer look between those time groups found that difference only became pronounced at around the 7-day postmortem time period. However, while it this degradation was pronounced starting at the 7-day postmortem period, an examination of the postmortem samples alone found that there was no real pattern that could be discerned. This overall study utilized two constituent studies that examined osteopontin degradation (Ch. 2.3 and Ch. 3.2), each yielding similar yet differing results. Specifically, Ch. 2.3, comparing unembalmed biopsy samples which were labeled as “perimortem” in Ch. 3.2, found that there was no significant difference between the unembalmed and the embalmed groups until the outliers were removed. Meanwhile, Ch. 3.2 found that there was a significant difference between the time groups, but those differences

lacked a real pattern and only became discernible at around the 7-day postmortem period. Given that both studies examined the difference and degradation of osteopontin between effective time groups, the next step is to combine these two studies (Ch. 2.3 and Ch. 3.2) and determine if there was a discernible pattern that extended beyond the 14-day postmortem period, to the 6-month period.

When combined, the results of Ch. 2.3 and Ch. 3.2 found a significant variation in the pixel intensity's standard deviations using both a Kruskal-Wallis H-test and Spearman rho correlation test ( $p=0.009$ ;  $r=-0.469$ ;  $\eta^2=0.248$ ), although there was not a significant difference in the mean pixel intensity when accounting for 5 time groups [perimortem – 6-month] ( $p=0.063$ ;  $\eta^2=0.129$ ) (see Figs. 5.1.1 – 5.1.3). Additionally, there was a weak negative correlation with regards to the mean intensity data ( $r=-0.363$ ;  $p=0.017$ ) and a moderate negative correlation with regards to the standard deviation data ( $r=-0.491$ ,  $p<0.001$ ). However, when one explores the pairwise post hoc tests from the Kruskal-Wallis H-tests for mean intensity, like with the Ch. 3.2, no real discernible pattern exists. Specifically, only two of 10 pairs yielded a significant difference: that of the perimortem – 7-day postmortem ( $p=0.012$ ), and perimortem – 14-day postmortem ( $p=0.010$ ) (see Table 5.1-1). Interestingly, there was not a significant difference between the perimortem – 6-month postmortem ( $p=0.063$ ), further indicating that there is no real pattern in the degradation of osteopontin between the now 5 time groups. When it comes to the pairwise post hoc results from the standard deviation analyses, four of the 10 groups yielded significant differences including perimortem – early-postmortem ( $p=0.015$ ), – 7-day postmortem ( $p=0.009$ ), – 14-day postmortem ( $p=0.003$ ), – 6-month postmortem ( $p=0.002$ ) (see Table 5.1-2). These pairwise results, though not indicating a significant difference between the various postmortem groups, do indicate that there was a decline from the perimortem group.

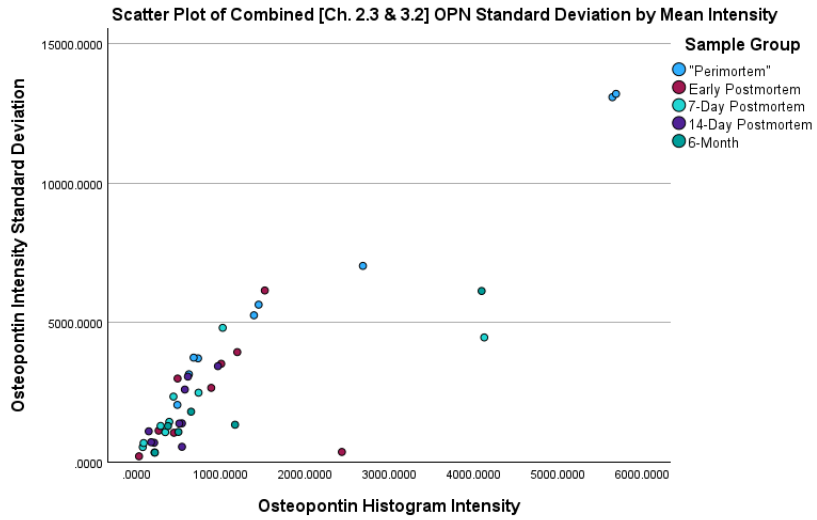


**Figure 5.1.1: Scatter plot of combined Ch. 2.3 & Ch. 3.2 mean intensity and standard deviation.**

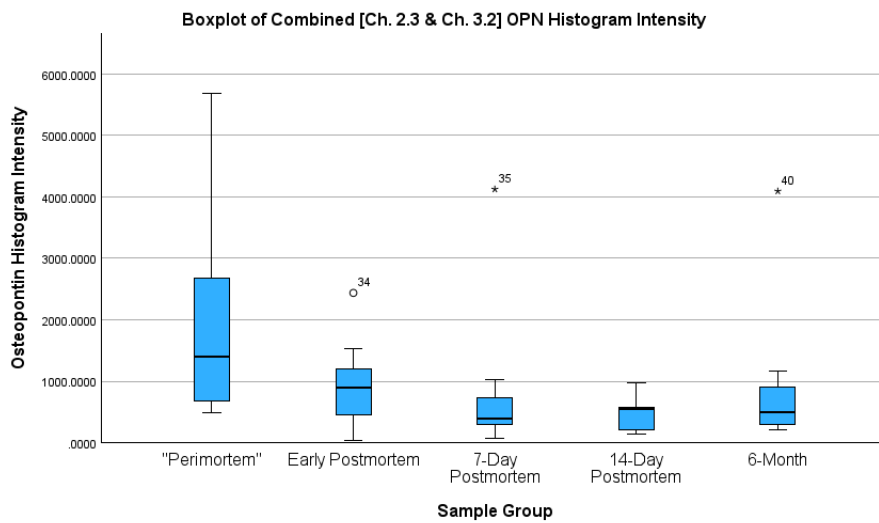


**Figure 5.1.2: Boxplot of combined Ch. 2.3 & Ch. 3.2 osteopontin mean intensity.**

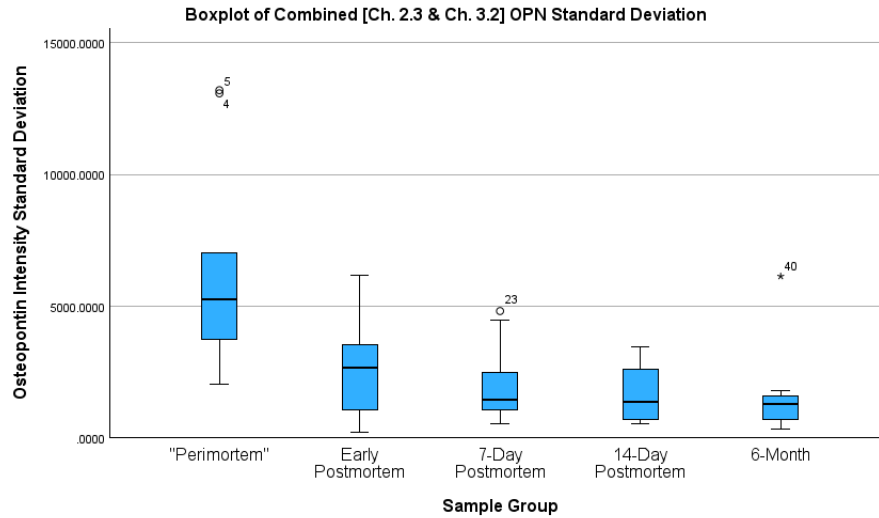


**Figure 5.1.3: Boxplot of combined Ch. 2.3 & Ch. 3.2 osteopontin standard deviation intensity data.**

**Table 5.1-1: Post hoc pairwise results from combined Ch. 2.3 & Ch. 3.2 osteopontin mean intensity.**

Sample 1-Sample 2	Test Statistic	Std. Error	Std. Test Statistic	Sig.	Adj. Sig. <sup>a</sup>
14-Day Postmortem-7-Day Postmortem	0.444	5.919	0.075	0.940	1.000
14-Day Postmortem-6-Month	-3.762	6.328	-0.594	0.552	1.000
14-Day Postmortem-Early Postmortem	6.778	5.919	1.145	0.252	1.000
14-Day Postmortem-"Perimortem"	15.333	5.919	2.590	0.010	0.096
7-Day Postmortem-6-Month	-3.317	6.328	-0.524	0.600	1.000
7-Day Postmortem-Early Postmortem	6.333	5.919	1.070	0.285	1.000
7-Day Postmortem-"Perimortem"	14.889	5.919	2.515	0.012	0.119
6-Month-Early Postmortem	3.016	6.328	0.477	0.634	1.000
6-Month-"Perimortem"	11.571	6.328	1.829	0.067	0.675
Early Postmortem-"Perimortem"	8.556	5.919	1.445	0.148	1.000

Each row tests the null hypothesis that the Sample 1 and Sample 2 distributions are the same. Asymptotic significances (2-sided tests) are displayed. The significance level is .050.

<sup>a</sup>. Significance values have been adjusted by the Bonferroni correction for multiple tests.

**Table 5.1-2: Post hoc pairwise results of combined Ch. 2.3 & Ch. 3.2 osteopontin standard deviation data.**

Sample 1-Sample 2	Test Statistic	Std. Error	Std. Test Statistic	Sig.	Adj. Sig. <sup>a</sup>
6-Month-14-Day Postmortem	1.762	6.328	0.278	0.781	1.000
6-Month-7-Day Postmortem	4.095	6.328	0.647	0.518	1.000
6-Month-Early Postmortem	5.206	6.328	0.823	0.411	1.000
6-Month-"Perimortem"	19.651	6.328	3.105	0.002	0.019
14-Day Postmortem-7-Day Postmortem	2.333	5.919	0.394	0.693	1.000
14-Day Postmortem-Early Postmortem	3.444	5.919	0.582	0.561	1.000
14-Day Postmortem-"Perimortem"	17.889	5.919	3.022	0.003	0.025
7-Day Postmortem-Early Postmortem	1.111	5.919	0.188	0.851	1.000
7-Day Postmortem-"Perimortem"	15.556	5.919	2.628	0.009	0.086
Early Postmortem-"Perimortem"	14.444	5.919	2.440	0.015	0.147

Each row tests the null hypothesis that the Sample 1 and Sample 2 distributions are the same. Asymptotic significances (2-sided tests) are displayed. The significance level is .050.

<sup>a</sup>. Significance values have been adjusted by the Bonferroni correction for multiple tests.

However, as noted in Ch. 2.3 and 3.2, there were outliers within those studies. The question becomes what the nature of those outliers is. As noted in Ch. 3.2.3.1, outliers can arise due to artifacts from the processing and imaging of histological slides, or as a result of biological differences within the samples themselves. To address these possibilities, as conducted in Ch. 3.2, two methodologies were employed: one where the individual outliers were removed from the individual statistics, and one where the whole individual was removed. A z-score analysis was conducted in IBM™ SPSS® v.29 (219) to identify and ultimately exclude those outliers.

When examining the results of the combined osteopontin Kruskal-Wallis H-test with individual outliers removed, a significant difference does appear with  $p=0.022$  ( $\eta^2=0.214$ ) with the mean intensity and the standard deviation results dropping to  $p=0.014$  ( $\eta^2=0.251$ ) demonstrating that there was a measurable and significant variation (Figs 5.1.4 - 5.1.6). When examining the post hoc pairwise tests for the mean intensity, the results found that, like with the outliers included, there is not a clear discernible pattern within the 10 pairs, though it does appear that a declination does become significant at around the 7-day postmortem period as this is when a significant difference begins to exist. Specifically, there is a significant difference between the perimortem – 7-day postmortem ( $p=0.003$ ), – 14-day postmortem ( $p=0.008$ ), and – 6-month

postmortem pairs ( $p=0.023$ ) (see Table 5.1-3). Additionally, when examining the post hoc pairwise results for the standard deviation data, again like with the outliers included, four of the 10 pairs are found to be significant. Specifically, those pairs are the ones with perimortem coupled with each of the postmortem groups: early-postmortem ( $p=0.037$ ), 7-day postmortem ( $p=0.011$ ), 14-day postmortem ( $p=0.008$ ), and 6-month postmortem ( $p<0.001$ ) (see Table 5.1-4). In addition to the Kruskal-Wallis H-tests, a Spearman Rho correlation test for both the mean intensity and standard deviation yielded moderate negative correlations at  $r=-0.436$  ( $p=0.005$ ) for the mean intensity and  $r=-0.517$  ( $p<0.001$ ) for the standard deviations. These results, coupled with the Kruskal-Wallis H-tests and the subsequent post hoc pairwise tests indicate that there is a possible relationship between the mean pixel intensity and standard deviation data, and time postmortem.

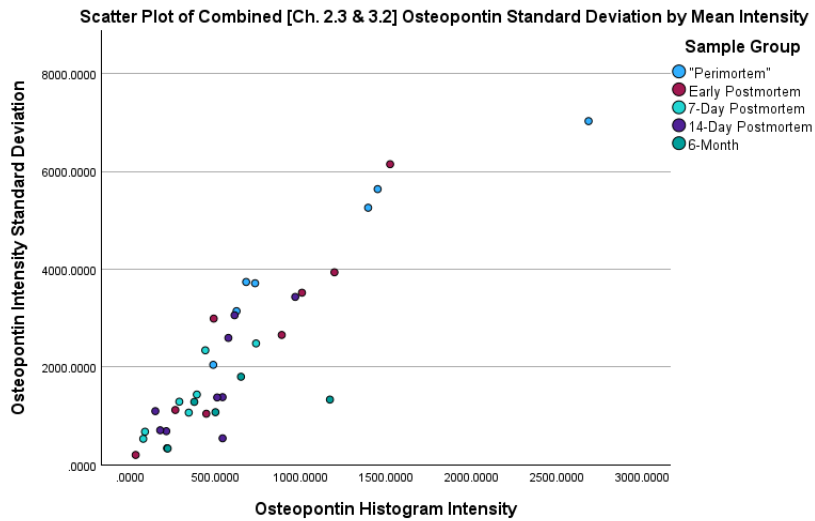


**Figure 5.1.4: Scatter plot of combined Ch. 2.3 & Ch. 3.2 osteopontin mean intensity and standard deviation data with individual outliers removed.**

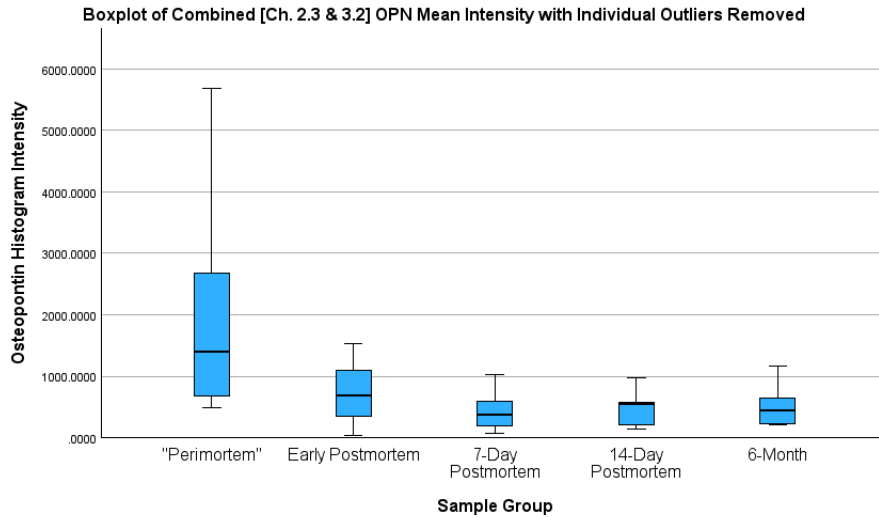


**Figure 5.1.5: Boxplot of combined Ch. 2.3 & Ch. 3.2 osteopontin mean intensity data with individual outliers removed.**

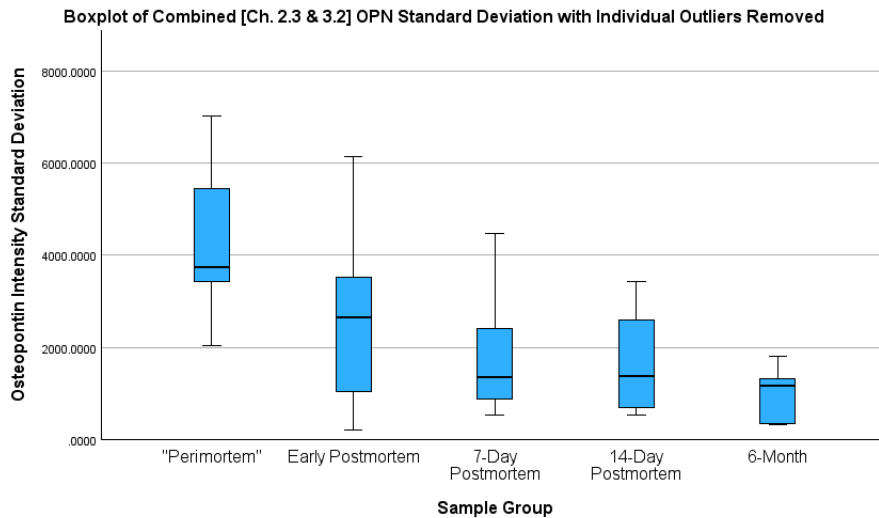


**Figure 5.1.6: Boxplot of combined Ch. 2.3 & 3.2 osteopontin standard deviation data with individual outliers removed.**

**Table 5.1-3: Post hoc pairwise combined Ch. 2.3 & Ch. 3.2 mean intensity results with individual outliers removed.**

Sample 1-Sample 2	Test Statistic	Std. Error	Std. Test Statistic	Sig.	Adj. Sig. <sup>a</sup>
7-Day Postmortem-14-Day Postmortem	-2.542	5.681	-0.447	0.655	1.000
7-Day Postmortem-6-Month	-3.042	6.314	-0.482	0.630	1.000
7-Day Postmortem-Early Postmortem	7.500	5.845	1.283	0.199	1.000
7-Day Postmortem-"Perimortem"	17.097	5.681	3.010	0.003	0.026
14-Day Postmortem-6-Month	-0.500	6.161	-0.081	0.935	1.000
14-Day Postmortem-Early Postmortem	4.958	5.681	0.873	0.383	1.000
14-Day Postmortem-"Perimortem"	14.556	5.511	2.641	0.008	0.083
6-Month-Early Postmortem	4.458	6.314	0.706	0.480	1.000
6-Month-"Perimortem"	14.056	6.161	2.281	0.023	0.225
Early Postmortem-"Perimortem"	9.597	5.681	1.689	0.091	0.911

Each row tests the null hypothesis that the Sample 1 and Sample 2 distributions are the same. Asymptotic significances (2-sided tests) are displayed. The significance level is .050.

<sup>a</sup>. Significance values have been adjusted by the Bonferroni correction for multiple tests.

**Table 5.1-4: Post hoc pairwise results of combined Ch. 2.3 & Ch. 3.2 osteopontin standard deviation data with individual outliers removed.**

Sample 1-Sample 2	Test Statistic	Std. Error	Std. Test Statistic	Sig.	Adj. Sig. <sup>a</sup>
6-Month-14-Day Postmortem	5.667	6.009	0.943	0.346	1.000
6-Month-7-Day Postmortem	5.958	6.158	0.968	0.333	1.000
6-Month-Early Postmortem	8.889	6.009	1.479	0.139	1.000
6-Month-"Perimortem"	20.905	6.343	3.296	0.001	0.010
14-Day Postmortem-7-Day Postmortem	0.292	5.540	0.053	0.958	1.000
14-Day Postmortem-Early Postmortem	3.222	5.375	0.600	0.549	1.000
14-Day Postmortem-"Perimortem"	15.238	5.746	2.652	0.008	0.080
7-Day Postmortem-Early Postmortem	2.931	5.540	0.529	0.597	1.000
7-Day Postmortem-"Perimortem"	14.946	5.901	2.533	0.011	0.113
Early Postmortem-"Perimortem"	12.016	5.746	2.091	0.037	0.365

Each row tests the null hypothesis that the Sample 1 and Sample 2 distributions are the same. Asymptotic significances (2-sided tests) are displayed. The significance level is .050.

<sup>a</sup>. Significance values have been adjusted by the Bonferroni correction for multiple tests.

Because outliers may be of a biological origin rather than artifactual in nature, a second method of addressing outliers is to remove the individual from the test rather than the individual outlier. When re-assessing the tests with whole individuals removed, the results of both the

Kruskal-Wallis H-test and the Spearman Rho correlation tests mirror in interpretation that with the outliers included. In particular, the results of the Kruskal-Wallis H-test for the mean intensity data found no significant difference with  $p=0.056$  ( $\eta^2=0.180$ ) while the results of the standard deviation test did yield a significant difference with  $p=0.008$  ( $\eta^2=0.340$ ) (see Fig. 5.1.7 – 5.1.9). When examining the post hoc pairwise results, like that with the outliers included, the only two significant pairs for mean intensity were perimortem – 7-day postmortem ( $p=0.004$ ), and perimortem – 14-day postmortem ( $p=0.026$ ) (see Table 5.1-5). The standard deviation post hoc pairwise results also mirrors those with the outliers included with four of the 10 significant pairs being the perimortem tied to each of the postmortem groups with early-postmortem ( $p=0.047$ ), 7-day postmortem ( $p=0.003$ ), 14-day postmortem ( $p=0.009$ ), and 6-month postmortem ( $p<0.001$ ) (see Table 5.1-6). Further, the results of the Spearman Rho correlation tests found a weak negative correlation for the mean intensity ( $r=-0.363$ ,  $p=0.035$ ), and a moderate negative correlation for the standard deviation data ( $r=-0.574$ ),  $p<0.001$ ).

Further, when examining the boxplots generated for the mean intensity, while that with the outliers included (Fig. 5.1.2) and individual outliers excluded (Fig. 5.1.5) demonstrate a subtle “U” pattern, with whole outliers excluded (Fig. 5.1.8) this “U” pattern remains present. That said it should be noted that there is limited but acknowledged difference between the 14-day and 6-month postmortem samples. In particular, the 6-month shows a slightly expanded range and higher mean. However, with all, the central low point is the 7-day postmortem group. This pattern suggests that the hypothesis that mean pixel intensity would decrease as postmortem time increases is not necessarily valid. When examining the data and results from Ch. 3.2, the hypothesis is weak, it does still hold water. There was no discernible pattern, but the decrease of the means, and the post hoc results demonstrating a significant difference at the 7-day postmortem mark indicates that a weak pattern may exist. However, this pattern may be masked by artifacts which fluorescence and mimic targeted material. However, the addition of the 6-month sample from Ch. 2.3, though demonstrating a significant difference from the CHUM samples, demonstrates an increase, rather than decrease from the 14-day postmortem sample. That said, as the fact that Ch. 2.3 did not utilize a repeated measure sample and was independent of the samples used in Ch. 3.2, one cannot exclude the presence of artifacts within this sample, that are artificially inflating the pixel intensity in comparison to the 14-day postmortem.

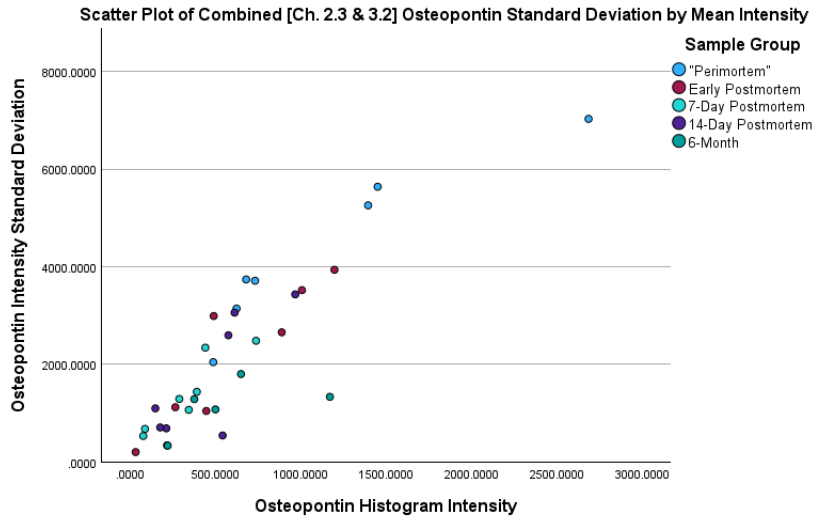


**Figure 5.1.7: Scatter plot of combined Ch. 2.3 & Ch. 3.2 osteopontin mean intensity and standard deviation data with whole outliers removed.**

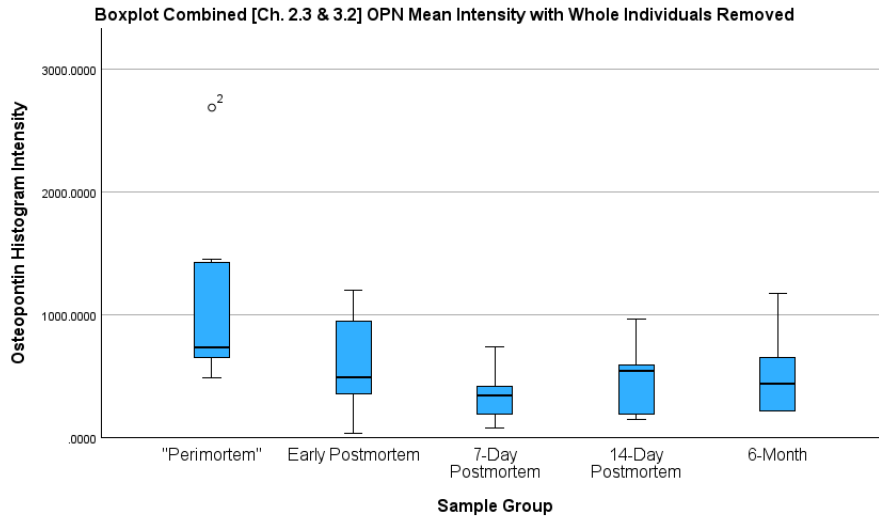


**Figure 5.1.8: Boxplot of combined Ch. 2.3 & Ch. 3.2 osteopontin mean intensity data with whole outliers removed.**

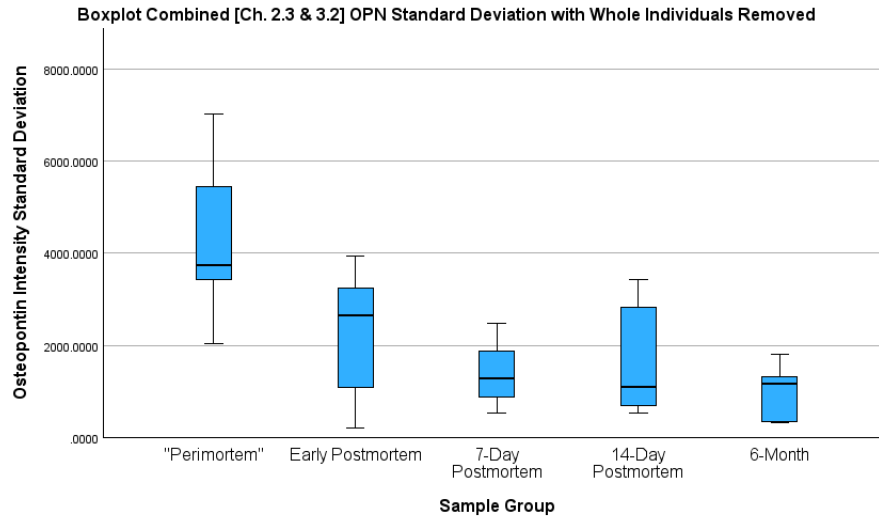


**Figure 5.1.9: Boxplot of combined Ch. 2.3 & Ch. 3.2 standard deviation data with whole outliers removed.**

**Table 5.1-5: Post hoc pairwise results for mean intensity of combined Ch. 2.3 & Ch. 3.2 with whole outliers removed.**

Sample 1-Sample 2	Test Statistic	Std. Error	Std. Test Statistic	Sig.	Adj. Sig. <sup>a</sup>
7-Day Postmortem-14-Day Postmortem	-3.429	5.323	-0.644	0.519	1.000
7-Day Postmortem-6-Month	-5.048	5.540	-0.911	0.362	1.000
7-Day Postmortem-Early Postmortem	7.143	5.323	1.342	0.180	1.000
7-Day Postmortem-"Perimortem"	15.286	5.323	2.872	0.004	0.041
14-Day Postmortem-6-Month	-1.619	5.540	-0.292	0.770	1.000
14-Day Postmortem-Early Postmortem	3.714	5.323	0.698	0.485	1.000
14-Day Postmortem-"Perimortem"	11.857	5.323	2.228	0.026	0.259
6-Month-Early Postmortem	2.095	5.540	0.378	0.705	1.000
6-Month-"Perimortem"	10.238	5.540	1.848	0.065	0.646
Early Postmortem-"Perimortem"	8.143	5.323	1.530	0.126	1.000

Each row tests the null hypothesis that the Sample 1 and Sample 2 distributions are the same. Asymptotic significances (2-sided tests) are displayed. The significance level is .050.

<sup>a</sup>. Significance values have been adjusted by the Bonferroni correction for multiple tests.

**Table 5.1-6: Post hoc pairwise results for standard deviation of combined Ch. 2.3 & Ch. 3.2 with whole outliers removed.**

Sample 1-Sample 2	Test Statistic	Std. Error	Std. Test Statistic	Sig.	Adj. Sig. <sup>a</sup>
6-Month-7-Day Postmortem	2.619	5.540	0.473	0.636	1.000
6-Month-14-Day Postmortem	4.476	5.540	0.808	0.419	1.000
6-Month-Early Postmortem	7.762	5.540	1.401	0.161	1.000
6-Month-"Perimortem"	18.333	5.540	3.309	0.001	0.009
7-Day Postmortem-14-Day Postmortem	-1.857	5.323	-0.349	0.727	1.000
7-Day Postmortem-Early Postmortem	5.143	5.323	0.966	0.334	1.000
7-Day Postmortem-"Perimortem"	15.714	5.323	2.952	0.003	0.032
14-Day Postmortem-Early Postmortem	3.286	5.323	0.617	0.537	1.000
14-Day Postmortem-"Perimortem"	13.857	5.323	2.603	0.009	0.092
Early Postmortem-"Perimortem"	10.571	5.323	1.986	0.047	0.470

Each row tests the null hypothesis that the Sample 1 and Sample 2 distributions are the same. Asymptotic significances (2-sided tests) are displayed. The significance level is .050.

<sup>a</sup>. Significance values have been adjusted by the Bonferroni correction for multiple tests.

Multiple factors have been found to be affect the overall presence of both OPN and OC. Factors such as health, age, sex, etc. may play a role in the base level of both OC and OPN found within each individual. When combining the OPN data for both Ch. 2.3 and Ch. 3.2, the results of the Kruskal-Wallis H-test found no significant variation in mean pixel intensity on account of age cohort (Table 5.1-7). Similarly, sex found no significant difference with the results of the Mann-Whitney U-test (Table 5.1-7). However, it should be noted, that for the Mann-Whitney U-test regarding sex, the distribution of males and females is so out of balance and the *n*-count within the female cohort is so small, the non-significant results were as expected and can be considered a major limitation of the test. As a result, a similar study with a more robust cohort may find that sex does have an impact on the overall results.

**Table 5.1-7: Combined (Ch. 2.3 & 3.2) osteopontin age and sex results. Note: Perimortem in this table is the same as “unembalmed” sample in Ch. 2.3 as the 6-Month is the “embalmed”.**

		Test		<i>p</i> -Value	<i>H/U</i> -Statistic
Osteopontin	Mean Pixel Intensity	Age	Perimortem	<i>p</i> =0.504	<i>H</i> =6.267
			Early Postmortem	<i>p</i> =0.703	<i>H</i> =6.333
			7-Day Postmortem	<i>p</i> =0.809	<i>H</i> =6.333
			14-Day Postmortem	<i>p</i> =0.158	<i>H</i> =6.333
			6-Month	<i>p</i> =0.423	<i>H</i> =6.000
	Standard Deviation	Age	Perimortem	<i>p</i> =0.504	<i>H</i> =6.267
			Early Postmortem	<i>p</i> =0.766	<i>H</i> =6.333
			7-Day Postmortem	<i>p</i> =0.742	<i>H</i> =6.333
			14-Day Postmortem	<i>p</i> =0.519	<i>H</i> =6.933
			6-Month	<i>p</i> =0.423	<i>H</i> =6.000
Osteopontin	Mean Pixel Intensity	Sex	Early Postmortem	<i>p</i> =0.556	<i>U</i> =13.000
			7-Day Postmortem	<i>p</i> =0.111	<i>U</i> =17.000
			14-Day Postmortem	<i>p</i> =1.000	<i>U</i> =10.000
			6-Month	<i>p</i> =1.000	<i>U</i> =5.000
	Standard Deviation	Sex	Early Postmortem	<i>p</i> =1.000	<i>U</i> =11.000
			7-Day Postmortem	<i>p</i> =0.190	<i>U</i> =16.000
			14-Day Postmortem	<i>p</i> =0.556	<i>U</i> =13.000
			6-Month	<i>p</i> =1.000	<i>U</i> =6.000

Examining the rest of the study, for the perimortem sample, the range of intensity for osteocalcin detected was 1839.4 at the high end and 285.08 at the low end, though most were between 623.19 – 877.91, meanwhile for the postmortem sample was between 2379.51 – 121.06 with most between 422.61 – 890.46. Here, though, there was no pattern as the means varied with a 48.72% difference between the highest mean intensity and lowest (14-day postmortem and 7-day postmortem). Similarly, with the standard deviations the variability was between a mean of 3673.75 (14-day postmortem) and 2138.42 (7-day postmortem) yielding a difference of 52.83%. The results of Ch. 4.2 studying cellular degradation found a significant, correlated, and

predictable decrease over the four time-groups (perimortem – 14-day postmortem) as well. When coupled and weighed with the results of Ch. 3.2, the use of cellular degradation was shown to be potentially the better marker for determining the postmortem interval in a period of 2 weeks post somatic death.

## 5.2 Limitations and Future Projects

There are some limitations with this study that must be recognized. The first of these limitations is the sample size. For the main portion of this study, the protein and cellular studies, this project had a total sample size of 18 individuals divided between 9 perimortem and 9 postmortem. While low when compared to typical histological studies, this project was more in line with decompositional research, which relies on the study of deceased individuals. As such, a sample size of 18 is more in line with recent decompositional research (236-238). Additionally, to account for a low sample size, power and eta-squared effect size analyses were run which yielded mixed results ranging between a moderate to a large while the power ranged from a low probability of a correct result (0.356 [embalmed/unembalmed]) to a high probability (0.890 [OPN standard deviation]). A future study should increase the number of samples, both in the perimortem and postmortem sample groups in order to incorporate more individual variation. In addition to the sample size, assigned sex variation should also be taken more into account. This study was weighted more towards those who were male, comprising 14 of the 18 individuals. As such, this project was not able to assess the effect assigned sex has on either protein or cellular abundance, which could ultimately affect the rate of degradation. This study did show, even with those samples from female individuals, that a significant degradation of both osteopontin and osteocalcin does take place, though when examining deeper, there was no clear pattern to that degradation. With a more balanced sample, however, the results may prove slightly different, and a more true representation will be had. Additionally, future research should try and incorporate both a more balanced and wide range of ages within the sample group. While age was not necessarily found to be a factor within this study, it cannot be overlooked that the perimortem group was significantly younger than the postmortem group. Further, within each group there was limited variation with most samples being within 15 years of each other. Age has been known to affect osteoclastic activity which can likewise affect osteopontin activity (228, 234), as such future research should take care, if possible, to broaden and control the ages of the samples.

One way to validate this study while mitigating these variables, and others, would be to replicate this study using animal models such as mice. Animal studies are rather common in clinical studies regarding protein and cellular studies as they can control for factors such as age, sex, physiological health, postmortem interval, time to fixation, and others. A review of PubMed found over 2,132 studies with mouse as an osteopontin model, 284 osteocalcin studies, and 813 osteoclastic studies (52). Additionally, the use of animal studies would allow for an increase in subject number which would ultimately invalidate the effects of issues such as artifacts and given a generally more accurate baseline of fluorescence and cellular count.

That said, animal studies are generally eschewed in forensic anthropological research, being limited mainly towards soft tissue decomposition. The limited ability to translate direct animal studies to exact human physiology invalidates their use in the legal context such as their admissibility in a criminal court of law. Even with soft tissue decomposition, recent studies have shown that the use of porcine models is not necessarily the best replicator of human decomposition (117, 239, 240). Animal studies can be useful in future research related to the present study, however. Given that the human study did find some significant variations, the use of a robust animal study could be used as the beginning stages of developing a controlled postmortem interval model for use in the field, though ultimately such a study would need to be confirmed using human subjects before it can be used in forensic and medico-legal contexts.

### 5.3 Reflections

Upon reflection of the cumulation of this study, two areas do demonstrate promise as being potential tools for future PMI estimation: histotaphonomy found in Ch. 2.2 and cellular (i.e. osteoclast) degradation in Ch. 4.2. With regards to the histotaphonomy portion, while there is debate on the viability of the RGB methodology, what was demonstrated is that there is a variance in the strengths of the emissions wavelengths between samples of differing diagenetic levels (fresh vs diagenetically altered). However, while Ch. 2.2 did demonstrate there was a difference between the diagenetically altered samples and the fresh samples, it must be noted that this study could not differentiate if those wavelength differences were from diagenetic biological or mineral agents. Furthermore, this particular study only looked at what can be termed as a longer PMI period, with the second phase of Ch. 2.2 not even considered “forensic” (i.e. < 75 years), but rather archaeological in nature. Chapter 2.2 used a postmortem sample group that

was 5 years and (at minimum) 2,300 years postmortem. While Ch. 2.2 can be considered a success in that it was able to distinguish the diagenetically altered sample groups, a more fulsome study would utilize decomposing remains and collect skeletal elements on a systematic schedule beginning with early skeletalization and ending after multiple years. This would allow researchers the ability to better target when diagenetic alterations become fluorescently viable and thus better able to develop a more accurate and useable PMI estimation tool. Additionally, as the second phase of Ch. 2.2 was able to find, a better avenue for analyses would be assessments on individual wavelengths rather than RGB assessments. This would allow for a more accurate representation of the targeted wavelengths rather than confounding wavelength strength as a single wavelength may present differently on multiple RGB channels.

The second portion of this study that generated positive results was that of the degradation of osteoclasts and their use as a potential PMI tool (Ch. 4.2). The results of Ch. 4.2 was able to find a significant and predictable degradation of osteoclasts as the postmortem interval progressed. Further, this study found that degradation demonstrated a clear pattern. That said, while Ch. 4.2 did demonstrate positive results, there were a number of areas that could be avenues for improvement. Specifically, while Ch. 4.2 did utilize a Friedman repeated measures test for the postmortem sample, the U of T postmortem sample was independent of the perimortem CHUM sample. A better model would utilize a postmortem sample that is derived from the same individuals as the perimortem samples. Additionally, while this study was able to quantify the osteoclasts through to the 14 day postmortem mark, this quantification could not assess the viability of the cells. A more robust study would assess both cellular abundance and viability as a means of assessing the postmortem interval. Additionally, future studies in osteoclast degradation needs to have a more robust number of individuals within the study, taking into account both sex and age. Further, such a study, like that with Ch. 2.2, would be better served by using remains experiencing active decomposition. Such a process would also incorporate environmental factors involved in soft tissue decomposition, which may have an impact on osteoclast degradation. That said, however, there are questions regarding the methodology of Ch. 4.2, specifically the use of laser scanning confocal microscopy. While one of the implied goals of this cumulative study was to find a singular imaging tool, in the case of osteoclast imaging, there is little gained for the cost. A longstanding traditional method of quantifying osteoclasts is polarized microscopy. Laser scanning confocal microscopy adds 3-

dimensional imaging, which allows for a more thorough quantification, 2-dimensional polarized imaging has long been verified in research with stains and imaging costs that are considerably more attractive to budget-tight agencies and departments.

The portion of this study that showed the least promise was that of the protein degradation (Ch. 2.3 & Ch. 3.2). While there was a significant difference found in the degradation of osteopontin, that difference came with no real pattern. There appears to be a significant difference by the 7-day postmortem period, but when the two studies are combined, the mean pixel intensity appears to then increase. These two studies appear to be the ones most susceptible to artifacts which may have an impact on the results. While, specifically, the results of Ch. 3.2 indicate the artifacts may be masking a true significant decreasing pattern, a more robust study is needed to address the artifact issues and verify that the suspected masked decrease is a true decrease. In addition, a more robust study should also consider sex and age, similar to Ch. 4.2, as well as utilizing a decompositional environment to determine if the decompositional process and environment has an effect. Most importantly, a more robust study should be verified against well tested methodologies such as ELISA, as a means of confirming that mean pixel intensity does in fact correlate to actual protein quantification.

In all of these studies, one of the most important factors that must be considered before adopting them into a valid and useable postmortem interval methodology is the implication and application of individuality. The body habitus can yield a wide range of physiological features including cellular and protein counts. The present studies used a low population, which could have an impact on the final results. Only with a wider population cohort with individualizing factors taken into account can a PMI method be created. While the incorporation of the histochemical portions of this study (proteins and cells) with the histotaphonomic may ultimately yield a precise postmortem model, it would require the forensic practitioner having a baseline understanding of the decedent's underlying cellular and protein situations. While at this stage this may be an impossible task, it might be possible to work backwards using current methodologies. The axiom in forensic science is that a practitioner utilizes multiple methodologies in any given assessment. Should a viable postmortem methodology be developed from the present cumulative study, one could apply a triple modality of OPN, OPN:OC, and osteoclast levels gather from the remains and compare them to already existing methodologies to develop a more accurate postmortem interval with greater precision that can become closer

somatic time of death. Even with the exclusion of the protein portion of this cumulative study, the osteoclast levels alone, when coupled with existing methodologies can aid in improving precision and accuracy in PMI estimation.

## 5.4 Implications

The results of this study have multiple implications in a variety of areas of study. At the forefront, this study was able to demonstrate that by using histotaphonomic and histochemical means, this study showed promise in developing a more accurate method of establishing the postmortem interval. Current methods for estimating the postmortem interval begins with utilizing the mortis triad (rigor, algor, and livor mortis) which can be fairly accurate up to 72-hours postmortem, as well as the use of vitreous humor and gingival tissues, both of which can be accurate just up to 7-days. However, as one progresses beyond this window, the estimates become both less accurate and less precise, particularly when the stages of early and advanced decomposition begin. Additionally, in cases of dismemberment (occurring through natural, accidental, or criminal activity) use of the mortis triad and similar early tissue-targeted methods may not even be viable. The results of this study, specifically the cellular data, have demonstrated that histochemical analyses may be useful in developing a more accurate and precise postmortem interval, following further research. In particular, the osteoclastic degradation study found that there was an element of predictability with the Kernal Ridge regression, demonstrating that it could be used to develop a tool and an accurate PMI could be made in a postmortem window of within 14-days. The protein fluorescence portion of the study, however, was much more complicated, and though yielding some significant results also demonstrated no clear pattern. This suggests that more research is needed before OPN and OC degradation can be considered a viable tool in PMI estimation. However, by converting the osteoclast portion of this study, and by improving the protein portion, these can also be used to help in understanding the death and post-death events, answer judicial questions, and subsequently assist in averting miscarriages of justice.

When examining the wider theories of death, as described in Chapter 1, the results of this study not only demonstrate that systemic death occurs at variable rates from somatic death, but that the skeletal system “dies” approximately 24-48 hours postmortem, demonstrated by noting that there is a significant decrease in osteoclasts <48hours postmortem. This project lends

credence to the notion that the body's systems do not completely shut down immediately following the cessation of cardiopulmonary function; but rather, like a large computer or industrial system, in stages. When examining the body as a whole, it is known that neurological activity ceases within minutes of cardiopulmonary function. The results of this project demonstrate that death of the skeletal system occurs 24 – 48 hours after cardiopulmonary cessation.

In the end, the goal of this research was to gain a better understanding of the degradation of protein and nature of cellular activity in the early postmortem interval (14 days post somatic death), further elucidating the decompositional process in the skeletal system. The results of this study have found a significant decrease in the levels of osteopontin over time while noting that osteocalcin remains relatively static over the period, though acknowledging that there was a lack of a clear pattern in those protein changes. Additionally, this study noted a significant and theoretically predictable decrease in osteoclastic abundance over that same period, and points to a migration of cells in the perimortem and early (<14 days) postmortem period. These results have demonstrated that it may be possible to create an accurate postmortem interval model using cellular degradations which can be used in the early postmortem period when the soft tissue may be too degraded for a precise PMI estimate.

That said, while this study has shown potential in the use of laser scanning confocal microscopy in forensic investigations to assist with the determination of the postmortem interval, this study is preliminary, and that more research is required on multiple fronts before an accurate model of PMI is developed. Among those factors that need to be studied is a baseline of both protein abundance and the quantification of fluorescence in all of the skeletal elements (bone). Further, a baseline of osteoclastic abundance within each bone is also needed before an accurate PMI model can be created that would stand up to the medico-legal rigor and used in forensic investigations. While age and assigned sex were found to not be significant within these studies, it is known that these factors do have physiological influence in the abundance of osteopontin, osteocalcin, and osteoclasts. Therefore, future research would be needed to again develop a universal baseline in order to develop a forensically viable model. And lastly, while this project did not consider population affinity or ancestry (race), it is possible, given external skeletal traits associated with ancestral population, that this, too, may influence a universal baseline of both protein abundance as well as osteoclastic abundance, and would need to likewise be studied in

order to develop a forensically viable PMI model that could be utilized in a court of law. In the end, however, this project, the histotaphonomic, protein, and cellular studies, has shown to be a good first step with this research.

## References

1. Zilg B, Bernard S, Alkass K, Berg S, Druid H. A new model for the estimation of time of death from vitreous potassium levels corrected for age and temperature. *Forensic Science International*. 2015 2015/09/01/;254:158–66.
2. Foster SN, Smith PR, Biggs M, Ruddy GN, Hollingbury FE, Morley SR. Estimation of postmortem interval using vitreous potassium levels in cases of fatal road traffic collision. *Archiwum Medycyny Sądowej i Kryminologii/Archives of Forensic Medicine and Criminology*. [journal article]. 2016:71–82.
3. Focardi M, Lanzilao L, Bonari A, Lazzeretti M, Lorubbio M, Ognibene A, Gualco B, Fanelli A, Pinchi V. Improvement in estimation of time since death by albumin and potassium concentrations in vitreous humor. *Forensic Science International*. 2020 2020/09/01/;314:110393.
4. Mazzotti MC, Fais P, Palazzo C, Fersini F, Ruggeri A, Falconi M, Pelotti S, Teti G. Determining the time of death by morphological and immunohistochemical evaluation of collagen fibers in postmortem gingival tissues. *International Journal of Legal Medicine*. 2019 2019/07/01/;39:1–8.
5. Srirangarajan S, Sindhu V, Raju S, Rao RJ, Prabhu S, Rudresh V. Evaluation of gingival tissue samples for predicting the time of death using histological and biochemical tests. *Forensic Science International*. 2021 2021/07/01/;324:110850.
6. Cardoso HF, Santos A, Dias R, Garcia C, Pinto M, Sergio C, Magalhaes T. Establishing a minimum postmortem interval of human remains in an advanced state of skeletonization using the growth rate of bryophytes and plant roots. *International Journal of Legal Medicine*. 2010 Sep;124(5):451–6.
7. Cattaneo C, Gibelli D. Postmortem Interval: Anthropology. *Wiley Encyclopedia of Forensic Science*.
8. Marks MK, Love JC, Dadour IR. Taphonomy and time: estimating the postmortem interval. *Hard evidence: case studies in forensic anthropology*. Ch. 2<sup>nd</sup> ed. Upper Saddle River, NJ: Prentice Hall; 2009;165–78.
9. Boaks A, Siwek D, Mortazavi F. Temporal degradation of bone collagen: a histochemical approach. *Forensic Science International*. 2014;240:104–10.
10. Bell LS. Histotaphonomy. In: Crowder CM, Stout SD, editors. *Bone Histology: An Anthropological Perspective*. Ch. 9. Boca Raton, FL: CRC Press; 2011;241–51.
11. Megyesi MS, Nawrocki SP, Haskell NH. Using accumulated degree-days to estimate the postmortem interval from decomposed human remains. *Journal of Forensic Sciences*. 2005 May;50(3):618–26.

12. Moffatt C, Simmons T, Lynch-Aird J. An Improved Equation for TBS and ADD: Establishing a Reliable Postmortem Interval Framework for Casework and Experimental Studies. *Journal of Forensic Sciences*. 2016;61(S1):S201–S7.
13. Smith DH, Ehrett C, Weisensee K, Tica C. Commentary on: Megyesi MS, Nawrocki SP, Haskell NH. Using accumulated degree-days to estimate the postmortem interval from decomposed human remains. *J Forensic Sci*. 2005;50(3):618–26. doi: 10.1520/JFS2004017; and Moffatt C, Simmons T, Lynch-Aird J. An improved equation for TBS and ADD: Establishing a reliable postmortem interval framework for casework and experimental studies. *J Forensic Sci*. 2016;61(Suppl 1):S201–S207. doi: 10.1111/1556-4029.12931. *Journal of Forensic Sciences*. 2023;68(1):355–8.
14. Mann RW, Bass WM, Meadows L. Time since death and decomposition of the human body: variables and observations in case and experimental field studies. *Journal of Forensic Sciences*. 1990 Jan;35(1):103–11.
15. Bass WM. Outdoor decomposition rates in Tennessee. In: Haglund W, Sorg M, editors. *Forensic Taphonomy: The Postmortem Fate of Human Remains*. Ch. Boca Raton, FL: CRC Press; 1997;181–6.
16. Galeotti S. Thanatology. In: Lerner KL, Lerner BW, editors. *The Gale Encyclopedia of Science*. Ch. 5th ed. Farmington Hills, MI: Gale; 2014.
17. Alters SM. Death through the ages: a brief overview. *Death and Dying: End-of-Life Controversies*. Ch. Detroit, MI: Gale; 2010.
18. Oxford English Dictionary. Oxford, England: Oxford University Press; 2002 [cited 2015 April 04]. Available from: <http://dictionary.oed.com/>.
19. Alters SM. Redefining death. *Death and Dying: End-of-Life Controversies*. Ch. Detroit, MI: Gale; 2010.
20. *Brain Injury and Brain Death: Practice Guidelines*. Minneapolis, MN: American Academy of Neurology; 2016 [updated 2016; cited 2016 April 26]; Available from: <https://www.aan.com/>.
21. Community Mental Health Centers Extension, Pub. L. No. 95-922, Stat. 92 3412 (9 November, 1978).
22. Abram MB, Fox RC, Garcia-Palmieri M, Graham FK, Jonsen AR, Krim M, Medearis Jr. DN, Motulsky AG, Scitovsky AA, Walker CJ, Williams CA. Defining Death: A Report on the Medical, Legal and Ethical Issues in the Determination of Death. In 1984-0-450-057, Washington, D.C.: Research, President's Commission for the Study of Ethical Problems in Medicine and Biomedical and Behavioral Research (U.S. Government Printing Office), 1981.
23. Standring S, editor. *Gray's Anatomy: The Anatomical Basis of Clinical Practice*. 40<sup>th</sup> ed. London: Churchill-Livingstone: Elsevier, 2008.

24. Einhorn TA, Gerstenfeld LC. Fracture healing: mechanisms and interventions. *Nature reviews: Rheumatology*. 2015;11(1):45–54.
25. McKibbin B. Biology of fracture healing in long bones. *Journal of Bone and Joint Surgery*. 1978;60-B(2):150–62.
26. McLean F, Urist M. *The Healing of Fractures*. Philadelphia, PA: J. B. Lippincott Co, 1955.
27. Adams MA. Functional anatomy of the musculoskeletal system. In: Standring S, editor. *Gray's Anatomy: The Anatomical Basis of Clinical Practice*. Ch. 5. 41<sup>st</sup> ed. Philadelphia, PA: Elsevier; 2016;81–122.
28. Walsh WR, Walton M, Bruce W, Yu Y, Gillies RM, Svehla M. Cell structure and biology of bone and cartilage. In: An YH, Martin KL, editors. *Handbook of Histology Methods for Bone and Cartilage*. Ch. 2. Totowa, NJ: Humana Press; 2003;35–58.
29. Poundarik AA, Diab T, Sroga GE, Ural A, Boskey AL, Gundberg CM. Dilatational band formation in bone. *Proceedings of the National Academy of Sciences*. 2012;109(47):19178–83.
30. Burr DB. Bone Growth, Modeling, and Remodeling. In: Burr DB, Allen MR, editors. *Basic and Applied Bone Biology*. Ch. 5. 2nd ed. London: Academic Press; 2019;85–100.
31. Burr DB. Bone Morphology and Organization. In: Burr DB, Allen MR, editors. *Basic and Applied Bone Biology*. Ch. 1. 2nd ed. London: Academic Press; 2019;3–26.
32. Teitelbaum SL. Osteoclasts: What Do They Do and How Do They Do It? *American Journal of Pathology*. 2007;170(2):427–35.
33. Yahara Y, Nguyen T, Ishikawa K, Kamei K, Alman BA. The origins and roles of osteoclasts in bone development, homeostasis and repair. *Development*. 2022;149(8).
34. Ikenishi R, Kansu M, Ishida M, Harihara A, Matsui S, Yahara I, Kitagawa T. Determination of Fluoride Ion in Animal Bone by Microdiffusion Analysis. *Analytical Chemistry*. 1990;62:2636–9.
35. Xiao Y, Zijl S, Wang L, Daniel, Maarten, Arjan, Borst J. Identification of the common origins of osteoclasts, macrophages, and dendritic cells in human hematopoiesis. *Stem Cell Reports*. 2015;4(6):984–94.
36. Arai F, Miyamoto T, Ohneda O, Inada T, Sudo T, Brasel K, Miyata T, Anderson DM, Suda T. Commitment and differentiation of osteoclast precursor cells by the sequential expression of C-Fms and receptor activator of nuclear factor  $\kappa$ B (rank) receptors. *Journal of Experimental Medicine*. 1999;190(12):1741–54.
37. O'Connor JF, Cohen J. Dating Fractures. In: Kleinmann PK, editor. *Diagnostic Imaging of Child Abuse*. Ch. 7. 2<sup>nd</sup> ed. St. Louis, MO: Mosby; 1998;168 – 77.

38. Agnew AM, Bolte IV JH. Bone fracture: biomechanics and risk. In: Crowder CM, Stout SD, editors. *Bone Histology: An Anthropological Prospective*. Ch. 8. Boca Raton, FL: CRC Press; 2012;221–40.
39. Love JC, Derrick SM, Wiersema JM. Healing and Interpretation. In: Love JC, Derrick SM, Wiersema JM, editors. *Skeletal Atlas of Child Abuse*. Ch. 6. New York: Humana Press; 2011;85–101.
40. Rubin KM, Stock MK. Early signs of fracture repair in the human rib cage: implications for forensic casework. *Journal of Forensic Sciences*. 2019;64(3):672–9.
41. Boyce BF, Yao Z, Xing L. Osteoclasts have multiple roles in bone in addition to bone resorption. *Critical Reviews in Eukaryotic Gene Expression*. 2009;19(3):171–80.
42. Teitelbaum SL, Ross FP. Genetic regulation of osteoclast development and function. *Nature Reviews: Genetics*. 2003;4(8):638–49.
43. Kylmaja E, Nakamura M, Tuukkanen J. Osteoclasts and Remodeling Based Bone Formation. *Current Stem Cell Research & Therapy*. 2016;11(8):626–33.
44. Takeyama K, Chatani M, Takano Y, Kudo A. In-vivo imaging of the fracture healing in medaka revealed two types of osteoclasts before and after the callus formation by osteoblasts. *Developmental Biology*. 2014;394(2):292–304.
45. Lo CH, Baratchart E, Basanta D, Lynch CC. Computational modeling reveals a key role for polarized myeloid cells in controlling osteoclast activity during bone injury repair. *Scientific Reports*. 2021;11.
46. Schell H, Lienau J, Epari DR, Seebeck P, Exner C, Muchow S, Bragulla H, Haas NP, Duda GN. Osteoclastic activity begins early and increases over the course of bone healing. *Bone*. 2006;38(4):547–54.
47. Ma Q, Liang M, Wu Y, Luo F, Ma Z, Dong S, Xu J, Dou C. Osteoclast-derived apoptotic bodies couple bone resorption and formation in bone remodeling. *Bone Research*. 2021;9(1).
48. Soysa NS, Alles N. Positive and negative regulators of osteoclast apoptosis. *Bone Reports*. 2019;11.
49. Gill-King H. Chemical and ultrastructural aspects of decomposition. In: Haglund WD, Sorg MH, editors. *Forensic Taphonomy: The Postmortem Fate of Human Remains*. Ch. Boca Raton, FL: CRC Press; 1997;93–104.
50. What is the time frame for transplanting organs? Denver, CO: Donor Alliance; 2025 [updated 2025 February 21; cited 2025 May 05]; Available from: <https://www.donoralliance.org/>.
51. Organs & tissues. Richmond, VA: Donate Life America; 2025 [updated 2025; cited 2025 May 05]; Available from: <https://donatelife.net/donation/organs/tissue-donation/>.

52. PubMed. Washington, D.C.: National Library of Medicine, National Institute of Health; 2024 [updated 2024; cited 2024 May 31]; Available from: <https://pubmed.ncbi.nlm.nih.gov/>.
53. O'Regan A, Berman JS. Osteopontin: a key cytokine in cell-mediated and granulomatous inflammation. *International Journal of Experimental Pathology*. 2000;81(6):373–90.
54. Bailey S, Karsenty G, Gundberg C, Vashishth D. Osteocalcin and osteopontin influence bone morphology and mechanical properties. *Annals of the New York Academy of Sciences*. 2017;1409(1):79–84.
55. Chen Y, Bal BS, Gorski JP. Calcium and collagen binding properties of osteopontin, bone sialoprotein, and bone acidic glycoprotein-75 from bone. *Journal of Biological Chemistry*. 1992;267(34):24871–8.
56. Reinholt FP, Hulthén K, Oldberg A, Heinegård D. Osteopontin--a possible anchor of osteoclasts to bone. *Proceedings of the National Academy of Sciences*. 1990;87(12):4473–5.
57. Roach HI. Why does bone matrix contain non-collagenous proteins? The possible roles of osteocalcin, osteonectin, osteopontin and bone sialoprotein in bone mineralisation and resorption. *Cell Biology International*. 1994;18(6):617–28.
58. Ross FP, Chappel J, Alvarez JI, Sander D, Butler WT, Farachcarson MC, Mintz KA, Robey PG, Teitelbaum SL, Cheresch DA. Interactions between the bone matrix proteins osteopontin and bone sialoprotein and the osteoclast integrin  $\alpha$ v $\beta$ 3 potentiate bone resorption. *The Journal of Biological Chemistry*. 1993;268(13):9901–7.
59. Tavakol M, Vaughan T. The role of the osteocalcin-osteopontin protein complex in bone biomechanics: a key contributor to energy dissipation at mineral-mineral interfaces. *Biophysical Journal*. 2022;121(3):332a–a.
60. Nickel Oe, Laurencin D, McCallum SA, Gundberg CM, Vashishth D. NMR Investigation of the Role of Osteocalcin and Osteopontin at the Organic–Inorganic Interface in Bone. *Langmuir*. 2013;29(45):13873–82.
61. Wang KX, Denhardt DT. Osteopontin: Role in immune regulation and stress responses. *Cytokine & Growth Factor Reviews*. 2008;19(5):333–45.
62. Liaw L, Almeida M, Hart CE, Schwartz SM, Giachelli CM. Osteopontin Promotes Vascular Cell Adhesion and Spreading and Is Chemotactic for Smooth Muscle Cells In Vitro. *Circulation Research*. 1994;74(2):214–24.
63. Icer MA, Gezmen-Karadag M. The multiple functions and mechanisms of osteopontin. *Clinical Biochemistry*. 2018;59:17–24.
64. Rittling SR, Singh R. Osteopontin in Immune-mediated Diseases. *Journal of Dental Research*. 2015;94(12):1638–45.
65. Lund SA, Giachelli CM, Scatena M. The role of osteopontin in inflammatory processes. *Journal of Cell Communication and Signaling*. 2009;3(3-4):311–22.

66. Boskey AL, Posner AS. Bone Structure, Composition, and Mineralization. *Orthopedic Clinics of North America*. 1984;15(4):597–612.
67. Staines KA, MacRae VE, Farquharson C. The importance of the SIBLING family of proteins on skeletal mineralisation and bone remodelling. *Journal of Endocrinology*. 2013;219(2):X1–X.
68. Denhardt DT, Guo X. Osteopontin: a protein with diverse functions. *Faseb j*. 1993 Dec;7(15):1475–82.
69. Lian JB, McKee MD, Todd AM, Gerstenfeld LC. Induction of bone-related proteins, osteocalcin and osteopontin, and their matrix ultrastructural localization with development of chondrocyte hypertrophy in vitro. *Journal of Cellular Biochemistry*. 1993;52(2):206–19.
70. Bernardis MT, Qin C, Jiang S. MC3T3-E1 cell adhesion to hydroxyapatite with adsorbed bone sialoprotein, bone osteopontin, and bovine serum albumin. *Colloids and surfaces, B, Biointerfaces*. 2008;64(2):236–47.
71. Si J, Wang C, Zhang D, Wang B, Zhou Y. Osteopontin in Bone Metabolism and Bone Diseases. *Medical Science Monitor*. 2020;26:e919159–e.
72. Mohtasham N, Saghravarian N, Fatemi B, Vahedi M, Afzal-Aghaee M, Kadeh H. A comparative study of osteopontin and MMP-2 protein expression in peripheral and central giant cell granuloma of the jaw. *Brazilian Journal of Otorhinolaryngology*. 2019;85(2):150–6.
73. Burr DB, Allen MR, editors. *Basic and Applied Bone Biology*. 2nd ed. London: Academic Press, 2019.
74. Bonewald LF, Johnson ML. Osteocytes, mechanosensing and Wnt signaling. *Bone*. 2008;42(4):606–15.
75. Bonewald LF. The amazing osteocyte. *Journal of Bone and Mineral Research*. 2011;26(2):229–38.
76. Karsenty G. Osteocalcin: A Multifaceted Bone-Derived Hormone. *Annual Review of Nutrition*. 2023;43(1):55–71.
77. Komori T. Functions of Osteocalcin in Bone, Pancreas, Testis, and Muscle. *International Journal of Molecular Sciences*. 2020;21(20):7513.
78. Moser SC, van der Eerden BCJ. Osteocalcin — A versatile bone-derived hormone. *Frontiers in Endocrinology*. 2019;10:794–.
79. Hauschka PV, Lian JB, Cole DEC, Gundberg CM. Osteocalcin and matrix Gla protein: vitamin K-dependent proteins in bone. *Physiological Reviews*. 1989;69(3):990–1047.
80. Karsenty G, Ferron M. The contribution of bone to whole-organism physiology. *Nature*. 2012;481(7381):314–20.

81. Berezovska O, Yildirim G, Budell WC, Yagerman S, Pidhaynyy B, Bastien C, van der Meulen MCH, Dowd TL. Osteocalcin affects bone mineral and mechanical properties in female mice. *Bone* (New York, NY). 2019;128:115031–.
82. Neve A, Corrado A, Cantatore FP. Osteocalcin: Skeletal and extra-skeletal effects. *Journal of Cellular Physiology*. 2013;228(6):1149–53.
83. Ducy P, Desbois C, Boyce B, Pinero G, Story B, Dunstan C, Smith E, Bonadio J, Goldstein S, Gundberg C, Bradley A, Karsenty G. Increased bone formation in osteocalcin-deficient mice. *Nature*. 1996;382(6590):448–52.
84. Manolagas SC. Osteocalcin promotes bone mineralization but is not a hormone. *PLOS Genetics*. 2020;16(6):e1008714.
85. Nikel O, Poundarik AA, Bailey S, Vashishth D. Structural role of osteocalcin and osteopontin in energy dissipation in bone. *Journal of Biomechanics*. 2018;80:45–52.
86. Clarke B. Normal bone anatomy and physiology. *Clinical Journal of Social Nephrology*. 2008 Nov;3 Suppl 3(Suppl 3):S131–9.
87. Oftadeh R, Perez-Viloria M, Villa-Camacho JC, Vaziri A, Nazarian A. Biomechanics and mechanobiology of trabecular bone: a review. *Journal of Biomechanical Engineering*. 2015 Jan;137(1):0108021–01080215.
88. Diemar SS, Møllehave LT, Quardon N, Lylloff L, Thuesen BH, Linneberg A, Jørgensen NR. Effects of age and sex on osteocalcin and bone-specific alkaline phosphatase—reference intervals and confounders for two bone formation markers. *Archives of Osteoporosis*. 2020;15(1):26–.
89. Gerdhem P, Ivaska KK, Alatalo SL, Halleen JM, Hellman J, Isaksson A, Pettersson K, Väänänen HK, Åkesson K, Obrant KJ. Biochemical Markers of Bone Metabolism and Prediction of Fracture in Elderly Women. *Journal of Bone and Mineral Research*. 2004;19(3):386–93.
90. Ingram RT, Park YK, Clarke BL, Fitzpatrick LA. Age- and gender-related changes in the distribution of osteocalcin in the extracellular matrix of normal male and female bone. Possible involvement of osteocalcin in bone remodeling. *Journal of Clinical Investigation*. 1994;93(3):989–97.
91. Szulc P, Delmas PD. Biochemical Markers of Bone Turnover in Men. *Calcified Tissue International*. 2001;69:229–34.
92. Johnston E, Buckley M. Relative Protein Abundances and Biological Ageing in Whole Skeletal Elements. *Journal of Proteome Research*. 2021;20(1):538–48.
93. Terai K, Takano-Yamamoto T, Ohba Y, Hiura K, Sugimoto M, Sato M, Kawahata H, Inaguma N, Kitamura Y, Nomura S. Role of osteopontin in bone remodeling caused by mechanical stress. *Journal of Bone and Mineral Research*. 1999 Jun;14(6):839–49.

94. Nomura S, Takano-Yamamoto T. Molecular events caused by mechanical stress in bone. *Matrix Biology*. 2000 2000/05/01/;19(2):91–6.
95. Du Y, Mao L, Wang Z, Yan K, Zhang L, Zou J. Osteopontin - The stirring multifunctional regulatory factor in multisystem aging. *Frontiers in Endocrinology*. 2022;13.
96. Carvalho MS, Poundarik AA, Cabral JMS, Da Silva CL, Vashishth D. Biomimetic matrices for rapidly forming mineralized bone tissue based on stem cell-mediated osteogenesis. *Scientific Reports*. 2018;8(1).
97. Chang IC, Chiang TI, Yeh KT, Lee H, Cheng YW. Increased serum osteopontin is a risk factor for osteoporosis in menopausal women. *Osteoporosis International*. 2010 Aug;21(8):1401–9.
98. Khosla S, Melton LJ, Atkinson EJ, O'Fallon WM, Klee GG, Riggs BL. Relationship of serum sex steroid levels and bone turnover markers with bone mineral density in men and women : A key role for bioavailable estrogen. *Journal of Clinical Endocrinology and Metabolism*. 1998;83(7):2266–74.
99. Vlot MC, Klink DT, den Heijer M, Blankenstein MA, Rotteveel J, Heijboer AC. Effect of pubertal suppression and cross-sex hormone therapy on bone turnover markers and bone mineral apparent density (BMAD) in transgender adolescents. *Bone*. 2017;95:11–9.
100. Cho E-H, Cho K-H, Lee HA, Kim S-W. High Serum Osteopontin Levels Are Associated with Low Bone Mineral Density in Postmenopausal Women. *Journal of Korean Medical Science*. 2013;28(10):1496.
101. Reza S, Shaukat A, Mahmud M, Arain T, Reza U, Waheed F. Evaluation of Osteopontin in Combination with Bone Turnover Markers for the Assessment of Osteoporosis in Postmenopausal Women. *British Journal of Medicine and Medical Research*. 2016;14(6):1–11.
102. Buckley M, Anderung C, Penkman K, Raney BJ, Götherström A, Thomas-Oats J, Collins MJ. Comparing the survival of osteocalcin and mtDNA in archaeological bone from four European sites. *Journal of Archaeological Science*. 2008;35:1756–64.
103. Collins MJ, Gernaey AM, Nielsen-Marsh CM, Vermeer C, Westbroek P. Slow rates of degradation of osteocalcin: green light for fossil bone protein? *Geology*. 2000;28(12):1139–42.
104. Ostrom PH, Gandhi H, Strahler JR, Walker AK, Andrews PC, Leykam J, Stafford TW, Kelly RL, Walker DN, Buckley M, Humpala J. Unraveling the sequence and structure of the protein osteocalcin from a 42 ka fossil horse. *Geochimica et Cosmochimica Acta*. 2006;70(8).
105. Smith CI, Craig OE, Prigodich RV, Nielsen-Marsh C, Jans MME, Vermeer C, Collins MJ. Diagenesis and survival of osteocalcin in archaeological bone. *Journal of Archaeological Science*. 2005;32:105–13.
106. Cabriol N, Pommier MT, Gueux M, Payen G. Comparison of lipid composition in two types of human putrefactive liquid. *Forensic Science International*. 1998 Jun 8;94(1-2):47–54.

107. Carter DO, Yellowlees D, Tibbett M. Cadaver decomposition in terrestrial ecosystems. *Naturwissenschaften*. 2007 Jan;94(1):12–24.
108. Galloway A. The process of decomposition: a model from the Arizona-Sonoran desert. In: Haglund W, Sorg M, editors. *Forensic Taphonomy: The Postmortem Fate of Human Remains*. Ch. Boca Raton, FL: CRC Press; 1997;139–50.
109. Janaway RC, Percival, S. L., Wilson, S. A. Decomposition of Human Remains. In: Percival SL, editor. *Microbiology and Aging*. Ch. 14. New York: Springer; 1995;313–34.
110. Sledzik P. Forensic taphonomy: postmortem decomposition and decay. In: Reichs K, editor. *Forensic Osteology: Advances in the Identification of Human Remains*. Ch. Springfield, IL: Charles C Thomas; 1998;109–19.
111. Vass AA. Beyond the grave-understanding human decomposition. *Microbiology Today*. 2001;28:190–3.
112. Clark MA, Worrell MB, Pless JE. Postmortem changes in soft tissues. In: Haglund W, Sorg M, editors. *Forensic Taphonomy: The Postmortem Fate of Human Remains*. Ch. Boca Raton, FL: CRC Press; 1997;151–65.
113. Damann FE, Carter DO. Human decomposition ecology and postmortem microbiology. In: Pokines JT, Symes SA, editors. *Manual of Forensic Taphonomy*. Ch. 3. Boca Raton, FL: CRC Press; 2014;37–49.
114. Galloway A, Birkby WH, Jones AM, Henry TE, Parks BO. Decay rates of human remains in an arid environment. *Journal of Forensic Sciences*. 1989;34(3):607.
115. Komar DA, Buikstra JE. *Forensic anthropology: contemporary theory and practice*. New York: Oxford University Press, 2008.
116. Rodriguez WC, Bass WM. Insect activity and its relationship to decay rates of human cadavers in East Tennessee. *Journal of Forensic Sciences*. 1983;28(2):423–32.
117. Smith AC. The effects of sharp-force thoracic trauma on the rate and pattern of decomposition. *Journal of Forensic Sciences*. 2014;59(2):319–26.
118. Marks M, Tersigni M. Decomposition, Patterns and Rates. *Encyclopedia of Forensic and Legal Medicine*. Ch. St. Louis, MO: Elsevier; 2005.
119. Jans MME. Microscopic Destruction of Bone. In: Pokines JT, Symes SA, editors. *Manual of Forensic Taphonomy*. Ch. 2. Boca Raton, FL: CRC Press; 2014;19–36.
120. Jans MME, Kars H, Nielsen-Marsh CM, Smith CI, Nord AG, Arthur P, Earl N. *In situ* preservation of archaeological bone: a histological study within a multidisciplinary approach. *Archaeometry*. 2002;44(3):343–52.
121. Jans MME, Nielsen-Marsh CM, Smith CI, Collins MJ, Kars H. Characterisation of microbial attack on archaeological bone. *Journal of Archaeological Science*. 2004;31:87–95.

122. Bell LS. Palaeopathology and diagenesis: an SEM evaluation of structural changes using backscattered electron imaging. *Journal of archaeological science*. 1990;17(1):85–102.
123. Bell LS. Identifying postmortem microstructural change to skeletal and dental tissues using backscattered electron imaging. In: Bell LS, editor. *Forensic Microscopy of Skeletal Tissues: Methods and Protocol*. Ch. 11. New York: Springer; 2012;173–90.
124. Bell LS, Skinner MF, Jones SJ. Speed of post mortem change to the human skeleton and its taphonomic significance. *Forensic Science International*. 1996;82:129–40.
125. Cvetko M, Knific T, Frangež R, Motaln H, Rogelj B, Alibegović A, Gombač M. Postmortem chondrocyte viability in porcine articular cartilage: Influence of time, temperature, and burial under winter conditions. *Journal of Forensic Sciences*. 2024;69(3):1094–101.
126. Dix J, Ernst MF. *Handbook for Death Scene Investigators*. Boca Raton, FL: CRC Press, 1999.
127. Burton JF. Fallacies in the Signs of Death. *Journal of Forensic Sciences*. 1974;19(3):529–34.
128. *Death Investigation: A Guide for the Scene Investigator*. In, Washington, D.C.: U.S. Department of Justice, National Institute of Justice (U.S. Government Printing Office), 1999.
129. Smith AC. The effect of sharp-force thoracic trauma on the rate and pattern of decomposition in New England [Thesis (M.S.)]. Boston, MA: Boston University, 2012.
130. Behrensmeyer AK. Taphonomic and Ecologic Information from Bone Weathering. *Paleobiology*. 1978;4(2):150–62.
131. Pokines JT, Baker JE. Effects of burial environments on osseous remains. In: Pokines JT, Symes SA, editors. *Manual of Forensic Taphonomy*. Ch. 5. Boca Raton, FL: CRC Press; 2014;73–114.
132. Ruiz López JL, Partido Navadijo M. Estimation of the post-mortem interval: a review. *Forensic Science International*. 2025;369:112412.
133. Abd Elazeem EA, Ismail MME, Zaghoul HS, Selim AO, Gaballah MH, Oraby EEA, Gaballah IF. Estimation of postmortem interval in myocardial stab wounds and firearm injuries: An immunohistochemical comparative study using C5b-9 and cardiac Troponin C. *Forensic Science International*. 2021 2021/07/01;324:110846.
134. Kumar S, Ali W, Singh US, Kumar A, Bhattacharya S, Verma AK, Rupani R. Temperature-dependent postmortem changes in human cardiac Troponin-T (cTnT): an approach in estimation of time since death. *Journal of Forensic Sciences*. 2016;61(S1):S241–S5.
135. Prieto-Bonete G, Perez-Carceles MD, Luna A. Morphological and histological changes in eye lens: Possible application for estimating postmortem interval. *International Journal of Legal Medicine*. 2015 2015/11/01;17(6):437–42.

136. Komar DA. Forensic taphonomy in a cold climate region: A field study in central Alberta and a potential new method for determining time since death [Dissertation]. Edmonton, AB: University of Alberta, 1999.
137. Komar DA. Decay rates in a cold climate region: a review of cases involving advanced decomposition from the Medical Examiner's Office in Edmonton, Alberta. *Journal of Forensic Sciences*. 1998;43(1):57–.
138. Komar DA. Twenty-seven years of forensic anthropology casework in New Mexico. *Journal of Forensic Sciences*. 2003 May;48(3):521–4.
139. Statheropoulos M, Spiliopoulou C, Agapiou A. A study of volatile organic compounds evolved from the decaying human body. *Forensic Science International*. 2005 Oct 29;153(2-3):147–55.
140. Aturaliya S, Lukasewycz A. Experimental forensic and bioanthropological aspects of soft tissue taphonomy: 1. Factors influencing postmortem tissue desiccation rate. *Journal of Forensic Sciences*. 1999;44(5):893–.
141. Carter DO, Yellowlees D, Tibbett M. Moisture can be the dominant environmental parameter governing cadaver decomposition in soil. *Forensic Science International*. 2010 Jul 15;200(1-3):60–6.
142. Shean BS, Messinger L, Papworth M. Observations of differential decomposition on sun exposed v. shaded pig carrion in coastal Washington State. *Journal of Forensic Sciences*. 1993;38(4):938–49.
143. Campobasso CP, Di Vella G, Introna F. Factors affecting decomposition and Diptera colonization. *Forensic Science International*. 2001;120:18–27.
144. Boyle S, Galloway A, Mason RT. Human Aquatic Taphonomy in the Monterey Bay Area. In: Haglund WD, Sorg MH, editors. *Forensic Taphonomy: The Postmortem Fate of Human Remains*. Ch. Boca Raton, FL: CRC Press; 1996;605–14.
145. Breitmeier D, Graefe-Kirci U, Albrecht K, Weber M, Tröger HD, Kleemann WJ. Evaluation of the correlation between time corpses spent in in-ground graves and findings at exhumation. *Forensic Science International*. 2005;154:218–23.
146. Manhein MH. Decomposition Rates of Deliberate Burials: A Case Study of Preservation. In: Haglund WD, Sorg MH, editors. *Forensic Taphonomy: The Postmortem Fate of Human Remains*. Ch. Boca Raton, FL: CRC Press; 1996;469–82.
147. Adlam RE, Simmons T. The Effect of Repeated Physical Disturbance on Soft Tissue Decomposition—Are Taphonomic Studies an Accurate Reflection of Decomposition? *Journal of Forensic Sciences*. 2007;52(5):1007–14.
148. De Jong GD, Hoback WW, Higley LG. Effect of Investigator Disturbance in Experimental Forensic Entomology: Carcass Biomass Loss and Temperature. *Journal of Forensic Sciences*. [10.1111/j.1556-4029.2010.01552.x]. 2011;56:143–9.

149. Introna F, Suman TW, Smialek JE. Sarcosaprophagous Fly Activity in Maryland. *Journal of Forensic Sciences*. 1991 Jan;36(1):238–43.
150. Spicka A, Johnson R, Bushing J, Higley LG, Carter DO. Carcass mass can influence rate of decomposition and release of ninhydrin-reactive nitrogen into grave soil. *Forensic Science International*. 2011 Jun 15;209:80–5.
151. Dautartas AM. *The Effect of Various Coverings on the Rate of Human Decomposition*. Knoxville, TN: University of Tennessee-Knoxville, 2009.
152. Kelly JA, van der Linde TC, Anderson GS. The influence of clothing and wrapping on carcass decomposition and arthropod succession during the warmer seasons in central South Africa\*. *Journal of Forensic Sciences*. 2009 Sep;54(5):1105–12.
153. Love J, Marks M. Taphonomy and time: estimating the postmortem interval. In: Steadman DW, editor. *Hard evidence: case studies in forensic anthropology*. Ch. 13. 1<sup>st</sup> ed. Upper Saddle River, NJ: Prentice Hall; 2002;160–75.
154. Junod CA, Pokines JT. Subaerial Weathering. In: Pokines JT, Symes SA, editors. *Manual of Forensic Taphonomy*. Ch. 11. Boca Raton, FL: CRC Press; 2014;287–314.
155. Sognaes R. Microradiographic observations on demineralization gradients in the pathogenesis of hard-tissue destruction. *Archives of Oral Biology*. 1959;1:106–21.
156. Sognaes R. Histologic evidence of developmental lesions in teeth originating from Paleolithic, prehistoric and ancient man. *American Journal of Pathology*. 1956;32:547–78.
157. Sognaes R. Postmortem microscopic defects in the teeth of ancient man. *AMA Archives of Pathology*. 1955;59:559–70.
158. Sognaes R. Studies on dental paleopathology. II. Differential diagnosis of postmortem histopathology of teeth. *Journal of Dental Research*. 1949;28:660.
159. Syssovena P. Postmortem changes to human teeth with time. *Sudebnd-Medisthinskaya Ekspertiza I Kriminalistika na sluzhbe Sletsshviya*. 1958;2:213–8.
160. Falin LI. Histological and histochemical studies of human teeth of the Bronze Age and Stone Age. *Archives of Oral Biology*. 1961;5:5–13.
161. Marchiafava V, Bonucci L, Ascenzi A. Fungal osteoclasia: a model of dead bone resorption. *Calcified Tissue Research*. 1974;14:195–210.
162. Schmidt CW, Moore CR, Leifheit R. A preliminary assessment of using white light confocal imaging profiler for cut mark analysis. In: Bell LS, editor. *Forensic Microscopy for Skeletal Tissues: Methods and Protocols*. Ch. 14. New York: Springer; 2012;235–48.
163. Maggiano C, Dupras TL, Schultz M, Biggerstaff J. Confocal laser scanning microscopy: a flexible tool for simultaneous polarization and three-dimensional fluorescence imaging of archaeological compact bone. *Journal of Archaeological Science*. 2009;36:2392–401.

164. Maggiano C, Dupras TL, Schultz M, Biggerstaff J. Spectral and photobleaching analysis using confocal laser scanning microscopy: a comparison of modern and archaeological bone fluorescence. *Molecular and Cellular Probes*. 2006;20:154–62.
165. Hedges REM, Millard AR, Pike AWG. Measurements and relationships of diagenetic alteration of bone from three archaeological sites. *Journal of Archaeological Science*. 1995;22:201–9.
166. Turner-Walker G, Syversen U. Quantifying histological changes in archaeological bone using BSE-SEM image analysis. *Archaeometry*. 2002;44(3):461–8.
167. Hackett CJ. Microscopical focal destruction (tunnels) in exhumed bones. *Medicine, Science, and the Law*. 1981;21(4):243–65.
168. Inoué S. Foundations of confocal scanned imaging in light microscopy. In: Pawley J, editor. *Handbook of Biological Confocal Microscopy*. Ch. 1. 3<sup>rd</sup> ed. New York: Springer; 2006;1–19.
169. Paddock SW, Eliceiri KW. Laser scanning confocal microscopy: history, applications, and related optical sectioning techniques. In: Paddock SW, editor. *Confocal Microscopy: Methods and Protocols*. Ch. 2<sup>nd</sup> ed. New York: Springer; 2014;9–47.
170. Hibbs AR. *Confocal Microscopy for Biologists*. New York: Springer Publishing, 2012.
171. Pawley JB. Points, pixels, and gray levels: digitizing image data. In: Pawley JB, editor. *Handbook of Biological Confocal Microscopy*. Ch. 4. 3<sup>rd</sup> ed. New York: Springer; 2006;59–79.
172. Capasso L, D'Anastasio R, Guarnier S, Viciano J, Marigliò. Bone natural autofluorescence and confocal laser scanning microscopy: Preliminary results of a novel useful tool to distinguish between forensic and ancient human skeletal remains. *Forensic Science International*. 2017;272(March).
173. Blouin S, Roschger A, Varga F, Misof B, Spitzer S, Roschger P, Klaushofer K. Confocal Laser Scanning Microscopy - A Powerful Tool in Bone Research. *Wien Med Wochenschr*. 2018;168:314–21.
174. Paddock SW, editor. *Confocal Microscopy: Methods and Protocols*. 2<sup>nd</sup> ed. New York: Springer, 2014.
175. Scarano A, Iezzi G, Adriano P. Common fixatives in hard-tissue histology. In: An YH, Martin KL, editors. *Handbook of Histology Methods for Bone and Cartilage*. Ch. 9. Totowa, NJ: Humana Press; 2003;159–65.
176. Jenkins LL, Burg KJL. Tissue harvesting and fixation. In: An YH, Martin KL, editors. *Handbook of Histology Methods for Bone and Cartilage*. Ch. 8. Totowa, NJ: Humana Press; 2003;143–58.
177. Ross MH, Pawlina W. Methods. In: Ross MH, Pawlina W, editors. *Histology: A Text and Atlas*. Ch. 1. 6<sup>th</sup> ed. Philadelphia, PA: Wolters Kluwer; 2011;1–21.

178. Jones CG. Scanning electron microscopy: preparation and imaging for SEM. In: Bell LS, editor. *Forensic Microscopy for Skeletal Tissue: Methods and Protocols*. Ch. 1. New York: Springer; 2012;1–20.
179. Valentine G, Piper K. Preparation of mineralized tissue for light microscopy. In: Bell LS, editor. *Forensic Microscopy for Skeletal Tissue: Methods and Protocols*. Ch. 3. New York: Springer; 2012;37–50.
180. Wighton AHJ, Jones CG, Bell LS. Plastic embedding and polishing of bone for reflected light and electron microscopy. In: Bell LS, editor. *Forensic Microscopy for Skeletal Material: Methods and Protocols*. Ch. 2. New York: Springer; 2012;21–36.
181. Bozzola JJ. Conventional specimen preparation techniques for transmission electron microscopy of cultured cells. In: Kuo J, editor. *Electron Microscopy: Methods and Protocols*. Ch. 1. New York: Springer; 2014;1–19.
182. Bozzola JJ. Conventional specimen preparation techniques for scanning electron microscopy of biological specimens. In: Kuo J, editor. *Electron Microscopy: Methods and Protocols*. Ch. 7. New York: Springer; 2014;133–50.
183. Bacallao R, Sohrab S, Phillips C. Guiding principles of specimen preservation for confocal fluorescence microscopy. In: Pawley JB, editor. *Handbook of Biological Confocal Microscopy*. Ch. 18. 3<sup>rd</sup> ed. New York: Springer; 2006;368–80.
184. Coxon FP. Fluorescence imaging of osteoclasts using confocal microscopy. In: Helfrich MH, Ralston SH, editors. *Bone Research Protocols*. Ch. 25. 2nd ed. New York: Springer; 2012;401–24.
185. Imaris v.9.0. Oxford, U.K.: Bitplane, Oxford Industries; 2022.
186. Rasband W. FIJI/ImageJ© v.1.50i. Washington, DC: National Institutes of Health; 2012.
187. Smith AC, Watamaniuk L, Rogers T. Use of laser scanning confocal microscopy in detection of diagenesis in bone. *Journal of Forensic Sciences*. 2022;67(1):92–101.
188. Policy on Euthanasia. Boston, MA: Tufts University; 2025 [updated 2025; cited 2025 May 26]; Available from: <https://viceprovost.tufts.edu/animal-care-use-policies>.
189. Euthanasia (IACUC). Boston, MA: Boston University; 2025 [updated 2025; cited 2025 May 26]; Available from: <https://www.bu.edu/research/forms-policies/euthanasia-guidelines-iacuc/>.
190. Capasso L, D'Anastasio R, Guarnier S, Viciano J, Mariggì M. Bone natural autofluorescence and confocal laser scanning microscopy: Preliminary results of a novel useful tool to distinguish between forensic and ancient human skeletal remains. *Forensic Science International*. 2017;272(March).
191. Bell LS, editor. *Forensic Microscopy for Skeletal Materials*. New York: Springer, 2012.

192. Alunni-Perret V, Muller-Bolla M, Laugier J, Lupi-Pegurier L, Bertrand M, Staccini P, Bolla M, Quatrehomme G. Scanning electron microscopy analysis of experimental bone hacking trauma. *Journal of Forensic Sciences*. 2005;50:1–6.
193. Watamaniuk L, Smith AC, Dion N, Ste-Marie LG. Comparison between laser scanning confocal microscopy and traditional light microscopy in forensic histo-osteology. 2018 Annual Meeting of the American Society for Bone and Mineral Research, 2018 29 September; Montréal, QC. American Society for Bone and Mineral Research; 2018.
194. Troiano NW, Ciovacco WA, Kacena MA. The Effects of Fixation and Dehydration on the Histological Quality of Undecalcified Murine Bone Specimens Embedded in Methylmethacrylate. *Journal of Histotechnology*. 2009 2009/03/01;32(1):27–31.
195. Schindelin J, Arganda-Carreras I, Frise E. Fiji: an open-source platform for biological-image analysis. *Nature Methods*. 2012;9(7):676–82.
196. Zen 2 core SP1 v.2.0. Jena, Germany: Carl Zeiss Microscopy GmbH; 2016.
197. IBM®. SPSS© Statistics v.27.0. Chicago: Integrated Business Machinery; 2020.
198. Parfitt AM, Drezner MK, Glorieux FH, Kanis JA, Malluche H, Meunier PJ, Ott SM, Recker RR. Bone histomorphometry: Standardization of nomenclature, symbols, and units: Report of the asbmr histomorphometry nomenclature committee. *Journal of Bone and Mineral Research*. 1987;2(6):595–610.
199. Microsoft™. Excel® v.15.0. Richmond, WA: Microsoft™ Corp; 2013.
200. McNamara G, Yanai A, Khankaldyyan V, Laug WE, Boden J, Webster K, Li Y, Wen R. Low Magnification Confocal Microscopy of Tumor Angiogenesis. In: Paddock SW, editor. *Confocal Microscopy: Methods and Protocols*. Ch. 6. 2nd ed. New York: Springer; 2014;149–76.
201. Stajić M. Toxicology in Postmortem Pathology. In: McManus LM, Mitchell RN, editors. *Pathobiology of Human Disease*. Ch. San Diego: Academic Press; 2014;3440–3.
202. Jones GR. Postmortem Specimens. In: Siegel JA, Saukko PJ, Houck MM, editors. *Encyclopedia of Forensic Sciences (Second Edition)*. Ch. Waltham: Academic Press; 2013;270–4.
203. Burkhart KJ, Nowak TE, Blum J, Kuhn S, Welker M, Sternstein W, Mueller LP, Rommens PM. Influence of formalin fixation on the biomechanical properties of human diaphyseal bone. *Biomedizinische Technik*. 2010;55(6):361–5.
204. Zhang G, Wang S, Xu S, Guan F, Bai Z, Mao H. The Effect of Formalin Preservation Time and Temperature on the Material Properties of Bovine Femoral Cortical Bone Tissue. *Annals of Biomedical Engineering*. 2019;47(4):937–52.
205. Garnero P. The contribution of collagen crosslinks to bone strength. *BoneKEy reports*. 2012;1:182–.

206. Blackwell LS, Martinez M, Fournier-Goodnight A, Figueroa J, Appert A, Vats A, Wali B, Sayeed I, Reisner A. Patterns of Osteopontin Expression in Abusive Head Trauma Compared with Other Causes of Pediatric Traumatic Brain Injury. *Journal of Pediatrics*. 2020;227:170–5.
207. García MFM, Martin A, Fushimi S, Feldman S, Pastorino NF, Juárez JN, Jammal MV, Missana LR. Optimization for Bone Samples Embedded in Methyl Methacrylate. *Journal of Hard Tissue Biology*. 2022;31(3):181–6.
208. Akkiraju H, Bonor J, Nohe A. An Improved Immunostaining and Imaging Methodology to Determine Cell and Protein Distributions within the Bone Environment. *Journal of Histochemistry & Cytochemistry*. 2016;64(3):168–78.
209. O'Malley JT, Merchant SN, Burgess BJ, Jones DD, Adams JC. Effects of Fixative and Embedding Medium on Morphology and Immunostaining of the Cochlea. *Audiology and Neurotology*. 2009;14(2):78–87.
210. Osteopontin Monoclonal Antibody (7C5H12); Protocols. Waltham, MA: Thermo Fischer Scientific; 2024 [updated 2024; cited 2022 September 01]; Available from: <https://www.thermofisher.com/antibody/product/Osteopontin-Antibody-clone-7C5H12-Monoclonal/MA5-17180>.
211. Goat anti-Mouse IgG (H+L) Cross-Adsorbed Secondary Antibody, Alexa Fluor™ 555. Waltham, MA: Thermo Fisher Scientific; 2025 [updated 2025; cited 2025 July 17]; Available from: <https://www.thermofisher.com/antibody/product/Goat-anti-Mouse-IgG-H-L-Cross-Adsorbed-Secondary-Antibody-Polyclonal/A-21422>.
212. Goat anti-Rabbit IgG (H+L) Cross-Adsorbed Secondary Antibody, Alexa Fluor™ 488. Waltham, MA: Thermo Fisher Scientific; 2025 [updated 2025; cited 2025 July 17]; Available from: <https://www.thermofisher.com/antibody/product/Goat-anti-Rabbit-IgG-H-L-Cross-Adsorbed-Secondary-Antibody-Polyclonal/A-11008>.
213. Hibbs AR. What is Fluorescence? In: Hibbs AR, editor. *Confocal Microscopy for Biologists*. Ch. 8. New York: Springer; 2012;189–200.
214. Hibbs AR. Fluorescent Probes. In: Hibbs AR, editor. *Confocal Microscopy for Biologists*. Ch. 9. New York: Springer; 2012;201–38.
215. Hibbs AR. Fluorescence Immunolabelling. In: Hibbs AR, editor. *Confocal Microscopy for Biologists*. Ch. 11. New York: Springer; 2012;259–77.
216. Coyle IP. Confocal imaging of fluorescently labeled proteins in the *Drosophila* larval neuromuscular junction. In: Paddock SW, editor. *Confocal Microscopy: Methods and Protocols*. Ch. 9. 2<sup>nd</sup> ed. New York: Springer; 2014;201–12.
217. ZEN Blue v.3.4. Jena, Germany: Carl Zeiss Microscopy GmbH; 2021.
218. Snoddy AME, Miszkiewicz JJ, Loch C, Tromp M, Buckley HR. An image analysis protocol for the quantification of interglobular dentine in anthropological tooth sections. *American Journal of Physical Anthropology*. 2021;174(1):144–8.

219. IBM®. SPSS© Statistics v.28.0. Chicago: Integrated Business Machinery; 2022.
220. Smith AC. The use of laser scanning confocal microscopy in detecting bone microstructure using basic fuchsin and toluidine blue stains. 88th Annual Meeting of the American Association of Physical Anthropologists, 2019 27–30 March; Cleveland, OH. American Association of Physical Anthropologists; 2019.
221. Smith AC. Use of laser scanning confocal microscopy in osteological examinations. 45<sup>th</sup> Annual Meeting Canadian Association for Physical Anthropology, 2017 28 Oct 2017; Edmonton, AB. 2017.
222. Smith AC. Use of laser scanning confocal microscopy in bone damage timing. Graduate Research Colloquium, University of Toronto - Mississauga, 2017; Mississauga, ON. 2017.
223. Smith AC. When Bones Light Up: A Novel Way of Labeling Proteins and Cells and Its Potential Uses. 75<sup>th</sup> Annual Meeting of the American Academy of Forensic Sciences, 2023; Orlando, FL. American Academy of Forensic Sciences; 2023.
224. Turner JN, Lasek S, Szarowski DH. Confocal optical microscopy. In: Buschow KHJ, Cahn RW, Flemings MC, Ilshner B, Kramer EJ, Mahajan S, et al., editors. Encyclopedia of Materials: Science and Technology. Ch. Oxford: Elsevier; 2001;1504–9.
225. Smith AC. The effects of sharp-force thoracic trauma on the rate and pattern of decomposition. *J Forensic Sci.* 2014;59(2):319 – 26.
226. Higgs ND, Pokines JT. Marine environmental alterations to bone. In: Pokines JT, Symes SA, editors. *Manual of Forensic Taphonomy*. Ch. 8. Boca Raton, FL: CRC Press; 2014;143–80.
227. Osteocalcin Monoclonal Antibody (OC4-30); Protocols. Waltham, MA: Thermo Fischer Scientific; 2024 [updated 2024; cited 2022 September 01]; Available from: <https://www.thermofisher.com/antibody/product/Osteocalcin-Antibody-clone-OC4-30-Monoclonal/MA1-20786>.
228. Chung P-L, Zhou S, Eslami B, Shen L, Leboff MS, Glowacki J. Effect of Age on Regulation of Human Osteoclast Differentiation. *Journal of Cellular Biochemistry.* 2014;115(8):1412–9.
229. Pignolo RJ, Law SF, Chandra A. Bone Aging, Cellular Senescence, and Osteoporosis. *Journal of Bone and Mineral Research: Plus.* 2021;5(4).
230. Corrado A, Cici D, Rotondo C, Maruotti N, Cantatore FP. Molecular Basis of Bone Aging. *International Journal of Molecular Sciences.* 2020;21(10):3679.
231. Gardner C. Morphological analysis of osteoclastogenesis induced by RANKL in mouse bone marrow cell cultures. *Cell Biology International.* 2007;31(7):672–82.
232. Tiedemann K, Le Nihouannen D, Fong JE, Hussein O, Barralet JE, Komarova SV. Regulation of Osteoclast Growth and Fusion by mTOR/raptor and mTOR/rictor/Akt. *Frontiers in Cell and Developmental Biology.* 2017;5.

233. Blair HC, Teitelbaum SL, Ghiselli R, Gluck S. Osteoclastic Bone Resorption by a Polarized Vacuolar Proton Pump. *Science*. 1989;245(4920):855–7.
234. Becerikli M, Jaurich H, Schira J, Schulte M, Döbele C, Wallner C, Abraham S, Wagner JM, Dadras M, Kneser U, Lehnhardt M, Behr B. Age-dependent alterations in osteoblast and osteoclast activity in human cancellous bone. *Journal of Cellular and Molecular Medicine*. 2017;21(11):2773–81.
235. Gruber HE, Ivey JL, Thompson ER, Chesnut CH, 3rd, Baylink DJ. Osteoblast and osteoclast cell number and cell activity in postmenopausal osteoporosis. *Miner Electrolyte Metab*. 1986;12(4):246–54.
236. Wescott D, Steadman D, Miller N, Sauerwein K, Clemmons C, Gleiber D, McDanel C, Meckel L, Bytheway J. Validation of the Total Body Score/Accumulated Degree-Day Model at Three Human Decomposition Facilities. *Forensic anthropology*. 2018;1(3):143–9.
237. Wescott DJ. Recent advances in forensic anthropology: decomposition research. *Forensic Sciences Research*. 2018;3(4):278–93.
238. Lennartz A, Hamilton M, Weaver R. Moisture Content in Decomposing, Desiccated, and Mummified Human Tissue. *Forensic Anthropology*. 2020;3(1):1–16.
239. Matuszewski S, Hall MJR, Moreau G, Schoenly KG, Tarone AM, Villet MH. Pigs vs people: the use of pigs as analogues for humans in forensic entomology and taphonomy research. *International Journal of Legal Medicine*. 2020;134(2):793–810.
240. Connor M, Baigent C, Hansen ES. Testing the Use of Pigs as Human Proxies in Decomposition Studies. *Journal of Forensic Sciences*. 2018;63(5):1350–5.
241. Material Transfer Agreements. Toronto, ON: University of Toronto; 2025 [updated 2025; cited 2025 June 10]; Available from: <https://research.utoronto.ca/research-innovation-agreements/material-transfer-agreements>.
242. Material Transfer Agreements (MTA). Boston, MA: Boston University; 2025 [updated 2025; cited 2025 June 10]; Available from: <https://www.bu.edu/research/collaboration-partnership/industry-collaboration/material-transfer-agreements/>.
243. Research & Innovation. Hamilton, ON: McMaster University; 2025 [updated 2025; cited 2025 June 10]; Available from: <https://research.mcmaster.ca/home/support-for-researchers/forms-checklists/>.
244. Centre de Recherche. Montréal, QC: Centre Hospitalier de l'Université de Montréal; 2025 [updated 2025; cited 2025 June 10]; Available from: <https://www.chumontreal.qc.ca/en/crchum>.
245. Les ententes de transfert de matériel. Montreal, QC: Université de Montréal; 2025 [updated 2025; cited 2025 June 10]; Available from: <https://recherche.umontreal.ca/ressources/contrats/ententes-de-transfert-de-materiel/>.



## Appendices

### Appendix A

#### 6.1 Individual Sample Demographic Data

**Table 6.1-1: Sample demographic data for Ch. 3.2 & 4.2.  
Note date of death and Sample ID number have been  
removed to protect anonymity.**

Sample	Age	Assigned Sex	Category
1	57	M	Perimortem
2	52	M	Perimortem
3	53	M	Perimortem
4	52	M	Perimortem
5	50	M	Perimortem
6	57	M	Perimortem
7	30	M	Perimortem
8	51	M	Perimortem
9	47	M	Perimortem
10	93	M	Postmortem
11	90	F	Postmortem
12	70	M	Postmortem
13	80	M	Postmortem
14	85	F	Postmortem
15	96	M	Postmortem
16	88	M	Postmortem
17	108	F	Postmortem
18	90	F	Postmortem

## Appendix B

### 6.2 Protein Data

**Table 6.2-1: Raw protein data.**

Sample	Sample Group	Osteopontin Histogram Intensity	Osteopontin Intensity Standard Deviation	Osteocalcin Histogram Intensity	Osteocalcin Intensity Standard Deviation	OPN:OC Mean Intensity Ratio	OPN:OC Standard Deviation Ratio
1	"Perimortem"	1450.2800	5638.8300	877.9060	3323.7700	1.6520	1.6965
2	"Perimortem"	2686.6000	7029.5900	637.7620	2961.5400	4.2125	2.3736
3	"Perimortem"	731.7500	3713.5100	1839.4000	4334.0300	0.3978	0.8568
4	"Perimortem"	5645.0307	13079.7323	712.5220	3699.0000	7.9226	3.5360
5	"Perimortem"	5688.0800	13199.4000	331.9830	1945.4100	17.1336	6.7849
6	"Perimortem"	486.4790	2044.3200	526.3020	2258.3100	0.9243	0.9052
7	"Perimortem"	623.1890	3142.8530	1394.5570	5257.8560	0.4469	0.5977
8	"Perimortem"	679.5180	3739.1900	335.7140	1336.1100	2.0241	2.7986
9	"Perimortem"	1394.5600	5257.8600	285.0840	1610.0300	4.8918	3.2657
10	Early Postmortem	1196.9700	3937.0000	734.5137	3479.8057	1.6296	1.1314
10	7-Day Postmortem	287.5980	1290.0800	2082.3400	6023.6200	0.1381	0.2142
10	14-Day Postmortem	541.3430	541.3430	890.4600	3954.1500	0.6079	0.1369
11	Early Postmortem	489.2110	2989.9500	719.1830	3805.7900	0.6802	0.7856

<b>Sample</b>	<b>Sample Group</b>	<b>Osteopontin Histogram Intensity</b>	<b>Osteopontin Intensity Standard Deviation</b>	<b>Osteocalcin Histogram Intensity</b>	<b>Osteocalcin Intensity Standard Deviation</b>	<b>OPN:OC Mean Intensity Ratio</b>	<b>OPN:OC Standard Deviation Ratio</b>
11	7-Day Postmortem	343.0060	1066.6800	422.6090	1485.4000	0.8116	0.7181
11	14-Day Postmortem	967.2520	3433.4800	1125.9800	3410.0300	0.8590	1.0069
12	Early Postmortem	887.9970	2655.5000	1370.8300	5166.6200	0.6478	0.5140
12	7-Day Postmortem	737.4480	2482.1800	628.8440	2875.9600	1.1727	0.8631
12	14-Day Postmortem	611.5900	3058.6900	2379.5100	7664.6100	0.2570	0.3991
13	Early Postmortem	445.7730	1044.1000	2253.1700	6910.9300	0.1978	0.1511
13	7-Day Postmortem	390.4050	1436.3300	139.8200	407.0290	2.7922	3.5288
13	14-Day Postmortem	211.3020	687.4620	557.6680	2632.4700	0.3789	0.2611
14	Early Postmortem	1523.3000	6148.2000	204.3670	2052.2200	7.4537	2.9959
14	7-Day Postmortem	1024.1300	4808.4000	133.5400	689.5150	7.6691	6.9736
14	14-Day Postmortem	541.1390	1382.7600	504.5390	2056.2200	1.0725	0.6725
15	Early Postmortem	31.7822	200.7460	766.2860	3414.7600	0.0415	0.0588
15	7-Day Postmortem	76.2467	531.1680	683.2910	2534.6200	0.1116	0.2096
15	14-Day Postmortem	575.1610	2594.7900	1852.6400	8179.4700	0.3105	0.3172
16	Early Postmortem	1006.6200	3519.6600	407.3810	527.4840	2.4710	6.6725
16	7-Day Postmortem	86.5186	676.1600	606.9720	2693.2800	0.1425	0.2511
16	14-Day Postmortem	147.0180	1096.9200	121.0560	379.7100	1.2145	2.8888

<b>Sample</b>	<b>Sample Group</b>	<b>Osteopontin Histogram Intensity</b>	<b>Osteopontin Intensity Standard Deviation</b>	<b>Osteocalcin Histogram Intensity</b>	<b>Osteocalcin Intensity Standard Deviation</b>	<b>OPN:OC Mean Intensity Ratio</b>	<b>OPN:OC Standard Deviation Ratio</b>
17	Early Postmortem	264.2560	1120.3500	880.0020	3107.8400	0.3003	0.3605
17	7-Day Postmortem	440.0360	2341.2400	169.4360	773.2730	2.5971	3.0277
17	14-Day Postmortem	175.5260	705.9170	1298.0400	3523.9400	0.1352	0.2003
18	Early Postmortem	2437.4600	356.4620	651.8290	1452.0400	3.7394	0.2455
18	7-Day Postmortem	4125.6300	4463.7900	593.5770	1763.0600	6.9505	2.5318
18	14-Day Postmortem	509.5200	1376.9600	247.6460	1263.1200	2.0575	1.0901

## Appendix C

### 6.3 Cellular Data

**Table 6.3-1: Osteoclast count data**

Sample	Sample Group	Raw Osteoclast Count	Osteoclast Count by Bone Volume (per mm <sup>3</sup> )
1	"Perimortem"	64	0.1295
2	"Perimortem"	77	0.1379
3	"Perimortem"	41	0.1305
4	"Perimortem"	60	0.1193
5	"Perimortem"	48	0.0398
6	"Perimortem"	84	0.2160
7	"Perimortem"	65	0.1418
8	"Perimortem"	59	0.0945
9	"Perimortem"	65	0.1292
10	Early Postmortem	34	0.0764
10	7-Day Postmortem	11	0.0227
10	14-Day Postmortem	9	0.0179
11	Early Postmortem	32	0.0513
11	7-Day Postmortem	23	0.0402
11	14-Day Postmortem	12	0.0200
12	Early Postmortem	42	0.0524
12	7-Day Postmortem	28	0.0388
12	14-Day Postmortem	9	0.0129
13	Early Postmortem	31	0.0482
13	7-Day Postmortem	24	0.0352
13	14-Day Postmortem	10	0.0159
14	Early Postmortem	45	0.0982
14	7-Day Postmortem	30	0.0630

<b>Sample</b>	<b>Sample Group</b>	<b>Raw Osteoclast Count</b>	<b>Osteoclast Count by Bone Volume (per mm<sup>3</sup>)</b>
14	14-Day Postmortem	18	0.0385
15	Early Postmortem	51	0.0970
15	7-Day Postmortem	23	0.0426
15	14-Day Postmortem	12	0.0224
16	Early Postmortem	70	0.1724
16	7-Day Postmortem	20	0.0482
16	14-Day Postmortem	13	0.0338
17	Early Postmortem	48	0.0946
17	7-Day Postmortem	27	0.0547
17	14-Day Postmortem	11	0.0209
18	Early Postmortem	50	0.1091
18	7-Day Postmortem	37	0.0857
18	14-Day Postmortem	19	0.0427

## Appendix D

### 6.4 Ethical Approval

#### 6.4.1 Ethics Approval and Division of Anatomy Use of Samples Approval Letters

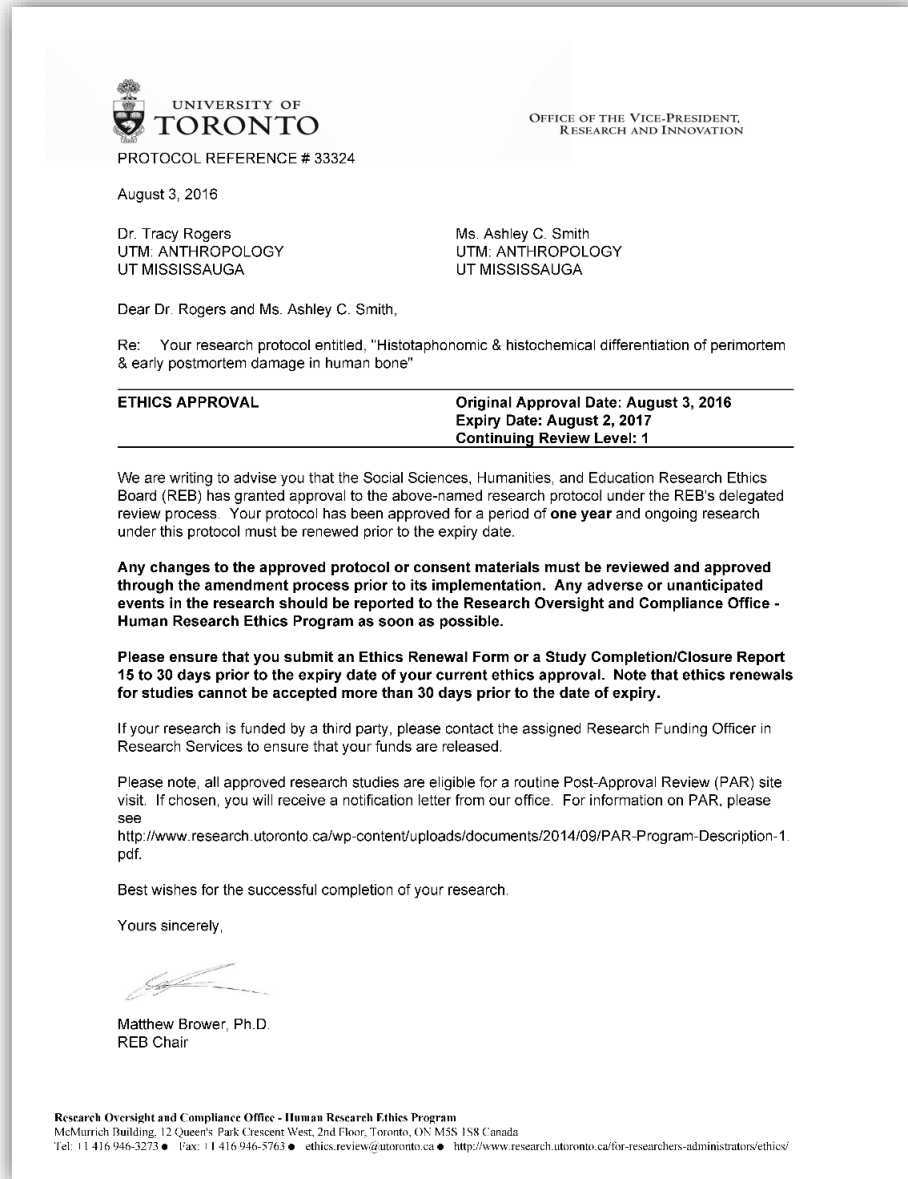


**Figure 6.4.1: University of Toronto Human Research Ethics Protocol #33324 initial approval letter.**



July 6, 2021

Tracy Rogers/ Ashley Ciunine Smith  
Department of Anthropology  
University of Toronto - Mississauga

Dear Ashley Ciunine Smith:

**Re: RESEARCH – Histochemical and Histopathologic differentiation of perimortem trauma from early postmortem- REF # ANA-034-2021**

I am pleased to inform you that your application for the use of anatomical material has been approved for **July 2021-April 2022 (on-going research)**. Your reference number is **ANA-034-2021**.

Infectious diseases are a potential threat for everyone involved in the handling of human tissue. The Division of Anatomy has adopted policies to reduce this risk wherever possible. Nevertheless, we cannot absolutely exclude the possibility of infection with pathogens or infectious disease. We therefore recommend that all samples be treated with the same precautions (i.e. Universal Precautions) afforded a live patient with communicable disease.

The availability of specimens is not always predictable and consequently, in some rare instances, the exact number of specimens requested cannot always be supplied.

**The estimated cost for materials is \$20.00 per specimen (15 in total)**

If an order is canceled and/or material is sent but not used, you will be charged a fee for the restocking/preparation of the materials for custom work, at our discretion.

If the material is to be used outside of the Division of Anatomy, you will also be required to pay the cost for transport to the alternate site and back to the Division by a licensed funeral director. All specimens must be returned to the Division of Anatomy within a reasonable time frame for cremation and burial in accordance with the provisions of the Anatomy Act of Ontario.

Enquiries regarding the specimens in this approved request for anatomical materials should be directed by email to **Mr. Ian Bell** ([i.bell@utoronto.ca](mailto:i.bell@utoronto.ca)).

You will be invoiced for the costs of the materials within 60 days of their use. Invoices are to be paid upon receipt. Invoices not paid after 30 days from receipt will be subject to a 10% service charge. Enquiries regarding invoices or debit memos for the order should be directed by email to **Anatomy Division** ([anatomy@utoronto.ca](mailto:anatomy@utoronto.ca)).

Regards,

A handwritten signature in black ink, appearing to be "Cindi Morshead".

Cindi Morshead, Ph.D.  
Professor & Chair  
Division of Anatomy, Department of Surgery

c.c. Ian Bell

DIVISION OF ANATOMY, DEPARTMENT OF SURGERY  
Medical Sciences Building, 1156-1 King's College Circle, Toronto, ON M5S 1A8 Canada  
Tel: +1 416 978-2690 • Fax: +1 416 978-3844

**Figure 6.4.2: University of Toronto Division of Anatomy sample approval letter. Note: 15 samples were approved but given the pace of collection post COVID-19 this was reduced to 9 individuals.**

## 6.4.2 Use of Samples Approval from CHUM

Use of Samples approval from the Department of Pathology, Laboratory of Bone Histomorphometry, Centre Hospitalier de l'Université de Montréal (CHUM) in Montréal, QC for use of the clinical and biopsy samples used in Ch. 2.2, 2.3, 3.2, 4.2, and 5.1 was based on the University of Toronto Human Research Protocol #33324 (Fig. 6.4.1). The timeline of approval is as follows:

- 1) 29 April 2016: Initial conversations via email begin between primary research and Dr. Natalie Dion at CHUM on project feasibility.
- 2) 18 August 2016: Initial web meeting between primary researcher, Dr. Tracy Rogers, Dr. Natalie Dion, Dr. Louis-George Ste-Marie (CHUM) on project objectives and avenues of CHUM collaboration.
- 3) 20 October 2016: Email between Dr. Natalie Dion and primary researcher on CHUM specimens.
- 4) 07 November 2016: Dr. Natalie Dion agrees to send samples for pilot project, confirms shipment of samples.
  - a. These samples were used in Phase 2 of Ch. 2.2
- 5) 08 January 2018: primary researcher and CHUM begin process of establishing formal collaboration for larger project
  - a. Project to include Ch. 2.3, 3.2, 4.2, and 5.1
- 6) 15 February 2018: Primary researcher delivers web presentation on project to Dr. Natalie Dion and Dr. Louis-George Ste-Marie from CHUM
- 7) 10 July 2018: Dr. Natalie Dion emails regarding project particulars, including ethics requirement.

NOTE: Only the material related to ethics has been included below, all else has been removed.

a. Hi Ashley,

I'm so happy to have news from you...The budget is almost finished. However, it has to be approved by Dr Ste-Marie and Dre Nguyen (chief of pathology department) before sending it to you...The problem encountered with ethics review, is that we do not have the consent of patients (or informed their family) for the use of their bone biopsy in a research project. This is a requirement of the CHUM lawyer. Meanwhile of finding a solution to this issue, is it possible to send me a PDF copy of your latest ethical approval letter? This has to be attached to documents submitted to our ethics committee...

I am looking forward to our future collaboration!

Best regards,

Natalie

- b. The University of Toronto Human Research Protocol #33324 (Fig. 6.4.1) was emailed on 10 July 2018
  - c. 7a was the only email received that communicated the need for ethics approval. No future communication noted CHUM ethics approval
- 8) 22 November 2018: Dr. Natalie Dion emails to confirm thin sectioning of samples has begun
- 9) 13 December 2018: Dr. Natalie Dion emails to confirm samples are ready to be shipped to the University of Toronto
- 10) 16 January 2019: Dr. Natalie Dion emails to confirm samples have been shipped to the University of Toronto
- 11) October 2024 – May 2025: Attempts made to verify CHUM ethics protocol applications and approvals by Primary Researcher through the Research Ethics Office of the CHUM and the University of Montreal
- 12) 27 May 2025: Communicated with Antonine Rigaud of the CHUM Research Ethics Office
  - a. No research ethics protocol applications or approvals found between July 2018 and January 2019 from either Dr. Dion, Dr. Ste-Marie, or Dr. Nguyen related to present project,
  - b. No protocol applications found related to the original project title, U of T Ethics Protocol Number, primary researcher, or supervisor,
  - c. No protocol application found that included keywords or goals related to the present project, or any historical variations of that project.

### 6.4.3 Material Transfer Agreements

In addition to ethics approvals and agreements for use of samples, such as approved by the University of Toronto Division of Anatomy (Fig. 6.4.2), another avenue that should have been explored prior to the execution of the various research projects was engaging in Material Transfer Agreements, specifically with regards to the samples that were not generated from within the University of Toronto system. These samples would include the non-human samples from Boston University used in Ch. 2.2, the Apollonian samples used in Ch. 2.2, and the clinical/unembalmed/perimortem/biopsy samples used in all chapters. Material Transfer Agreements, in general, are contractual agreements between institutions and researchers that define both the provenance and ethical history of the samples from the originating institution(s) and the terms of use for the samples from the receiving institution(s). In fact, however, they can be more complicated with their terms and requirements varying from institution to institution (241-245). While the technical need and applicability of MTAs could be questioned with regards to each institution, overall, the situation merits that the presence of such agreements is better from a safety, confidentiality, and ethical standpoint than the absence of an agreement. Further, while providing institutions (Boston University, CHUM, and McMaster) may not provide much clarity on the need for an MTA, as the primary researcher, and the research was conducted at the University of Toronto, then the overarching guiding institution should have been the University of Toronto.

1. When it comes to the University of Toronto's MTA guidelines, unfortunately the Vice President's Office of Research and Innovation does not provide many details regarding the applicability of MTAs. The U of T's webpage on MTAs (241) is mainly limited to *who* can apply (faculty) and the process of submission. There is, however, a template document on biological MTAs found on the webpage but even this template offers limited clarity as the University of Toronto MTA is designed for a more commercial and industrial sphere. The language of the template, including definitions are relegated to commercialization, patent rights, and intellectual property, while also generating liability shields as well (241).
2. The first external sample group that would require an MTA would be that of the 5-Year pig samples that derived from Boston University (originally from Tufts University) used in Ch. 2.2 Phase 1. The Boston University Office of Research offers the greatest guidance on the need and

use of MTAs of all institutions directly associated with this project (242). In Boston University's guidelines, however, it is recommended for non-human and non-hazardous materials exchanges take place for "basic research purposes without a formal legal agreement" unless certain criteria are met (242). Among those criteria where an MTA is required is when the material is obtained by Boston University from a third party (i.e., Tufts University) which "requires further action for transfer (e.g., another MTA, sponsored research agreement, purchase order, commercial purchase, or other restrictive agreement...)" (242). In this particular case, the samples were originally procured by Boston University from Tufts University via purchase order and after completion of a decomposition study at Boston University the remaining bones were to be destroyed. The bones used in Ch. 2.2 Phase 1 were collected from Boston University (specifically Donald Siwek, Ph.D.) years prior to the start of the present study, with full knowledge that they would be used in future Ph.D.-level research. At the time there was no mention of a need for an MTA from Boston University, suggesting that the original purchase order from Tufts University was non-restrictive in nature. While obtaining an MTA from Boston University would have still remained the most prudent avenue of approach to assure provenance and ethical handling both prior to and post receivership by the primary researcher, under the guidelines posted by Boston University, this does not appear to be an requirement given the nature of the remains and the present study, no MTA was needed (242).

3. The next set of samples that should have required an MTA would have been the Apollonian samples used in Ch. 2.2 Phase 2. These samples have a rather complicated provenance as while they were used under the auspices of the University of Toronto (under University of Toronto Human Research Protocol #33324), the samples were under the care of co-author and co-researcher Lelia Watmaniuk, M.Sc. as part of her, then, Ph.D. research. At the time of the research phase of the project, Lelia Watamaniuk, was a Ph.D. student at McMaster University. The samples themselves, however, were on-loan to Ms. Watamaniuk's PhD. Supervisor, Tracey Prowse, Ph.D. at McMaster University from Anne Keenleyside, Ph.D. of Trent University. According to Lelia Watamaniuk, Dr. Keenleyside was aware that the samples were used for the research projects that resulted in Ch. 2.2 Phase 2, and that they were secure in nature and used in an ethical manner, but Ms. Watamaniuk was not aware if there was any legal agreement such as an MTA related to the transfer of the Apollonian samples. Unfortunately, in 2022 Dr. Anne Keenleyside passed away, and her material, including the Apollonian collection have been

transferred and accessed into the Department of Anthropology at McMaster University. Additionally, when Lelia Watamaniuk was completed with the Apollonian samples used in her research, those, too, were returned and accessed into the collection at McMaster University. As the only direct relationship that existed between the primary researcher and an outside researcher was with McMaster University, an MTA with McMaster would have been prudent, similar to those with Boston University. However, the guidelines for MTAs with McMaster University are very limited, with almost all of the guidance being directed for commercial and intellectual property rights rather than ethical rights (243).

4. The last sample group with which an MTA would be required is the biopsy samples used as the clinical/unembalmed/perimortem samples in all chapters that came from the Centre Hospitalier de l'Université de Montréal (CHUM). For all of the sample groups derived from outside of the University of Toronto system, this sample group was the one in most need of an MTA as it utilized human tissues from individuals who theoretically were still living. However, while the need for an MTA with these samples is most clear cut, the guidelines for MTAs with both CHUM and the University of Toronto are not as clear cut. The primary area of complexity is that CHUM, though semi-independent of the Université de Montréal with its own Centre de Recherche, the CHUM Centre de Recherche does not have a page nor any reference to Material Transfer Agreements or Les Ententes de Transfert de Matériel (244). Though semi-independent, as CHUM's Centre de Recherche does not have a guideline on MTAs, one must turn to the Le Recherche at the Université de Montréal. With the Université de Montréal's Les Ententes de Transfert de Matériel there is almost no guidelines on the need and use, but rather is limited to definitions, particularly related to commercial, patent, and intellectual property rights with regards to materials and research (245).

With all of the samples used in the present study, regardless of their origin, the need for a binding legal agreement that defines the provenance, ethical history, and allowable use of the samples should have been obtained. However, while obtaining these agreements would have been beneficial, the guidance and language used by all of the institutions (University of Toronto, Boston University, McMaster University, and the Centre Hospitalier de l'Université de Montréal/ Université de Montréal) is either simplistic to the point of invalidating the use for this present study or, in the case of Boston University, expressly excludes the need of an MTA for the samples.

## Copyright Acknowledgements

This dissertation was developed from the publication articles using the following copyright information:

- I. Use of Laser Scanning Confocal Microscopy in the Detection of Diagenesis in Bone (Smith *et al* 2022): License # 1360128-1, ISSN 0022-1198, John Wiley & Sons, Approved 30 May 2023

In addition to the article listed above, two images were used with permission from copyrighted sources; specifically Figures 1.2.1 and 1.2.2. The following is the copyright information:

- II. Laser scanning confocal microscopy: history, applications, and related optical sectioning techniques (Paddock SW, Eliceiri KW 2012): License # 5591520070707, Springer, Approved 17 July 2023.